ASSESSMENT OF DAMAGE TOLERANCE LEVELS IN FRP SHIP STRUCTURES

HOLLY JACQUELINE PHILLIPS

Doctor of Philosophy

January 1997

Department of Ship Science

University of Southampton

TO

STEVE

UNIVERSITY OF SOUTHAMPTON

ABSTRACT

FACULTY OF ENGINEERING & APPLIED SCIENCE

SHIP SCIENCE

Doctor of Philosophy

ASSESSMENT OF DAMAGE TOLERANCE LEVELS IN FRP SHIP STRUCTURES

by Holly Jacqueline Phillips

This work deals with assessing the significance of delamination-type defects in FRP ship structures. The purpose of the work has been to identify the internal structural load path that leads to failure and the tolerance of the structure to delamination cracks once these have formed. The approach adopted in the investigation seeks to link material behaviour at laminate and structural levels and to compare stress-based criteria with fracture-based parameters.

At the laminate level, analytical models have been developed to examine the stability of delaminated beam panels. The influence on delamination on material stiffness properties and critical energy release rates have also been assessed. It has been shown that delaminations close to the material or structural surface are more likely to propagate than deeper ones. A similar study has been carried out for delaminations in typical generic structural elements such as top hat stiffeners and tee joints. In this instance the analysis was carried out using finite element techniques. The structural modelling confirmed the trends observed at laminate level and also pointed to defects in curved regions of the structure (e.g. roots of the overlaminate in a top hat stiffener or tee joint) as being more susceptible to propagation.

The second major facet of this work deals with comparing stress- and fracture-based criteria in context of damage tolerance. Here the focus has been entirely on the structural elements. Response of both the tee joint and top hat stiffeners to loading conditions that may be encountered in service has been studied. The finite element analysis has revealed that the primary causes for the structural delaminations are the high, through-thickness stresses in the overlaminate. The modelling has been based on evaluating G and J-integral for different delamination cracks in the tee joints and top hat stiffeners. A detailed parametric study has been conducted to examine the influence of crack location, boundary conditions, loading regimes and material choice on the likelihood of crack propagation. The study has revealed close agreement between high through-thickness stress regimes and large G values for cracks in such locations.

Overall, the results of this work form the first stage in enabling ship operators to draw-up guidelines for repair of defects in FRP structures.

CONTENTS

LIST OF FIGURES

LIST OF TABLES

LIST OF APPENDICES

Acknowledgements

I would like to thank the following :

Dr. Ajit Shenoi for his continual guidance and encouragement throughout the project.

Lt. Cdr. Mark Gray for his help and advice during the project and also his predecessor Lt. Cdr. Ken Holt who gave initial direction to the work.

Professor Geraint Price, Head of the Ship Science Department, for the use of the departmental facilities and Mr. Philip Wilson for answering all my questions with regard to the computing aspects.

My fellow co-workers in this project at DRA, Dunfermline, Richard Court, David Elliot, Philip Lay, Andrew Swift, Richard Trask and Professor John Sumpter, the Project Manager.

My colleagues in the Ship Science Department, Sue, Simon, Guy, Paul R, Leigh, Jan, Ming Yi and Paul W for their help and advice over the last few years.

1. INTRODUCTION

Fibre Reinforced Plastics (FRP) have been used in the marine industry for over 50 years. Small craft were constructed out of Glass Reinforced Plastics (GRP) using hand lay-up techniques and mainly cold-cure polyester resin with E-Glass reinforcement. Over the last twenty years, the use of plastics in the marine industry has increased dramatically. The main advantages of using FRP over the more traditional material of wood are that E-Glass and polyester resin are less costly, there are reduced maintenance and repair costs and probably most importantly, complex shapes can be easily fabricated. Table 1.1 shows typical mechanical properties of selected FRP laminates (Shenoi & Wellicome).

The construction of larger vessels over about 40 m in length traditionally incorporate steel since it is cheap. However, fishing boats are now more commonly built out of FRP owing to the dramatic weight savings over steel which allows for greater speeds to be achieved. This is a very important factor since fishing boats of UK waters commonly fish between 20 and 30 miles off shore. In addition, GRP has advantages in naval applications. For example, GRP is used in the construction of naval mine sweepers owing to its low magnetic signature. This is important so as not to activate any mines in the vicinity of the ship. GRP is, like any other structural material, subject to damage.

Damage in laminated composites can be caused as a result of environmental effects such as strength and stiffness losses due to humidity, temperature, impact, wave slamming loads and cyclic loads or residual stresses due to in-built thermal stresses resulting from the manufacturing processes. Residual stresses can be avoided by controlling the curing temperature and also the speed at which the layers of the laminate are built up. In some cases, only one layer of laminate per hour can be built up to allow for the increase in temperature due to the release of exotherms. The actual damage can take the form of resin matrix cracks, fibre splitting and delamination which is the most common type.

Delaminations frequently occur in ship structures such as tee connections and top hat stiffeners. Damage due to delamination in critical areas in these connections and stiffeners can greatly effect the structural integrity of the structure and hence the load bearing capabilities of the ship as a whole. 'Root whitening' or delamination, is frequently seen in both tee connections and top hat stiffeners. Current practice involves the identification and repair of all defects in such structures. Part of this work

investigates the possibility that certain defects under specific loading conditions may not have an adverse effect on the structural integrity of the structure. Such defects, however, must be carefully monitored for any further signs of damage.

The main aim of the current work is to understand more fully the damage tolerance of FRP ship structures.

Specific objectives are as follows :

(i) to examine current approaches of treating delamination-induced damage and its influence on the structural performance of FRP laminates and structural elements,

(ii) to derive analytical solutions to predict delamination onset and the subsequent consequences on the remaining structural integrity of the laminates typically used in ships,

(iii) to understand the influence of delaminations on the behaviour of ship structural elements such as tee joints and top hat stiffener connections.

2. DELAMINATION - INDUCED DAMAGE: A CRITICAL REVIEW

2.1 What is a Delamination ?

Delamination can be described as the separation of individual layers of a laminated structure. They occur as a result of interlaminar stresses which arise due to the mismatch in elastic constants of the adjacent laminae. The stage at which delamination occurs within a laminate depends upon a number of factors such as material properties, geometry and loading conditions. The failure of a laminate caused by delamination can be divided into three stages (Lagace) as shown in Figure 2.1 : (a) the initiation of delamination, (b) the growth of the delamination either with or without interaction with other damage modes and (c) failure of the laminate.

The interlaminar stresses which cause delamination are created by impacts, eccentricities in the structural load paths or from discontinuities within the structure itself. Typical design details which may induce the local out-of-plane loads which cause interlaminar stresses are (Garg) straight or curved free edges, ply terminations, bonded joints and bolted joints.

Highsmith and Reifsnider (1986) described delamination as being part of a damage development and accumulation process rather than as an isolated damage mode. Delaminations which occur can arise when one layer or ply debonds from another, for example due to high through-thickness stresses where the two layers are torn apart, or due to excessive interlaminar shear stresses where the two layers slide over each other. The effect of delaminations on the behaviour of laminated composites under various loading conditions is discussed in detail in the following sections.

2.2 Operational Experiences in Ships

The hulls of naval GRP ships are typically constructed of woven roving/chopped strand mat in a polyester resin. There are frequently many penetrations throughout the structure for access and piping for example. The openings are cut out of the finished laminate and may vary in size from 1 inch for an overboard discharge to 10 feet for larger openings in the main deck for equipment removal. The smaller holes which are not always reinforced may be the cause of cracks due to stress concentrations.

Cable compared three types of defect, void content, cracks from holes of different diameters and delamination length and calculated the quantity or dimension of each which would be necessary to cause failure at a given value of stress. This comparison was carried out in order to determine their relative importance. It was found that delaminations and cracks extending from circular cut outs were the critical defect types. It was reported that fishing boats were experiencing extensive delamination due to wave slamming loads. The hulls did not, however, fail catastrophically which emphasises the need for damage tolerance estimations.

The weakest links and most probable sources of failure in FRP ships are bonded structural connections such as tee joints and top hat stiffeners (Smith, 1972). This is due to the absence of load-bearing fibres across bonded interfaces, the low strength under tensile and shear forces of the thin layer of resin forming the bond, the occurrence of stress concentrations caused by geometric irregularities and manufacturing imperfections and the tendency of small cracks and imperfections within the bond to propagate under load.

2.3 Experimental Work on Laminates

O'Brien (1982) carried out a series of tensile tests on graphite-epoxy laminates. These laminates were specifically designed to delaminate due to high interlaminar normal stresses at the edges. The tests were carried out so as to calculate the experimental stiffness losses due to the presence of delaminations and to validate the analytical predictions. Chow and Yang also investigated the stiffness and strength losses due to edge delaminations in angle-ply graphite/epoxy laminates under tension. Finite element models were generated to yield the stress distributions along the interface of the delamination. Rybicki et. al. carried out both experimental and analytical studies to study the initiation and growth characteristics of free-edge delamination of boron/epoxy laminates under tension. Finite element models were used to determine the stiffness losses due to delamination in addition to estimate axial strains.

Suemasu investigated the compressive stability of composite panels with through-width multiple delaminations using analytical, numerical and experimental techniques. Teflon sheets were inserted in composite panels of woven glass/epoxy laminae to represent the delaminations. It was found that the compressive buckling load suddenly started to

decrease when the multiple delaminations reached a certain length. Highsmith and Reifsnider (1982) tested a series of glass/epoxy laminates in both static tension and tension-tension fatigue to investigate the effect of matrix cracking on the stiffness losses. The results were compared with those obtained from finite element modelling and for three out of the four specimen types were in good agreement.

Highsmith and Reifsnider (1986) carried out a series of experiments on graphite/epoxy laminates firstly to induce delamination within the specimens and then to measure the local surface displacements close to the delaminations. Kim & Soni tested a series of angle-ply graphite/epoxy laminates under in-plane tension and compression. The interlaminar stress levels at the onset of delamination have been calculated using an analytical approach and compared with the experimental values. A reasonable correlation was achieved.

Sczepanik-Weinmann et. al. carried out compression tests on composite panels of prepreg tapes of unidirectional carbon/epoxy with teflon film inserted to form the across-width delamination. The results showed that crack propagation occurred initially from one of the free edges. This was contrary to results of a 3D finite element analysis for which the highest values of the mode I and mode II strain energy release rates (see Appendix 2A) were found to be in the inner part of the specimen model. Compression tests were also carried out by Wang & Socie on prepreg E-Glass/epoxy laminates. Failure strains were measured for both unidirectional (UD) and cross-ply (CP) laminates and failure envelopes in terms of stress and strain were plotted. Under longitudinal compression, the UD laminates failed by delamination or fibre shear and CP laminates failed by delamination or by kink band. Under transverse compression, the UD laminates failed by delamination or matrix shear and CP laminates failed by delamination or kink band. In both cases, however, failure due to delamination occurred at lower stresses than failure by other modes.

Sun & Kelly investigated the failure modes in angle structures analytically and from experimentation for two different prepreg materials, graphite/epoxy and fiberglass/epoxy. The results showed that in the laminates with groups of 0 degree plies on the outer surface, the bending stresses were the most significant which caused radial bending cracks. On further loading, the high through-thickness tensile stresses caused failure due to delamination. The laminates not containing the 0 degree plies near the surface only

exhibited the delamination failure. These failure modes were evident from both the experiments and the analytical models.

2.4 Modelling Laminate Behaviour under Compressive Loads

In the case of a compressive in-plane loading, the reduction of load bearing capability of a delaminated beam or a delaminated strip of a long plate can be derived in terms of a critical buckling load. i.e the load at which the beam will buckle. Moshaiov & Marshall calculated the buckling load from a closed-form analytical solution whose derivation was based upon a linear differential equation with harmonic solutions by solving the continuity and compatibility conditions.

Moshaiov and Marshall also formulated an energy approach to the same problem. An equation for the potential energy of the delaminated strip was written in terms of the bending energy and work done by the external compressive load. A series of displacement functions were specifically selected so as to satisfy the continuity condition and hence yield the total potential energy in three series which each represent the three regions of the delaminated strip, the undelaminated region and the upper and lower delaminated regions. The total potential energy was then minimised to yield the eigenvalue which can be solved to yield the critical buckling load.

Simitses et. al. derived a one-dimensional model to predict the critical buckling loads for delaminated homogeneous plates. The model assumed that the plate material was linear elastic and that the delamination existed and would grow in a plane parallel to the reference plane. The properties of the plate were assumed to be homogeneous or, at most, orthotropic. In addition, the delamination was assumed to exist prior to the application of the compressive load. The primary state of the plate as it was loaded while the plate remains flat can be characterised by the boundary and continuity conditions. The solution of the buckling equations can be found from the boundary, continuity and kinematic continuity conditions using a perturbation technique. A system of 24 linear algebraic equations can be derived and reduced to 9 by manipulation. The characteristic equation can be solved by forcing the determinant of 9×9 matrix to equal zero. Thus the lowest eigenvalue which is obtained is a measure of the critical buckling load.

Chai et. al. used fracture mechanics-based criteria (also see Appendix 2A) to investigate delamination growth, stability and arrest of laminated plates. For a plate whose unbuckled portion can be considered as infinitely thick, the strain to cause buckling and the postbuckled shape can be calculated from beam theory. Equations for the buckled layer have been derived from which the strain energy release rate for the laminate can be calculated. Plots of strain energy release rate versus delamination length have been generated which indicate that delamination growth of an initially delaminated plate may be characterised as stable, unstable or as unstable growth followed by a stable growth. The variety of behaviour was found to be dependent upon the dimensions of the delamination, the load at which it was introduced and the fracture energy.

Ilic & Williams carried out a series of experiments on aluminium plates bonded with epoxy to investigate the buckling characteristics of a plate consisting of bonded isotropic layers containing a through-width delamination. Plots of strain energy release rates, G, versus delamination length have been generated using analytical, numerical and experimental approaches. It was concluded that local buckling appears to be the key factor defining the initiation of delamination growth under compressive loading. This is due to a rapid increase in the strain energy release rate when local buckling occurs. It was also found that following local buckling, G increased rapidly as the delamination length increased but then decreased towards an asymptotic value. In addition, it was suggested that for a given specimen, a critical delamination length exists below which any delaminations present cannot grow.

Pierson & Roorda discussed the buckling problem with relation to circular plates. The study was carried out for which the delaminated area was located between a near surface and midplane condition. A numerical integration was carried out to solve a fourth order formula in order to calculate the critical buckling load for clamped conditions. The main conclusions drawn were that a delamination close to the surface of a plate with a large radius possessed a significantly reduced buckling load when compared with the buckling load of an undelaminated plate. Partridge et. al. used numerical and analytical approaches to analyse delamination behaviour in circular laminates. Both approaches yielded values of the strain energy release rate, G, for different values of the delamination radius. Both methods gave consistent results which concluded that as the radius of the delamination increased, the strain energy release rate tended to an asymptotic value. Pavier & Clarke derived a special finite element so as to represent the

delamination buckling and growth in a composite laminate containing an embedded circular delamination. Values of the total strain energy release rate were calculated at points along the delamination edge for three applied compressive strains. The values compared extremely well with an existing three dimensional model for the same problem.

2.5 Analysis of Woven Laminates

Analytical solutions exist which allow the calculation of stiffness losses due to delamination which are based upon the intact laminate stiffness (see Section 2.6). Thus, in order to characterise the delamination behaviour of woven laminates it is necessary to obtain an approach which can yield the mechanical properties of the laminate prior to delamination.

Marine-type laminates used in the construction of the hull shell, bulkheads and out-of-plane joints consist largely of woven roving layers of E-glass embedded in a polyester resin. The woven fabric consists of warp and weft (or fill) yarns interwoven in two orthogonal directions. These types of fabrics are easier to handle and their fabrication costs are lower than the traditional unidirectional laminates. Out-of-plane joints such as tee connections and top hat stiffeners consist partly of mixed layers of woven layers and chopped strand mat layers. Since the exact lay-up sequence of each woven or mixed laminate may not be the same in each case, it is important to be able to estimate the mechanical properties of such laminates relatively simply.

A progression has been made from one-dimensional models to two-dimensional models and those applicable only to satin weaves and are discussed in Appendix 2B.

Experiments carried out by Ishikawa et. al. (1985) show that the elastic properties of eight harness carbon/epoxy satin weave are well predicted by the bridging model discussed in Appendix 2B. There is, however a discrepancy between the experimental derived moduli and the predictions based upon the fibre undulation model, or crimp model as it is sometimes named, both with and without bending constraints.

It is, therefore, necessary to turn to an alternative approach in order to predict the elastic properties of plain weave composites. Naik and Shembekar derived a two dimensional

model for a plain weave lamina which takes into account the inherent undulations in both the warp and the fill threads. Shape functions define the warp and fill yarn undulation and classical laminate plate theory is assumed to apply. Correlation between the predicted elastic properties and experimental results was found to be good. Shembekar and Naik extended the analyses to predict the elastic behaviour of plain weave laminates which also compare favourably with experimental results.

Two types of the two dimensional model discussed in Appendix 4C are described, namely the series-parallel model and the parallel-series model. Pieces of a section parallel to the loading direction are in series and are assumed to be under constant stress and pieces of a section across the loading direction have mid-plane strains which are assumed to be the same. An assembly of pieces of a section along the loading direction with an iso-stress condition is termed a series model and an assembly of pieces across the loading direction with an iso-strain condition is termed a parallel model. The series-parallel model (SP) involves the assemblage of pieces of a section along the loading direction with an iso-stress condition followed by an assemblage of pieces along the loading condition under an iso-strain condition. The parallel-series model (PS) involves an assemblage of pieces across the loading condition under iso-strain conditions followed by an assemblage of pieces across the loading direction under iso-stress conditions. The models also take into account the lamina shifts which occur naturally within woven laminates.

Shembekar and Naik carried out analyses to investigate the effect of laminate configurations for plain weave laminates on the elastic constants predicted by both the SP model and the PS model. The predictions given by both models were very similar but the values derived from the SP model tended to be lower than those derived from the PS model. In addition, Shembekar and Naik carried out a series of experiments on both carbon/epoxy and E-glass/epoxy laminates to compare their elastic properties with the theoretical predictions. The predicted models using both models were in very good agreement with the experimental results.

This section has described the models from the literature which can be used to predict the elastic properties of woven laminates. The mosaic model omitted the fibre continuity and undulation. The fibre undulation model considered the continuity and undulation of the threads but only for a one-dimensional strip of fabric. Neither the mosaic model nor

the fibre undulation model gave accurate predictions. The bridging model successfully predicted the elastic properties of eight-harness satin weaves. Since the woven laminates used in ship construction are largely plain weave, the SP two dimensional model has been used to calculate the elastic properties of marine-type woven laminates. However, none of the above models allow the calculation of entirely mixed laminates such as those consisting of any combination of chopped strand mat, unidirectional layers and woven layers and this requires investigation.

2.6 Strength and Fracture Criteria for Laminates

The presence of delaminations can greatly reduce the ability of a laminate to withstand load. Damage tolerance levels of a particular structure containing a defect depends largely on the type of loading configuration which it must sustain. The loading may be transverse, compressive, tensile or a combination of load conditions.

An analytical method was developed by Liu et. al. to investigate the interaction between matrix cracking and delamination propagation in $[0_n/90_m]$ symmetrical laminates subjected to a transverse concentrated line load. The model consisted of three parts, a stress analysis, a contact analysis and a failure analysis. The stress analysis calculated the stresses and deformations of the laminate. The contact analysis dealt with the condition of the surface of both the matrix cracks and the delaminations. By combining the stress and contact analyses, an equation for the total potential energy of the laminate was derived. The equation for total potential energy can be solved using a non-linear finite element technique and can then be minimised to yield the equilibrium equations. The failure analysis adopted failure criteria in order to predict the initiation of matrix cracking and delamination and to model the growth of initial damage. Crack propagation was modelled using a mixed mode fracture criteria.

The predicted load-displacement relationship for both flat panels and curved composite beams subjected to a concentrated line-loading compared very well with test data for graphite/epoxy laminates. The main conclusions of the work were that matrix cracking in the 90 degree plies initiated damage in the laminates which then resulted in the formation of delamination. In addition, delamination growth induced by intra-ply bending cracks was stable and progressive whereas delamination growth induced by intra-ply shear cracks was very unstable and catastrophic.

Tensile loadings may also cause the formation of delaminations due to the presence of imperfections such as voids or the presence of edge effects. High interlaminar stresses develop close to the laminate edge due to the mismatch in Poisson contraction of the individual plies. O'Brien (1982) utilised a simple rule-of-mixtures formulation in association with classical laminate theory to calculate the stiffness loss due to delamination. The derivation assumed that the sublaminates resulting from complete delamination(s) underwent the same axial strain and that the volume fraction of the phases (i.e the fibre and the matrix) which was used in the rule of mixtures was equal to the sublaminate thickness ratio, (i.e the sublaminate thickness ratio equalled the ratio of the sublaminate to the total laminate thickness). The approach can be adopted to investigate the stiffness loss due to either complete or partial delaminations. O'Brien also carried out experiments for angle-ply graphite/epoxy laminates which were especially designed to delaminate at the edges under a tensile loading, in order to verify the theory put forward. The experimental results compared extremely well with the rule of mixtures analysis.

O'Brien's method can be used to yield values of stiffness loss due to delamination and critical delamination onset strains for laminates under tension. However, there are a number of restrictions which should be noted as follows. In order to predict the stiffness loss of a delaminated laminate, the interface where the delaminations are most likely to occur must be known. Finite element modelling could be used to establish which interface is most likely to delaminate for each particular laminate under consideration but this is altogether time consuming. The method is, however, an extremely simple way of calculating which interfacial delamination would cause the greatest stiffness loss under tension for particular laminates. The methods described above to calculate stiffness loss for laminates under tensile loadings are applicable to unidirectional laminates where the rule of mixtures theory can be applied. In order to calculate the stiffness losses in woven or mixed laminates, an approach must first be adopted by which the elastic properties can be calculated using an adapted laminate theory.

The mixed mode fracture criteria used by Liu et. al. was adopted to predict the initiation of crack propagation. Onset of crack growth was based upon critical mode I and mode II strain energy release rates. The fracture criteria was introduced into a two dimensional numerical model and if delamination was predicted either as a result of matrix cracking or delamination, then an appropriate crack or delamination would be introduced into the

model. The results of the work showed that mixed mode fracture dominated onset of shear crack-induced delamination whilst mode I fracture dominated the onset of bending crack-induced delamination. The growth of a delamination induced by a bending crack was found to be governed by mode I fracture and that induced by a shear crack depended strongly on the critical mode II strain energy release rate. It was also concluded that ply orientation and curvature can greatly affect the response and the damage tolerance of laminated composites.

O'Brien (1982) derived an expression to predict the critical strain level at which delamination onset would occur. The critical strain value depends upon the critical strain energy release rate necessary to form the delamination, the stiffness of the undamaged laminate, the stiffness of the laminate containing the delamination and the total thickness of the laminate. The stiffness of the delaminated laminate can be carried out reasonably simply using a combined rule of mixtures and classical laminate theories as discussed above. The value of the critical strain energy release rate for the particular laminate can either be taken as a quoted material property from the literature for the laminate or calculated from a series of experiments.

Brewer and Lagace developed an analytical quadratic stress criterion which can be used to predict the stress at which delamination initiation occurs. The analytical predictions were compared with results using a strain energy release rate approach and experimental data. The results showed that for graphite/epoxy specimens of three different lay-ups, the strain energy release rate approach did not accurately correlate with the experimental data. The critical value of the strain energy release rate was found to be dependent upon the ply thickness. The quadratic stress criterion, however, showed excellent correlation with the delamination initiation stresses yielded from experiments.

An additional cause of delamination is that of matrix cracks which run parallel to the fibres in a layer. The interlaminar stresses which occur in the interfaces at the matrix crack tip may cause local delaminations to develop and grow. The equation used to calculate the critical strain for delamination onset due to edge delamination (or complete delamination) (O'Brien, 1982) was adapted to yield an equation to calculate the value of critical strain at which delamination occurred as a result of matrix cracks (O'Brien 1985). The latter value of critical strain depends upon the number of delaminations growing from the matrix ply crack, the modulus of the locally delaminated region, the

thickness of the uncracked layers, the modulus and thickness of the undamaged laminate and the critical strain energy release rate which was determined from experiments.

2.7 Structural Elements

2.7.1 Top Hat Stiffeners

The stiffness of large unsupported panels constructed of fibre reinforced plastic (FRP) materials is inherently low. Thus it is necessary to stiffen such panels by a suitable method, usually in the form of top hats. The top hat stiffener provides shear stress transmission between the shell and frame flanges as a result of local bending forces. Such bending forces may be the result of lateral pressure such as a slamming load or concentrated lateral loads.

There are various designs of top hat stiffeners. However, typical geometries comprise a flange plate (the shell) and 12 layers of overlaminate (the frame) which consist of woven roving E-glass and polyester resin, a fillet resin and a non-structural core material. The geometries of two types of Top Hat stiffeners are given in Figures 2.2 and 2.3. Figure 2.2 represents the type of top hat used in mine counter-measure vessels (type I) and Figure 2.3 shows the single role mine hunter (type II) type of top hat stiffener. The main difference between the two types top hat stiffeners is the back fill angle of the resin. Originally, the flange plates and overlaminate in the type I stiffeners were bolted down with non-magnetic titanium bolts to prevent them from peeling apart. This was extremely expensive and thus an alternative type of stiffener was sought which did not require the addition of bolts. The type II stiffener was the answer with one alteration being the angle of back fill. The type II needed a larger area of fillet bond because of the large stiffness difference between the frame and shell material and also because bolts were no longer used. In addition a highly flexible resin, urethane acrylate replaced the polyester with milled glass resin used in the type I stiffeners.

Dodkins et. al. carried out a sensitivity study with regard to the top hat design variables, fillet radius, overlaminate thickness, gap between base panel and stiffener and angle of fillet backfill. This sensitivity study was carried out for straight pull-off loads. There is also a need to investigate the internal stress distributions for other loading configurations such as three-point bending and reverse bending.

Shenoi and Hawkins, 1995 carried out a series of finite element investigations on top hat stiffener connections. This was to compare the effect of altering the overlaminate thickness, fillet angle of backfill, fillet radius and the gap between the lower tip of the web and the top of the flange on the behaviour of the top hat. For a straight pull off load, the model deflections and internal stress patterns were noted for each case. The results showed that, based upon stiffness and strength evaluations, the gap size and angle of backfill have only a limited effect on the top hat's performance. The fillet radius and overlaminate thickness, however, have a significant effect.

Smith, 1990 made a comprehensive study of top hat stiffened panels. He examined the compressive buckling of longitudinally and transversely stiffened panels using both analytical and numerical techniques. Smith focused more on the global buckling behaviour of the overall panel rather than on the internal stress distributions within the stiffener connections.

2.7.2 Tee Joints

Tee joints are constructed at the intersection of two orthogonal plates (web and flange). The joints are formed by placing laminated strips of reinforcement cloth on both sides of the joint (overlaminate). The resulting gap formed between the cloth and plates is filled with an appropriate resin. i.e one which is compatible with the cloth material and is generally one with a high yield strength. A typical tee joint configuration is shown in Figure 2.4. The flange (hull shell) and the web (bulkhead, for example) typically consist of E-glass woven roving (WR) cloth set in polyester resin. The overlaminate or boundary angle consists of layers of E-glass woven roving and layers of chopped strand mat (CSM) comprising chopped E-glass in a polyester resin. The fillet material in these joints is typically of urethane acrylate which is a flexible resin whose quoted strain to failure is 100 % (Scott Bader).

The main function of the tee connection is to transfer a variety of loads between the hull shell and the bulkhead and/or the deck. These loads may be a combination of flexural, tensile and shear loading. For example, if a watertight bulkhead was to flood, then the tee connection would be subjected to a bending moment and shear loadings. The typical type of failure of these types of connections is that of 'root whitening' which is caused by the presence of delaminations in the tee joint boundary angle. It is this type of

damage which is of most concern. Delaminations in such joints can occur as a result of different types of loading. For example, high through-thickness stresses caused by impact loads can cause a mode I (opening) type of delamination. In addition, a mode II (tearing) type of delamination may be the result of excessive interlaminar shear loads.

Hawkins & Shenoi and Shenoi & Hawkins, 1992 carried out a parametric study on the influence of fillet radius, number of plies in the boundary angle, material make-up of the boundary angle plies, edge gap between the web and flange of the joint and also the shape of the web edge. An experimental and numerical investigation was carried out for tee joints subjected to a 45 degree pull off load as shown in Figure 2.5. The three most significant variables were found to be the fillet radius, overlaminate thickness and gap size. The main conclusions were that the fillet radius should be as large as possible since this reduces the fillet stresses and thus delays failure. Premature delamination can be avoided by reducing the overlaminate thickness and thus reducing the through-thickness stresses. The gap size had little effect on the overall deflections or stresses in the overlaminate. Also, for fillet radii greater than 75 mm, gap size had little effect up to 20 mm.

A significant amount of work has been carried out to optimise the design of tee connections. Hawkins et. al. looked into the variations of tee joint design by carrying out a series of experiments to compare the joint stiffness variations and their failure modes. Shenoi and Hawkins, 1992 investigated the physical behaviour of tee joints for a variety of fillet resin material and joint geometries. A series of finite element (FE) models were generated to investigate the internal stress patterns and failure modes of each joint configuration. The FE models were generated using three dimensional (3D) solid and shell elements. In order to represent the laminate construction, it was necessary to use eight noded solid elements which can be stacked on top of each other to represent the boundary angle. In the boundary angle only two elements were used in the through-thickness direction.

Work has been extended to cover sandwich structure joints also. The geometry of a typical sandwich tee joint is shown in Figure 2.6. Hicks et. al. carried out a series of experiments and numerical analyses on sandwich tee joints. The core material was a PVC type of density 80 kg/m^3 and the inner skin was constructed of E-glass WR with the outer skin being made up of E-glass/Kevlar WR. The thin boundary angle was

constructed of E-glass bonding tape. The loading conditions for the experiments was a 45 degree pull off load. The load-deflection characteristics were investigated as were the internal stress patterns from the finite element results. The precise sequence of failure depends on the applied load and boundary conditions but there are common features. The dominant failure modes of these type of joints is cracking in the resin fillet or in the core of the web piece (Shenoi & Violette).

Theotokoglou & Moan carried out a series of straight pull off tests on sandwich tee joints. The core was a PVC core with density 100 kg/m^3 and the skins were constructed from E-Glass/Polyester. Two major failure modes were observed from the experiments, (i) failure in the laminate, glue and attachment lap and failure of the web core and (ii) shear fracture of the flange core. A series of nonlinear finite element models were also generated by Theotokoglou & Moan to investigate strain and stress distributions to determine the regions most susceptible to failure initiation. It was found that the strength of the sandwich tee joints was slightly influenced by the weight of the attachment lap but less dependent upon the lap geometry.

It was reported in Elliott and Hawkins et. al. that the main damage mode in single skin tee joints was that of delamination in the curved region of the boundary angle. Trask reported that the delamination was, in fact, within the inner layers chopped strand mat layers. Hawkins et. al. also reported that the delaminations occurred within the inner plies of the overlaminate.

Dodkins et. al. generated a series of finite element models to yield the internal stress distributions within tee joints of different geometric configurations. The analysis was only carried out for a 45 degree pull-off load and only two elements through the thickness of the overlaminate were modelled. There is a need to investigate alternative loading configurations and the resulting failure modes. In order to carry this out using finite element modelling, one element per layer through the thickness of the overlaminate must be modelled.

2.8 Drawbacks in Existing Work

The majority of experimentation and hence validation with analytical and/or numerical models has been carried out on materials generally used in the aerospace industry such

as graphite/epoxy angle-ply laminates. Materials used in the marine industry such as glass/polyester laminates have not been discussed in as much depth. In addition, the materials discussed are largely angle-ply or cross-ply unidirectional laminates. The marine industry commonly use woven laminates or mixed laminates which are comprised of a combination of woven, unidirectional and random short fibre composites such as chopped strand mat. Hence, the approaches discussed above must be directed towards typical marine-type laminates. Also, additional analytical approaches must be sought so as to analyse mixed laminates.

A large amount of work has been carried out on the study of delamination of beams and plates consisting of unidirectional laminates. Approaches include stiffness assessments of unidirectional laminates containing delaminations under different loading conditions and prediction of load or strain levels at which existing delaminations will propagate. Fracture mechanics approaches have also been used to predict delamination propagation based on critical values of strain energy release rates. These techniques, however, have not been applied to cracks present in marine-type structures.

Significant research has been carried out to analyse laminates under single-mode loading such as pure tension and pure compression. The loading configuration which is imparted to typical ship structural elements is rarely single-mode but mixed-mode. As a result, analytical solutions are not available for these types of components. Consequently, the structural assessment of delaminations in structures such as tee joints and top hat stiffeners cannot be carried out using analytical approaches owing to their complexity.

Limited work has, however, been directed towards the analysis of structural components. Strength- and stiffness- based approaches have been used to calculate the structural capabilities of laminated tee connections and top hat stiffeners. In both cases, the numerical models which have been generated do not represent each layer within the overlaminate. As a result, the internal stress patterns and most significantly the overlaminate through-thickness stresses, are not truly representative. In addition, in the case of the tee joints, delaminations between layers of the overlaminate cannot be modelled. In the case of top hat stiffeners, the overall behaviour of stiffened panels has been investigated rather than the stress distributions within the top hat itself, such as the fillet. In addition, the experimentation and numerical modelling has generally been restricted to one loading configuration.

The approaches adopted to identify regions of potential weakness in structural components have largely been strength-based. This is a useful method but it is limited in that specific parameters cannot be calculated to assess the stability of delaminations present in the structure. Fracture mechanics techniques also provide a useful basis but have been restricted to the analysis of laminated plates.

3. METHODOLOGY ADOPTED

3.1 Local Structure Assessment

It is necessary to yield approaches which can be used to assess the remaining load-bearing capability of laminates containing delaminations. The approaches discussed below analyse the response of laminates under tensile forces and those under compressive forces. The analysis used to calculate the elastic properties of both angle-ply, woven and mixed laminates under tension is discussed in Section 4.2. The analytical approach used to calculate laminate stiffness reduction due to delamination is discussed in Section 4.3. Section 4.4 investigates the compressive stability of delaminated beams for beams of varying thickness with across-width delaminations of varying lengths and through-thickness location. Three approaches are discussed, namely analytical and numerical approaches which have been validated from experimental data.

It is proposed that techniques involving the calculation of fracture mechanics criteria are to be used in the assessment of structural elements. Thus, it is first necessary to validate the method for simple laminates. This has been carried out using both an analytical approach and a numerical approach by way of finite element modelling.

The delaminations which occur in the tee joint boundary angles are primarily in the chopped strand mat layer (Trask). Thus a delamination in a layer of chopped strand mat has been represented by a straight crack in a layer of resin sandwiched between two layers of chopped strand mat. This model is analysed under loadings which represent the two modes of fracture, mode I (opening) and mode II (shearing). Both analytical and numerical techniques can be used to calculate the fracture parameters. These methods are discussed in Section 4.5.

3.2 Structural Element Strength-Based Assessment

Once the behaviour of delaminated laminates has been investigated, it is necessary to understand the behaviour of typical ship structural elements under various loading configurations and also how they behave when they contain delaminations. Two types of structural element have been focused on in this study, due to the large number of them present in FRP ships. These are top hat stiffeners and tee joints. Owing to the

complexity of the problem, the analysis is to be carried out using finite element (FE) modelling. The main aim of this work is to identify the regions of weakness within the structural element which are most susceptible to damage under a variety of loading conditions.

3.2.1 Top Hat Stiffeners

Stiffness and strength assessments are to be carried out using FE modelling for two types of top hat stiffener. The results of the modelling shall be compared with experimental findings to validate the model and to further understand the internal stress patterns within the stiffener when subjected to a selection of loading conditions. The loading conditions are chosen so as to represent as closely as possible the modes of loading which are present in the ship itself. These include, (i) a three point bending load which represents a docking load, (ii) a reverse bend which represents loading due to hull bending under hydrostatic loading and (iii) a straight pull-off load which is caused by inertia effects of machinery fixed to the top hat, for example. The internal stress distributions allow the regions within the stiffener which are most likely to damage to be identified. This work is discussed in Chapter 5.

3.2.2 Tee Joints

Stiffness and strength assessments are to be carried out on a typical tee joint configuration found in FRP ships. The model is to be generated so as to represent a tee joint loaded under a three point bending load. This is a typical load scenario which is present during docking. Experimental results (Elliott, 1994) show that the successive reductions in the joint stiffness are due to the delaminations which occur in the overlaminate. For this reason an iterative approach will be used which involves the generation of six finite element models. The first model represents the undamaged model and the second model represents the initial failure mode due to a fillet crack. Models three to five represent successive amounts of delamination in the overlaminate with model five representing the final failure scenario noted from the experiments. Model six represents additional delamination along both the overlaminate/web and overlaminate/flange interfaces. The internal stress patterns are to be investigated in each case and regions likely to be damaged identified. These models are discussed in Chapter 6.

3.3 Structural Element Energy-Based Assessment

The delaminations which occur in both types of structural element are most commonly found in the overlaminate material (Elliott, 1994). Thus, it is these delaminations which shall be represented using a fracture mechanics approach. The finite element models used in the strength assessment are to be adapted so as to include special elements which can be used to calculate fracture parameters such as the strain energy release rate, G, or the J-Integral, J.

In the first instance, the behaviour of the structure should be assessed as to whether it is linear or non-linear. If it is thought that the behaviour of the structural element is to be non-linear owing to the non-linear stress/strain characteristics of the fillet resin for example, then the J-integral must be calculated. The strain energy release rate is only applicable to linear elastic fracture mechanics (LEFM) so would not be applicable in this case. If, however, LEFM is found to be applicable then both the strain energy release rate and the J-integral are valid parameters and the calculated values of each are equal. i.e G = J. In the case of LEFM, the calculation of both parameters also provides a check that the correct value has been obtained.

It shall be assumed that a delamination can be represented by a crack in each case.

3.3.1 Top Hat Stiffeners

A series of finite element models shall be generated with a single delamination in the overlaminate material of the top hat stiffener. Values of the fracture parameters will be calculated with a view to understanding the effect of crack depth and crack length when the top hat stiffener is subjected to three loading conditions, three point bending, reverse bending and a straight pull-off load. The results of the study are given in Chapter 7.

3.3.2 Tee Joints

Finite element models are to be generated in order to investigate the presence of delaminations on the behaviour of a tee joint structural element. A sensitivity study will be carried out to look into the effect of loading condition, boundary condition, boundary location, material properties, crack depth and crack length on the values of J-integral

and/or strain energy release rates. In addition, the effect of the presence of two cracks in the overlaminate will be investigated, as well as the presence of a crack in the central curved region of the overlaminate. The results of the study are given in Chapter 8.

3.4 Comparison of the Two Approaches used in the Study of Tee Joints

It is important to determine whether similar trends and conclusions can be drawn regardless of which method has been employed. For this reason, the results derived from both the strength assessment and the energy-based assessment shall be compared in the case of the tee joints. The findings are reported in Chapter 9.

4. DELAMINATIONS IN LAMINATES

4.1 Background

Although delaminations are not the only type of defect which occur in laminated composites, they are considered to be the most common. Delaminations may be caused by high through-thickness stresses or, indeed, by excessive interlaminar shear stresses. The presence of delaminations within a laminate consequently effect its structural performance which depends upon the loading condition. Under tensile loads, delaminations tend to reduce the laminate stiffness and strength and under compressive loads, delaminations cause the laminate to be more susceptible to buckling. In order to calculate the stiffness losses due to delamination, it is first necessary to calculate the stiffness of the laminate which does not contain delaminations. This is because the stiffness reduction is directly related to the laminate stiffness prior to delamination. Section 4.2 discusses the methods by which the laminate stiffness can be calculated for either unidirectional, woven or mixed laminates. Section 4.3 discusses the analytical approach derived by O'Brien (1982) which can be used to calculate the stiffness loss due to delamination in unidirectional or angle-ply laminates.

Section 4.4 describes the method by which the critical buckling load of a delaminated beam under compression can be calculated and Section 4.5 introduces the way in which the calculation of fracture mechanics criteria can be used to assess the stability of specific cracks.

4.2 Calculation of Laminate Stiffness

Laminates can be constructed from either unidirectional (UD) plies, woven roving (WR) plies, layers of chopped strand mat (CSM) which is a random short fibre composite or a combination of all three types to yield a so-called mixed laminate. The laminate stiffness prior to delamination can be calculated from classical laminate theory (CLT) for unidirectional laminates and adapted CLT for woven or mixed laminates. These three methods are described below.

4.2.1 Unidirectional Laminates

The laminate stiffness can be calculated using classical laminate theory and depends upon the properties of the constituent fibre and resin properties, the orientation of each layer and the total laminate thickness. The laminate constitutive equation which relates the laminate stiffness matrices, in-plane forces and edge moments to the laminate mid-plane strains and curvatures is given in Equation 4.1. The derivation of Equation 4.1 is given in Appendix 4A.

$$\begin{bmatrix} \{N\} \\ \{M\} \end{bmatrix} = \begin{bmatrix} [A] & [B] \\ [B] & [D] \end{bmatrix} \begin{bmatrix} \{\varepsilon^0\} \\ \{\kappa\} \end{bmatrix} \qquad (4.1)$$

where: [A] is the in-plane stiffness matrix

[B] is the coupling stiffness matrix

[D] is the flexural stiffness matrix

{N} is the applied force vector

{M} is the applied moment vector

$\{\varepsilon^0\}$ is the laminate mid-plane strains vector

$\{\kappa\}$ is the laminate plate curvatures vector

The elements of the laminate compliance matrices [a], [b] and [d] can be calculated by inverting Equation 4.1. Thus, [a], [b] and [d] can be evaluated from the following equations.

$$\begin{aligned} [a] &= [A]^{-1} - [b][B][A]^{-1} \\ [b] &= -[A]^{-1}[B][d] \\ [d] &= ([D] - [B][A]^{-1}[B])^{-1} \end{aligned} \qquad (4.2)$$

Hence, the laminate material properties can be calculated from the elements of the laminate compliance matrix [a] and the laminate thickness, t. The full derivation of Equation 4.3 is shown in Appendix 4B.

$$E_x = \frac{1}{a_{11}\, t} \; ; \quad E_y = \frac{1}{a_{22}\, t} \; ; \quad G_{xy} = \frac{1}{a_{66}\, t} \; ; \quad \nu_{xy} = -\frac{a_{21}}{a_{11}} \qquad (4.3)$$

where: a_{11}, a_{22} etc. are elements of the laminate in-plane compliance matrix

E_x is the laminate longitudinal elastic modulus

E_y is the laminate transverse modulus

G_{xy} is the laminate shear modulus

υ_{xy} is the Poisson ratio

If the laminate is symmetrical then matrix [B] in Equation 4.2 equals zero and [a] = $[A]^{-1}$. Consequently, the in-plane stiffness of a laminate can be re-written as:

$$E_x = \frac{1}{X_{11}t} \tag{4.4}$$

where: X_{11} is the first element of the laminate in-plane stiffness matrix [A].

4.2.2 Woven Laminates

Chapter 2 discussed a variety of analytical approaches which can be used to calculate the mechanical properties of woven laminates. It has been concluded that the most appropriate method (Naik & Shembekar) is based on the approach used for unidirectional laminates but which also takes into account the inherent fibre undulations in both the warp and fill (or weft) direction. Figure 4.1 shows a typical unit cell of a woven lamina.

As discussed in Chapter 2, the series-parallel (SP) model has been used in this particular case since it tends to give lower values for laminate moduli than the parallel-series (PS) model. Thus, the estimates will be, at worst, conservative rather than too high.

The final equations for the average laminate compliance matrices based upon the SP model are shown in Equation 4.5, the derivation of which is given in Appendix 4C.

$$\bar{A}_{ij}^{sp}, \bar{B}_{ij}^{sp}, \bar{D}_{ij}^{sp} = \frac{1}{a_w+g_w} \int_0^{a_f+g_f} \bar{A}_{ij}^{s}(y), \bar{B}_{ij}^{s}(y), \bar{D}_{ij}^{s}(y) \tag{4.5}$$

where: A_{ij}^{sp}, B_{ij}^{sp} and D_{ij}^{sp} are the average in-plane stiffness constants calculated from the SP model

Inversion of Equation 4.5 gives rise to the average in-plane compliance constants similar to those given in Equation 4.2. Similar equations to those in Equation 4.3 can then be used to calculate the mechanical properties of the woven laminate.

4.2.3 Mixed Laminates

Since the majority of laminates used in the marine industry are comprised of a mixture of laminae such as UD and WR in top hat stiffeners (see Chapter 5) and WR and CSM in tee joint overlaminates (see Chapter 6), it is important to be able to calculate the mechanical properties of such laminates whose laminae could be stacked in any combination. Figure 4.2 shows a typical mixed laminate. Appendix 4D describes the method by which the stiffness matrices, [A], [B] and [D] can be calculated for a CSM lamina.

The overall stiffness matrices for a mixed laminate, $A_{ij}(x,y)_{MIX}$, $B_{ij}(x,y)_{MIX}$ and $D_{ij}(x,y)_{MIX}$ which are functions of the location in the x-y plane can be calculated from Equations 4.6.

$$
\begin{aligned}
A_{ij}(x,y)_{MIX},\ B_{ij}(x,y)_{MIX},\ D_{ij}(x,y)_{MIX} = \\
\sum_{k=1}^{M} A_{ij}^{k}(x,y)_{UD},\ B_{ij}^{k}(x,y)_{UD},\ D_{ij}^{k}(x,y)_{UD} \\
+ \sum_{k=1}^{N} A_{ij}^{k}(x,y)_{CSM},\ B_{ij}^{k}(x,y)_{CSM},\ D_{ij}^{k}(x,y)_{CSM} \\
+ \sum_{k=1}^{P} A_{ij}^{k}(x,y)_{WL},\ B_{ij}^{k}(x,y)_{WL},\ D_{ij}^{k}(x,y)_{WL}
\end{aligned}
\tag{4.6}
$$

where: M is the total number of Unidirectional (UD) laminae
N is the total number of Chopped Strand Mat (CSM) laminae
P is the total number of Woven Laminae (WL)

Inversion of Equation 4.6 gives rise to the average in-plane compliance constants similar to those given in Equation 4.2. Similar equations to those in Equation 4.3 can then be used to calculate the mechanical properties of the mixed laminate.

4.3 Laminate Stiffness Reduction due to Delamination

Laminates which have delaminated can be considered to be either completely or partially delaminated. Complete delamination indicates that the delamination has spread across the complete laminate width as well as along its length. Partial delamination, on the other hand implies that only part of the interface is delaminated. The analytical approach to calculate stiffness losses due to complete delamination is discussed in Section 4.3.1 and due to partial delamination in Section 4.3.2.

4.3.1 Stiffness Loss due to Complete Delamination

An example of complete delamination is given in Figure 4.3. In this particular figure, there are two complete delaminations which form three sublaminates. i.e the laminate is separated into three distinct regions. Equation 4.7, the derivation of which is given in Appendix 4E, gives the equation from which the stiffness of the completely delaminated laminate, E^*, can be calculated.

$$E^* = \frac{\sum_{j=1}^{n} E_j t_j}{t} \qquad (4.7)$$

The complete delamination(s) result in the formation of n sublaminates each of thickness t_j and stiffness E_j. The total laminate thickness is t.

4.3.2 Stiffness Loss due to Partial Delamination

Complete delamination is not always present as in the case of edge delamination (Wang). In this case, the delamination can be considered to be partial. Figure 4.4 shows an example of partial delamination. Appendix 4F describes the analysis of a partially delaminated laminate. The final equation gives the stiffness of the laminate which has been partially delaminated, E_p, and is given in Equation 4.8.

$$E_p = (E^* - E_{LAM}) \frac{A}{A^*} + E_{LAM} \qquad (4.8)$$

where: E_p is the stiffness of a partially delaminated laminate
E^* is the stiffness of a completely delaminated laminate
E_{LAM} is the intact laminate stiffness

A is the delaminated area

A^* is the total interfacial area

4.4 Instability of Delaminated Beams

Delaminations which form in laminated beams have the effect of reducing their compressive stability. It is important to be able to predict the critical buckling stress. i.e the compressive stress at which the delaminated beam will buckle. A simple closed-form analytical approach derived by Moshaiov & Marshall is to be used in this case. Other approaches have been discussed in Section 2.4. A numerical analysis by way of finite element modelling has also been carried out for comparative purposes.

4.4.1 Analytical Approach

Moshaiov & Marshall derived a simple one-dimensional model to calculate the stress at which a delaminated beam would buckle. The approach takes into account the delamination depth and length in addition to the material properties of the laminate. Figure 4.5 shows a diagram of a typical delaminated beam. The beam is considered to be split into three parts (i=1,2,3) : (1) represents the region of the beam which is not delaminated, (2) represents the delaminated region of the beam which has delaminated but not buckled and (3) represents the region of the beam which has both delaminated and buckled. The length and thickness of parts 1 to 3 are denoted by l1 to l3 and t1 to t3 respectively.

The theory described in Appendix 4G gives rise to the characteristic equation which is an implicit expression for λ_1 as shown in Equation 4.9.

$$\frac{\lambda_1 t_1^3}{6\sin\lambda_1 l_1}\cos\lambda_1 l_1 + \frac{\lambda_1 t_2^2 t_1}{6\sin\frac{\lambda_1 l_2 t_1}{2t_2}}\cos\frac{\lambda_1 t_1 l_2}{2t_2} + \frac{\lambda_1 t_3^2 t_1}{6\sin\frac{\lambda_1 l_3 t_1}{2t_3}}\cos\frac{\lambda_1 l_3 t}{2t_3} + \frac{t_1 t_2 t_3}{l_3} = 0 \qquad (4.9)$$

where: t_i is the thickness of part i (i=1,2,3).

l_i is the length of part i (i=1,2,3).

λ_1 relates the axial force per unit length to the laminate stiffness from Equation 4.10.

$$\lambda_i^2 = \frac{P_i}{D_i^*} \quad ; \quad D_i^* = \frac{Et_i^3}{12(1-\nu^2)} \tag{4.10}$$

and P_i is the axial force per unit length in the i^{th} part

D_i^* is the stiffness of the i^{th} part

t_i is the thickness of the i^{th} part

E is the Young's modulus

υ is the Poisson ratio

Equation 4.10 can be re-written for the critical case to give:

$$\lambda_{cr}^2 = \frac{P_{cr}}{D_i^*} \quad ; \quad D_i^* = \frac{Et_i^3}{12(1-\nu^2)} \tag{4.11}$$

Hence, the value for the critical load, P_{cr}, is obtained by first solving Equation 4.9 to yield λ_{cr}, and substituting this value into Equation 4.11 to yield P_{cr}. The value of the critical buckling stress, σ_{cr}, is obtained from Equation 4.12.

$$\sigma_{cr} = \frac{P_{cr}}{Area} \tag{4.12}$$

where: Area is the area of the ends of the beam subjected to the applied load

4.4.2 Finite Element Modelling Approach

The analytical approach described is peculiar to a beam or panel strip. The geometry under consideration is not always of such simplicity. Analysis of complex geometries such as tee joints and top hat stiffeners rely on numerical approaches such as finite element (FE) modelling. Therefore, since the results of the FE models generated for complex geometries cannot be compared with existing analytical solutions, it is important to compare the results of both approaches when applied to simple beams. Both three dimensional (3D) and two dimensional (2D) models have been generated to represent beams containing delaminations of various depths and lengths.

(A) Three Dimensional (3D) Models

The 3D model has been constructed of solid anisotropic brick elements whose details

are given in Appendix 4H. Each element is generated from eight nodes each of which has three translational degrees of freedom. In the FE model, an example of which is shown in Figure 4.6, the end of the beam subjected to the applied pressure is fixed in the through-thickness and across width direction. The other end of the beam is fixed in all three degrees of freedom. A buckling analysis which is discussed in Appendix 4I has been carried out to yield the value of stress at which the beam will buckle in addition to the buckled shape.

A sensitivity study has been carried out to determine the effect of mesh density on the value of critical stress and the buckled shape of the beam. The material properties and dimensions of the beams represented in the FE models are shown in Table 4.1.

Table 4.2 shows the effect of number of elements along the delamination length on the value of the critical buckling stress and the buckled shape. Diagrams of what is meant by 'typical' buckled shape and 'non-typical' buckled shape are shown in Figures 4.7(a) and 4.7(b) respectively. It is shown in Table 4.2 that the number of elements along the delamination length has a significant effect on both the value of the critical buckling stress and on the buckled shape. Figure 4.8 shows plots of the analytical and numerical values of critical buckling stress against the number of elements along the delamination length. The graph shows that as the number of elements along the delamination length increases, the value of critical buckling stress calculated from the FE models reduces towards the analytical value. The FE values below the analytical value do not give the correct buckled shape so can be considered to be invalid results.

The effect of the number of elements across the beam width has also been investigated. Table 4.3 gives the values for the element aspect ratio, critical buckling stress and the buckled shape. It is shown that the number of elements across the beam width has an insignificant effect on the value of the critical buckling stress.

(B) Two Dimensional (2D) Models

The 2D model has been constructed of structural solid elements whose details are given in Appendix 4J. Each element is generated from four nodes each of which has two translational degrees of freedom. In the FE model, the end of the beam subjected to the applied pressure is fixed in the through-thickness direction. The other end of the beam

is fixed in both degrees of freedom. The material properties and geometry of the models are as for the 3D beams but with zero properties in the across-width direction. Plane stress conditions have been applied since the beam width is considered to be of the same order as the beam thickness and length for the same beams as were considered in the 3D analysis.

The 2D models have been generated using an automatic meshing technique, where by there exists pre-set values for the maximum and minimum element aspect ratios. As a result there are no meshing problems such as those experienced with the 3D modelling. Therefore, it is the 2D modelling which has been used to compare with the analytical and experimental results in Section 4.4.3.

4.4.3 Comparison with Experimental Values

Values for the critical stress have been calculated analytically from Equations 4.9, 4.11 and 4.12 above, numerically from the 2D FE models and compared with experimentally derived data (Sumpter & Lay). Beams manufactured using two different methods have been tested, those hand laid up and those fabricated by means of vacuum assisted resin transfer moulding (VRT). All the beams tested each consist of approximately 25 layers of woven roving glass/polyester. Table 4.1 gives the material properties and dimensions of the two sets of beams; those of the hand lay-up beams in the first column and of the VRT beams in the second. For each of the two series of beams tested, a delamination was built into the beam at different through-thickness locations using PTFE film less than 15 μm thick. Figure 4.9 shows an example of one of the beams in the test rig. In addition, the length of the delamination was also varied. All the beams were loaded in compression until failure occurred and the stresses at which the first buckle and final failure occurred were noted.

(A) Hand Laid Up Beams

Figures 4.10(a) to 4.10(e) show the curves of critical buckling stress calculated from the analytical approach, 2D FE approach and the experimentally determined values for the hand laid up beams. The analytical and FE values are almost identical in each case. Figure 4.10(a) shows that the analytical and FE results are identical to the experimental value for a defect length of 40 mm. The values for shorter defects are slightly higher

than the experimental values. Figure 4.10(b) shows that the analytical and FE values are slightly higher than the experimental values up to a defect length of 60 mm and slightly lower for defect lengths greater than 60 mm. Figure 4.10(c) shows that the analytical and FE values are slightly higher than the experimental values up to a defect length of 60 mm but slightly lower for defect lengths greater than 60 mm. Figure 4.10(d) shows that the analytical and FE values are slightly higher than the experimental values up to a defect length of 100 mm but slightly and at times, significantly, lower for defect lengths greater than 100 mm. It should be noted, however that the experimental stress values for defect lengths of 180 mm and 200 mm could be higher than the first buckle stress since in certain cases it was difficult to define the point at which first buckle occurred. Consequently, the experimental critical buckling stress value is likely to be closer to the analytical and numerical values. Similar conclusions can be drawn with regard to the difference in results shown in Figure 4.10(e). The analytical and numerical values are significantly lower than the experimental values for all defect lengths considered.

(B) VRT Beams

Figures 4.11(a) to 4.11(d) show the curves of critical buckling stress calculated from the analytical approach, 2D FE approach and the experimentally determined values for the VRT beams. As for the hand laid up beams, the analytical and FE values are almost identical in each case. Figure 4.11(a) shows that the analytical and FE values of critical buckling stress are consistently higher than the experimental values. All three approaches give nearly identical values for a defect length of 40 mm but are significantly different for defect lengths of 20 mm and 30 mm. For defect lengths greater than and equal to 80 mm, Figure 4.11(b) shows that the three methods give virtually identical results. As the defect length reduces, the consistency in results also reduces. Figure 4.11(c) shows that the analytical and FE values are significantly higher than the experimental values for all values of defect length considered. For the two beams tested shown in Figure 4.11(d) it shows that the analytical and FE values are significantly higher than the experimental values.

4.4.4 Critical Buckling Stress Calculated using Stiffness Reduction Method

In the case of the VRT specimens, where the analytical and FE values for critical buckling stress differ significantly from the experimental values it is because they are

greater than the experimental values. This is shown clearly in Figure 4.11(c). It should be noted at this point that the value of the Young's modulus used in both the analytical and FE approaches is that of the laminate compressive modulus which has been determined as part of the experimental program (Sumpter & Lay). The laminate compressive modulus is that of a laminate which did not previously contain any delaminations. In order to truly represent the buckling behaviour of the delaminated beam, however, it is the compressive modulus of the laminate containing delaminations which is required.

It is assumed for the purposes of this analysis that the percentage stiffness loss of a laminate containing delaminations when subjected to a compressive load is equal to the percentage stiffness loss of the same laminate containing delaminations when subjected to a tensile load. Thus the approach used to calculate the stiffness loss in a laminate under tension which is discussed in Section 4.3 has been adapted in order to calculate the stiffness loss in a laminate under compression.

Figure 4.12 shows a representation of a tested specimen. The region containing the PTFE film, the delaminated region, is the shaded area of the sketch. The beam width is labelled b and the beam length is labelled L. The width of the delaminated region is labelled b2 which is in fact equal to the beam width, b and the delamination length is labelled L2. Equation 4.8 above which gives an equation to calculate the stiffness loss due to partial delamination, can be adapted for this particular case.

The parameter, A, which is termed the delaminated area is equal to b2 multiplied by L2. The parameter, A^*, which is termed the total interfacial area is equal to b multiplied by L. Thus Equation 4.8 can be written as Equation 4.13 for this case and assuming that the intact and delaminated portions act as independent components.

$$E_p = (E^* - E_{LAM}) \frac{L2}{L} + E_{LAM} \qquad (4.13)$$

where: E_p is the stiffness of a partially delaminated laminate

E^* is the stiffness of a completely delaminated laminate

E_{LAM} is the intact laminate stiffness

L2 is the length of the delamination

L is the total length of the beam

The steps used to calculate the stiffness of a partially delaminated beam under compression are as follows:

(i) Calculate laminate intact tensile stiffness, E_{LAM}, using classical laminate theory.

(ii) Calculate laminate stiffness as a result of complete delamination, E^*, using Equation 4.7.

(iii) Calculate laminate stiffness as a result of a partial delamination using Equation 4.13.

(iv) Calculate % stiffness loss due to partial delamination from (i) and (iii).

(v) The critical stress to cause buckling is directly proportional to the modulus, E, used in Equations 4.10 and 4.11. Reduce the value of E by the same % as calculated in (iv). This gives the new value of the critical buckling stress.

Table 4.4 gives the VRT beam results for E^* and E_p for each delamination length and depth. It can be noted that the values of E_p in all cases are only slightly less than the value of the intact laminate stiffness and as a result there is very little % stiffness lower and consequently negligible reduction in the critical buckling stress. Thus it can be concluded that excessive values of the critical buckling stress calculated from the analytical approach cannot be accounted for by the value of E used in Equations 4.10 and 4.11. This is because the stiffness loss due to partial delamination is only about 3 % at the most. The fact that the experimental values are significantly lower than the analytical and numerical values must be due to other factors. The tested specimens are constructed from layers of woven laminae. The analytical and finite element models incorporate only one value of E. It is likely that in the case of woven laminates, their orthotropic nature must be taken into account by adapting the models to include values of elastic moduli in the orthogonal directions. The undulating characteristics of the woven laminates is likely to be one of the main reasons why the tested specimens buckled at lower stresses than those predicted by the models.

4.5 Fracture Criteria

Section 2.6 discusses the approaches available in the literature which incorporate fracture mechanics parameters. Appendix 2A describes the fracture mechanics parameters which can be used in linear elastic fracture mechanics (LEFM) and in elastic-plastic fracture mechanics.

4.5.1 Analytical Approaches

4.5.1.1 Cracks in Isotropic Materials

The magnitude of the elastic stress field at the crack tip such as that shown in Figure 4.13 can be described by the stress intensity factor, K. The calculation of K characterises the crack growth and fracture behaviour as long as the crack tip stress field remains predominantly elastic. The elastic stress field equations in the vicinity of the crack can be derived for three modes of loading, i.e mode I (opening mode), mode II (shearing mode) and mode III (tearing mode) as shown in Figure 4.14. The effect of a mode III type loading is considered to be negligible and thus the following paragraphs only discuss mode I and mode II loadings.

The formula for a mode I stress intensity factor for an isotropic plate with a central crack under a tensile pressure load is readily available in the literature such as Ewalds & Wanhill. Equation 4.14 can be used to calculate the mode I stress intensity factor for an infinite plate with a central crack length of 2a under a tensile stress σ.

$$K_I = C\,\sigma\sqrt{\pi a} \tag{4.14}$$

C takes into account the specimen width and can be calculated from the following equation.

$$C = 1 + 0.256\left(\frac{a}{W}\right) - 1.152\left(\frac{a}{W}\right)^2 + 12.200\left(\frac{a}{W}\right)^3 \tag{4.15}$$

where: W is the plate width.

A non-dimensional or normalised value of K denoted by K_I can be written as:

$$\overline{K_I} = \frac{K_I}{\sigma\sqrt{\pi a}} = C \tag{4.16}$$

4.5.1.2 Cracks in Layered Isotropic Materials

The analytical methods derived by Sih & Chen have been used to calculate the mode I and mode II stress intensity factors for a specific application. Delaminations in the

boundary angles of tee joints (see also chapter 6) commonly occur in the chopped strand mat (CSM) layers. These delaminations can occur as a result of high through-thickness stresses caused by a mode I type of load, or as a result of high interlaminar shear stresses caused by a mode II type of load. Thus the approach can be adapted so as to represent a delamination, or crack, in a chopped strand mat layer under each of the mode I and mode II types of loading.

Figure 4.15 represents a polyester resin crack sandwiched between two layers of E-glass/polyester CSM. The crack is 10 mm in length and the resin layer is 5 mm thick. The material properties of the system are given in Table 4.5.

(A) Mode I

The normalised mode I stress intensity factor, $\Phi_I(1)$ is calculated from the theory described in Sih & Chen and the mode I stress intensity factor, K_I, can then be calculated from Equation 4.17.

$$K_I = \Phi_I(1)\,\sigma_o\sqrt{a} \qquad (4.17)$$

For the above scenario, $\Phi_I(1)$ is calculated to be 0.783. It is stated that 7 MPa is the ultimate through-thickness stress which can be sustained by an E-glass/polyester woven roving/CSM laminate (Bird & Allan). Thus it is this value of stress which shall be used in the analysis. The critical value of K_I, i.e the value at which a crack will propagate, stated by Lau & Rowlands for a compact tension (C-T) specimen of polyester resin is stated to be 2.98 MPa$\sqrt{m}$. Lee wrote that the value of $K_I$crit is dependent on the conditions, namely the temperature and cross-head speed. He concluded that for polyester resin, the value of $K_I$crit ranges between 1.0 MPa$\sqrt{m}$ and 5.0 MPa$\sqrt{m}$. The value quoted by Lau & Rowlands is, therefore consistent with Lee's results. Thus the range quoted by Lee will be used for the analysis in the following paragraphs.

For a 10 mm crack in a 5 mm thick resin layer and a value of $\Phi_I(1)$ of 0.783, Equation 4.17 can be used for three different calculations to determine whether crack propagation is likely: (i) To calculate the stress at which the crack will propagate for a given value of $K_I$crit and compare with the ultimate through-thickness stress of 7 MPa, (ii) To calculate the value of K_I for an applied stress of 7 MPa and compare with quoted values of $K_I$crit, or (iii) for an applied stress of 7 MPa and an assumed value of $K_I$crit, the

critical crack length at which propagation would occur can be calculated.

(i) If $K_I$crit equals 1.0 MPa√m then the stress at which propagation will occur is equal to 18.1 MPa and if $K_I$crit equals 5.0 MPa√m then the stress at which propagation will occur is equal to 90.5 MPa. Thus the values of stress are much greater than the experimental ultimate stress of 7 MPa. It is concluded that the analytical system of a resin crack between layers of CSM can sustain a higher load than in experiments.
(ii) For an applied stress of 7 MPa, the value of K_I equals 0.388 MPa√m. This value is lower than the lowest quoted critical value of 1.0 MPa√m and it can, therefore, be concluded that the 10 mm crack would not propagate under an applied stress of 7 MPa.
(iii) For an applied stress of 7 MPa and a value of $K_I$crit of 1.0 MPa√m, the critical crack length to cause propagation is equal to 66 mm. An assumed value of $K_I$crit of 5.0 MPa√m gives a critical crack length of 1650 mm. Thus crack propagation is not likely to occur until the crack reaches a length of 66 mm.

(B) Mode II

The normalised mode II stress intensity factor, $\Phi_{II}(1)$, has been calculated from the theory described in Sih & Chen and the mode II stress intensity factor, K_{II}, can then be calculated from Equation 4.18.

$$K_{II} = \Phi_{II}(1)\,\tau_o\sqrt{a} \qquad (4.18)$$

For the same crack scenario as for the mode I loading, $\Phi_{II}(1)$ is calculated to be 0.922. It is stated that 26 MPa is the ultimate interlaminar shear stress which can be sustained by an E-Glass/polyester woven roving/CSM laminate (Hancox & Mayer). It is this value of stress which shall be used in the analysis.

For a 10 mm crack in a 5 mm thick resin layer and a value of $\Phi_{II}(1)$ of 0.922, Equation 4.18 can be used for three different calculations to determine whether crack propagation is likely: (i) To calculate the stress at which the crack will propagate for a given value of K_{II}crit and compare with the ultimate interlaminar shear stress of 26 MPa, (ii) To calculate the value of K_{II} for an applied stress of 26 MPa and compare with quoted values of K_{II}crit, or (iii) for an applied stress of 26 MPa and an assumed value of K_{II}crit, the critical crack length at which propagation would occur can be calculated.

(i) If K_{II}crit equals 1.0 MPa√m then the stress at which propagation will occur is equal to 15.3 MPa and if K_{II}crit equals 5.0 MPa√m then the stress at which propagation will occur is equal to 76.5 MPa. Thus the values of stress at which crack propagation will occur lies in the range of 15.3 MPa to 76.5 MPa. This is consistent with the experimental value of 26 MPa which lies in the range.

(ii) For an applied stress of 26 MPa, the value of K_{II} equals 1.7 MPa√m. This value lies in the given range for K_{II}crit of 1.0 MPa√m to 5.0 MPa√m. Thus it can be concluded that under these conditions, the crack would propagate under an applied load of 26 MPa.

(iii) For an applied stress of 26 MPa and a value of K_{II}crit of 1.0 MPa√m, the critical crack length to cause propagation is equal to 3.5 mm. An assumed value of K_{II}crit of 5.0 MPa√m gives a critical crack length to cause propagation of 87 mm.

4.5.2 Numerical Approaches

4.5.2.1 Cracks in Layered Isotropic Materials

In order to further validate the use of finite element modelling for calculation of fracture parameters and to compare with the analytical results discussed in Section 4.5.1, an FE model has been generated to represent the resin crack sandwiched between two layers of CSM as in the analytical method. The elements used are two dimensional plain strain elements and their characteristics are described in Appendix 4K. A typical FE model of the crack is shown in Figure 4.16. As before, the resin crack is 10 mm in length and is embedded in a 5 mm thick layer of resin with the material properties given in Table 4.5. Two modes of loading have been investigated, namely mode I and mode II.

(A) Mode I

For an applied stress of 7 MPa, the normalised mode I stress intensity factor has been calculated from the FE model to be 0.739 using the value of the mode I stress intensity factor, K_I, and Equation 4.16. This can be compared with the value of 0.783 calculated from the analytical approach in Section 4.5.1. Thus the FE result is within 6 % of the analytical approach.

(B) Mode II

For an applied load of 26 MPa, the mode II stress intensity factor, K_{II}, is calculated from the FE model to be 1.23 MPa$\sqrt{m}$. The analytical approach in Section 4.5.1 gives a value for the non-dimensional mode II stress intensity factor, $\Phi_{II}(1)$ of 0.922. For an applied stress of 26 MPa, this gives a value of K_{II} of 1.7 MPa$\sqrt{m}$. Thus the FE result is within 30 % of the analytical value.

4.5.2.2 Multiple Cracks

Delaminations in laminated composites rarely occur singly. Multiple delaminations commonly occur with delaminations between numerous layers. An FE model has been generated of an arbitrary square isotropic 250 mm^2 plate containing not only a central crack of 30 mm but also a 30 mm crack parallel to the central crack but at a distance of 12.5 mm from it. The FE model of the plate is shown in Figure 4.17. The aim of the analysis is to investigate the effect of the additional crack on the original central crack for a mode I type of loading based on strain energy release rate calculations with the two central edge nodes fully clamped. Values of the strain energy release rate and J-integral have been calculated at the four crack tips. The values are listed in Table 4.6 and show the mode I and mode II stress intensity factors, strain energy release rate values calculated for the central crack (crack 1) prior to the introduction of the second crack in addition to the values for both cracks after the introduction of the second crack (crack 2).

The results show that the mode I stress intensity factors for the two crack tips of crack 1 reduce by 21 % due to the introduction of crack 2. However, the mode II stress intensity factors for the crack 1 tips increase by 2364 % due to the presence of crack 2. Thus, the effect of introducing crack 2 into the plate is to reduce the mode I stresses on crack 1 but to significantly increase the mode II stresses on crack 1.

4.6 Discussion and Implications

Existing analytical approaches have been discussed which enable the calculation of mechanical properties of angle-ply laminates and woven laminates. The approach used for the analysis of woven laminates has been adapted so that the mechanical properties

of mixed laminates can be calculated. Mixed laminates can consist of any combination of unidirectional laminae, woven laminae or layers of chopped strand mat.

The effect of delamination on the remaining structural behaviour of the laminate has been investigated for laminates under both tensile loading and compressive loading. Under a tensile loading, the amount of stiffness reduction due to delamination depends on the actual size of the remaining interface still intact between the two layers which have separated. Not surprisingly, the greatest stiffness reduction occurs when the two layers are completely separated. For a typical marine type laminate, one complete delamination can reduce the tensile stiffness of the remaining laminate by as much as 12 %. This reduction in stiffness has the effect of increasing the flexibility of the laminate which allows it to carry further load. As the load is increased, additional delaminations further reduce the stiffness of the laminate. Ultimately, the laminate contains a large number of delaminations and loses all load bearing capability.

Under compressive loading, the stress at which a delaminated beam will buckle is of importance. Analytical and numerical models have been derived and validated which both give a good predictive tool. They can be used to calculate the critical buckling stresses for delaminated beams of different thicknesses, materials and containing delaminations at varying through-thickness locations. Beams containing delaminations which are close to the surface will buckle at a lower stress than beams containing delaminations close to their mid-thickness. Additionally, long delaminations will cause beams to buckle at a lower stress than beams containing short delaminations. These conclusions can be drawn from experimental, analytical and numerical results. A comparison can also be made between the two methods of manufacture, namely hand lay-up and VRT. For both methods it can be noted that the predicted values of critical buckling stress, when compared with the experimental values, become less accurate as the defect depth increases. In the case of the hand lay-up beams, the predicted values tend to underestimate the critical buckling stress. In the case of the VRT specimens, however, the predicted values tend to overestimate the critical buckling stress.

On a more microscopic level, fracture mechanics parameters have been calculated for a resin crack under two modes of loading, mode I (opening) and mode II (shearing). Simple analytical models can be used to calculate the relevant parameters for a resin crack between two layers of chopped strand mat commonly found in ship's structures,

for cracks of different lengths in layers of various thicknesses. Critical crack lengths have been calculated for the two modes of loading assuming values of maximum applied load and critical stress intensity factors. Table 4.7 shows critical crack lengths for the two modes of loading for a straight crack in a 5 mm thick resin layer. The material properties of the system are given in Table 4.5. The assumed value of the stress intensity factor in each case is 1.0 MPa√m which is the lowest quoted value taken from the literature. Table 4.7 shows that for applied loads equal to the assumed maximum values, i.e 7 MPa for mode I and 26 MPa for mode II, the mode I type of loading is the most stable resulting in a critical crack length of 66 mm.

In addition, for a 10 mm crack the stress levels at which the crack will propagate are shown in Table 4.8. The table shows that a 10 mm crack is most stable under a mode I type of loading since it will not propagate until a higher level of stress is reached than in the case of the mode II type of loading. The results show that a 10 mm crack will propagate under a mode I load of 18.1 MPa or under a mode II load of 15.3 MPa.

The analysis up to now has been for a resin crack sandwiched between two layers of chopped strand mat. This represents a crack in the overlaminate material of tee joint boundary angles. It is, however, interesting to note that the quoted value for the interlaminar shear strength of chopped strand mat is 17 MPa (Hancock & Mayer) which is very similar to the results above. For a crack in a CSM layer, propagation will occur under a mode II configuration when the applied stress reaches 15.3 MPa.

5. STRENGTH ANALYSIS OF TOP HAT STIFFENERS

5.1 Purpose of Analysis

The main purpose of this chapter is to investigate the load transfer mechanisms within two types of stiffener (Phillips et. al.). From the internal stress response distributions for a number of loading types and a knowledge of the material ultimate failure stresses, the regions within the stiffeners which are most susceptible to damage, especially delaminations, have been identified.

The construction of large FRP structures such as a ship requires that large unsupported panels are laid up. The stiffness of such panels is low and requires some form of stiffening arrangement. The usual method is by the addition of top hat stiffeners. The geometries of two types of top hat stiffeners are given in Figures 5.1 and 5.2. The main difference between the two types of top hat stiffeners is the back fill angle of the resin and has been discussed in Chapter 2.

Owing to the large difference in stiffness between the top hat section and the panel, the joint between them is under high loads. Out-of-plane loads are caused by hydrostatic pressure, docking or explosive loadings and in-plane loads which can be tensile or compressive are caused by hull bending loads. In-service applied loads and boundary conditions which are transferred to the top hat stiffener can be simulated in the laboratory. For example, a three-point bending test simulates docking or berthing loads, a reverse bending test simulates loads present due to the attachment of machinery and a straight pull-off load represents the load which must be sustained by the stiffener due to the presence of machinery during a slamming or explosive load. Figure 5.3 shows schematics of the three loading configurations: (a) three point bending, (b) reverse bending and (c) straight pull-off load.

5.2 Features of the FE Models

All the finite element (FE) models discussed here have been generated using the software package ANSYS (ANSYS).

5.2.1 Modelling Considerations

A series of models have been generated using two dimensional (2D) structural solid elements. The characteristics of these elements are given in Appendix 4J. A typical model used in the analyses is given in Figure 5.4. Each of the 12 layers in the overlaminate is represented by one element through the thickness. The flange plate of the top hat stiffener has been represented by one element through the thickness. Conditions of plain strain have been assumed throughout.

5.2.2 Loads, Material Properties and Boundary Conditions

The loads applied to the structural model attempt to mimic those in an experimental investigation (Elliott, 1994). The load types considered are: (a) three-point bending, (b) reverse bending and (c) straight pull-off. Figure 5.5 shows the FE models for three load conditions. For each of these configurations, stress distributions have been computed (i) at the load at which initial damage was noted and (ii) at the failure load of the stiffener. The exception has been the case of the type II stiffener where the failure in the reverse bend and pull-off tests is catastrophic; Consequently only one load has been applied to the models in these cases.

The material properties (Shenoi & Hawkins, 1995 & Vosper Thornycroft (UK) Limited) used in the FE model generation are given in Table 5.1.

Figures 5.5(a), 5.5(b) and 5.5(c) also show the boundary conditions applied to the models. In the case of the three-point bend shown in Figure 5.5(a), the model has been restrained in the y-direction at two constraint locations which are at a distance of 600 mm apart. Boundary conditions have been chosen to represent, as close as possible, the condition of simple supports. However, to prevent the occurrence of rigid body motions of the FE model it was also necessary to restrain one of the constraint nodes in the x-direction also.

5.3 Stiffness Characterisation

The first step which is necessary to validate the FE models is by comparing the FE model stiffness with that of the equivalent tested specimen. This is best carried out by

comparing the FE model initial stiffness with the experimental load-deflection curve. The FE model and experimental initial stiffnesses of the two types of top hats under each of the three loading configurations are shown in Table 5.2.

5.3.1 Comparison of FE and Experimental Results for the Type I Top Hat

(A) Three-Point Bending

The stiffener tested (Elliott, 1994) showed linear load-deflection behaviour up to a load of 13.5 kN. At this load level, initial failure occurred at the interface of the fillet and overlaminate. The initial stiffness of the test specimen is 696.8 N/mm. The initial stiffness of the FE model is 731.2 N/mm, i.e the FE model is 5 % stiffer than the test specimen.

(B) Reverse Bending

The experimental load-deflection curve is linear up to a load of 5 kN when the fillet was seen to crack. The experimental initial stiffness of the stiffener is 384.6 N/mm. The FE model gives a stiffness of 713 N/mm, i.e it is 85 % stiffer than the tested specimen. A sensitivity study has been carried out to account for possible variations in material properties, stiffener geometry and loading geometry. This is discussed in Section 5.4.1.

(C) Straight Pull-Off

The experimental load-deflection curve is linear up to a load of 5.5 kN when the fillet was seen to crack. The experimental initial stiffness of the stiffener is 1000.0 N/mm. The FE model gives a stiffness of 620.6 N/mm, i.e is 38 % more flexible than the tested specimen. A sensitivity study similar to that discussed in the case of the reverse bend has also been carried out and is detailed in Section 5.4.2.

5.3.2 Comparison of FE and Experimental Results for the Type II Top Hat

(A) Three-Point Bending

The stiffener tested (Elliott, 1994) showed linear load-deflection behaviour up to a load

of 12.5 kN had been reached. At this load level, delaminations in the overlaminate were visible and there was a reduction in stiffness. The initial stiffness of the test specimen is 740.7 N/mm. The stiffness of the FE model is 820.9 N/mm, i.e it is 11 % stiffer than the test specimen.

(B) Reverse Bending

The experimental load-deflection curve is almost linear up to a load of 17.0 kN when the stiffener failed. The experimental initial stiffness of the stiffener is 303.0 N/mm. The FE model gives a stiffness of 639.1 N/mm, i.e it is 110 % stiffer than the tested specimen. A sensitivity study has been carried out to account for possible variations in loading geometry. This is discussed in Section 5.4.3.

(C) Straight Pull-Off

The experimental load-deflection curve is linear up to a load of 15.0 kN when the stiffener failed. The experimental initial stiffness of the specimen is 880 N/mm. The FE model gives a stiffness of 639 N/mm, representing 27 % more flexibility than the tested specimen. A sensitivity study has been carried out to account for possible variations in loading geometry. This is discussed in Section 5.4.4.

5.4 Sensitivity Studies

In the cases where the difference between the stiffness of the FE structural model is significantly large, a sensitivity study has been carried out to account for these discrepancies. The implications of these studies are outlined in Section 5.4.5 below.

5.4.1 Type I Top Hat Stiffener - Reverse Bend

The initial stiffness of the FE model discussed in Section 5.3.1(B) was 85 % stiffer than the initial stiffness of the tested specimen prior to failure. A sensitivity study has been carried out to account for the difference in the stiffnesses of the FE model and the tested specimen. Eight variations on the original FE model have been investigated for the reverse bend loading case. The original values of the material properties are given in Table 5.1.

(A) Woven Roving/ Polyester Moduli:

Since the material properties of composites are subject to variations, the values of E_x and E_y have been reduced by 10 % and 20 % of the original values which are given in Table 5.1.

(B) Fillet Resin Modulus:

The value of resin modulus may not be exactly equal to that quoted for the material. Therefore, the value of the resin elastic moduli have been reduced by 10 % and 20 % of the original values.

(C) Span between supports:

The location of the supports may not have been located in exactly the same location as in the experiments so the effect on the FE model stiffness has been calculated for two cases for which the supports are 620 mm and 640 mm apart. The original support span being 600 mm.

(D) Size of overlaminate/flange interface:

The length of the interface between the overlaminate and flange has been reduced by 20 mm and 40 mm from the original case for which the interface length equalled 220 mm.

(E) Combination of Effects (A) to (D):

The first combination includes a 10 % reduction in the moduli of the woven roving/polyester, a 20 mm increase in the support span and a 20 mm reduction in the size of the overlaminate/flange interface. The second combination includes a 20 % reduction in the moduli of the woven roving/polyester, a 40 mm increase in the support span and a 40 mm reduction in the size of the overlaminate/flange interface.

(F) Core Modulus:

Although the core is non-structural and should not contribute to the load-carrying capability of the stiffener, the value of the core modulus has been reduced to 10^{-10} MPa to ensure that it has an insignificant effect on the overall stiffness of the top hat.

(G) Presence of Fillet Void:

Experience in the analysis of tee joint strength (discussed in Chapter 6) has shown that voids can be present in the fillet resin which lead to premature failure of the joint. In this study, a void has been placed in the fillet resin of the stiffener model by removing a single element and calculating the new stiffness of the top hat.

(H) Change method by which load is applied to FE model:

The original method of applying the reverse bending load has been to apply loads at the nodes along the crown of the FE model. In this case, the steel plate which was present in the experiments has also been modelled and the load applied by means of a uniformly

distributed load along the plate.

Table 5.3 show the results of the sensitivity study. The moduli of the woven roving/polyester which is used in the overlaminate have a significant effect on the mechanical stiffness of the top hat. The reduction in the modulus gives an identical reduction in top hat overall stiffness. A reduction in the fillet resin modulus also gives a marked reduction in the overall top hat stiffness. A reduction in resin modulus would be caused by the presence of voids. Voids are extremely difficult to avoid during the manufacture of these types of structures. An increase in the span size between supports increases the flexibility of the stiffener. The size of the overlaminate/flange interface had very little effect on the overall top hat stiffness.

Two combination effects were represented in (E). The second combination of effects gave rise to an FE model stiffness of 458.3 N/mm. The experimental initial stiffness of the specimen tested under reverse bend was 384.6 N/mm. Hence, the FE model from the sensitivity study in this case is 19 % stiffer than the tested specimen. This combination of effects gives an improvement on the original model.

The modulus of the non-structural core material had a negligible effect on the top hat stiffness from the FE model. This is expected since the core material bears no load and is in fact removed in other test configurations. The presence of the void in the fillet reduced the stiffness of the FE model by a negligible amount. The FE model stiffness reduced from 713 N/mm in the original model to only 712 N/mm for the model which includes the void. The experimental set-up used a plate across the crown of the top hat to transfer the load to the stiffener. The original FE model did not take the plate into account. The revised model which includes the plate in the FE model gives an initial stiffness of 679 N/mm. The stiffness of this model is marginally closer to that of the tested top hat.

The implications of these studies are outlined in Section 5.4.5 below.

5.4.2 Type I Top Hat Stiffener - Pull-Off Load

A similar sensitivity study for cases (A), (B), (C) and (H) above has been carried out as for the reverse bend except that the values in (A) and (B) have been increased rather

than decreased in the case of the reverse bending load. Also in (C), the span has been reduced rather than increased. This is because in this case, the original FE model is more flexible than the tested specimen where as in the case of the reverse bend test, the FE model was stiffer than the tested top hat. Table 5.4 shows the results of the sensitivity study in the case of the pull-off test.

Similar trends to those discussed in Section 5.4.1 have been found. The modulus of the woven roving/polyester and the size of the span had a marked influence on the overall stiffness of the top hat.

An important point to note, however, is that the modulus value of the fillet resin had very little effect on the stiffness of the top hat in the case of the pull-off load. In the case of the reverse bend, the change in fillet modulus had a large effect on the top hat stiffness. This can be explained by the fact that the initial failure mode in the reverse bend test was that of a crack in the fillet. In the pull-off test the initial failure was a crack along the interface of the fillet and the flange plate. Thus, since the fillet itself did not crack, the fillet does not contribute to the failure mode of the stiffener under a pull-off load.

The original FE model used to represent the pull-off load did not contain the steel plate which was present in the experimental test configuration. A revised model has been generated which includes the steel plate to simulate the loading mechanism more accurately. The FE model generated which includes the plate is shown in Figure 5.6. The stiffness of the FE model containing the plate is 930 N/mm which is within 7 % of the experimental specimen stiffness of 1000 N/mm and is a marked improvement.

5.4.3 Type II Top Hat Stiffener - Reverse Bend

Since the initial stiffness of the type II finite element model for a three point bending load has been shown to be within 11 % of the experimental initial stiffness, the material properties and stiffener geometry used can be considered to be reasonable. Thus, only the method of load application has been changed to try and improve the stiffness accuracy of the FE model under a reverse bending load. As with the type I stiffener, the steel plate used in the experiments to apply the load, has also been modelled in the FE model. The initial stiffness of the tested top hat is equal to 303 N/mm. The FE model

containing the steel plate gives a stiffness of 616 N/mm which is a slight improvement on the previous value but is still only within 103 % of the experimental value. As with the type I top hat, the addition of the steel plate into the FE model only gives a marginal improvement with regard to the initial stiffness.

5.4.4 Type II Top Hat Stiffener - Pull-Off Load

The FE model which does not include the steel plate gives a stiffness which is only within 27 % of the experimental value. The steel plate has also been included in the case of the type II top hat. The FE model containing the steel plate gives a value of stiffness of 897 N/mm. This value is within 2 % of the experimental stiffness value of 880 N/mm. Hence, the inclusion of the steel plate in the FE model gives a significant improvement with regard to the stiffness.

5.4.5 Implications

The results of the sensitivity study show that the stiffness of the FE models which have been generated to simulate both a reverse bend type and a straight pull-off type of load is effected significantly by the chosen value of the modulus of the woven roving/polyester and also the size of the span. It shows that it is important to choose the correct material properties for the overlaminate material in particular. Since the stiffness values from the FE models of both types of top hat under a three point bending load are very close to the respective experimental stiffnesses, it can be concluded that the values of the material properties selected and stiffener geometry are acceptable. Therefore, it can be concluded that it is the method of loading representation which is responsible for the differences in stiffness for the top hats under reverse bending and pull-off. In the case of the type I top hat under a pull-off load, this is shown by comparing the stiffness value of the FE model without the steel plate (620.6 N/mm) and the stiffness of the FE model with the steel plate included (930 N/mm). The latter value is within 7 % of the experimental stiffness value. The equivalent comparison for the type II stiffener is within 2 % of the experimental stiffness value.

5.5 Stress Patterns

The stress distributions of interest are the fillet principal stress, overlaminate through-

thickness and in-plane stresses, flange plate through-thickness and in-plane stresses. It is also necessary to compare the load transfer mechanisms predicted from the FE models with some experimentally derived failure modes. A summary of the experimental failure patterns (Elliott) is given in Table 5.5.

5.5.1 Type I Top Hat Stiffener

Table 5.6 shows the value and location of the maximum stress for each load level and load configuration for the type I stiffener.

(A) Three-Point Bending

The most significant stress patterns for the top hat at the experimental initial load of 13.5 kN are shown in Figure 5.7(a): the overlaminate through-thickness stresses and Figure 5.7(b): the flange in-plane stresses. The magnitude of the fillet principal stress is the greatest in the central region in the fillet as shown in Table 5.6 but is less than the ultimate value. Thus, the fillet is unlikely to fail at this load. The region of the overlaminate which is under both the highest in-plane and through-thickness stresses is the outer region in the curved part above the fillet as shown in Figure 5.7(a). Delaminations are likely to form due to high through-thickness stresses. Although the flange is unlikely to fail, the region under the greatest in-plane stress is the inner central part below the core. The region of the flange under the highest through-thickness stress is in the outer central part as shown in Table 5.6.

The value of the maximum principal stress in the fillet at the stiffener experimental failure load of 16.5 kN is 18.09 MPa. The ultimate tensile strength (UTS) of the fillet material in the literature (Hawkins & Shenoi) is 26 MPa; so the fillet would remain intact at this load. This corresponds to the failure mode in the experiments in which the fillet itself did not crack. The initial damage was seen along the interface of the fillet with the overlaminate. The in-plane stress in the overlaminate at 16.5 kN is not great enough to cause failure. The through-thickness stress at the initial failure load of 13.5 kN, however, is greater than the quoted interlaminar tensile strength (ILTS) of 7 MPa for the woven roving/polyester (Bird & Allen). Hence the FE model predicts that delaminations would occur near to the outer surface of the overlaminate at 13.5 kN due to through-thickness stresses greater than the ILTS of the material. This exactly matches

the experimental findings. The ultimate tensile strength of the flange material is 207 MPa. At a load of 13.5 kN the in-plane stress in the flange plate is not enough to cause failure. At 16.5 kN, however, the in-plane stress in the flange is 208 MPa which is greater than the UTS. The FE model predicts that the flange plate would fail in the centre of the upper surface at a load of 16.5 kN, which exactly mirrors the experimental findings.

(B) Reverse Bending

The material properties and top hat geometry used to represent the top hat under a three point bending load gave similar results to those derived experimentally. Therefore, in the case of the reverse bend, it is likely that it is the way in which the load is represented which causes the discrepancies between the FE model and the experimental stiffnesses. Thus, the FE model used to yield the internal stress patterns is the model from the sensitivity study part (H) which includes the steel plate in the load representation. The most significant stress pattern for the top hat at the experimental initial load of 5 kN is shown in Figure 5.8(a): the overlaminate through-thickness stresses.

At a load of 5 kN, the fillet principal stress is 4.8 MPa which is much less than the UTS of 26 MPa. The FE model, therefore, does not predict fillet failure at this load level. The initial failure mode in the experiments, however, was that of fillet cracking. The presence of voids within the fillet would cause higher stresses which could have caused premature failure. An additional model has been run which contained a void in the fillet in the same location as the region of maximum principal stress obtained from the undamaged model. The fillet maximum principal stress given from the revised model containing the void is still only 6.6 MPa. It must be pointed out, however that during the experiments, once the fillet cracks had formed they did not extend in any way on further loading. This indicates that large voids may have been present in the fillets prior to loading which opened out due to the nature of the load but did not cause any further damage within the fillets. The experimental load/deflection curve showed no sudden loss of stiffness and an FE model containing a void in the resin exhibits an almost identical value of stiffness as the model not containing voids. Thus it seems likely that the cracks in the fillet were due to the voids opening out under load with no loss of top hat stiffness.

The in-plane stresses in the overlaminate are lower than the in-plane failure stress but the through-thickness stresses in the overlaminate predicted by the FE model are 21 MPa along the interface of the overlaminate and the fillet as shown in Figure 5.8(a). This is about three times the ILTS so delaminations would be predicted in this location. No delaminations, however, were visible in the experiments in this location. The high through-thickness stresses may have caused a debond between the overlaminate and the fillet which in turn caused the fillet crack. The FE model predicts maximum in-plane and through-thickness stresses in the flange plate which are not high enough to cause failure at a load of 5 kN. This is consistent with the experimental initial failure mode at 5 kN.

The fillet principal stress at a load of 14 kN which is the experimental failure load is 13 MPa which is still less than the UTS of the fillet resin. Also, the in-plane and through-thickness stresses in the flange are less than the respective ultimate strengths. The experimental failure mode, however, at 14 kN was that of damage on the lower surface of the flange plate in the centre.

(C) Straight Pull-Off

The FE model used to yield the internal stress patterns within the stiffener is the model from the sensitivity study part (H) which includes the steel plate to apply the load. This model yielded a value of stiffness within 7 % of the experimental top hat stiffness so is considered to represent the tested specimen reasonably well. The most significant stress pattern for the top hat at the experimental initial load of 5.5 kN is shown in Figure 5.9(a): the overlaminate through-thickness stresses.

The maximum values of stress for the fillet principal stress, overlaminate in-plane and through-thickness and flange in-plane and through-thickness stresses are given in the lower two rows of Table 5.6. The fillet maximum principal stress at the stiffener experimental failure load of 7 kN is 7.8 MPa. This is much lower than the UTS of the fillet material of 26 MPa. The FE model would not, therefore, predict fillet failure at this load. This corresponds to the experimental failure mode in which no fillet cracks were visible.

The maximum in-plane stresses in the overlaminate and in the flange are less than the

UTS (in-plane) stress of 207 MPa at a load of 7 kN. Therefore, no failure is predicted at this load from the FE model as a result of high in-plane stresses. The maximum through-thickness stress of 2.8 MPa in the flange is lower than 7 MPa which is the ILTS. The maximum through-thickness stress in the overlaminate, however, is higher than the ILTS. The FE model would predict delamination of the overlaminate in the curved region close to the fillet due to high through-thickness stresses as shown in Figure 5.9(a).

5.5.2 Type II Top Hat Stiffener

Table 5.7 shows the value and location of the maximum stress for each load level and load configuration for the type II stiffener.

(A) Three-Point Bending

The most significant stress patterns for the top hat at the experimental failure load of 14.5 kN are shown in Figure 5.10(a): the fillet principal stresses, Figure 5.10(b): the overlaminate through-thickness stresses and Figure 5.10(c): the flange in-plane stresses. At a load of 12.5 kN which is the initial failure load of the top hat in the tests, the FE model would predict a maximum fillet principal stress of 23 MPa. This is approaching the UTS of the fillet of 26 MPa. The location of this maximum stress is in the fillet corner adjacent to the interface of the core and the flange as shown in Figure 5.10(a). The photograph of the damaged specimen (Elliott, 1992) indicates that there is a gap between the flange and the core in this location. The crack is likely to have formed due to the high fillet principal stresses and then continued along the core/flange interface.

The through-thickness stresses in the overlaminate at a load of 12.5 kN are greater than the ILTS of 7 MPa. The FE model would predict delaminations due to high through-thickness stresses in the curved region of the overlaminate towards the outer surface. This is in the exact location where delaminations were seen in the experiments at a load of 12.5 kN and is shown in Figure 5.10(b).

At the experimental failure load of 14.5 kN, the in-plane stresses in the flange are approaching the UTS of 207 MPa. The FE model predicts these high in-plane stresses in the centre of the flange plate on the inner surface as shown in Figure 5.10(c). Damage

was visible in this location in the experiments as the top hat approached final failure.

(B) Reverse Bending

The FE model containing the steel plate has been used to generate the stress patterns within the top hat stiffener. The most significant stress pattern for the top hat at the experimental failure load of 17 kN is shown in Figure 5.11(a): the flange through-thickness stresses.

In the experiments, the type II top hat failed catastrophically under the reverse bend. No damage was visible until the flange plate failed in tension in the centre on the outer surface at a load of 17 kN. At this load the FE model would predict that all the values of maximum in-plane and through thickness stresses in the overlaminate, maximum fillet principal stress and flange in-plane stresses are less than the limiting values. However, the maximum through-thickness stress in the flange is equal to 9 MPa at a number of locations along the flange plate as shown in Figure 5.11(a). Thus, the delaminations visible in the experiments at this load in the lower central plies of the flange plate are likely to be due to excessive through-thickness stresses.

(C) Straight Pull-Off

The most significant stress pattern for the top hat at the experimental failure load of 17 kN is shown in Figure 5.12(a): the overlaminate through-thickness stresses. This test also gave rise to catastrophic failure at a load of 15 kN. At this load the overlaminate became completely detached from the flange plate. Of the two specimens which were tested, one became detached on one side only where as the second specimen became detached on both sides. There was no other visible signs of failure within the specimens. At a load of 15 kN the FE model would predict that no damage would occur in the flange plate, fillet or in the overlaminate due to in-plane stresses since all the maximum stress values in these regions are less than the ultimate values. However, delaminations would be predicted due to high through-thickness stresses in the curved part of the overlaminate close to the fillet.

5.6 Discussion

5.6.1 Stiffness Correlation

For both types of top hat stiffeners, the stiffness of the FE models compares extremely well with the initial stiffness of the tested specimens under the three point bending load configuration. In the case of the reverse bend test, the FE models of both types of top hat gave rise to about twice the stiffness when compared with the experimental initial stiffnesses. In order to take into account this pronounced increase in stiffness a sensitivity study has been undertaken. The results of the study showed that the stiffness of the FE model is greatly influenced by reducing the moduli of the woven roving/polyester material which makes up the overlaminate and the flange. A 25 % reduction in the in-plane and through-thickness moduli results in a corresponding change in the slope of the load/deflection curve. In addition, the inclusion of the steel plate in the FE model for the pull-off load increased the model stiffness to within 7 % (type I) and 2 % (type II) of the experimental stiffness thus indicating the importance of correctly representing the loading configuration in order to validate the FE models.

5.6.2 Assumed Material Properties and Boundary Conditions

In the case of the three point bending load, the FE models of both types of top hat gave very similar values of stiffness when compared with the stiffness of the tested specimen. Therefore, under this loading condition, the assumed material properties were close to those of the actual specimen material. In order to represent as closely as possible the simple support conditions, two nodes were constrained only in the vertical direction. This represents the test case where the flange of the top hat stiffeners were positioned on the supports and were assumed not to move in the vertical direction. In order to prevent rigid body motions of the FE model, one of the two constraint nodes was also restricted in translation in the horizontal direction. This is not the case in the tested specimen where the test piece is free to move around the support. Since the initial stiffness of the FE model under three point bending is very similar to the experimental initial stiffness, it is shown that this additional boundary condition does not invalidate any subsequent results.

5.6.3 Comparison of FE Stress Patterns with Experimental Damage

The internal stress distributions in the two types top hat which have been predicted by the FE models for a three point bending load compare very well with the respective failure modes of the tested specimens. The predictions of the stress patterns for both types in the case of the reverse bend and pull-off loads, however, are not as consistent with the experimental failure modes. Tensile tests on the fillet material carried out by Read indicate the UTS of the fillet may in fact be of the order of 16 MPa as opposed to the quoted value of 26 MPa. This may explain the premature fillet failure which was seen in the case of the type I top hat under a reverse bending load. The pull-off tests on both types of top hat showed that no damage occurred other than the overlaminate becoming detached from the flange plate on one (type I) or both (type II) sides. The FE models, however, predict that delaminations would occur in the curved region of the overlaminate close to the fillet due to high through thickness stresses. Therefore, the premature peeling of the overlaminate from the flange plate could have been caused due to poor bonding between the overlaminate and the flange.

5.6.4 Comparison Between the Two Types of Top Hat Stiffener

The only difference between the two top hat stiffeners is the geometry of the fillet but there are marked variations in their behaviour under the three modes of loading. Under the three point bending load, the type I top hat initial and final failure loads are slightly greater than the equivalent values for the type II top hat. However, the values of the maximum principal stresses in the fillet are significantly greater for the type II than those for the type I. The stress distributions in the overlaminate and in the flange are very similar for both types of top hat and the maximum values are of a similar magnitude. In the case of the reverse bend tests, the final failure mode in both cases was that of damage in the lower, central regions of the flange but the type I top hat also sustained initial failure in the form of fillet cracking. The maximum principal stresses in the type I fillet are significantly higher than those in the type II top hat. In addition, the overlaminate through-thickness stresses are significantly greater in the case of the type I than for the type II. Both types of top hat behaved in a similar manner in the straight pull-off test with one complete side of the overlaminate becoming separated from the flange. The exception being that one of the type II top hats failed on both sides at a load more than twice the failure load of the type I. Under reverse bending and

straight pull-off loads, the type II top hat stiffener behaves in a more catastrophic manner than the type I. This could have serious structural consequences since there are no signs of damage prior to final failure.

5.7 Concluding Remarks - Identification of Delamination Prone Areas

The damage prone areas in both types of top hat stiffener are (i) in the curved region of the overlaminate and (ii) in the central region of the flange plate. This is indicated by the presence of high through-thickness stresses in the curved region of the overlaminate and also the presence of high in-plane stresses in the flange. For example, Figure 5.7(a) shows the overlaminate through-thickness distribution at the experimental three point bending test initial failure load of 13.5 kN. It show that the outer regions in the curved part of the overlaminate are subjected to the highest through-thickness stresses which are greater than the ILTS of the material and are thus most susceptible to delamination damage. Also, Figure 5.7(b) shows the in-plane stress distribution in the flange plate at the experimental three point bending test initial failure load of 13.5 kN. It shows that the maximum in-plane stress in the flange plate is greater than the failure stress and occurs in the central inner plies of the flange. This damage, however, is due to high in-plane stresses and is not likely to be delamination. Delamination damage primarily occurs under three point bending loads, where it appears in the curved region of the overlaminate. It is these regions which shall be studied further in Chapter 7, from an energy perspective with a view to identifying damage tolerance.

6. STRENGTH ANALYSIS OF TEE-JOINTS

6.1 Purpose of Analysis

The main aim of this chapter is to investigate the load transfer mechanisms within a typical tee joint. From the internal stress patterns and a knowledge of the material ultimate strengths, the regions of the joint which are most susceptible to damage (mainly in the form of delaminations) have been identified.

Figure 6.1 shows a diagram of a typical tee joint. The main function of a tee joint in a ship is to transmit flexural, tensile and shear loads between the two orthogonal panels which may be in the form of a bulkhead, side shell or deck. Flexural or tensile loads may cause the plies in the web or the flange to peel off. Also, shear loads could result in the separation of the boundary angle (or overlaminate) from the base plate. Finally, flexural loads could cause the plies in the overlaminate to separate from each other due to interlaminar tearing.

A tee joint is typically subjected to a docking or berthing type of load such as that shown in Figure 6.2. This load scenario can be represented experimentally by a three-point bending test.

6.2 Features of the FE Models

6.2.1 Modelling Considerations

Both three dimensional (3D) and two dimensional models (2D) have been generated in order to represent a tee joint under a three-point bending load.

Previous tee joint research has involved the generation of three dimensional (3D) finite element models (Shenoi & Hawkins, 1992). An investigation has been carried out to compare the results which were achieved from a 2D model with those from a 3D model. These results are discussed in Appendix 6A. The results showed that the 2D model gave consistent results with the 3D model. Owing to the ease of model generation and greater simplicity of the 2D model, it is this type which has been used in all further analysis. In order that the individual delaminations between the layers in the overlaminate can be

modelled, it is important that each layer is modelled with one element through the thickness of each layer. A typical two dimensional (2D) finite element tee-joint model is shown in Figure 6.3.

All models incorporated the large deflection option which takes into account the effect of large strains on the stiffness matrices of the materials in the joint. The effect on the results is shown in Section 6.3.5.

6.2.2 Loads, Boundary Conditions and Material Properties

The loads which have been applied to the models have been chosen so as to represent the loads at which damage has been observed in three point bending experiments (Elliott, 1992).

In order to represent simple support conditions, the finite element model is constrained in two locations. The positions of the constraints are shown in Figure 6.3. Both nodes are prevented from translation in the y-direction such that the boundary conditions represented in all the finite element models are those of simple supports. In order to prevent rigid body motions, one of the constraint nodes has also been restricted in the x-direction.

The linear material properties for the overlaminate, web, flange used in the FE models are given in Table 6.1. The fillet material, however, possesses a non-linear stress-strain curve which is shown in Figure 6.4. The initial modulus of the fillet material is taken to be 1500 MPa (Shenoi & Hawkins, 1992) which was found to be a more appropriate value than 500 MPa which is the quoted value for the urethane acrylate fillet material. Hence, all the models incorporate the non-linear material option to take into account the non-linear behaviour of the fillet material. The effect of using the non-linear materials option is discussed in Section 6.3.4.

6.2.3 Simplified Tee Joint Models

A simplified tee joint model consisting of one element through the thickness of the overlaminate gives a good preliminary insight into the stress distributions within the joint and also into the load transfer mechanisms. It is not, however, possible to insert

delaminations within such a model. Owing to its simplicity, the model is quick and easy to generate. In order to represent as closely as possible the material which is present in the overlaminate, the material properties must first be estimated. This can be carried out using two methods.

Method A assumes that the elastic properties of the actual materials used are available and known and uses a percentage of the properties of each layer depending on the relative amounts of each material. Method B involves calculating the properties using an adapted laminate analysis technique. Section 4.2.3 in Chapter 4 discusses the method by which the elastic properties of mixed layered composites can be calculated from an adapted laminate analysis. The overlaminate material in the tee joints can be considered to be a mixed laminate with layers of woven roving/polyester, (WR), and chopped strand mat/polyester, (CSM). Both methods will be discussed in Sections 6.2.3 (A) and (B) respectively. Section 6.2.3 (C) compares the results from both methods.

(A) Method A

The tee joint which is currently under consideration consists of 11 plies in the overlaminate, namely 6 plies of CSM and 5 plies of WR. The in-plane modulus and through-thickness modulus of the single elements through the thickness of the overlaminate are assumed to be in the same proportions as the actual number of layers. For example the through-thickness modulus equals 6/11 of the CSM through thickness modulus plus 5/11 of the WR through-thickness modulus. The load applied to the model under three point bending is 5500 N which is equal to the experimental load at which the first sign of damage was seen in the way of fillet cracks (Elliott, 1994). Figures 6.5(a), 6.5(b) and 6.5(c) show the stress distributions of the fillet principal stresses, the overlaminate in-plane stresses and the overlaminate through-thickness stresses respectively.

(B) Method B

The adapted laminate theory discussed in Section 4.2.3 is used to calculate the overall laminate properties of the 11 layered overlaminate material used in the tee joints. The WR layers are assumed to have 50 % undulation i.e. along a unit cell of material half of the warp tow is straight and half is undulating.

(C) Results for Both Methods

Table 6.2 shows the maximum deflections, maximum fillet principal stresses, maximum overlaminate in-plane stresses and maximum overlaminate through-thickness stresses for the two methods compared with the results of an FE model of a tee joint which contains one element per layer through the thickness of the overlaminate (model 1). The maximum stress and deflection values for model 1 are given in Table 6.3. Figures 6.6(a), 6.6(b) and 6.6(c) show the fillet principal stress distribution, overlaminate in-plane stress distribution and overlaminate through-thickness stress distribution for model 1 and can be compared with Figures 6.5(a), 6.5(b) and 6.5(c) from method A. It can be shown that the fillet principal stress distribution is similar in the lower regions of the fillet. The region of maximum principal stress is also in the same location but the value from method A is slightly higher than that for model 1. The distributions in the upper region of the fillet are noticeably different. The overlaminate in-plane stress distributions are similar for both models but the value of the maximum in-plane stress for method A is considerably lower than that for model 1. The overlaminate through thickness stress distributions differ significantly. This is due to the fact that the single element through the thickness of the overlaminate in the model using method A has a linear stress distribution. However, the region of maximum through-thickness stress is in the same location for both model 1 and the model using method A. This indicates that delamination would be predicted for both models due to high through-thickness stresses. The value of the maximum through-thickness stresses are very similar since the through-thickness moduli of the WR layers and the CSM layers are equal.

For method B, and an applied load of 5500 N, the distributions for the fillet principal stress, S_P, the overlaminate in-plane stress, $S_{i\text{-}p}$ and the overlaminate through-thickness stress, $S_{t\text{-}t}$ are very similar to those from method A. The maximum value of S_P is equal to 11.3 MPa, the maximum value of $S_{i\text{-}p}$ is equal to 40.4 MPa and the maximum value of $S_{t\text{-}t}$ is equal to 6.74 MPa. The region of maximum through-thickness stress is in the same location as for model 1 and the model using method A.

The result of this study emphasises a number of points. Firstly that it is possible to simply calculate the mechanical properties of a mixed laminate consisting of layers of woven roving and layers of chopped strand mat using an adapted laminate theory. In order to make preliminary predictions of the behaviour of a structural component under

specific loading conditions, the calculated material properties of the laminate can be entered into a simplified FE model. Table 6.2 shows that the values of maximum deflection are very similar for the detailed FE model, model 1 which contains one element per layer and the models using methods A and B which only contain one element through the thickness of the tee joint overlaminate. In addition, the values of maximum stresses are reasonably close for the three cases.

The calculation of the mechanical properties from the adapted laminate theory in combination with a simplified FE model gives a very good first estimate of the structures behaviour and the location of regions under high stresses. However, if a more detailed analysis is required such as including actual delaminations, then a model must be generated which contains one element per layer through the thickness of the overlaminate.

6.2.4 Two Dimensional (2D) Model

The elements used to generate the models are 2D structural solid elements which have been used in FE models in Chapter 4 and whose characteristics are given in Appendix 4J. Plane strain conditions are assumed to prevail in the 2D models since the joints on board ships can be considered wide in relation to the length and thickness. One element is modelled per layer of the overlaminate material. For the 2D models, the finite element load is equal to the applied load per unit width of the joint which in this case is 100 mm. Constraints for the 2D case mirrored those adopted for the 3D model.

6.3 Tee Joint Damage Modelling

The formation of delaminations in the overlaminate of a joint is commonly termed as 'root whitening'. In order to understand the consequences of root whitening under a typical load configuration, experiments must be performed. The experimental load/deflection curve gives vital clues as to the extent of the damage, at what loads it occurs and the corresponding loss in stiffness due to the damage. It is also necessary to be able to pin point the exact location within the joint where the delamination occurred. Papers such as Shenoi & Hawkins, 1992 and Hawkins et. al. discuss the failure modes of particular joints but do not give an exact location and extent of the damage due to delamination. Therefore, alternative experimental results had to be found.

6.3.1 Damage Representation, Experimental Evidence

Elliott (1994) carried out a series of three point bending experiments on tee joints. A typical load-deflection curve yielded from the tests is shown in Figure 6.7. The points marked A to D correspond to the loads at which damage was observed in the tests, the details of which are given in Table 6.4. It can be noted from the graph that changes in slope of the load-deflection curve occur at loads of 5500 N, 7500 N, 8600 N, 11500 N, 13000 N, 17600 N and 19000 N when the specimen finally failed. These changes of slope are due to stiffness reductions due to progressive damage to the joint. The exact location and extent of the delamination damage could be obtained from these tests. Consequently, a series of detailed 2D FE models have been generated to mirror the experimental load-deflection curve.

6.3.2 Modelling Details

The FE models have been tailored to mimic the damage observed in the tests. The experimental failure patterns (Elliott 1994) are given in Table 6.4. The analyses have been carried out with the following objectives: (i) to correctly represent the stiffness reduction due to the successive delaminations in the boundary angle, (ii) to predict the damage progression within the joint and (iii) to ultimately predict the failure mode of the joint. The damage zones (i.e the debond, fillet crack and delaminations) in the joints have been modelled by inserting a small gap between the relevant elements.

A total of 6 models, numbered 1 to 6 have been generated to represent the undamaged tee joint (model 1), the successive damage (A to D) noted in the experiments shown in Table 6.4 (models 2-5) and a tee joint containing additional delamination (model 6). Values of maximum deflection, overlaminate in-plane and through-thickness maximum stresses and fillet principal stresses have been calculated for each model at each load level.

6.3.3 Initial Stiffness Validation

The initial stiffness of the 2D finite element model, model 1, has been compared with the stiffness of the tested specimens. The maximum values of deflection for the tee joint under a load of 5500 N are given in Table 6.5 for both the experimental joint and the

finite element model. This load level corresponds to the load at which the experimental load-deflection curve becomes non-linear. By comparing the values of maximum deflection it is shown that the stiffness of the model is within 13 % of the stiffness of the tested joint.

6.3.4 Effect of using Non-Linear Fillet Material Properties

Except for model 1 for which only one load has been applied, a series of load steps corresponding to the changes in slope of the experimental load-deflection curve have been applied to the full 2D FE models to investigate the effect on the stiffness of the non-linear fillet material stress-strain curve. The stiffness of the joint at each load level has also been calculated. Table 6.6 gives a selection of the values of maximum deflection, fillet principal stresses and strains and overlaminate maximum in-plane and through-thickness stresses and joint stiffness for the loads investigated. The values of stiffness of the joint at each load level are almost equal for each load, thus indicating that the inclusion of the non-linear material stress-strain curve has no effect on the overall stiffness of the joint.

This was not unexpected since the damage sustained by the tested joint was dictated by the overlaminate rather than the fillet material. For tee joints with a thin overlaminate, however, the response of the tee joint is largely dependent upon the fillet resin (Shenoi & Hawkins). Consequently the correct representation of the resin non-linear stress/strain curve is much more important.

6.3.5 Effect of using Non-Linear Geometry

Due to the nature of the applied load, large deflections may cause distinctive changes in the model geometry. For example, a 45 degree pull-off load shown in Figure 6.8 initially causes the web of the joint to bend. As the deflections become larger, the 45 degree pull-off load is acting more like an axial pull-off load. The large deflection option alters the material stiffness matrices accordingly to take this increase in strain into account. A large deflection analysis has been carried out on all the models at a number of load steps to note the effect on the tee joint stiffness. Table 6.7 shows the values of maximum deflection and hence the stiffness achieved at two load levels for model 1. It can be noted that the joint stiffness is almost unaffected by the inclusion of the non-

linear geometry option.

6.3.6 Correlation with Experimental Load-Deflection Curve

Graphs showing points on the load versus deflection (P/δ) curve for each of the six models compared with the experimentally derived curve are shown in Figures 6.9(a) to 6.9 (f).

From Figure 6.9(a) it can be seen that the 2D undamaged model (Model 1) gives very similar values of deflection and hence initial stiffness to those obtained from the linear section of the experimental load-deflection curve. Model 2 results yield a stiffness of 1796 N/mm for a load of 5500 N, which is 20 % greater than the equivalent value yielded from the experimental curve at this load. The points on the P/δ curve are almost identical to those for model 1 for the loads considered. This can be seen in Figure 6.9 (b).

The points on the P/δ curve generated for model 3 are given in Figure 6.9(c). The results show a certain amount of stiffness reduction. i.e for a given load, the value of deflection calculated for model 3 is greater than that for both models 1 and 2. When comparing models 3 and 4, it can be seen that there is very little stiffness reduction due to the increased amount of delamination in the overlaminate in model 4. This can be noted when comparing Figures 6.9(c) and 6.9(d). The stiffness at a load of 10000 N for model 3 is 1762 N/mm and for model 4 is 1639 N/mm which is only a 7 % reduction. It can be noted that the deflections are very low when compared with the experimental values at the equivalent loads.

Model 5 represents the full experimental damage scenario. It can be noted that for only a small amount of delamination between the web/overlaminate interface and the flange/overlaminate interface, there is a large reduction in stiffness to 1265 N/mm for a load of 19000 N. This is clearly seen when comparing Figures 6.9(d) and 6.9(e). This value of stiffness is an 18 % reduction from the equivalent value for model 4 of 1548 N/mm. The deflections yielded from the FE models are approaching the equivalent experimental values.

In an attempt to achieve similar deflections to those obtained from experiment, model

6 was analysed which contains the same damage as model 5 but with further delaminations along the web/overlaminate and flange/overlaminate interfaces. This amount of delamination does give values of deflections close to the experimental values although there is still some difference, as can be seen from Figure 6.9(f).

It is likely that there was internal damage which was not visible during the experiments. In addition, it is possible that there was more delamination along the web/overlaminate and flange/overlaminate interfaces than was visible during the tests. This would account for the increased flexibility and hence deflection of the joint for a given load. To confirm this hypothesis, an FE model of the flange plate alone was generated and loaded in three point bending. The central deflection at a load of 19 kN is equal to 27.7 mm which is within 0.8 % of the experimental maximum deflection of the entire joint. This result shows that the tee joint behaviour is ultimately dictated by the stiffness of the flange plate. In addition, a 2D tee joint finite element model has been generated to represent complete delamination along the entire overlaminate/flange interface. The fillet material elements, however, remained in contact with the flange. The value of the maximum deflection at the tip of the web for this model equalled 21.6 mm for an applied load of 19 kN. This suggests that there may have been substantially more delamination along the flange/overlaminate interface than could be observed from the experiments.

Five notable features can be concluded:

(i) The stiffness of each of the finite element models generated appears to be higher than that of the tested specimens at the equivalent loads.
(ii) There was no visible damage which occurred at 8600 N to explain the sudden stiffness loss at this load. Poor resin impregnation, however, within the woven roving layers thus giving rise to a delamination would account for the sudden loss of stiffness at 8600 N. This would, as a result, give rise to larger deflections for a given load.
(iii) From a comparison of the stiffness values calculated at a load of 19000 N which is the experimental failure load of the joint, models 4 and 5 show that an increase in the amount of delamination along the web/overlaminate and flange/overlaminate interfaces greatly increases the deflections. It is likely that a certain amount of delamination between the web/overlaminate and flange/overlaminate occurred earlier than was visible with the naked eye.

(iv) The stiffness of an FE model of the flange plate alone is almost identical to the stiffness of the tested tee joint. It can be concluded from this that at the time of failure, the overlaminate and fillet did not significantly contribute to the stiffness of the tee joint. Thus, the final failure of the tee joint is dictated by the flange plate alone.

(v) Importantly, however, the stiffness losses associated with the numerically generated load-deflection curves mirror the stiffness losses of the tested specimens with reasonable accuracy.

6.4 Stress Patterns

MODEL 1

The first sign of damage in the experiments was noted at 5500 N when the fillet was seen to crack. It was this value of load which has been used to evaluate the theoretical deflection obtained from the undamaged model. This has been used to assess the accuracy of the model. The values of the maximum fillet principal stress, maximum overlaminate in-plane stress and maximum overlaminate through-thickness stresses are given in Table 6.8.

The distributions for fillet principal stress, S_p, overlaminate in-plane, $S_{i\text{-}p}$, and through-thickness, $S_{t\text{-}t}$, stresses are shown graphically in Figures 6.6(a), 6.6(b) and 6.6(c) respectively. The maximum value of fillet principal stress is 8.6 MPa at 5500 N which would not be enough to cause failure since the ultimate tensile stress of the fillet material can be taken as 26 MPa (Scott Bader). The maximum value occurs in the upper fillet corner where the overlaminate material meets the web and is shown in Figure 6.6(a).

The maximum value of in-plane stress in the overlaminate occurs on its outer surface near the centre and is shown in Figure 6.6(b). A value of 53 MPa is not enough to cause failure since the in-plane tensile strength of the overlaminate material is taken to be 207 MPa (Shenoi & Hawkins).

The distribution for the overlaminate through-thickness stresses is shown in Figure 6.6(c) and has a maximum value of 6.3 MPa. This would be enough to cause failure since it is approximately equal to the quoted interlaminar tensile strength of 7 MPa (Bird &

Allan). The maximum value of the overlaminate through-thickness stress occurs near the lower fillet corner indicating likely delamination along the flange/overlaminate interface.

MODEL 2

Only the fillet was seen to crack in the experiments but it is likely that a small debond would have occurred first as this would induce higher stresses in the fillet causing it to fail. Stress results have been obtained for this model at five different load levels.

Since the internal stress distribution for this model is almost identical to that of the undamaged model (model 1), plots of the stress distributions have not been repeated. Alternatively, the values of the maximum fillet principal stress, maximum overlaminate in-plane stress and maximum overlaminate through-thickness stresses are given in Table 6.9 in addition to a sketch of the exact location of each stress.

At a load of 5500 N, Table 6.9 shows that the maximum value of the fillet principal stress occurred in the upper fillet corner. The magnitude is, however, lower than the fillet ultimate tensile strength of 26 MPa. In addition, the strains in the fillet have been found to be of the order of 0.5 % which is negligible compared with the quoted elongation at break value of 100 % (Scott Bader). The regions of maximum overlaminate in-plane and through-thickness stresses are in the same location as for model 1. As the applied load is increased, the overlaminate through-thickness stresses increase above the ultimate stress thus indicating that delaminations would occur.

As the load is increased, the location of the regions of maximum stress remain in the same location as for lower loads. The size of the region under maximum stress, however, enlarges slightly as the load is increased.

MODEL 3

This model represents the debond, the crack in the fillet and the first delamination. The values of the maximum fillet principal stress, maximum overlaminate in-plane stress and maximum overlaminate through-thickness stress and their locations are given in Table 6.10.

At a load of 5500 N the maximum principal stress in the fillet, S_p, occurs in the upper fillet corner on the damage side of the model as before. High values of S_p are obtained in the upper fillet corner on the non-damage side. The region of maximum stress appears to be smaller than in the case of model 2. The maximum value of $S_{i\text{-}p}$ in the overlaminate is in a similar region as model 2 and is of a similar magnitude.

The maximum value of $S_{t\text{-}t}$ in the overlaminate occurs at the upper end of the inserted delamination. For example, at a load of 7500 N, the magnitude of this stress has been taken to be 29 MPa which is high in comparison with the equivalent value at the lower end of the delamination of about 8 MPa. The reason for this high value is that no explicit failure criterion has been set in the models used here. Hence a value higher than the interlaminar tensile strength indicates failure in a qualitative sense.

The exceptionally high stresses have been found to be due to the presence of singularities. To be certain of this, the average nodal stresses have been noted for the nodes along the delamination passing around the radius of the overlaminate in model 3 at a load of 7500 N. Figure 6.10 shows the distribution of nodal average stresses around the delamination. Position 12 represents the node at the delamination tip whose through-thickness stress is exceptionally high when compared with the other nodal values. The exceptionally high values calculated can therefore be explained by the presence of singular stresses. Hence, the actual value of maximum overlaminate through-thickness stress at a load of 7500 N is taken to be of the order of 8 MPa having removed the effect of the singularity. All values of through-thickness stresses stated from now on have had the effect of the singularity removed.

Table 6.10 shows that as the applied load increases the through-thickness stresses in the overlaminate increase to values greater than the ultimate stress and would thus cause further delamination.

MODEL 4

This model represents the debond, the crack in the fillet and further delaminations. The values of the maximum fillet principal stress, maximum overlaminate in-plane stress and maximum overlaminate through-thickness stresses and their locations are given in Table 6.11.

At a load of 10000 N the maximum fillet principal stresses occur in the region of the lower fillet corner, again indicating that damage along the flange/overlaminate interface is likely. The magnitude of the maximum S_p is approaching the failure load of the fillet. At a load of 15000 N the principal stress distribution in the fillet is the same as at a load of 10000 N except that there is an additional high stress region in the upper fillet corner on the other side of the web.

The principal stress distribution in the fillet at a load of 19000 N is the same as at a load of 15000 N except that there is an additional high stress region in the lower fillet corner on the other side of the web. The maximum value of $S_{i\text{-}p}$ in the overlaminate is in a similar region as model 3. Failure due to overlaminate in-plane stresses would not be predicted to occur at this load since the maximum stress value is less than the ultimate tensile strength of 207 MPa. At a load of 19000 N, however, the maximum in-plane stress in the overlaminate is greater than the ultimate stress and thus damage is predicted at this load. The maximum value of overlaminate through-thickness stress occurs near the ends of the inserted delaminations and their magnitude is great enough to indicate propagation.

MODEL 5

This model represents the completely damaged joint as observed from experiments at the failure load of 19000 N. The values of the maximum fillet principal stress, maximum overlaminate in-plane stress and maximum overlaminate through-thickness stresses and their locations are given in Table 6.12.

At a load of 5500 N the maximum principal stress in the fillet occurs in the lower region of the fillet. A region of high principal stress also occurs at the lower end of the inserted crack. There are also regions of high fillet principal stresses in the upper and lower fillet corners on the other side of the web at a load of 17000 N.

The value for the maximum in-plane stresses in the overlaminate increase steadily as the applied load increases. At a load of 15000 N and above, the magnitude is such that damage would be predicted. The maximum value of the overlaminate through-thickness stress is significantly lower than that for the same load for previous models. The magnitude also suggests that further delamination is unlikely.

MODEL 6

This model represents the completely damaged joint as observed from experiments at the load of 19000 N as well as additional delamination along the web/overlaminate and flange/overlaminate interfaces. The values of the maximum fillet principal stress, maximum overlaminate in-plane stress and maximum overlaminate through-thickness stresses and their locations are given in Table 6.13.

The stress distributions yielded from this analysis are similar to those generated for model 5. The overlaminate in-plane and through-thickness stresses are lower than the equivalent ultimate values thus suggesting that no further damage or delamination is likely.

6.5 Discussion

6.5.1 Stiffness Correlation

The experimental load-deflection curve has been modelled satisfactorily. However, the numerical results did not give as much deflection for a given load as that which occurred in the experiments. This could be due to a number of reasons. It is possible that damage was present in the joint prior to loading, due to such factors as fabrication technique and method of fillet injection. An FE model of the flange plate alone gives an almost identical value of stiffness as the specimen at the failure load. This indicates that the overlaminate does not contribute to the load bearing capability of the joint close to failure.

It has been shown that the presence of delaminations in the overlaminate material of a tee joint under three point bending causes a stiffness reduction of the joint. The overlaminate material in this case is built up of 11 plies of woven roving (WR) and chopped strand mat (CSM) in a polyester resin. The exact lay-up, starting from the inner ply is, CSM, CSM, WR, CSM, CSM, WR, CSM, CSM, WR, WR, WR. In the case of the tee joint under a three point bending load, the delaminations have been found to occur between the second CSM layer and first WR layer (i.e between plies 2 and 3). On further loading, a delamination appeared between the first WR and the third CSM layer (i.e between plies 3 and 4). It is this latter delamination which shall be discussed below.

The stiffness reduction for a delamination between plies 3 and 4 has been calculated from the analytical stiffness reduction technique discussed in Section 4.3.1. The value of stiffness of the mixed laminate which makes up the overlaminate has been calculated from the equations in Section 4.2.3. The overall stiffness reduction has been calculated to be 9.0 %. The experimental stiffness reduction due to the presence of a delamination in this location is equal to 15 %. The finite element representations of the tee joint discussed above give a stiffness reduction of 9.2 % due to the presence of the delamination.

It has thus been shown that the analytical model discussed in Section 4.3.1, although intended for the analysis of angle-ply laminates, gives a reasonable value of the stiffness reduction of a delaminated mixed laminate when compared with finite element representations. However, the stiffness reduction calculated from the analytical model is significantly lower than the stiffness reduction of a tested specimen. The discrepancies between the amount of stiffness reduction calculated from the analytical model and the experimental stiffness reduction can be explained by the fact that the analytical approach assumes that the laminate is initially flat and under pure tension. This is not the case in the experiments where flexural and shearing loads are also present and where the overlaminate is initially curved.

6.5.2 Assumed Material Properties and Boundary Conditions

Since the assumed material properties may not completely represent the actual values of the materials used in the joint, a series of analyses have been carried out to investigate the effect of varying two of the material properties. For the undamaged 2D model (model 1), the fillet elastic modulus has been varied in addition to the WR value of the Poisson Ratio. Table 6.14 shows the values of deflection, maximum fillet principal stresses and strains and the maximum overlaminate through-thickness and in-plane stresses for an applied load of 5500 N for each of the analyses in addition to the results for the original model. From the table it is shown that if the fillet elastic modulus is reduced from 1500 MPa to 500 MPa, the maximum deflection of the joint increases by 6.7 %. On the other hand an increase in fillet elastic modulus from 1500 MPa to 3500 MPa reduces the maximum deflection by 3.3 %.

The assumed material properties used in the FE models are given in Table 6.1. Any

uncertainties with respect to the assumed material properties are not likely to differ by large amounts. Consequently, the stiffness and internal stress patterns of the model representing the tee joint will not vary significantly. Thus the initial values used in the FE models have not been altered.

Since delaminations rarely occur smoothly between two layers, it is assumed that the stiffness of the material in the vicinity of the delamination(s) is reduced due to the local damage associated with the delamination(s). Table 6.15 shows the effect on the joint stiffness when the stiffness of certain elements is reduced. Table 6.15 shows, however, that this has very little effect on the overall joint stiffness.

Stresses in the fillet are low and not adequate to cause the experimentally observed failure. As indicated earlier, the fillet failure may have been due to imperfections or flaws. Importantly, stress patterns in the overlaminate seem to adequately mirror the damage scenario seen in the experiments. In addition, tensile tests have been carried out by Read on small specimens of urethane acrylate resin which is the material used in the tee joint fillets. The ultimate tensile stress was estimated to be of the order of 16-17 MPa rather than the quoted value of 26 MPa. This also explains the premature failure of the fillet.

6.5.3 Comparison of Finite Element Stress Patterns with Experimental Damage

MODEL 1

At a load of 5500 N the high principal stresses in the upper fillet corners indicate that damage is likely along the web/overlaminate interface. Figure 6.6(a) shows the stress distribution. The resulting stresses in the fillet at a load of 5500 N equal to 9 MPa would not be enough to cause failure of the fillet material which has a UTS of 26 MPa. It is possible that either an initial flaw or void was already present in the fillet due to fabrication processes. This flaw may have caused premature failure in the joints. Further research (Elliott, March 1996), however, in which a series of tensile tests were carried out on the urethane acrylate fillet material gave rise to a number of interesting points:

(i) Problems were experienced in the test specimen manufacture due to the large number of voids.

(ii) The voids present in the specimens led to a reduction in the elongation of the material from 100 % which is the quoted value (Scott Bader) to less than 5 % and in the worst case to 1.7 %.

(iii) Elliott suggested that the presence of the voids led to the premature fillet failure which was seen in the tee joint experiments.

In order to check whether or not the presence of voids in the fillet gave rise to the experimental premature failure of the fillet, a series of finite element models have been generated which contain voids in the fillet. The load applied to the models was 5500 N in each case which is the experimental load at which the fillet was seen to crack. The values of the fillet principal stresses and strains calculated for each model are given in Table 6.16. The model containing a void in the region of highest principal stress (shown in Figure 6.6(a)) gives a maximum principal stress of 14.3 MPa and a strain of 0.8 %. This indicates that the presence of voids in the fillet greatly increases the principal stresses in the fillet.

As already mentioned, Read discovered that the UTS of the fillet material was of the order of 16 MPa and not 26 MPa quoted by the manufacturers. It is thus likely that the premature failure of the fillet could be due to the presence of voids in the fillet.

The highest values of through-thickness stress in the overlaminate occur in the lower three to four layers of the overlaminate in two distinct regions as shown in Figure 6.6(c). This is consistent with the delaminations which were seen in the experiments.

MODEL 2

At a load of 5500 N the principal stress in the fillet is lower than the fillet ultimate tensile stress of 26.0 MPa. In addition, the strains in the fillet were found to be of the order of 0.5 % which is negligible compared with the quoted elongation at break value of 100 %. This result indicates that the fillet would not fail at this load.

The through-thickness stress distribution at this load is similar to that for model 1 at the corresponding load level and indicates that the delamination would progress. At a load of 7500 N at which the first signs of delamination were visible, high through-thickness overlaminate stresses occur near the lower fillet corner, indicating that there would be

delamination along the flange/overlaminate interface.

MODEL 3

At a load of 7500 N high regions of through-thickness overlaminate stresses occur in the central regions of the overlaminate where the delaminations are present indicating that further damage in these regions is likely. When the load is increased to 10000 N, a much greater region of high through-thickness overlaminate stresses is present which is consistent with the observed failure at this load indicating numerous delaminations in this region.

MODEL 4

At loads of 10000 N and 19000 N, regions of high through-thickness overlaminate stresses indicate that delaminations are likely along the web/overlaminate and flange/overlaminate interfaces. This is consistent with the experimental findings.

MODEL 5

At a load of 19000 N stresses in the fillet are still low and not great enough to cause the experimentally observed failure. As indicated earlier, the fillet failure is likely to have been due to imperfections or flaws. Importantly, stress patterns in the overlaminate seem to adequately mirror the damage scenario seen in the experiments. The maximum values of the overlaminate through-thickness have reduced significantly indicating that further delamination is unlikely. The introduction of the delaminations into the model has the effect of relieving these stresses within the boundary angle. The in-plane stresses, however, are much greater than the ultimate stress level at loads above 15000 N. This would indicate damage on the outer surface of the boundary angle.

6.5.4 Identification of Delamination Prone Areas

The initial decision to use a two dimensional model rather than a three dimensional model has allowed the generation of a large number of models since the models are less complex to produce without the loss of accuracy. The series of full 2D models has given an indication of the stiffness reduction due to the progressive delaminations within the

joint. As a result of the stress analyses it has been possible to identify the regions which are most susceptible to damage. The curved region of the overlaminate is inherently the region in the joint which is most prone to delamination.

The stress values yielded from the analyses have given an indication as to whether delaminations would be likely to form. It has, therefore, possible to determine areas which are initially prone to delamination.

In order to fully understand the load transfer mechanisms within the joint, it is necessary to investigate the overlaminate in-plane and through-thickness distributions along two paths as shown in Figure 6.11. The tee joint which has been investigated in this manner is the undamaged tee joint model (model 1) under a three point bending load of 7.5 kN. This is the load level at which the first delamination occurred in the experiments. Two paths, numbered '1' and '2' have been defined which pass through the thickness of the overlaminate in different locations. The in-plane and through-thickness stresses at all the nodal locations along each path have been calculated. The path analysis has also been carried out for the model containing the initial delamination in the overlaminate (model 3).

Figure 6.12(a) and 6.12(b) shows the in-plane and through-thickness stresses calculated at 12 nodal positions along path 1 for model 1. Figure 6.13(a) and 6.13(b) show the equivalent results for model 3. In the Figures, '1' is the inner-most node defining the overlaminate and '12' is the outer-most node of the overlaminate, close to the surface. The in-plane stresses and through-thickness stresses calculated along path 2 are given in Figures 6.14(a) and 6.14(b) for model 1 and Figures 6.15(a) and 6.15(b) for model 3.

Figure 6.12(a) shows that the in-plane stresses gradually increase from the inner regions to the outer regions of the overlaminate. Thus, at higher loads, damage is more likely to occur in the outer plies. Figure 6.12(b) shows that the through-thickness stresses steadily rise towards the centre of the overlaminate and then drop dramatically as the outer plies are reached. This shows that at higher loads, delaminations are more likely to occur in the inner or central regions of the overlaminate rather than close to the surface of the overlaminate. This is consistent with the experimental findings (Elliott). The oscillatory nature of the curve occurs because the inner most node at position 1 is

not at the location of the maximum through-thickness stress. The following nodes in positions 2-8 pass through the regions of higher through-thickness stress which then tails off as the outer layers are reached.

Figure 6.13(a) shows a similar distribution as in Figure 6.12(a) except that there is a drop in the in-plane stress at node position 4. The delamination tip is at node position 3 and it is due to the presence of the tip that the in-plane stress drops. Figure 6.13(b) shows that the through-thickness stress is greater than the ILTS in the inner regions of the overlaminate and that it gradually reduces close to the surface.

Figure 6.14(a) shows that the value of the in-plane stress is greatly dependent upon the type of material present in each layer. The values of the in-plane stress have been calculated at nodes along the path which are at the interface between two layers of the overlaminate with one element modelled per layer. The graph shows distinct peaks at the nodes which are at the interface between a layer of WR and a layer of CSM (nodes at positions 3, 4, 6, 7 and 9). This is due to the difference in the values of the in-plane stiffness of the WR and CSM layers. The nodes in positions 10, 11 and 12 are located between layers of WR. The outer regions of the overlaminate are under the highest in-plane stresses.

Similar findings have also been reported by Dulieu-Smith et. al.. Thermoelastic stress analyses have been carried out on tee joints tested under static 45 degree pull-off loads. Plots of the sum of the principal stresses have been plotted at points along a path crossing from the outer edge of the overlaminate under tension, through the web plate and to the outer edge of the overlaminate under compression. The principal stresses in this case have been assumed to be equal to the through-thickness stress and in-plane stress. The ultimate aim is to be able to separate these two components of stress from the results of the thermoelastic technique in conjunction with a photoelastic technique which measures the principal strains. Figure 6.16 shows an example of the thermoelastic signal for one path. The thickness of the overlaminate in this case is about 15 mm. The ordinate shows the summation of the principal stresses at each point along the path. There is a distinct jagged appearance to the curve which is likely to be due to the difference of the materials used in each layer.

Figure 6.14(b) shows that the through-thickness overlaminate stresses in the region close

to the fillet are greater than the ILTS of 7 MPa. The node in position 1 is in the exact location of the maximum through-thickness stress at this load. The through-thickness stress gradually decreases towards the outer layers of the overlaminate. This corresponds with the experimental findings that a delamination occurred within approximately ply 3 of the overlaminate under a three point bending load (Elliott, 1994).

Figure 6.15(a) shows that the peak in-plane stress occurs close to the delamination tip at position 3. The reason why the values of in-plane stress do not rise close to the outer surface of the overlaminate as in the case of model 1 shown in Figure 6.14(a) is because the presence of the delamination re-distributes and tends to even out the stresses. Along path 2, the in-plane stress contours are very similar from the centre to the outside of the overlaminate. Figure 6.15(b) shows that the highest through-thickness stress also occurs close to the delamination tip at position 3. This is to be expected, since it is likely that the delamination would propagate at this load due to high through-thickness stresses.

It has been shown that the delaminations form in the inner regions of the overlaminate due to high through-thickness stresses. These delaminations have the effect of reducing the through-thickness stresses. On further loading the through-thickness stresses cause additional delaminations. There reaches a point whence the through-thickness stresses have dropped significantly, even at high loads, and thus delamination due to through-thickness stresses ceases. However, the presence of the delaminations in the inner regions of the overlaminate causes an increase in the in-plane stresses in the outer regions of the overlaminate. Thus, damage is subsequently caused in these outer regions due to high in-plane stresses.

Similar results have been obtained in Chapter 4 for a square plate containing straight cracks. Under a mode I, opening, type of load acting perpendicular to the crack front, it has been shown that the presence of a second crack reduces the mode I stress intensity factor thus indicating that crack propagation is less likely to occur due to through-thickness stresses. The presence of the second crack dramatically increases the mode II stress intensity factor. This indicates that crack propagation is much more likely to occur due to in-plane shear stresses when a number of cracks are present in the laminate.

6.6 Stress Patterns for a 45 Degree Pull-Off Load

The stiffness and stress distributions for model 1, discussed above, have also been yielded for a 45 degree pull-off load. The results have been compared with published data obtained from similar tee joints (Shenoi & Hawkins, 1992). Figure 6.17 (Sample B) shows a typical experimental load/deflection plot. The figure shows that there is a significant drop in stiffness when the applied load reaches about 5 kN, indicating that delaminations have formed. Further load application shows additional load carrying capability up to 11 kN resulting in further delamination and final failure at 15 kN. For an applied load of 5 kN, which is the load at which delaminations occurred in the experiments, the deflection calculated from the FE model is equal to 3.48 mm. This corresponds very well with the equivalent value from the experimental load/deflection curve. At a load of 5 kN, the maximum through-thickness stress in the overlaminate is equal to 7.5 MPa in the inner regions of the overlaminate indicating that delaminations are likely to occur in these regions because this value is greater than the quoted ILTS of 7 MPa (Bird & Allan). This corresponds directly to the experimental findings for which delaminations occurred within the third ply of the overlaminate at a load of 5 kN. Consequently, the model is not only consistent with data from a three point bending load but also with data determined from a 45 degree pull-off load.

6.7 Conclusions

The simplified tee joint model which uses material properties calculated from the adapted laminate theory would predict delamination in the inner regions of the overlaminate for a three point bending load of 5500 N. Thus using this simplified method it is possible to identify the region most susceptible to damage. It is a good first step but the more detailed models containing one element per layer of overlaminate are necessary so as to exactly represent the delaminations which occur under load.

The finite element models containing delaminations can appropriately represent the stiffness reduction due to delamination which has been seen in three point bending experiments. In addition, the resulting internal stress distributions indicate regions within the overlaminate under high through-thickness stresses. These regions which would be likely to delaminate directly correspond with the regions of the tested tee joint overlaminate which contained delaminations.

The reason why the finite element model did not correctly predict fillet failure is explained by the fact that the experimental tee joints contained a significant number of voids which reduced the ultimate tensile stress of the fillet material. Finite element models containing voids in the fillet successfully predicted that premature failure would have occurred since the voids had the effect of increasing the fillet principal stresses.

Under three point bending, the presence of the delaminations in the overlaminate has the effect of relieving the stress which enables the structure to continue sustaining load. On further loading, the through-thickness stresses increase again thus resulting in delaminations. This damage continues as the load is increased. This is shown well by comparing the through-thickness stresses for models 3 and 4 at a load of 10000 N. For model 3 the equivalent value is 10.7 MPa which would result in delaminations forming since it is greater than the ILTS. For model 4, the maximum value of through-thickness stress is 5.5 MPa which does not indicate that delaminations are likely to form. As the load is again increased for model 4, the through-thickness stresses increase above the ILTS and thus indicate the likely formation of delaminations.

The in-plane stresses in the outer regions of the overlaminate increase as the amount of delamination increases in the inner regions. It can, therefore, be concluded that initially, the delaminations arise on the inner surface of the overlaminate due to the presence of high through-thickness stresses. As loading increases, the delaminations which form have the effect of relieving the through-thickness stresses. As the load increases, the in-plane stresses increase and ultimately cause damage close to the outer surface of the overlaminate.

7. FRACTURE BEHAVIOUR OF TOP HAT STIFFENERS

7.1 Introduction

Chapter 5 discussed the strength approach adopted in order to assess the integrity of two types of top hat stiffener under three loading configurations. In the case of the three point bending load scenario, the failure modes of the two types were very similar. Both types of top hat initially failed by delamination in the curved part of the overlaminate near the outer surface and then by flexural failure in the central region of the flange plate on the inside. In the case of the reverse bend, both types of top hat ultimately failed in flexure in the flange in the central region of the outer surface. In the case of the pull-off load, both top hat types failed by the overlaminate separating completely from the flange plate. This chapter focuses on delamination damage. Since under three point bending loads, both types of top hat stiffener initially failed due to delaminations in the curved region of the overlaminate, only the type I stiffener shall be discussed in this chapter. It is assumed that delaminations can be treated as cracks.

Using the fracture mechanics approach, it is possible to determine the most critical crack lengths and depths for cracks in the curved region of the overlaminate for a top hat under three point bending, reverse bending and straight pull-off loads (Phillips et. al.). Although, delaminations did not occur in the overlaminate in the case of the reverse bending or the pull-off loads, it is important to assess the damage tolerance of delaminations under these modes of loading. A three-point bending type load may initially cause the formation of the delaminations but the load scenario may change to be that of a reverse bend or pull-off type.

7.2 Fracture Mechanics Criteria used in the Approach

Two dimensional linear elastic fracture mechanics (LEFM) models have been used to calculate mode I and mode II stress intensity factors which, in turn, have been used to evaluate strain energy release rates, G. The theoretical basis has been outlined previously in Appendix 2A and Chapter 4. The load-deflection characteristics of the top hat stiffener under the three modes of loading discussed in Chapter 5 are almost linear. For this reason, only the strain energy release rate has been calculated in each case.

7.3 Modelling Details

The FE model used in the strength analyses discussed in Chapter 5 has been adapted so as to include a region containing cracks. The crack elements are six-noded triangular elements with their mid-side nodes at the quarter point. The details of the crack elements are given in Appendix 4K. Figure 7.1 shows a typical FE model used in the analysis and the region containing the crack is shown in Figure 7.2.

Investigations showed that under certain conditions the two crack faces crossed over each other, i.e under a tensile load, the vertical displacement of the top crack face was in fact less than the vertical displacement of the lower crack face. In order to prevent this from occurring, a number of 'gap' elements were inserted along the crack face. The gap element behaves as a linear spring in compression but the tensile stiffness drops to zero thus not inhibiting the crack face should it open. In addition, the unloaded crack face is generated using nodes at the same location since the gap element allows connection of two nodes which are initially coincident. The problem of crack faces overlapping has been discussed by Pavier & Clarke and Tian & Swanson, the latter stating that four methods exist which can be used to overcome this problem: (a) application of displacement constraints on the crack face nodes, (b) application of nodal loads on the crack face, (c) application of gap elements at the crack interface or (d) to assume that the overlapping effect is negligible. Long & Swanson also used gap elements to prevent interpenetration. Details of the gap elements used in the model are given in Appendix 7A. A check has been made to confirm that the presence of the gap elements does not affect the calculated values of the strain energy release rate. This has been done by comparing the results from two models with and without the gap elements present. The two sets of results are identical indicating that the presence of the gap elements has no effect on the calculations.

7.4 Loads, Material Properties and Boundary Conditions

The material properties used in the finite element model are given in Table 7.1. Conditions of simple supports have been applied to each of the FE models. The applied load in each case is chosen as 10 kN in each case. The significance of this load is that it is below any delamination damage which occurred in the three point bend and reverse bend tests (Elliott, 1992). Thus, any cracks inserted in the model should be stable at this

load. Additionally, since the strain energy release rates are proportional to the square of the applied load, it is simple to interpolate values for different load values.

7.5 Sensitivity Studies

A series of two dimensional models have been generated and values of G calculated at the crack tip furthest from the centre line of the top hat. The calculation of G requires that the face of the crack is parallel to the global x-axis. This crack tip (marked *) is shown in Figure 7.2.

7.5.1 Three Point Bending

The strength analysis discussed in Section 5.5.1 (A) showed that the failure mode of the top hat under a three point bending load consisted of delaminations in the overlaminate. For this reason, the cracks which have been modelled are located in this region. Two sensitivity studies have been carried out for cracks in the overlaminate, namely effect of crack depth and crack length on the calculated values of the strain energy release rate, G.

(A) Crack Depth

Figure 7.3 shows the variation of G with crack depth. It can be noted that there is a peak value of G which corresponds to a crack depth of 4 mm. Cracks which are deeper than 4 mm give rise to lower values of G. It is anticipated that the reason why the value of G calculated for the crack at 2 mm depth is lower than expected is due to the proximity of the crack to the surface. Cracks close to the surface are more difficult to model than those deeper within the overlaminate due to the limited area available to mesh with elements. This problem can be avoided to a degree, by refining the mesh close to the surface. All the values of G are, however, less than the critical value of 0.5 kJ/m^2. This indicates that none of these cracks under the three point bend would propagate. The trend does, however, suggest that under three point bending, cracks which are deeper within the overlaminate are less likely to propagate than those nearer the surface.

(B) Crack Length

Figure 7.4 shows the variation of G with crack length. Each crack is at a depth of 6 mm from the outer surface of the overlaminate. It can be noted from the graph that the values of G increase at a steady rate as the crack length increases. The critical value of G is 0.5 kJ/m^2. From the graph in Figure 7.4, this value of G corresponds to a crack length of about 38 mm. Therefore, it can be concluded that cracks greater than 38 mm in length at a depth of 6 mm under these loading conditions are likely to propagate.

7.5.2 Reverse Bending

The effect of crack depth and crack length on the calculated values of the strain energy release rate has been investigated for a top hat under a reverse bending load.

(A) Crack Depth

Figure 7.5 shows the variation of G for four crack depths. A similar trend as for the three point bending load is found. All the values of G, however, are lower for each crack depth when compared with the equivalent value for the crack under a three point bend load. As for the three point bending load, deeper cracks are less likely to propagate than those close to the surface.

(B) Crack Length

Figure 7.6 shows the variation of G for a variety of crack lengths. It can be noted that none of the values are greater than the critical value of 0.5 kJ/m^2. Thus under a reverse bend load of 10 kN cracks less than 55 mm would not be expected to propagate.

7.5.3 Straight Pull-Off

The effect of crack depth and the effect of crack length has also been investigated for the case of a straight pull-off load.

(A) Crack Depth

Figure 7.7 shows the effect of crack depth on the calculated values of G, the strain energy release rate. It can be seen from the graph that a similar peak occurs at a depth of 4 mm as occurred in the case of the three point bend load. The peak value which occurs for a crack at a depth of 4 mm occurs at a value which is marginally lower than for an equivalent crack under a three point bending load but higher than for an equivalent crack under a reverse bending load. It can be concluded that deep cracks are less likely to propagate than cracks close to the surface.

(B) Crack Length

Figure 7.8 shows the variation of G for different crack lengths. All the cracks in this case are at a depth of 6 mm from the outer surface of the overlaminate. A similar trend as for the three point bend is achieved. There is a gradual increase in G for increasing values of crack length. The critical value of 0.5 kJ/m^2 for G corresponds to a crack length of about 30 mm. Therefore, it can be concluded that under a straight pull-off load of 10 kN cracks at a depth of 6 mm will propagate if they are greater than 30 mm in length.

7.6 Typical In-Service Load Conditions

7.6.1 Introduction

The effect of crack depth and length for the three different loading conditions discussed in the preceding chapters have been analysed at a load level of 10 kN. Naval vessels are likely to be in-service under extreme conditions due to warfare and environmental conditions. Shock loadings due to the proximity of the vessel to an exploding mine result in excessive loadings on the structure. Shock trials on such vessels have been carried out which yield values of shock loads which must be sustained by the hull structure (Sumpter). Therefore, in order to investigate the damage tolerance levels of top hat stiffeners under typical in-service loadings, the loads applied to the FE models must be representative. It is necessary to represent a dynamic load by a static load.

7.6.2 Calculation of In-Service Load

The shock load which has been applied to tee joints in shock tests (see Chapter 8) is said to represent the type of damage which occurs in-service, namely root whitening. It is assumed in this case that the acceleration which is applied to the tee joints to represent an in-service load can also be applied to the top hat stiffeners in this investigation. In order to simulate a shock load, a three point bending load, F, can be applied to the flange which is equal to:

$$F = M \times a \qquad (7.1)$$

where: M is the mass of the top hat stiffener and equals 4.8 kg
a is the acceleration experienced by the tee joint in the shock tests and is approximately equal to 2000 m/s^2.

From Equation 7.1, the applied force, F, which must be applied to the top hat flange is calculated to be 9.8 kN. The shock load can be represented by applying this load of 9.8 kN as a three point bend load, as shown in Figure 7.9.

7.6.3 Calculation of Critical Crack Length for the In-Service Condition

Values of the strain energy release rate have been calculated for cracks of different depths and lengths for the type I top hat stiffener under a three point bending load of 9.8 kN. The curve of strain energy release rate versus crack length at this load is almost identical to that at a load of 10 kN which is shown in Figure 7.4. Therefore, it can be concluded that for curved cracks at approximately mid-depth, those greater than 38 mm are likely to propagate under an in-service load condition.

7.7 Discussion

Figure 7.10 shows the effect of crack depth on the values of G, for all three modes of loading at loads of 10 kN. Ignoring the values calculated at depths of 2 mm, the results show that surface cracks are more likely to propagate than deep cracks. This is a consistent results for all three loading configurations considered. Figure 7.11 shows the effect of crack length on values of G, for all three modes of loading. The graph shows that the crack is most likely to propagate under a straight pull-off load. The crack is next

likely to propagate under a three point bending load and is most stable under a reverse bending load. The critical crack length for a straight pull-off load can be calculated from the curve to be 30 mm. This is assuming that the critical value of the strain energy release rate is equal to 0.5 kJ/m^2.

A typical in-service loading can be represented by a three point bending load. A three point bending load of 9.8 kN has been found to represent a typical in-service load. From this it can be concluded that curved cracks in the overlaminate at approximately mid-depth, are likely to propagate once they reach 38 mm in length.

8. FRACTURE BEHAVIOUR OF TEE JOINTS

8.1 Introduction

Chapter 6 discussed the strength approach used to assess the structural adequacy of tee joints. The material within the tee joint is deemed to have failed if the level of stress predicted by the finite element model is greater than a limiting value for the particular material. The regions within the tee joint which are most susceptible to damage have been shown to be within the overlaminate. The damage has been shown to be delamination-induced. Assuming that delaminations can be represented by cracks, it is possible to explore the sensitivity of crack propagation with regard to different geometric and material features of the tee joint.

This chapter discusses a fracture mechanics based approach to determine whether or not a particular crack will propagate under specified loading and boundary conditions. The criteria which have been calculated in the analyses are discussed in Section 8.2. A series of two dimensional (2D) finite element models have been generated using the ANSYS package (Solecki) which contain a variety of crack geometries and locations (Shenoi et. al. 1996), the details of which are given in Section 8.3. In addition, the loading and boundary conditions have been varied.

8.2 Fracture Mechanics Criteria used in the Approach

Two dimensional linear elastic fracture mechanics (LEFM) models have been used to calculate mode I and mode II stress intensity factors which, in turn, have been used to evaluate strain energy release rates. The theoretical basis has been outlined in Appendix 2A and Chapter 4. The approach adopted here is similar to that used for top hat stiffeners as outlined in Section 7.2. In addition, owing to the possible non-linear characteristics of the tee joint, values of the J-integral have also been calculated since the strain energy release rate is only valid in the case of LEFM. The J-integral can also be calculated for problems of LEFM and can be compared with values for the strain energy release rate since in LEFM the strain energy release rate is numerically equal to the J-integral.

8.3 Modelling Details

The finite element model generated in Chapter 6 (model 1) used to represent the undamaged tee joint, such as the one shown in Figure 8.1, has been adapted so as to include a region containing crack elements. Figure 8.2 shows the enlarged regions of the joint overlaminate ((a) flat region and (b) curved region) which contain the crack elements. In Chapter 6, it was stated that a significant amount of damage was seen in the overlaminate under a three point bending load. This is also the case for tee joints of a similar configuration under a 45 degree pull off load (Shenoi & Hawkins, 1992) where delaminations were seen in the curved region of the overlaminate. Therefore, all the models generated in this chapter contain cracks which are within the overlaminate region. The crack elements used are six-noded triangular elements with their midside nodes at the quarter point. This results in the required singularities in the strain at the crack tip. The crack tip elements used in the analyses are the same as those discussed in Chapter 4, the details of which are given in Appendix 4K. The method used to insert crack elements into the existing model are given in Appendix 8A. One restriction in using this approach is that the material in the cracked region is assumed to be homogeneous. Conditions of plane strain have been assumed since the tee joints are considered to be long in relation to their width. As in the case of the top hat stiffener models, gap elements have been included to prevent interpenetration of the two crack faces, details of which are given in Appendix 7A.

8.4 Loads, Material Properties and Boundary Conditions

The applied load chosen in all cases is 10 kN which is the load at which a significant amount of delamination occurred in the tee joints when loaded under a three point bending load (Elliott). In addition, a series of 45 degree pull off tests have been carried out by Shenoi & Hawkins, 1992 which show that a large amount of delamination occurs up to a load of 10 kN. It is also approaching the failure load of the joint. Thus, at this load level, values of the strain energy release rate and J-integral would be greater than the corresponding critical values indicating that crack propagation is likely.

The material properties used in the analysis, unless otherwise stated, are shown in Table 8.1. As mentioned in the previous section, the crack elements are assumed to have homogeneous properties, so values for the separate in-plane and through-thickness

moduli are not acceptable. The value for their elastic moduli is assumed to be between the value of the overlaminate in-plane moduli (13060 MPa for the WR and 6890 MPa for the CSM) and the through-thickness moduli (7770 MPa for both the WR and the CSM). A value of 10000 MPa has been chosen for the elastic modulus of the crack elements and 0.25 for the Poisson's ratio.

To represent the most severe type of loading, a 45 degree pull off load has been applied in each case under fully clamped conditions which have been modelled by restricting two nodes in both translational degrees of freedom.

8.5 Verification of the J-Integral

Since all the analysis discussed in Chapter 4 involved only linear elastic fracture mechanics, the J-integral has not yet been discussed. Since the J-integral is to be used in the analysis of cracks in tee joints, it is necessary to verify its use. Section 4.5.3 discusses the verification of the use of the strain energy release rate, G, by comparing FE derived values with results from an analytical model, for a crack in a square plate. Values of J-integral have also been calculated for this model and the values of G (analytical), G (FE) and J-integral (FE) are given in Table 8.2. It can be seen that all three values are very similar.

Initially, all the values of the J-integral which have been calculated were calculated at the right hand crack tip (marked * in Figure 8.2(b)) i.e. in order that the orientation of the crack tip is such that its face is parallel to the x-axis of the tee joint model and perpendicular to the y-axis. For these cases the existing software macro could be used. Consequently, the existing macro could only be used in a limited number of cases and an alternative approach had to be sought in order to calculate the J-integral values at crack tips which are orientated at angles to the global x-axis. An alternative macro is required in the case of crack tips in the curved part of the overlaminate. The existing macro has been adapted to be able to calculate the J-integral values at crack tips with any orientation relative to the xy plane of the tee joint model. The adapted macro is given in Appendix 8B.

In order to verify that the adapted macro gives correct results, a simple 2D FE model of a 250 mm^2 square isotropic plate containing a horizontal central crack of length 30

mm subjected to an arbitrary pressure load of 100 MPa has been generated and is shown in Figure 8.3. The two central nodes on both sides are restricted in both the translational degrees of freedom (x- and y- directions). The J-integral values using both the existing macro and the adapted macro have been calculated at both crack tips. In addition, to verify the J-integral calculated using the adapted macro, three FE models have been generated of a 250 mm^2 square plate with a 30 mm straight crack at various angles to the global x- axis. Figure 8.4 shows the three locations of the crack. The values of the J-integral have been calculated at both crack tips and compared with the calculated values of strain energy release rate. The results are given in Table 8.3.

It can be seen that the adapted macro gives identical results to the existing macro for a straight central crack. In addition, the values of the J-integral calculated from the adapted macro for cracks at different orientations compare very well with the values of the strain energy release rate. It is also interesting to note that the values of both the J-integral and strain energy release rate increase as the crack rotates from 0 degrees to 30 degrees and then fall as the crack is rotated from 30 degrees to 60 degrees.

8.6 Sensitivity Studies

8.6.1 Effect of Loading Conditions

Both 45 degree pull-off and three point bend load configurations have been modelled for a horizontal crack of length 10 mm at a depth of 6 plies from the outer surface of the overlaminate adjacent to the flange plate. This is at approximately mid-depth since the overlaminate is 11 plies thick.

Table 8.4 shows the J-integral values calculated from the finite element models for each loading condition. The results indicate that although the 45 degree pull-off is the worst condition, there is little possibility of the crack propagating since the strain energy release rate is well below the critical value of 0.5 kJ/m^2 (Court).

8.6.2 Effect of Boundary Conditions

The boundaries used in the models were those of rigid clamping and simple supports. The load level applied was as before. Table 8.5 shows the J-integral values calculated

for each boundary condition. It can be seen that the clamped condition gives marginally higher values than the simple supports. Thus, in the case of a ship, a tee joint which is fixed both sides of the web due to two tanks, for example, would present more serious consequences than if the joint was able to move more freely.

8.6.3 Effect of Boundary Locations

For the 45 degree pull-off load, the clamped boundaries have been set at three different spans. Figure 8.5 shows the J-integral values calculated for each condition. The trend indicates that the J-integral value is higher if the clamped boundaries are close together. For example, if the flange plate (hull shell) of the tee joint is stiffened on both sides of the web (bulkhead) then damage is most likely to occur if the stiffeners are close together.

8.6.4 Effect of Material Properties of Crack Elements

The crack elements used in this case have been assumed to have homogeneous properties. As a result, only one value of the elastic modulus can be chosen. In order to identify the effect of varying the modulus, the value of elastic modulus of the crack elements was set to three different values and the J-integral calculated in each case. Figure 8.6 shows the J-integral values calculated for each value of elastic modulus. It can be observed that the value of the J-integral is higher for low values of elastic modulus. This result must be taken into account when calculating the critical crack lengths (see Section 8.6.6) since the critical crack lengths will reduce if the assumed value of the crack element elastic modulus is reduced. i.e if the material is assumed to be less stiff. The influence of each of the in-plane and through-thickness moduli of the overlaminate materials must be estimated, in order to enter an appropriate value for the crack element elastic modulus.

8.6.5 Effect of Crack Depth

Up to now, only horizontal cracks have been considered. The experiments and finite element analyses discussed in Chapter 6 indicate that the delaminations most commonly occur within the curved region of the overlaminate. In this investigation, models have been generated to study the effect on the J-integral values of the crack depth for both

horizontal cracks and curved cracks. Figure 8.7 gives the values for the J-integral for the different crack configurations for both (a) horizontal and (b) curved cracks. The results indicate that for both curved cracks and horizontal cracks, the J-integral values are greater for deep cracks. i.e deep cracks are most likely to propagate.

8.6.6 Effect of Crack Length

In the case of a horizontal crack, the J-integral values for four different crack lengths have been calculated, see Figure 8.8. The right hand crack tip in each case remained in the same location and the length of the crack has been determined by the position of the left hand crack tip. It can be noted from the graph that long horizontal cracks give rise to higher values of the J-integral than shorter cracks.

In the case of curved cracks, a series of 9 models have been generated containing cracks of different lengths at approximately mid-depth of the overlaminate. From the results of section 8.6.5, it has been shown that deep cracks are more likely to propagate than cracks near the surface. Thus, the values of critical crack length calculated at the mid-depth are considered to be average values. Equivalent models which contain deeper cracks, would yield lower values for the critical crack lengths. Figure 8.9 shows an example of the finite element mesh generated for one particular case. The right hand crack tip (marked *) remained in the same location. The other tip was moved to 9 different locations around the radius of the overlaminate. It should be pointed out that the left tip of the longest crack extends into the vertical region of the overlaminate adjacent to the web.

The most severe loading condition has been found to be that of a 45 degree pull-off load under clamped conditions. These conditions have been applied in each case with an applied load of 10 kN and the constraints at 50 mm from each end of the joint. Figure 8.10 shows the values of the J-integral calculated at the right hand crack tip, for each crack length.

The results show that the maximum value of the J-integral occurs between crack lengths of 25 mm and 36 mm. This is in the region of maximum curvature of the overlaminate. The critical value of the strain energy release rate for the overlaminate material is quoted to be equal to 0.5 kJ/m^2 (Court). If a line is drawn across from the ordinate axis at this

value to the curve, the critical crack length for this loading configuration is equal to 16 mm. It can be concluded, therefore, that cracks longer than 16 mm are likely to propagate under these conditions.

In order to calculate the values of the J-integral at the left hand crack tip, it has been necessary to generate additional finite element models with a linear crack face close to the left hand tip. Four models representing cracks of four different lengths have been generated. Since the coordinate system for the left hand crack tip is not parallel to the global model coordinate system it is necessary to calculate the rotation angle of the crack local coordinate system with respect to the global model coordinates. A short program has been written to calculate the rotation angle and is discussed in Appendix 8B. The J-integral values have been calculated using the adapted macro at the left hand crack tip and using the existing macro at the right hand crack tip. In addition, strain energy release rates for both tips have been calculated, since all the analyses are linear elastic.

Figure 8.11 shows the strain energy release rate values and J-integral values calculated at both crack tips for four crack lengths, for cracks at approximately mid-depth. The results calculated at the left hand tip are higher than those at the right hand tip. This is to be expected, since the through thickness stresses in the curved region of the overlaminate are much greater than those in the flat region of the overlaminate. The curve for the left hand tip has a peak prior to that for the right hand tip. This indicates that the crack tips approaching the region of maximum curvature are the most likely to propagate. The critical strain energy release rate for the overlaminate material has been taken as 0.5 kJ/m^2 as already mentioned. Assuming this critical value, the critical crack length based on the values at the left hand tip can be calculated to be 8 mm. This is half the critical crack length of 16 mm based on the values at the right hand tip.

8.6.7 Modelling Two Cracks in the Overlaminate

Delaminations rarely occur singly (Elliot, Shenoi et. al. 1995). Thus it is important to investigate the effect of multiple cracks on the structural integrity of the tee joint. A 2D finite element model has been generated which contains two curved cracks, the enlarged crack region of which, is shown in Figure 8.12. As for the previous models, a 45 degree pull off load of 10 kN has been applied to the model. The values of the strain energy

release rate have been calculated at the two right hand crack tips (both marked *). The values of the mode I and mode II stress intensity factors and the strain energy release rate values are given in Table 8.6. In the table, model 1 contains a single crack and model 2 contains two cracks. The value for the strain energy release rate calculated at the right hand tip in the case of a single curved crack (model 1) is equal to 2.82 kJ/m^2. Thus, the presence of the second crack serves so as to reduce the strain energy release rate at the original crack tip by more than 60 %. It can therefore be concluded that the formation of the second crack is stress relieving and temporarily prolongs the life of the tee joint. It is also interesting to note that the formation of the second crack reduces the mode I stress intensity factor at the lower crack.

This conclusion has also been reached from the results of the tee joint strength analysis (Chapter 6) for a tee joint under a three point bending load. It was concluded that the initial delaminations formed in the inner regions of the overlaminate due to high through-thickness stresses. As loading increased, further delaminations formed until the through-thickness stresses actually reduced such that no further delamination was likely. The presence of the delaminations, therefore, reduces the through-thickness stresses but increases the in-plane stresses in the outer regions of the overlaminate. Ultimately, high in-plane stresses would be likely to cause damage in the outer regions of the overlaminate.

8.6.8 Curved Crack Modelled in the Central Region of the Overlaminate

The effect of curved crack length discussed in Section 8.6.6 was for a series of cracks in the overlaminate for which the right hand crack tip, in the horizontal region above the flange, was kept in the same location and the crack length was increased around the overlaminate radius. An FE model has also been generated which contains a curved crack in the overlaminate but whose right hand tip is moved closer to the curved region of the overlaminate as shown in Figure 8.13. A 45 degree pull-off load of 10 kN has been applied to the model. For the crack shown in the figure, which is 34.8 mm long, the value of the strain energy release rate at the left hand crack tip is equal to 0.1 kJ/m^2. For a similar but slightly longer crack whose right hand tip extends into the flat region of the overlaminate, the value of the strain energy release rate at the left hand tip is equal to 3 kJ/m^2. Thus, it can be concluded that a crack which extends into the flat part of the overlaminate is much more likely to propagate than one which is contained

entirely within the curved region.

8.7 Typical In-Service Load Conditions

8.7.1 Introduction

The sensitivity study discussed above allows the identification of critical crack geometries and loading conditions. In addition, it highlights the relative importance of specific cracks and their likelihood to propagate. The applied load of 10 kN used above, corresponds to the load at which damage was seen in static tests. In order to assess in-service damage tolerance levels, however, it is necessary to apply a typical in-service type of load to the FE models discussed above.

The tee joints under consideration are commonly used in minehunters which may be subjected to shock loads due to explosions under wartime conditions or slamming loads due to wave pressures or indeed impact loads with dockside or other vessels. The problem, therefore, requires that a dynamic shock or impact load must be represented by a static load. This has been carried out as follows.

8.7.2 Calculation of Applied Loads

Shock tests have been carried out on a variety of tee joint configurations (Sumpter). In order to simulate the type of damage, namely root whitening, which has been seen in tee joints on board ships, a large mass was fixed to the web of the tee joint on one side. This is shown diagrammatically in Figure 8.14. When the shock load is applied to the shock table, the web bends in such a way that root whitening occurs in the overlaminate on the opposite side of the web from the added mass. The added mass causes the root whitening in a similar manner in which a bulkhead, for example, causes root whitening due to inertia effects. In order to simulate a shock load, a pressure load, P, has been applied to the flange in the FE model.

$$P = \frac{F}{A} \tag{8.1}$$

where: A is the area of the flange exposed to the pressure load

F is the force which can be calculated from Equation 8.2

$$F = (M+m) \times a \tag{8.2}$$

where: m is the mass of the tee joint

M is the mass of the added mass

a is the acceleration experienced by the tee joint in the shock tests and whose value is typically about 2000 m/s^2.

In addition a direct force, F*, is applied at the centre of mass of the added mass, where F* is defined as:

$$F^* = M \times a \tag{8.3}$$

In this case, the added mass applied to the web of the tee joints in the shock tests is equal to 16.8 kg and the mass of the tee joint is equal to 3.933 kg. From Equations 8.1 and 8.2, the applied pressure load along the flange is calculated to be 0.709 N/mm^2. From Equation 8.3 the applied force, F*, which must be applied to the added mass equals 34.47 kN. Figure 8.15 shows the finite element representation of the tee joint with the added mass. The tee joint model used is the undamaged model (model 1) which has been discussed in Chapter 6. One element per layer of overlaminate material has been generated in order to represent the individual layers of WR and CSM which make up the overlaminate.

8.7.3 Stress Patterns

The pressure load of 0.709 N/mm^2 has been applied to the flange and the load of 34.47 kN has been applied to the added mass. The overlaminate through-thickness stress distribution is shown in Figure 8.16. The maximum value of the through-thickness stress is 9.7 MPa, which is greater than the ILTS of 7 MPa (Bird & Allan), would cause the delaminations or root whitening associated with the failure mode of this type of joint. Figure 8.17 shows a typical overlaminate through-thickness stress distribution for a tee joint under a 45 degree pull-off load. The plot shown is for a 45 degree pull-off load of 10 kN. It can be seen by comparing Figures 8.16 and 8.17 that although the stress distributions are slightly different, the locations of the peak through-thickness stresses in the two cases are virtually identical. It can therefore be assumed that since the static 45 degree pull-off load gives rise to a similar distribution of through-thickness stress as the simulated shock load, then it can be used to simulate a typical in-service load condition.

8.7.4 45 Degree Pull-Off Load Representing In-Service Condition

Since the through-thickness stress in the overlaminate is directly proportional to the applied static 45 degree pull off load, then it is simple to calculate that an equivalent 45 degree pull off load which would result in a through-thickness stress in the overlaminate of 9.7 MPa. From Figure 8.17 it can be deduced that the equivalent load is equal to 4.2 kN.

8.7.5 Calculation of Critical Crack Lengths for the In-Service Condition

The finite element models discussed in Sections 8.6.2 to 8.6.6 inclusive are all for 45 degree pull off loads of 10 kN. However, since the values of strain energy release rate and J-integral are proportional to the square of the applied load, then the equivalent values can be simply calculated for an applied load of 4.2 kN.

Figure 8.18 shows the J-integral values calculated at the right hand crack tip for a crack at approximately mid-depth of the overlaminate under a 45 degree pull off load of 4.2 kN. It shows that the maximum value of the J-integral occurs at a crack length of 35 mm and is equal to 0.515 kJ/m^2. The critical value for the overlaminate material is equal to 0.5 kJ/m^2 which indicates that cracks greater than 35 mm are likely to propagate under these loading conditions. Figure 8.19 shows a plot of J-integral values and strain energy release rates calculated at both crack tips against curved crack length. It shows that for an assumed critical strain energy release rate of 0.5 kJ/m^2, the critical crack length is equal to approximately 22 mm for values calculated at the left hand crack tip under this loading configuration.

8.8 Discussion

The fracture mechanics approach discussed in this chapter allows the damage tolerance of certain cracks to be quantified. The sensitivity study discussed in Sections 8.5.1 to 8.5.6 yielded criteria which can be used in the assessment of damage tolerance levels. The results showed that a 45 degree pull-off load gives greater values of the J-integral than a three point bend load, clamped conditions give greater values of the J-integral than simple support conditions, boundaries close together give greater values of the J-integral than boundaries far apart, low crack element modulus gives greater values of

the J-integral than high crack element modulus, deep cracks give greater values of the J-integral than surface cracks and long horizontal cracks give greater values of the J-integral than short horizontal cracks.

In the case of the curved cracks, the critical length of a crack which will propagate under a 45 degree pull-off load with clamped boundaries subjected to a load of 10 kN is 8 mm for values calculated at the left hand tip and 16 mm for values at the right hand crack tip.

A typical in-service shock load has been represented by a static 45 degree pull off load of 4.2 kN based on the comparison of the overlaminate through-thickness stress distributions for both load scenarios. A 45 degree pull off load of 4.2 kN gives rise to a critical crack length of 35 mm for a curved overlaminate crack at approximately mid-thickness for values calculated at the right hand crack tip or equivalently 22 mm for values calculated at the left hand crack tip. Thus it is important to calculate values at both crack tips since the delamination is likely to favour propagation in one direction rather than the other.

The analysis carried out in this chapter assumes that the cracks shall propagate along the existing line of the crack face, i.e it does not take into account delaminations which are prone to jumping across interfaces. In addition, the FE models generated here assume that cracks have pre-existed in specific locations. In reality, cracks arise due to high through-thickness stresses or stress concentrations, for example. The formation of a delamination serves so as to relieve the local stress. As loads increase, however, they may cause the formation of a new delamination in an additional region of high stress rather than propagation of the initial crack. For these reasons, a crack extension analysis would give a more accurate estimation as to the full extent of the damage tolerance of the tee joints. The method discussed here does, however, draw our attention to the most damage critical areas within the joint and also to those most prone to delamination damage. In addition, critical crack lengths can be calculated which determine the damage tolerance of the tee joints.

8.9 Concluding Remarks

The main conclusions which can be drawn from the fracture mechanics studies on the

tee joints are as follows :

(i) The region of a tee joint which is most susceptible to damage is the curved region of the overlaminate.

(ii) Curved cracks in the boundary angle are likely to propagate around the radius under a typical in-service load represented by a static 45 degree pull-off load. Curved cracks greater than 50 mm are unlikely to propagate under this loading regime. This is in direct correlation with three point bending tests in which delamination damage occured primarily in the curved region of the overlaminate (Elliot). It can, therefore, be concluded that eventhough delamination is likely to occur in the curved region of the overlaminate, thay will only propagate around the radius of the boundary angle and then arrest.

(iii) Deep cracks within the overlaminate are much more likely to propagate than cracks near the surface and must, therefore, be closely monitered in existing vessels.

(iv) In order to fully ascertain the stability of specific cracks within the overlaminate, this method needs to be validated. This could be carried out by inserting films of PTFE tape of a specific length and location within the overlaminate. The tee joints containing the PTFE could then be tested and the load at which the cracks propagated noted. From the FE analysis, one value of strain energy release rate is known for a particular load level. These values of load can than be compared with those obtained experimentally at which crack propagates.

9. COMPARISON OF STRENGTH-BASED AND ENERGY-BASED APPROACHES WHEN APPLIED TO TEE JOINTS

9.1 Introduction

Two different approaches have been used to investigate the behaviour of tee joints containing delaminations. The first used a stiffness- and strength-based approach to identify regions within the joint most likely to be damaged. Stress patterns have been compared with limiting values of maximum stress with those calculated at locations within the joint. The stress distributions which have been analysed are those of the overlaminate through-thickness stresses and the overlaminate in-plane stresses. The results of this study are discussed in Section 9.3.

In the case of the energy-based approach, the delaminations have been treated as cracks and values of J-integral have been calculated at both tips for cracks at different locations within the overlaminate material. If the calculated value is greater than an assumed critical value then the particular crack would be assumed to propagate at that load level. The results of this study are discussed in Section 9.4.

The loading condition considered in this chapter is that of a 45 degree pull-off load since it is deemed to be the most severe type of loading which can be applied to a tee joint. The magnitude of the load is 10 kN in each case.

9.2 The Problem

It has been shown that delaminations (or cracks) commonly occur within the overlaminate of the tee joint under both three point bending loads and 45 degree pull-off loads. In the analysis which follows, the two approaches shall be used in order to predict whether a delamination (or crack) would propagate under the given conditions. Two single delaminations shall be modelled in each case to represent delaminations of two different lengths.

9.3 Strength-Based Assessment

The material properties of the models are the same as those discussed in Chapter 6 and

are given in Table 6.1.

Two FE models have been generated to represent a tee joint containing a single delamination of two different lengths. The delamination in both cases has been modelled at a depth of 6 plies from the outer surface of the overlaminate on one side. The delamination extends from the flat region above the flange around the radius. Figures 9.1(a) and 9.1(b) show the location of the delamination in the FE models (a) and (b) respectively. The two crack tips are marked A and A* in Figure 9.1(a) and B and B* in Figure 9.1(b). A 45 degree pull off load of 10 kN has been applied to both the models with the delamination on the tension side. The overlaminate in-plane and through-thickness stress distributions have been analysed and the maximum values recorded in both cases.

Model (a)

Figure 9.2 shows the in-plane overlaminate stress distribution for which the maximum value is 141.1 MPa in the outer plies of the overlaminate. Figure 9.3 shows the through-thickness overlaminate stress distribution for which the maximum value is 43.5 MPa at the tip marked A^*. As with the models discussed in Chapter 6, it is likely that the actual magnitude of the peak through-thickness stress is due to the presence of a singularity. If the stresses due to the singularity are removed, then a more realistic value for the maximum through-thickness stress is of the order of 10 MPa at tip marked A^*. From this it can be concluded that under this load, the crack would propagate around the radius since the maximum through-thickness stress is greater than the ILTS of 7 MPa (Bird & Allan).

Model (b)

The stress distributions for this model are similar to those for model (a) except for the magnitudes of the maximum stresses. The maximum overlaminate in-plane stress is 211 MPa and the maximum overlaminate through-thickness stress is 30 MPa at the tip marked B^*. The maximum through-thickness stress is greater than the ILTS and consequently, further delamination would be predicted. Values of through-thickness stress greater than the ILTS are also predicted at the tip marked B. Thus, further delamination would be predicted from both ends of the existing delamination.

9.4 Energy-Based Assessment

Values of the J-integral which have been calculated must be compared with the critical value of the strain energy release rate for the material under consideration. If the calculated value is greater than the critical value then crack propagation would be predicted. For the material under consideration in this study, the critical value for the strain energy release rate is equal to 0.5 kJ/m^2 (Court).

Two FE models have been generated which contain a single curved crack in the same locations as the delaminations which have been modelled for the strength assessment in Section 9.3 above. Figure 9.4 shows the locations of the two cracks. The short crack equivalent to the delamination in model (a) above is defined by tips marked C and C^*. The long crack equivalent to the delamination in model (b) above is defined by tips marked D and D^*. The value of the J-integral has been calculated at both tips for a load of 10 kN in each case. For the crack CC^*, the value of the J-integral is calculated to be 0.2 kJ/m^2 at the tip marked C and 0.7 kJ/m^2 at the tip marked C^*. Consequently, crack propagation would be predicted from the tip marked C^*. For the crack DD^*, the value of the J-integral is calculated to be 2.9 kJ/m^2 at the tip marked D and 3.4 kJ/m^2 at the tip marked D^*. Thus, crack propagation would be predicted from both crack tips at this load.

9.5 Comparison of Results

The strength-based approach has shown that under a 10 kN 45 degree pull-off load, the short delamination would be expected to grow around the radius due to high through-thickness stresses. The energy-based approach is in direct correlation with this result, predicting that crack propagation would occur around the radius due to a value of the J-integral greater than the critical value. Also, both approaches suggest that further delamination is likely from both tips in the case of the longer delamination.

9.6 Conclusions

It has been shown that two approaches can be used to assess the damage tolerance of specific delaminations which are inherently present in tee joint boundary angles. The first approach uses strength-based criteria to determine firstly whether damage is likely

to occur in specific regions and secondly whether further delamination is likely based upon limiting values of stress. The strength-based approach successfully predicts the regions within which damage is likely to occur. Difficulties, however, do arise due to the presence of singularities at the two tips of the delaminations.

The second, energy-based, approach implements the calculation of fracture mechanics parameters such as the J-integral. The calculated values are compared with pre-determined critical values to determine whether the delaminations are likely to propagate.

A comparison of the two methods has shown that similar conclusions can be reached from both methods. It is considered that both methods complement each other and should be carried out in combination if possible.

10. DISCUSSION AND FURTHER WORK

The main aim of the work has been to understand more fully the damage tolerance of FRP ship structures. This has been carried out by assessing the structural consequences of delaminations in particular, in laminates and in structural components. The methods used have included analytical and numerical approaches. Both strength - based and energy - based techniques have been employed to identify regions most susceptible to delaminations. These methods have also been used to predict whether an existing delamination (or crack) is likely to propagate under a given set of conditions.

Existing analytical approaches have been extended in order to calculate the mechanical properties of mixed laminates. i.e those which contain layers of chopped strand mat, unidirectional (or angle-ply) and woven layers. This is an important capability since the mechanical properties of specific laminates is not always readily available.

The behaviour of delaminated plates under compressive loads has been investigated for woven laminates using analytical and numerical models. The results have been compared with published data and show good agreement. The critical buckling stress of laminated plates containing delaminations across their width is shown to be dependent upon the length and depth of the delamination. The longer the delamination then the lower the critical buckling stress indicating that the plate is more likely to buckle. In addition, plates containing delaminations close to the surface are more likely to buckle than those with deep delaminations.

Existing analytical solutions for calculating the mode I and mode II stress intensity factors for a crack in a layered isotropic material have been adapted for a particular application. The delaminations which form in the overlaminate of tee joints commonly occur within the chopped strand mat layers. Therefore, the existing models have been tailored to represent a resin crack sandwiched between two layers of chopped strand mat. This represents a crack in a resin rich area of a chopped strand mat (CSM) layer. For a 10 mm crack and an assumed critical stress intensity factor of 1.0 MPa$\sqrt{m}$, the stress at which the crack is likely to propagate under the two modes of loading has been calculated. The values of stress are found to be 18 MPa for the mode I loading and 15 MPa for the mode II loading. From this it can be noted that the crack is most likely to propagate under a mode II type of loading. The value calculated for the mode II type

of loading directly correlates with the quoted value of the interlaminar shear strength of CSM of 17 MPa. Critical crack lengths have also been calculated which indicate the maximum length of a crack which would be stable and not propagate under a given set of conditions. Therefore, this technique can be used to assess the stability of specific cracks and hence the damage tolerance of the material. This laminate level work has been extended to cover generic structural elements such as top hat stiffeners and tee joints.

Detailed finite element models have been generated to represent two types of top hat stiffener. Internal stress patterns have been yielded for both types of top hat under each of three loading configurations which are representative of typical in-service loads, namely three point bending, reverse bending and straight pull-off loads. The finite element results compare well with experimental findings. The most notable are that under a three point bending type load, the delaminations which occurred in the overlaminate in both types of stiffener are due to excessive through-thickness stresses and the damage in the flange is due to excessive in-plane stresses. The failure of both types of top hat under this mode of loading is that of either partial or complete separation of the stiffener from the flange. It is anticipated that the inclusion of the interface between the overlaminate and flange plate would explain this mode of failure. The analysis has shown that the curved region of the overlaminate close to the fillet is a delamination prone area in both types of top hat stiffener.

Finite element models have also been generated to represent single skin tee joints. Previous models have only represented one or two elements through the thickness of the overlaminate. This method does not allow for the introduction of delaminations between layers of the overlaminate into the model and does not give rise to detailed stress contours within the overlaminate. Therefore, models containing one element per layer have been generated here. This allows delaminations to be introduced between the layers of the overlaminate as required. In addition, this more detailed modelling gives rise to improved internal stress distributions, most importantly in the through-thickness direction.

An iterative approach has been used to represent tee joints under three point bending loads. Delaminations have been incorporated into the numerical models to mirror the experimental failure modes of the joints. The finite element models predict the stiffness

reduction well when compared with the experimentally derived load/deflection curve. The fillet failure which occurred in the experiments but which is not predicted by the FE models, can be attributed to the fact that voids were found to be present in the fillet resin. These had the effect of increasing the fillet principal stresses and causing the premature failure of the fillet.

The internal stress distributions which have been generated indicate that the initial delaminations which form in the inner regions of the overlaminate are a result of high through-thickness stresses. The formation of the delaminations serves as to relieve the through-thickness stresses. Further loading causes additional delaminations to form due to high through-thickness stresses. As the number of delaminations increases, it has been shown that, subsequently, it is the high in-plane stresses which are likely to cause damage in the outer regions of the overlaminate. The overlaminate in-plane stress distributions have been plotted along a path which runs through the overlaminate thickness. This stress distribution shows that there are distinct peaks in the in-plane stress which occur at the interface between layers of chopped strand mat and layers of woven roving.

Crack elements have been introduced into the numerical models of both the top hat stiffeners and the tee joints to represent delaminations and have allowed values of the strain energy release rate to be calculated. These have been used to assess the stability of specific cracks and their likelihood to propagate. This energy-based approach shows that in the case of the top hat stiffeners, a curved crack in the overlaminate is most likely to propagate under a pull off load, the critical crack length of which is 31 mm for a 10 kN applied load. The cracks are less likely to propagate under a three point bending load and are most stable under a reverse bending load. The results also show that surface cracks are more likely to propagate than cracks deep within the overlaminate surface.

In the case of the tee joints, the results of the FE models have shown that greater values of the J-integral are obtained for application of a 45 degree pull off load rather than a three point bending load, clamped conditions rather than simple supports and use of a short span rather than a long span. In addition, low values of crack element elastic modulus gives greater values of J than high values. The results have also shown that under a 45 degree pull off load, deep cracks are more likely to propagate than cracks closer to the surface. Under a 45 degree pull off load of 10 kN, a critical crack length

of 8 mm has been calculated. This is the maximum crack length which would be stable under these conditions. The results also show that once the cracks have propagated around the radius of the overlaminate then the crack becomes more stable and is not likely to propagate further.

A comparison has been made between the strength assessment and energy-based assessment of tee joints under a 45 degree pull off load. It is shown that the two methods yield similar results. For example, the strength assessment yields high values of through-thickness stress in the curved region of the overlaminate indicating that the formation of delaminations is likely at a load of 10 kN. The energy-based approach predicts high values of the J-integral at a load of 10 kN in similar regions of the overlaminate. Thus predicting also that crack propagation is likely to occur.

The current work has highlighted some areas which require further investigation:

The delaminations which have been introduced into the finite element models have been manually generated from a knowledge of experimental results. The ideal situation would involve a crack extension technique where a crack is automatically generated if certain stress or energy based conditions are violated. For example, if the calculated strain energy release rate was found to be greater than a pre-determined critical value then the crack would be automatically extended. This technique would also allow delaminations to jump across layers of the overlaminate.

The behaviour of ship's components under static loading configurations have been successfully represented using both strength- and energy- based approaches. In order to represent typical in-service dynamic loads, however, an assumed static load situation has been adopted. Since typical in-service loading conditions are largely dynamic, these existing models must be adapted so as to be able to represent dynamic loads such as impact and fatigue load scenarios.

Other than the material parameters such as the critical stress intensity factors and strain energy release rates it is important to identify the key material and geometric parameters which cause certain structures to be more sensitive to delamination damage than others. For example, a sensitivity study on the existing FE models of tee joints containing cracks could be carried out to investigate the effect of tee joint geometry, overlaminate,

flange, web and fillet material. The top hat stiffener connections and tee joints in high speed craft are commonly constructed of sandwich materials. The propagation of cracks within these type of connections could be investigated using a similar approach to that discussed here for the single skin components.

11. CONCLUSIONS

This work has been concerned with the damage tolerance levels in laminated composites. Existing analytical techniques have been adapted and extended to represent specific problems connected with the delamination behaviour of composite plates. Numerical modelling has been carried out on typical ship structural elements such as tee joints and top hat stiffener connections so as to investigate the internal load transfer mechanisms and thus identify areas of weakness within the structure. Additionally, fracture mechanics criteria have been incorporated into the model allowing the stability of specific cracks to be assessed. The principal thrust of the work has thus been to study the significance of delaminations (or cracks) in different parts of a structure.

The main conclusions from this work are as follows :

(i) Existing analytical approaches have been used to assess the stability of woven laminated plates under compressive loadings. Previous work does not cover these types of materials. The results have been compared with numerically derived values and experimental data. It has been found that plates containing delaminations are more likely to buckle when the delaminations are long or close to the surface of the plate.

(ii) An existing analytical model has been used to calculate values of stress intensity factors for modes I and II for a specific problem. Delaminations (or cracks) commonly occur within the chopped strand mat layers of tee joint overlaminates. Consequently, the problem has been represented by a resin crack sandwiched between two layers of chopped strand mat. For applied loads equal to the ILTS (equivalent to a mode I load) and the ILSS (equivalent to a mode II load), critical crack lengths have been calculated for which propagation is likely. The results have shown that a crack would reach a greater length before propagating under a mode I type load than under a mode II type load. This method can be used to assess the damage tolerance on a material level.

(iii) It has been shown that the delamination prone areas in top hat stiffeners are located in the curved region of the overlaminate close to the outer surface. The delaminations are likely to be due to excessive through-thickness stresses. The damage which occurs in the flange is likely to be due to excessive in-plane stresses in the case of three point bending loads and due to excessive through-thickness stresses in the case

of reverse bending loads.

(iv) An iterative procedure has been used to characterise the damage which occurs in tee joints under a three point bending load. Three important features have been brought out as a result. Firstly, the initial delaminations which form in the inner regions of the boundary angle are caused by excessive through-thickness stresses. Secondly, the delaminations which form have the effect of relieving the stresses and allowing further loading to take place. Thirdly, the subsequent damage which forms in the outer regions of the boundary angle is caused as a result of high in-plane stresses.

(v) In tee joint overlaminates, excessive in-plane stresses occur at the interface of the chopped strand mat layers and the woven roving layers. Hence, damage is likely in these locations.

(vi) Calculation of fracture parameters with regard to delaminations in the top hat overlaminates, have shown that curved delaminations are most likely to propagate under a straight pull-off load. They are next likely to propagate under a three point bending load and are most stable under a reverse bending load. Also, delaminations close to the surface are more likely to propagate than deep delaminations in the case of all three loading scenarios.

(vii) In the case of a tee joint under a 45 degree pull-off load, both straight and curved delaminations in the overlaminate are more likely to propagate if they are deep rather than close to the surface. Also, delaminations at approximately mid-depth, are likely to propagate once they have reached the curved part of the overlaminate.

(viii) The results of this work have shown that it is possible to predict the damage tolerance of laminates and structural elements based on either a strength - based or energy - based approach.

LIST OF REFERENCES

ANSYS User's Manual Version 5, Swanson Analysis Systems, Inc., Houston, PA, USA, 1992.

Bird, J. & Allan, R.C.. The Determination of the Interlaminar Tensile Strength of Ship Type Laminates. Proc. 7 th International Conference on Experimental Stress Analysis, Haifa, Israel, 1982, pp. 91-104.

Brewer, J.C. & Lagace, P.A.. Quadratic Stress Criterion for Initiation of Delamination. Journal of Composite Materials, Volume 22, December 1988, pp. 1141-1154.

Cable, C.W.. The Effect of Defects in Glass-Reinforced Plastic (GRP). Marine Technology, Volume 28, Number 2, March 1991, pp. 91-98.

Carlson, R.L. & Kardomateas, G.A.. An Introduction to Fatigue in Metals and Composites. Publ. Chapman & Hall, London, 1996. ISBN 0 412 57200 1.

Chai, H., Babcock, C.D. & Knauss, W.G.. One dimensional modelling of failure in laminated plates by delamination buckling. Int. J. Solids and Structures, Volume 17, Number 11, 1981, pp. 1069-1083.

Chow, C.L. & Yang, F.. Elastic Damage Analysis of Interlaminar Stress Distributions in Symmetrical Composite Laminates with Edge Delamination Cracks. Proc. Institution of Mechanical Engineers, Part C, Volume 208, 1994, pp. 1-11.

Court, R.S.. Fracture Toughness of Woven Glass Reinforced Composites. DRA/SMC/CR943111. December 1994.

Dodkins, A.R., Shenoi, R.A. & Hawkins, G.L.. Design of Joints and Attachments in FRP Ships' Structures. Marine Structures, Volume 7, 1994, pp 365-398.

Dulieu-Smith, J.M, Shenoi, R.A., Read, P.J.C.L., Quinn, S. & Moy, S.S.J.. Thermoelastic Stress Analysis of a GRP Tee Joint. Journal of Applied Composite

Materials. (Submitted for Publication).

Elliott, D.M.. (1994) Mechanical Testing of Composite Joints - Interim Report. DRA/AW/AWS/TR94212. April 1994.

Elliott, D.M.. (1996) Fatigue Performance of Damaged and Undamaged GRP T-Joints. DRA/SMC/TR963012. March 1996.

Ewalds, H.L. & Wanhill, R.J.H.. Fracture Mechanics, Publs. Arnold & DUM, 1986. ISBN 0 7131 3515 8.

Garg, Amar, C.. Delamination-A Damage Mode in Composite Structures, Engineering Fracture Mechanics, Volume 29, Number 5, 1988, pp. 557-584.

Hancock, N.L. & Mayer, R. M., Eds., Design Data for Reinforced Plastics : A Guide for Engineers and Designers. Chapman & Hall, Publs., 1994. ISBN 0 412 493209.

Hawkins, G.L., Holness, J.W., Dodkins, A.R. & Shenoi, R.A.. The strength of bonded tee-joints in FRP ships. Plastics, Rubber and Composites Processing and Applications, Volume 19, Number 5, 1993, pp. 279-284.

Hawkins, G.L. & Shenoi, R.A.. A Parametric Study to Determine the Influence of Geometric Variations on the Performance of a Bulkhead to Shell Plating Joint. Proceedings of the 9th International Conference on Composite Materials, ICCM/9, Madrid, 12-16 July, 1993, Volume IV, pp. 97-104.

Hicks, I.A., Read, P.J.C.L. & Hawkins, G.L.. Tensile Compressive and Flexure Characteristics of Tee Joints in Foam-Core Sandwich Structures. Proceedings of the 3rd International Conference on Sandwich Construction, Southampton, 12-15 September, 1995, Paper 11/UK15.

Highsmith, A.L. & Reifsnider, K.L.. (1986) On Delamination and the Damage Localisation Process. Fracture of Fibrous Composites ASME, AMD-Volume 74, 1986, pp. 71-87.

Highsmith, A.L. & Reifsnider, K.L.. (1982) Stiffness-Reduction Mechanisms in Composite Laminates. Damage in Composite Materials, ASTM STP 775, Reifsnider, K.L., Ed., American Society for Testing and Materials, 1982, pp. 103-117.

Hwang, W. & Han, K.S., Statistical Study of Strength and Fatigue Life of Composite Materials. Composites, Volume 18, Number 1, January 1987. pp. 47-53.

Ilic, S. & Williams, J.F.. Compression Failure Modes in Composites. Theoretical and Applied Fracture Mechanics, Volume 6, 1986, pp. 121-127.

Irwin, G.R. & Kies, J.A.. Critical Energy Rate Analysis of Fracture Strength. Welding Journal, Research Supplement, April 1954, pp. 193s-198s.

Ishikawa, T & Chou, T-W. (1982 a). Elastic Behaviour of Woven Hybrid Composites. J. Composite Materials, Volume 16, January 1982, pp. 2-19.

Ishikawa, T & Chou, T-W. (1982 b). Stiffness and Strength Behaviour of Woven Fabric Composites. Journal of Materials Science, Volume 17, 1982, pp. 3211-3220.

Ishikawa, T. & Chou, T-W. (1983). One-Dimensional Micromechanical Analysis of Woven Fabric Composites. Journal of the American Institute of Aeronautics and Astronautics (AIAA), Volume 21, Number 12, December 1983, pp. 1714-1721.

Ishikawa, T., Matsushima, M. & Hayashi, Y.. Experimental Confirmation of the Theory of Elastic Moduli of Fabric Composites. J. Composite Materials, Volume 19, September 1985, pp. 443-458.

Kim, R.Y. & Soni, S.R.. Experimental and Analytical Studies on the Onset of Delamination in Laminated Composites. J. Composite Materials, Volume 18, January 1984, pp. 70-80.

Kimpara, I., Hamamoto, A. & Takehana, M.. Trans. JSCM, Volume 3, Number 1/2, 1977, pp. 21-26.

Lagace, P.A.. Delamination : From Initiation to Final Failure, ICCM/9, Madrid, 12-16 July 1993, Volume I, Ed. Antonio Miravete, pp. 120-122.

Lau,H. & Rowlands, R.E., Correlating Matrix and Composite Fracture Response at Different Temperatures. Proceedings of the Ninth International Conference on Composite Materials. ICCM/9, Volume V, Composites Behaviour, Ed. Antonio Miravete, Madrid, 12-16 July, 1993, pp. 827-833.

Lee, Ed., International Encyclopedia of Composites, Volume 5, 1989.

Lekhnitskii, S.G.. Theory of Elasticity of an Anisotropic Elastic Body. Ed. Brandstatter, Julius, J., Publ. Holden-Day Inc., San Francisco, 1963.

Liu, S., Kutlu, Z. & Chang, F.-K.. Matrix Cracking and Delamination in Laminated Composite Beams Subjected to a Transverse Concentrated Line Load. J. Composite Materials, Volume 27, Number 5, 1993, pp. 436-470.

Long, B.J. & Swanson, S.R.. Ranking of Laminates for Edge Delamination Resistance. Composites, Volume 25, Number 3, 1994, pp. 183-188.

Moshaiov, A. & Marshall, J.. Analytical Determination of the Critical Load of Delaminated Plates. Journal of Ship Research, Volume 35, Number 1, March 1991, pp. 87-90.

Naik, N.K.. Woven Fabric Composites. Technomic, Publ. 1994.

Naik, N.K. & Shembekar, P.S.. Elastic Behaviour of Woven Fabric Composites: I-Lamina Analysis. Journal of Composite Materials, Volume 26, Number 15, 1992, pp. 2196-2225.

O'Brien, T.K., (1982). Characterisation of Delamination Onset and Growth in a Composite Laminate. In *Damage in Composite Materials*, ASTM STP 775, K. L. Reifsnider, Ed., American Society for Testing and Materials, 1982, pp. 140-167.

O'Brien, T.K., (1985). Analysis of Local Delaminations and Their Influence on Composite Laminate Behaviour. In *Delamination and Debonding of Materials*, ASTM STP 876, W. S. Jonson, Ed., American Society for Testing and Materials, Philadelphia, 1985, pp. 282-297.

Partridge, C., Waechter, R.T., Williams, J.F. & Jones, R.. Understanding Delamination Behaviour in a Circular Laminate. Theoretical and Applied Fracture Mechanics, Volume 13, 1990, pp. 99-104.

Pavier, M.J. & Clarke, M.P.. A Specialized Composite Plate Element for Problems of Delamination Buckling and Growth. Composite Structures, Volume 34, 1996, pp. 43-53.

Phillips, H.J., Moss, C.E. & Shenoi, R.A.. Damage Tolerance of FRP Top-Hat Stiffeners. 1st International Conference on Composites Science and Technology, Durban, South Africa, 18-20 June, 1996.

Pierson, J.K. & Roorda, J.. Delamination Buckling in Circular Plates. Thin-Walled Structures, Volume 18, 1994, pp. 161-175.

Read, P.J.C.L. Fatigue Characterisation of FRP Structural Tee Joints, PhD thesis under preparation, Department of Ship Science, University of Southampton, UK.

Rice, J.R.. A Path Independent Line Integral and the Approximate Analysis of Strain Concentration by Notches and Cracks. J. Applied Mechanics, Volume 35, June 1968, pp. 379-386. Trans. ASME, The American Society for Testing and Materials.

Rybicki, E.F., Schmueser, D.W. & Fox, J.. An Energy Release Rate Approach for Stable Crack Growth in the Free-Edge Delamination Problem, J. Composite Materials, Volume 11, October 1977, pp. 470-487.

Scott Bader, Data Sheet for Crestomer 1152PA resin.

Sczepanik-Weinmann, M., Steinmetz, G., Arendts, F.J. & Hansel, C.. Numerical and Experimental 3-D Delamination Behaviour of an Anisotropic Layered Plate under

Compression Loading. Proceedings of the Ninth International Conference on Composite Materials. ICCM/9, Volume VI, Composites Properties & Applications, Ed. Antonio Miravete, Madrid, 12-16 July, 1993, pp. 736-743.

Shembekar, P.S. & Naik, N.K.. Elastic Behaviour of Woven Fabric Composites: II - Laminate Analysis. Journal of Composite Materials, Volume 26, Number 15, 1992, pp. 2226-2246.

Shenoi, R.A. & Hawkins, G.L.. (1995) An Investigation into the Performance Characteristics of Top-Hat Stiffener to Shell Plating Joints. Composite Structures, Volume 30, 1995, pp. 109-121.

Shenoi, R.A. & Hawkins, G.L.. (1992) Influence of material and geometry variations on the behaviour of bonded tee connections in FRP ships. Composites, Volume 23, Number 5, September 1992, pp. 335-345.

Shenoi, R.A., Phillips, H.J. & Read, P.J.C.L.. Fracture Mechanics Criteria for Determining Integrity of Tee Joints in FRP Structures. 1 st Australasian Congress on Applied Mechanics, ACAM - 96, 21-23 February 1996.

Shenoi, R.A., Read, P.J.C.L. & Hawkins, G.L., Fatigue failure mechanisms in Fibre-reinforced Plastic Laminated Tee Joints. International Journal of Fatigue, Volume 17, Number 6, 1995, pp. 415-426.

Shenoi, R.A. & Violette, F.L.M.. A study of Structural Composite Tee Joints in Small Boats. Journal of Composite Materials, Volume 24, Number 6, June 1990, pp. 644-666.

Shenoi, R.A. & Wellicome, J.F., Eds. Composite Materials in Maritime Structures, Ocean Technology Series 4, Cambridge University Press, Publ., 1993.

Sih, G.C. & Chen, E.P.. Cracks in Composite Materials, Mechanics of Fracture Series no. 6., Martinus Nijhoff, Publ., 1981.

Simitses, G.J., Sallam, S. & Yin, W.L.. Effect of Delamination of Axially Loaded

Homogeneous Laminated Plates. Journal of the American Institute of Aeronautics and Astronautics (AIAA), Volume 23, Number 9, September 1985, pp. 1437-1444.

Smith, C.S.. (1990) Design of Marine Structures in Composite Materials. Publ. Elsevier Applied Science. 1990.

Smith, C.S.. (1972) Structural Problems in the Design of GRP Ships. Proceedings of the Symposium on GRP Ship Construction, RINA, October 1972, pp. 33-56.

Solecki, J.S.. Fracture Mechanics, A Revision 4.4 Tutorial, ANSYS, Swanson Analysis Systems, Inc.. 1989.

Suemasu, H.. Effects of Multiple Delaminations on Compressive Buckling Behaviors of Composite Panels, J. Composite Materials, Volume 27, Number 12, 1993, pp. 1172-1192.

Sumpter, J.D.G., Final Review of Project Support Tasking DNA1217 - Damage Tolerance in FRP Ship's Structure. DRA/SMC/CR963033. May 1996.

Sun, C.T. & Kelly, S.R.. Failure in Composite Angle Structures, Part I: Initial Failure. J. Reinforced Plastics and Composites, Volume 7, May 1988, pp. 220-232.

Swanson Analysis Systems, Inc., Fracture Mechanics. ANSYS Tutorial, 1989.

Theotokoglou, E.E. & Moan, T.. Experimental and Numerical Study of Composite T-Joints. Journal of Composite Materials. Volume 30, Number 2, 1996, pp.190-209.

Tian, Z. & Swanson, S.R.. Effect of Delamination Face Overlapping on Strain Energy Release Rate Calculations. Composite Structures, Volume 21, 1992, pp. 195-204.

Timoshenko & Young. Theory of Structures. Publs. McGraw-Hill, 1945.

Trask, R., Microstructural Analysis of Fatigue and Shock Damaged T Joints. DRA/SMC/TR963013. March 1996.

FIGURES

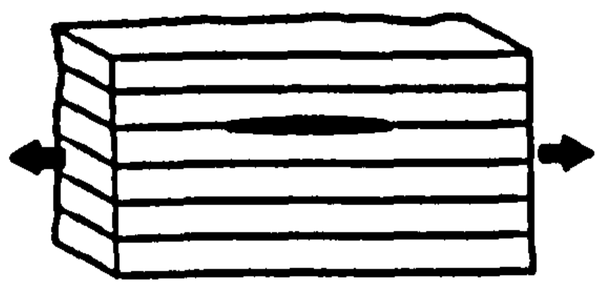

Figure 2.1 Stages of Delamination :

(a) Initiation of Delamination

(b) Growth of Delamination

(c) Failure of Laminate

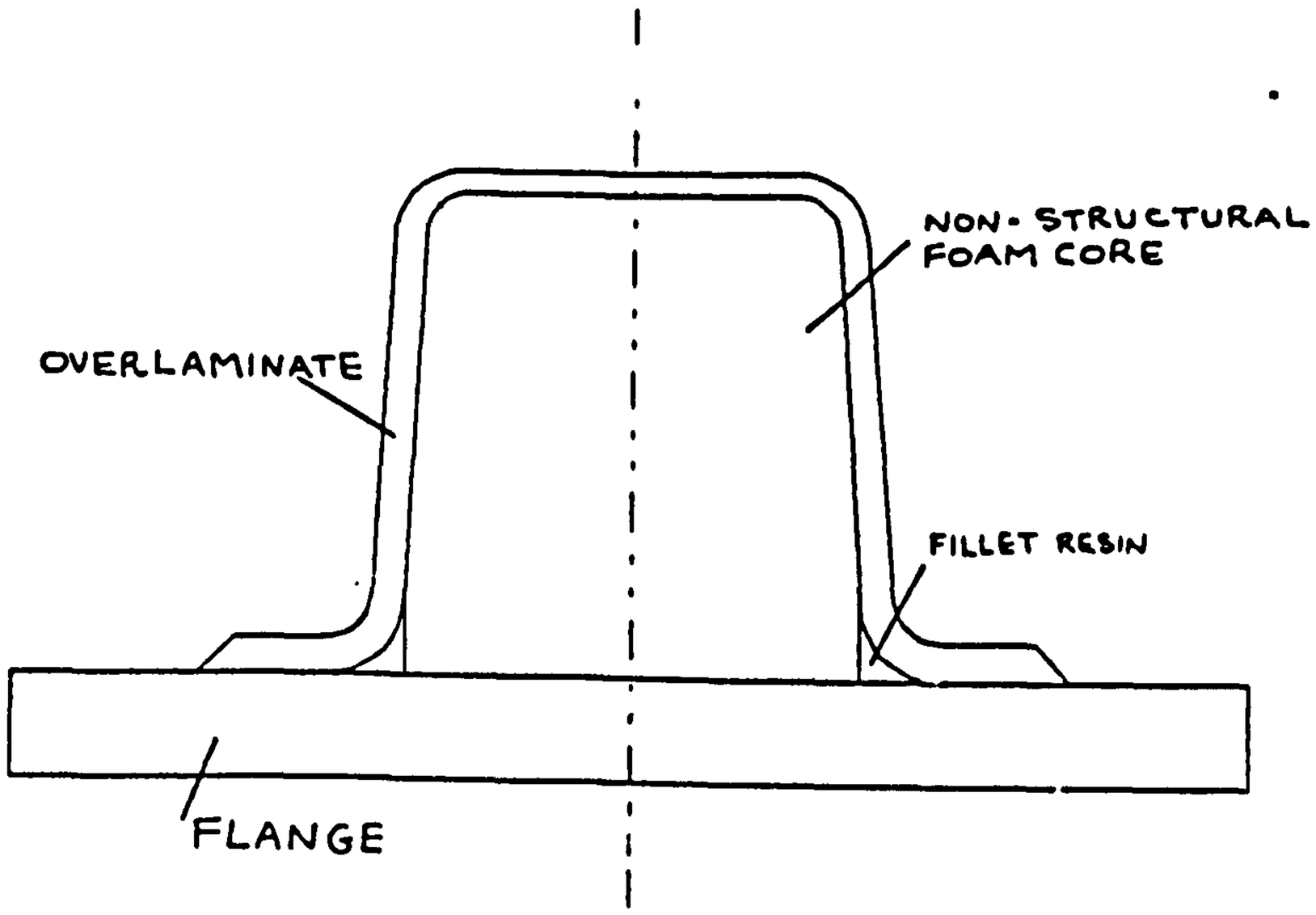

Figure 2.2 Type I Top Hat Stiffener

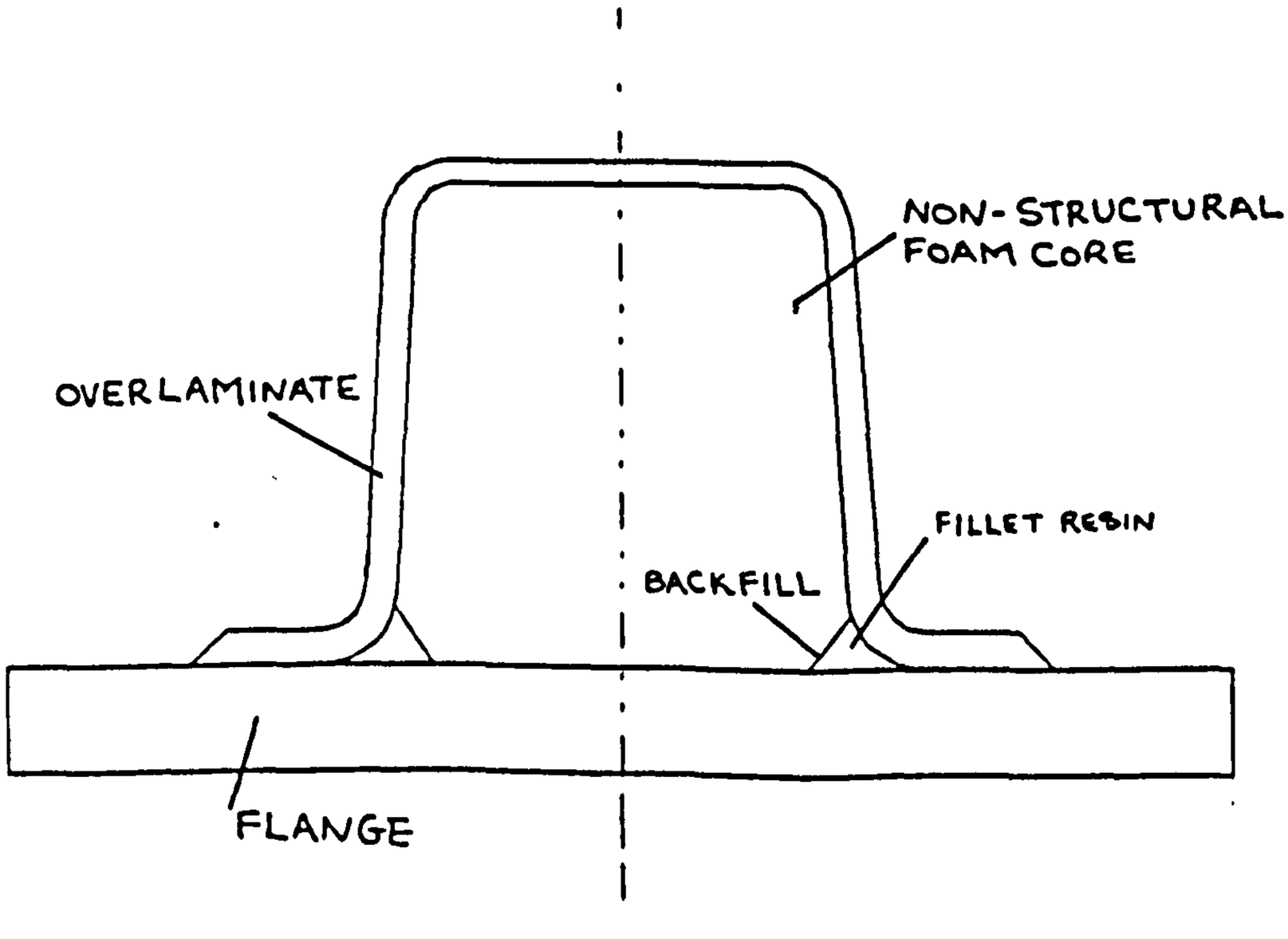

Figure 2.3 Type II Top Hat Stiffener

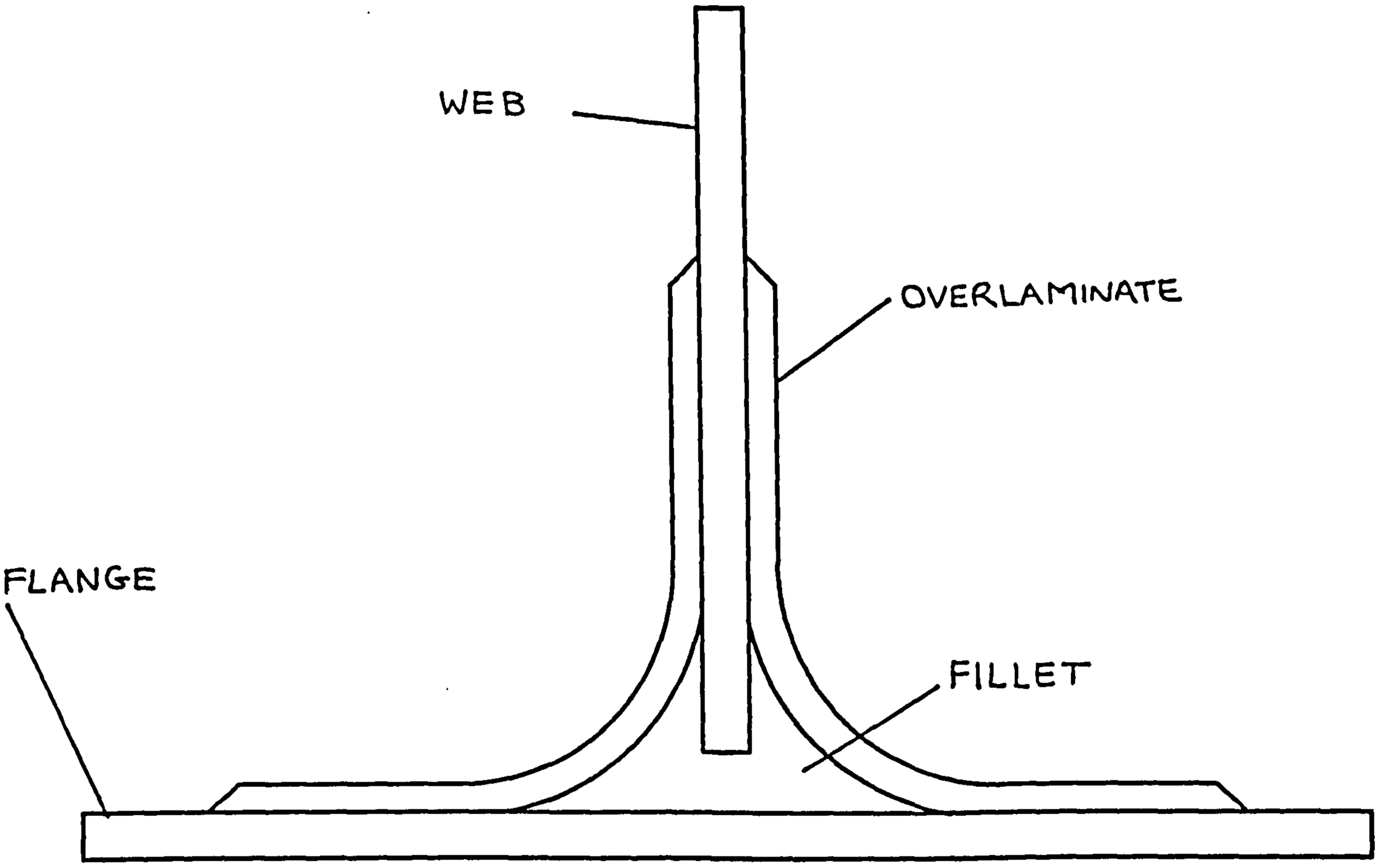

Figure 2.4 Typical Tee Joint Configuration

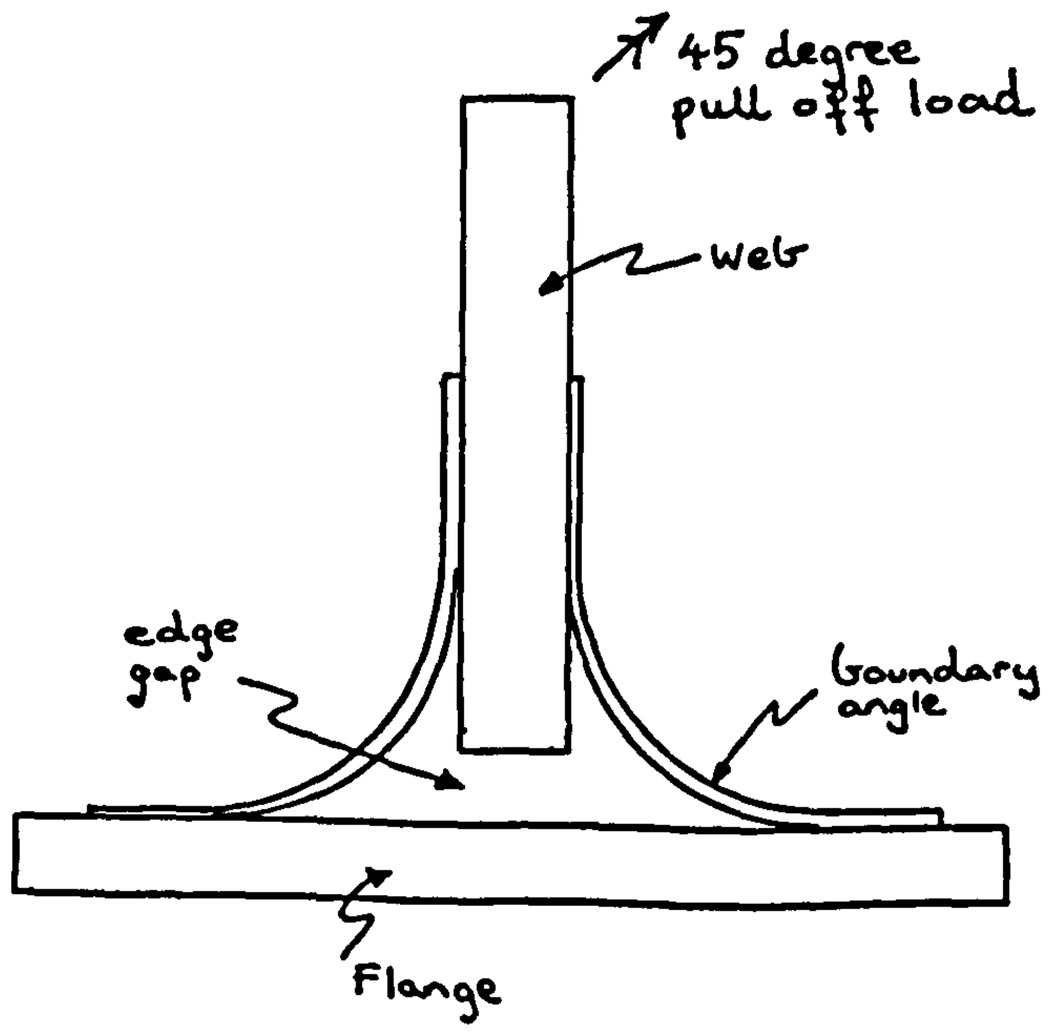

Figure 2.5 Tee Joint under a 45 Degree Pull-Off Load

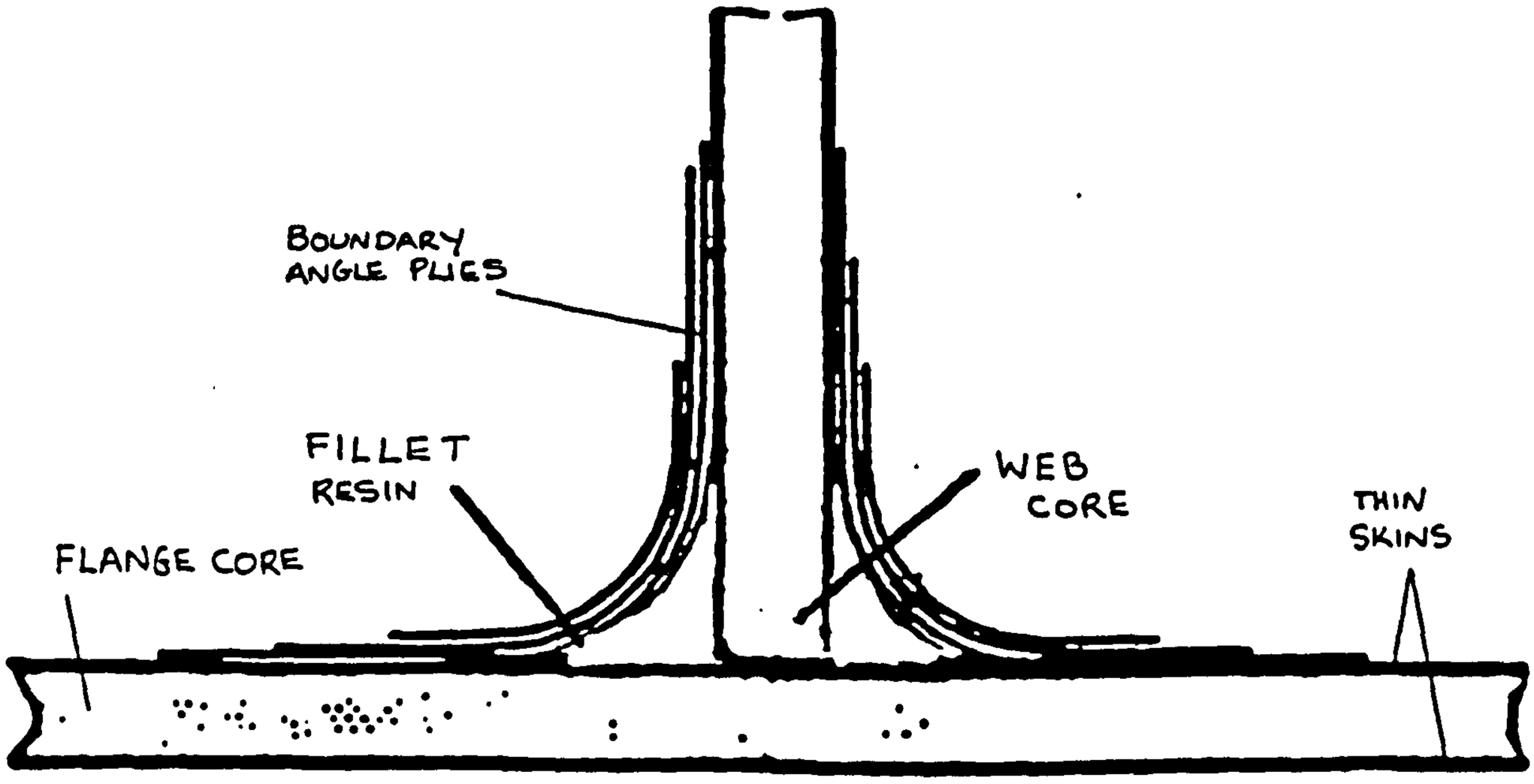

Figure 2.6 Example of Sandwich Tee Joint Configuration

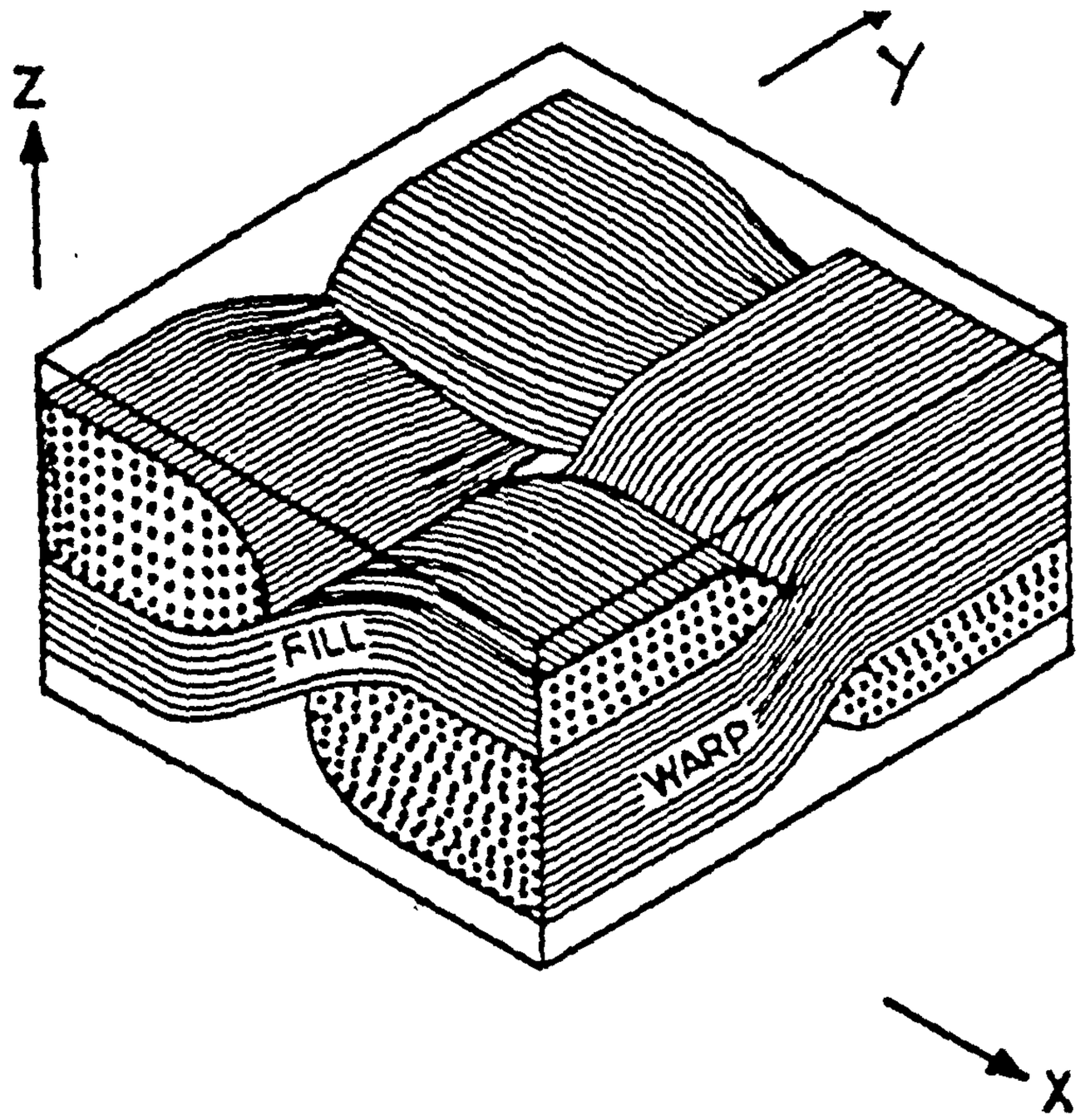

Figure 4.1 Unit Cell of Woven Laminate
(taken from Naik & Shembekar)

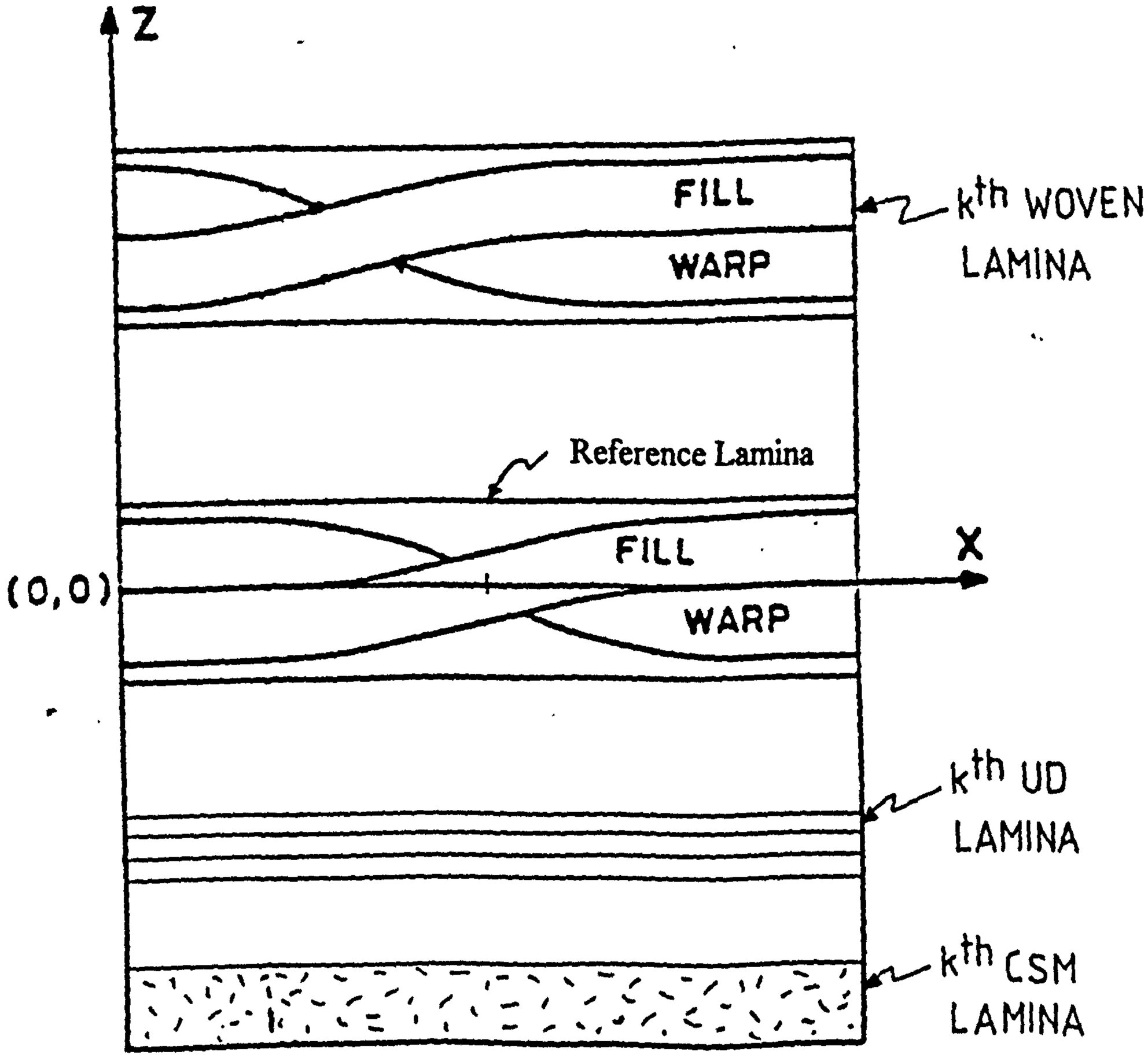

Figure 4.2 Laminate with Mixed Layers

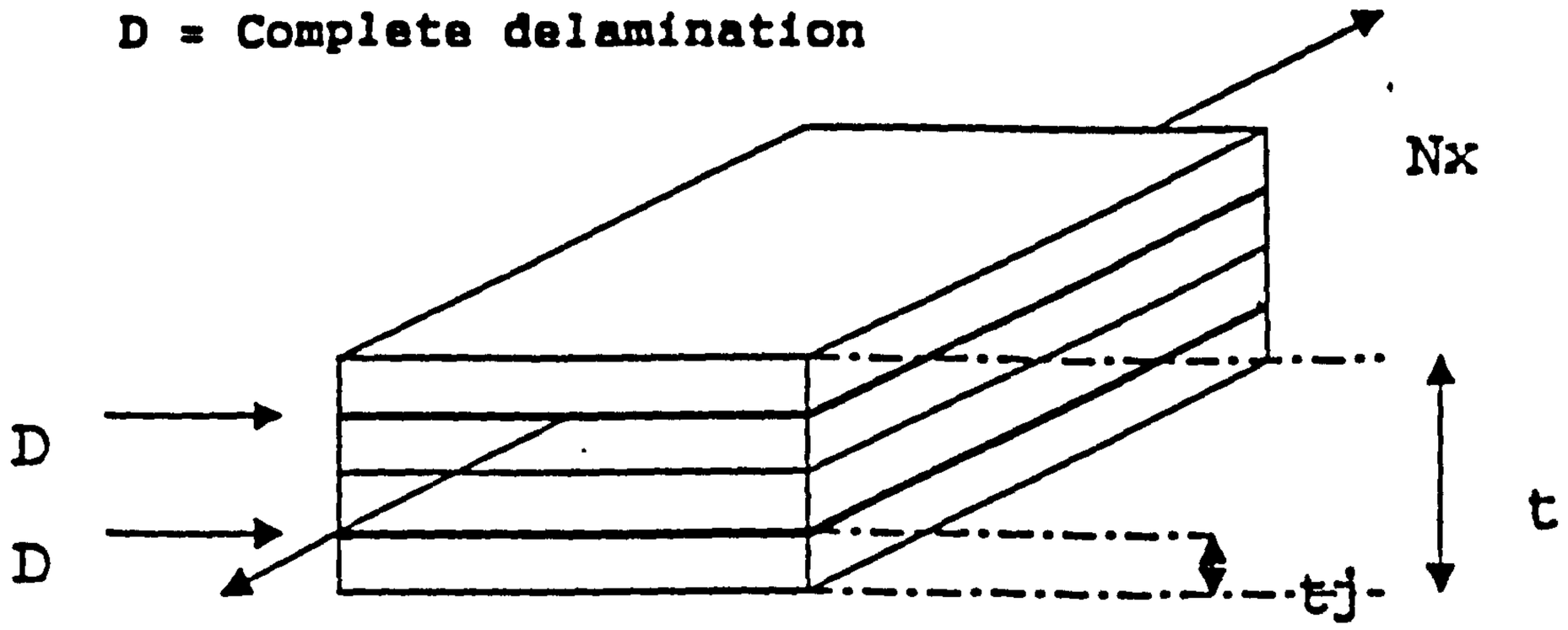

Figure 4.3 Completely Delaminated Laminate

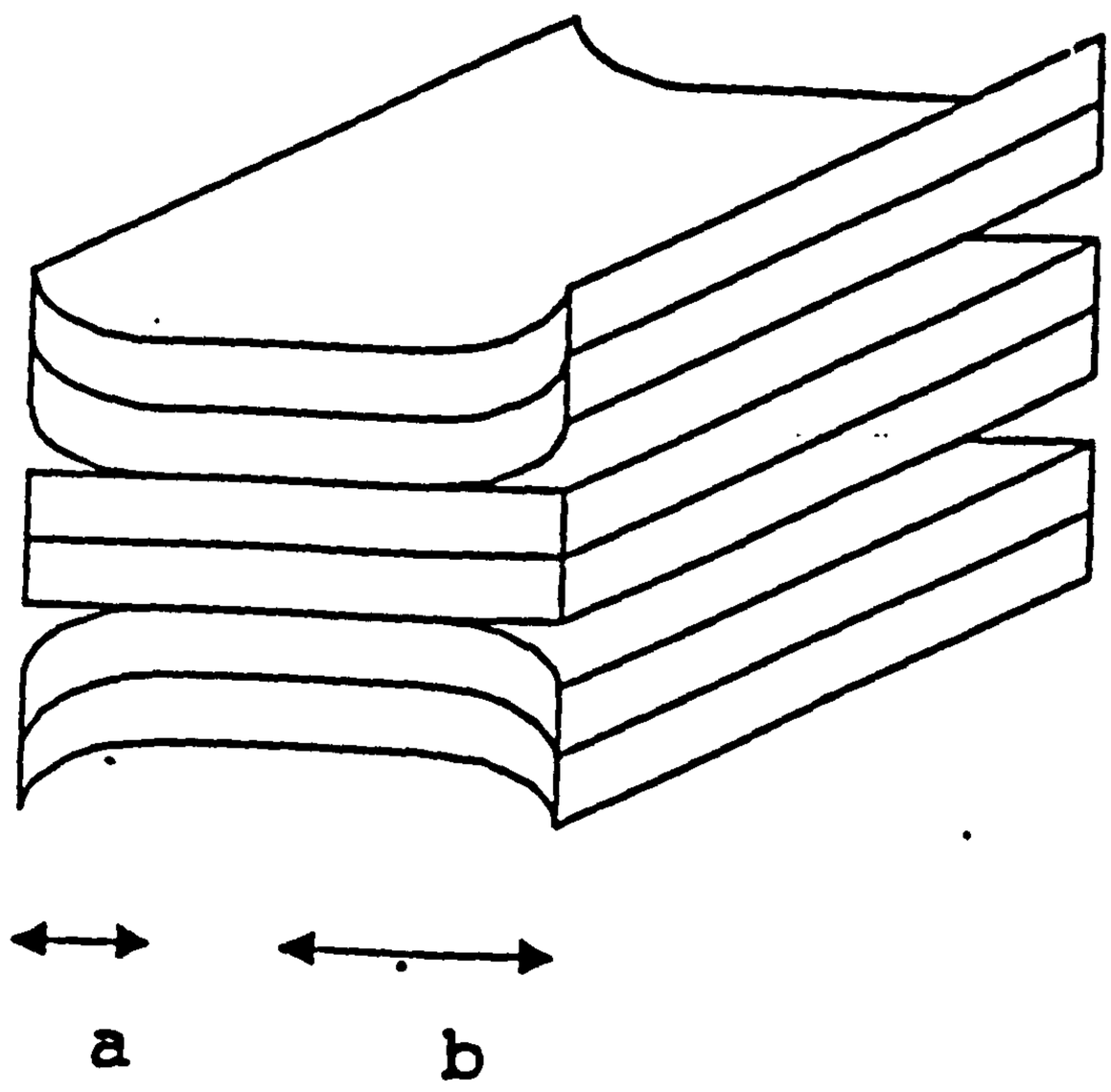

Figure 4.4 Partially Delaminated Laminate

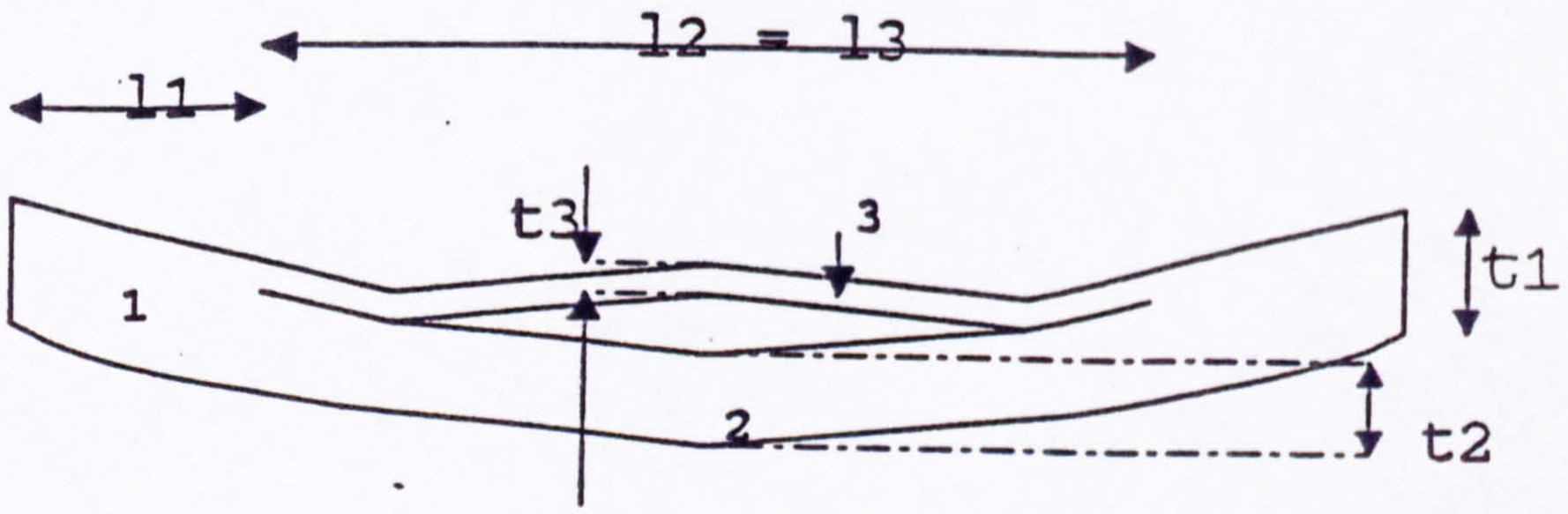

Figure 4.5 Three Regions of a Delaminated Beam

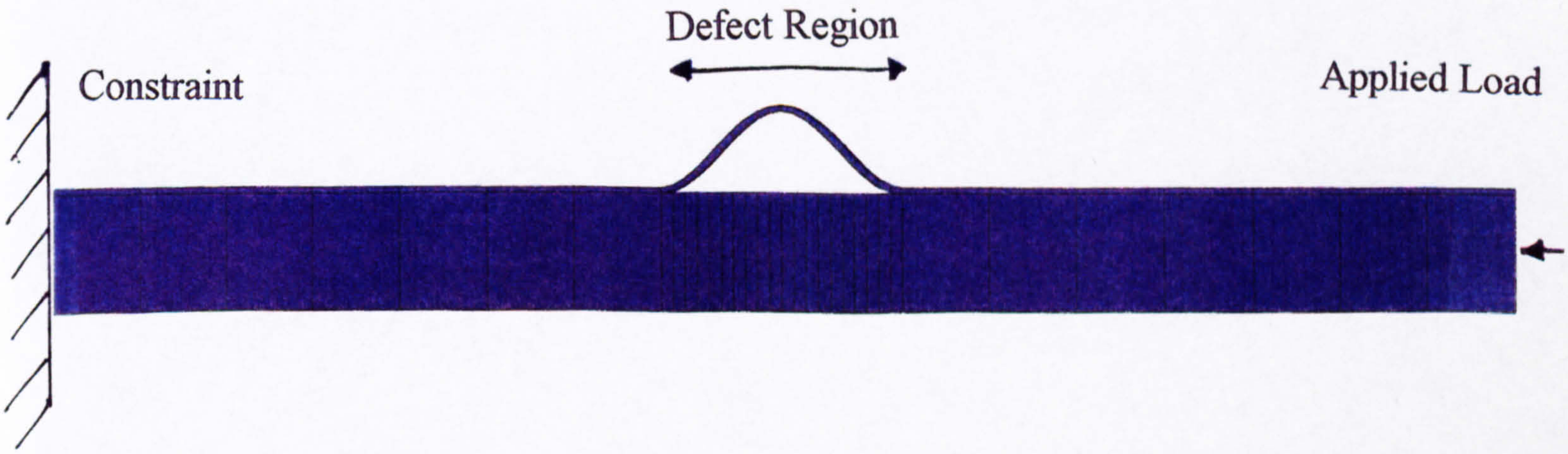

Figure 4.6 Three Dimensional Finite Element Model of a Delaminated Beam

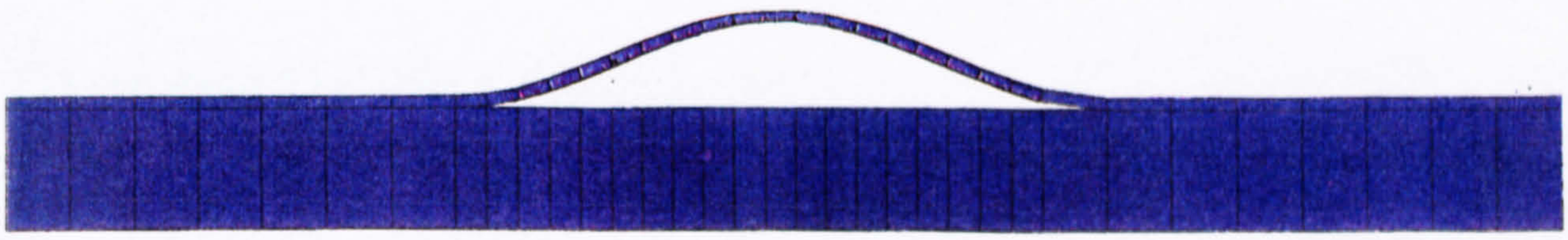

Figure 4.7(a) Typical Buckled Shape

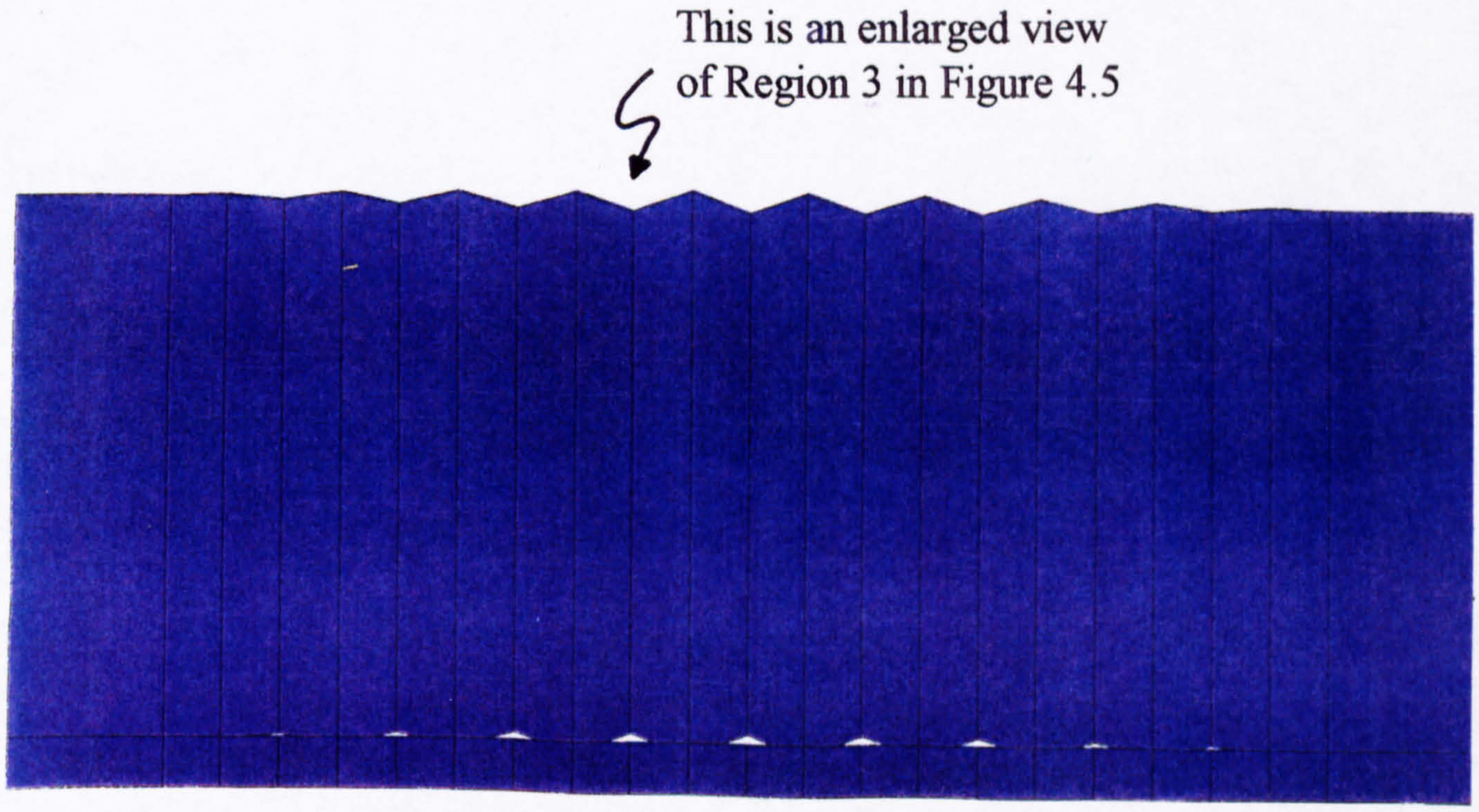

Figure 4.7(b) Non-Typical Buckled Shape

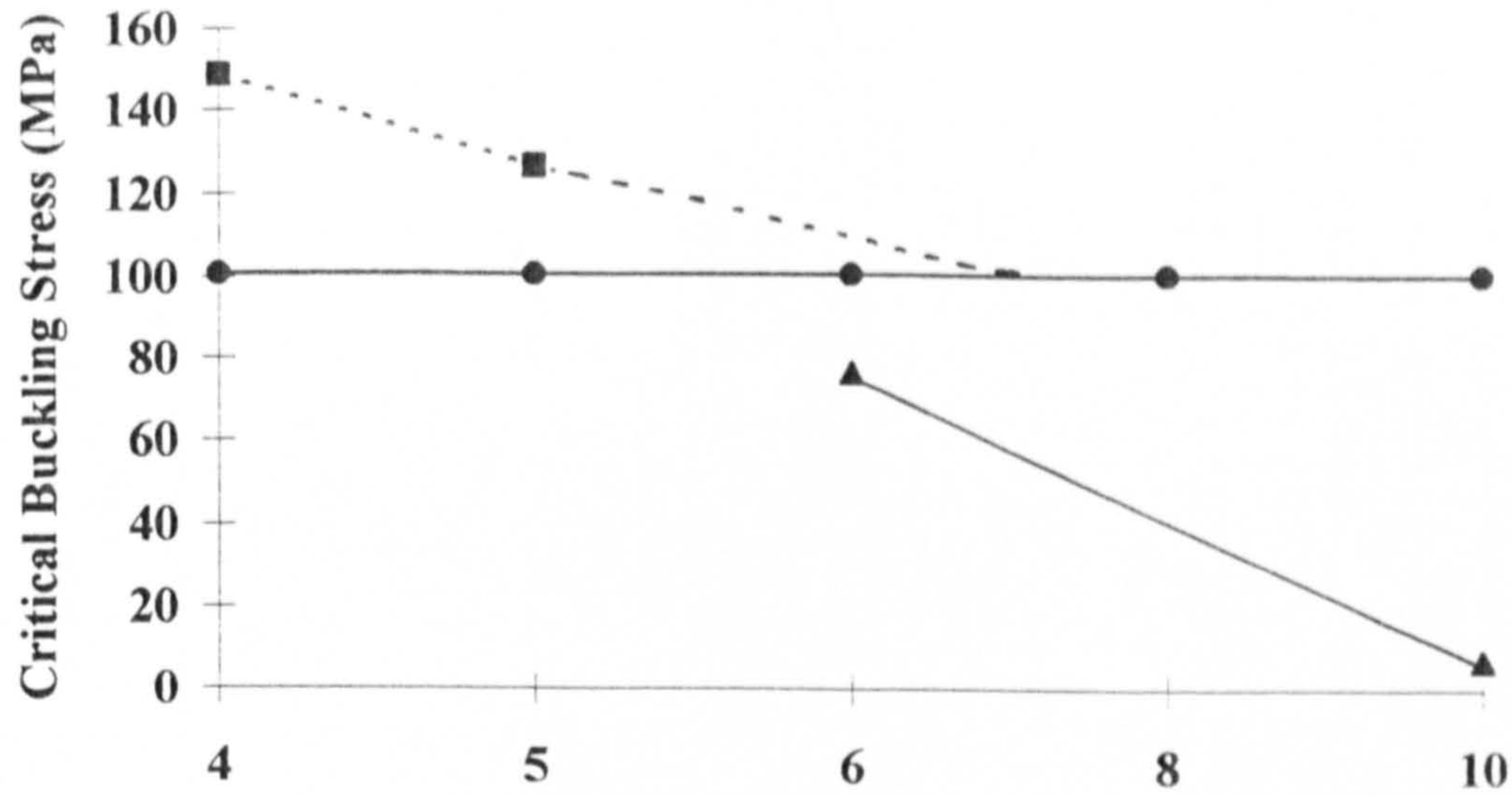

Figure 4.8 Critical Buckling Stress versus Number of Elements along Delamination Length

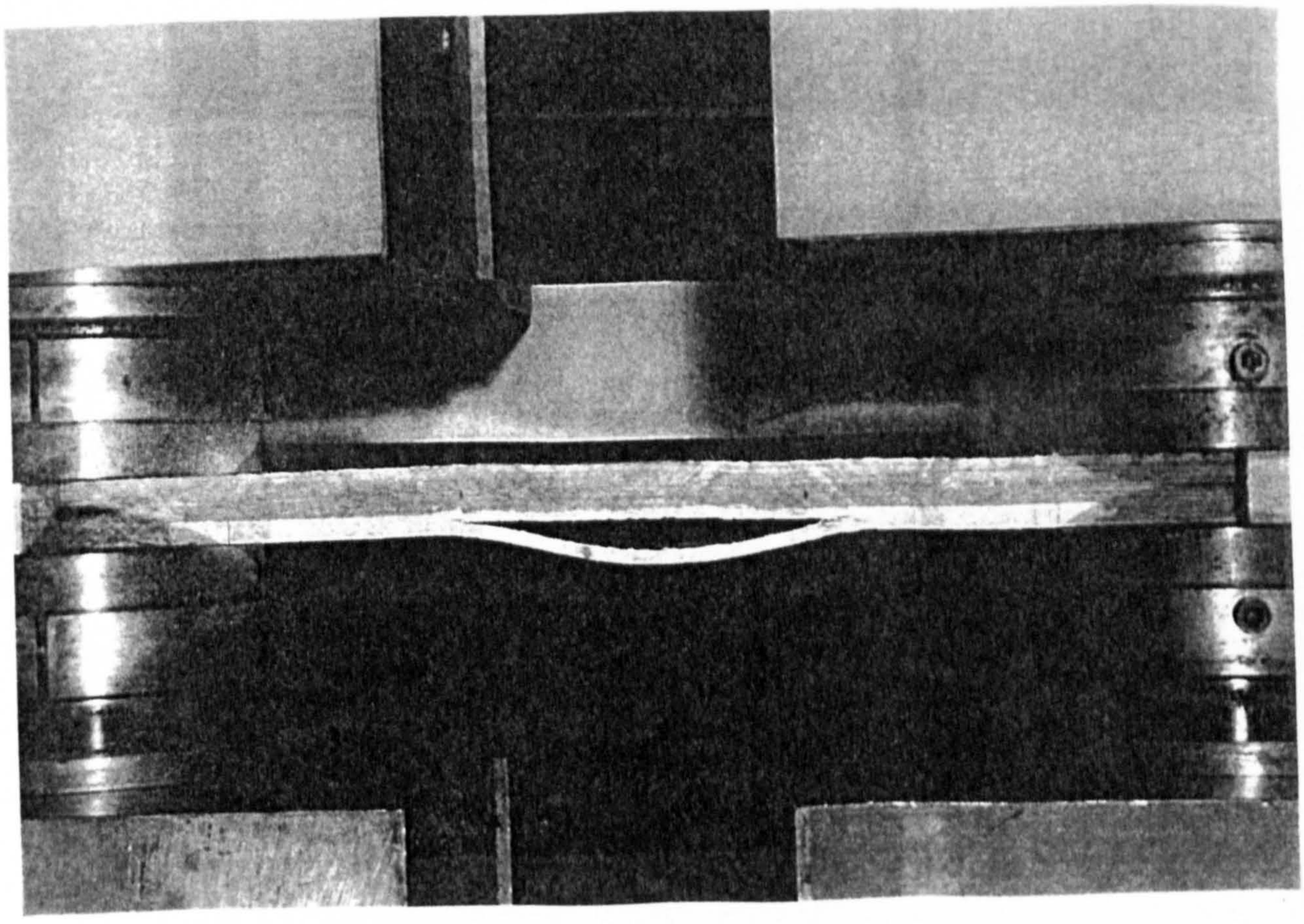

Figure 4.9 Delaminated Beam in Test Rig (Taken from Sumpter)

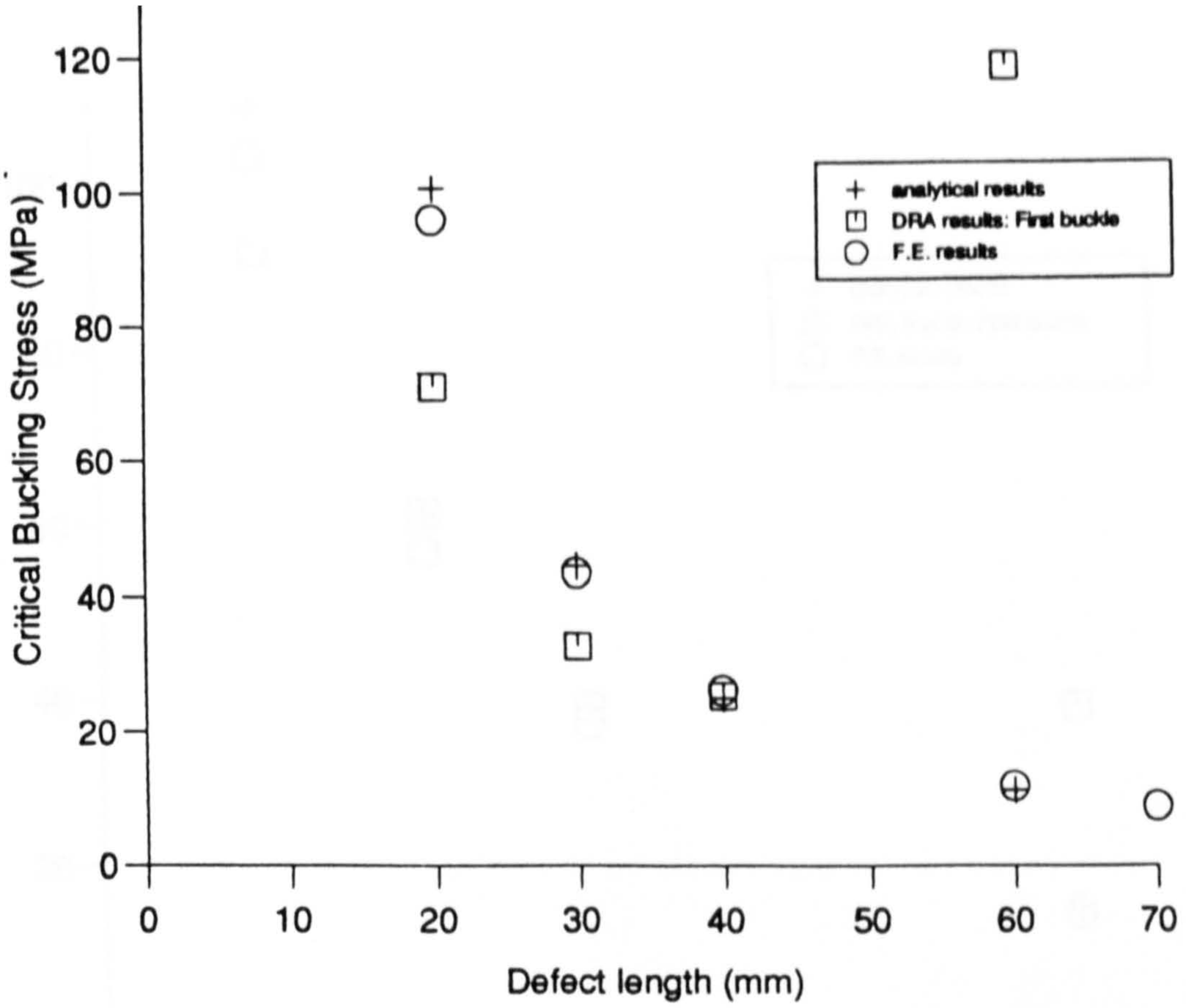

Figure 4.10 Critical Buckling Stress vs. Defect Length for Hand Lay-up Beams:
(a) Defect Depth = 0.8 mm

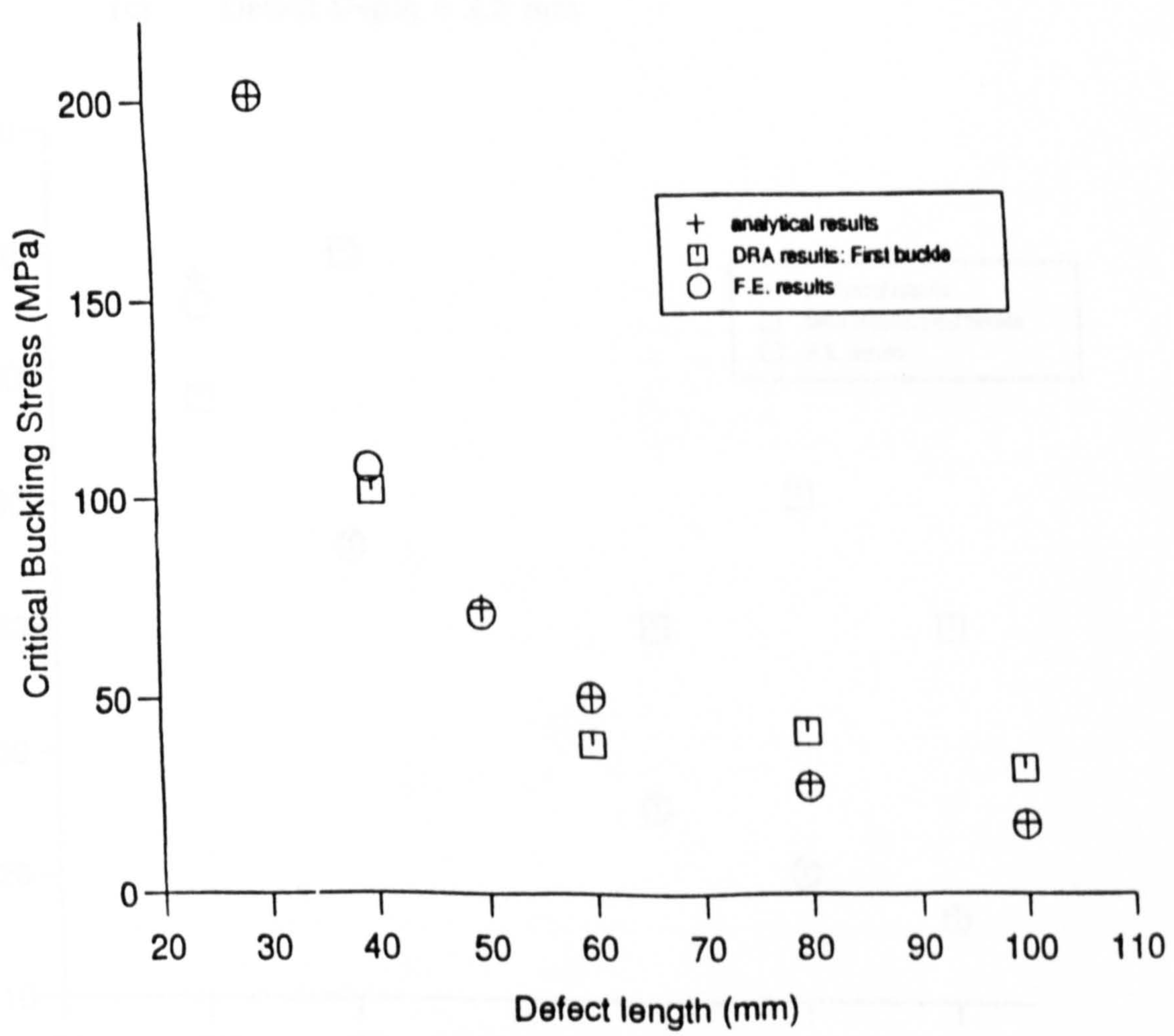

Figure 4.10 Critical Buckling Stress vs. Defect Length for Hand Lay-up Beams:
(b) Defect Depth = 1.7 mm

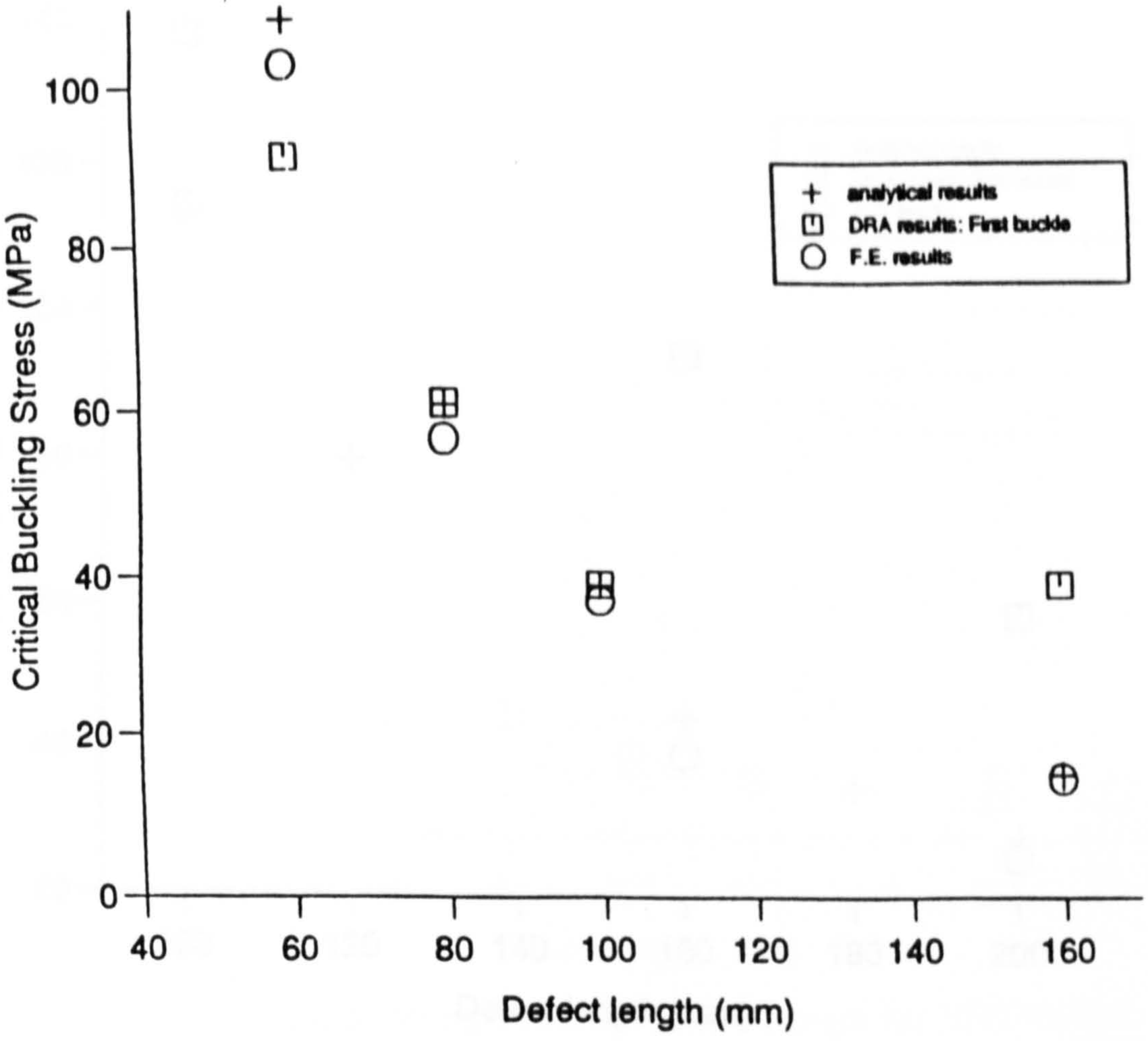

Figure 4.10 Critical Buckling Stress vs. Defect Length for Hand Lay-up Beams:
(c) Defect Depth = 2.5 mm

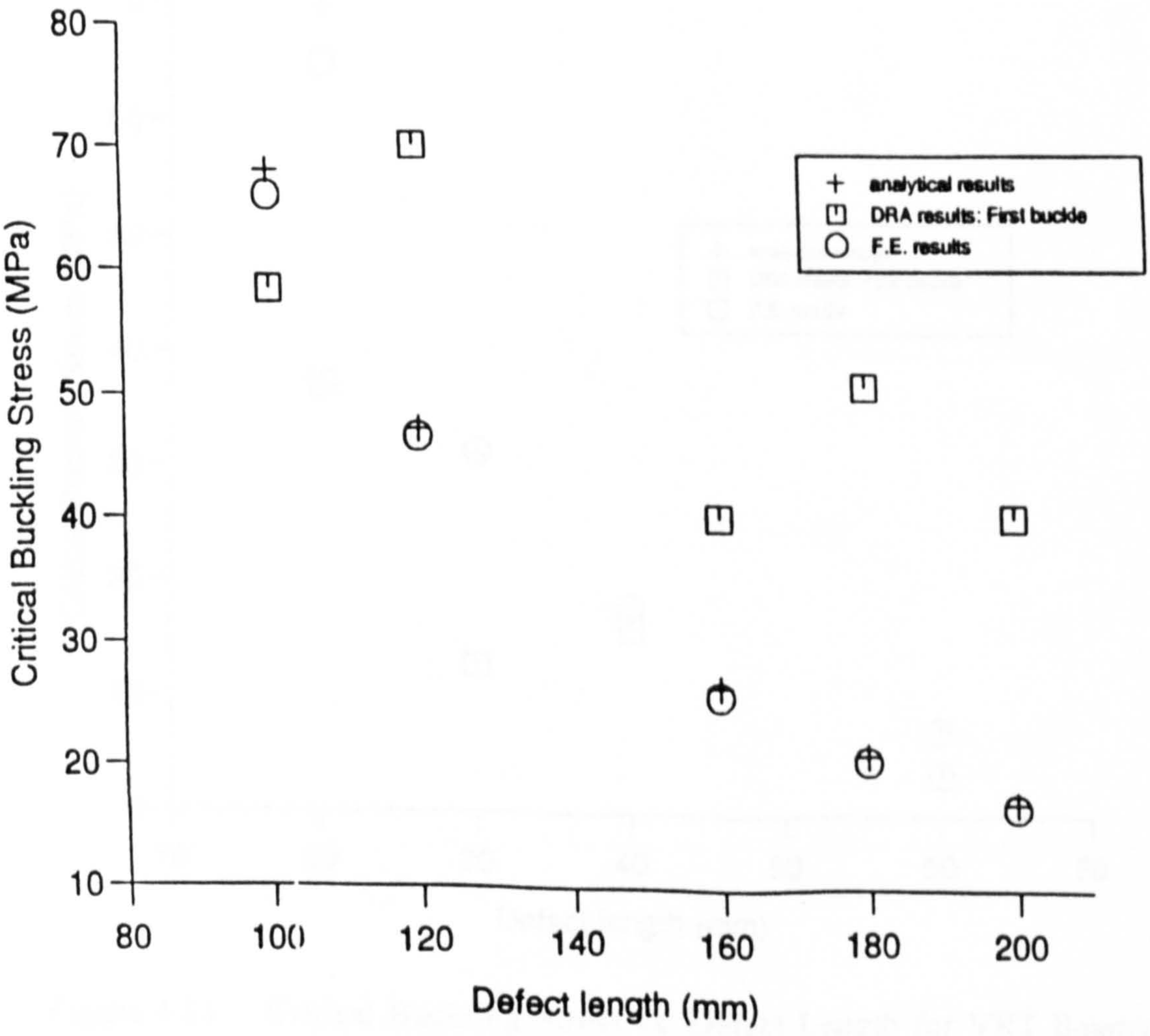

Figure 4.10 Critical Buckling Stress vs. Defect Length for Hand Lay-up Beams:
(d) Defect Depth = 3.3 mm

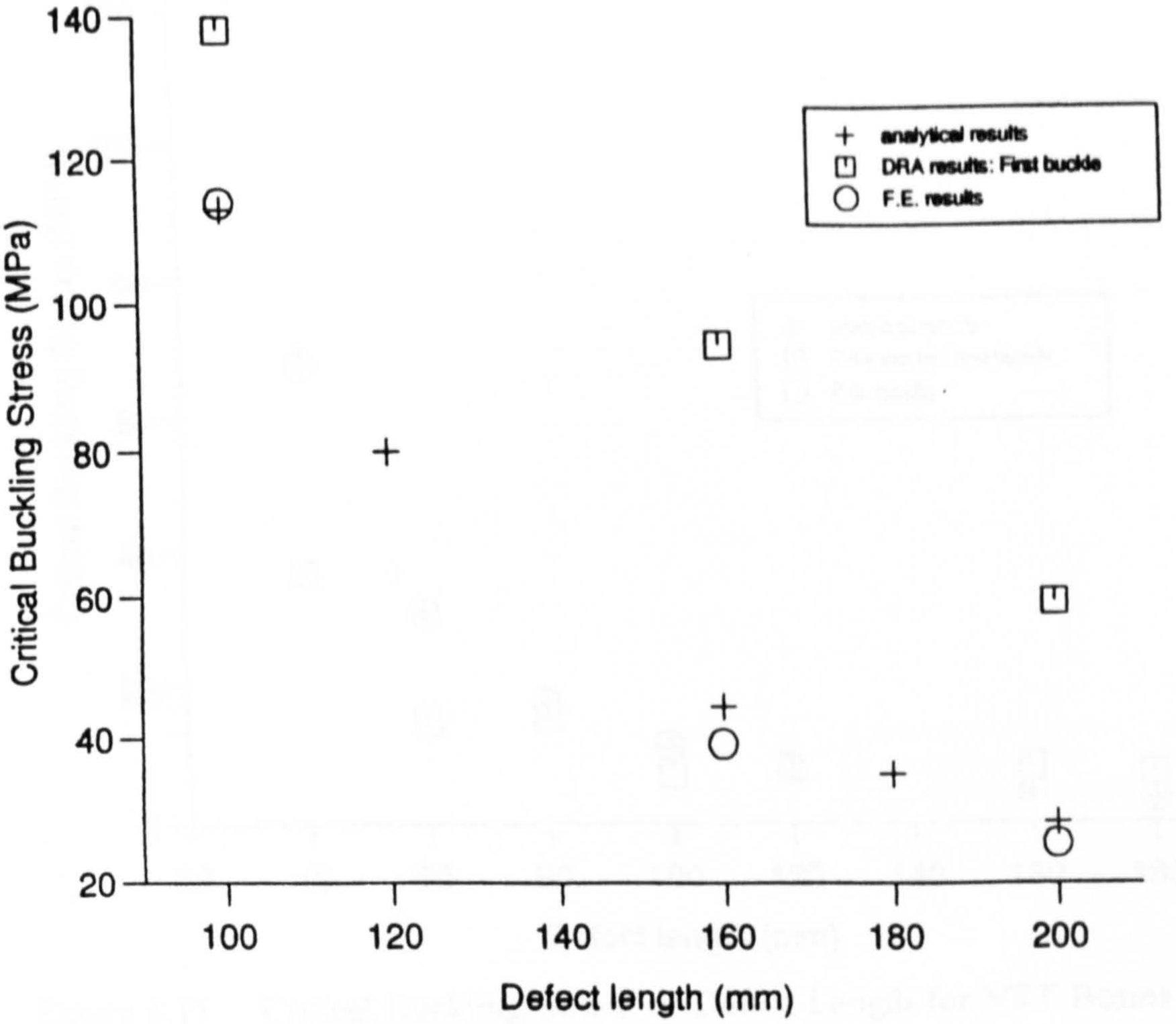

Figure 4.10 Critical Buckling Stress vs. Defect Length for Hand Lay-up Beams:
(e) Defect Depth = 4.2 mm

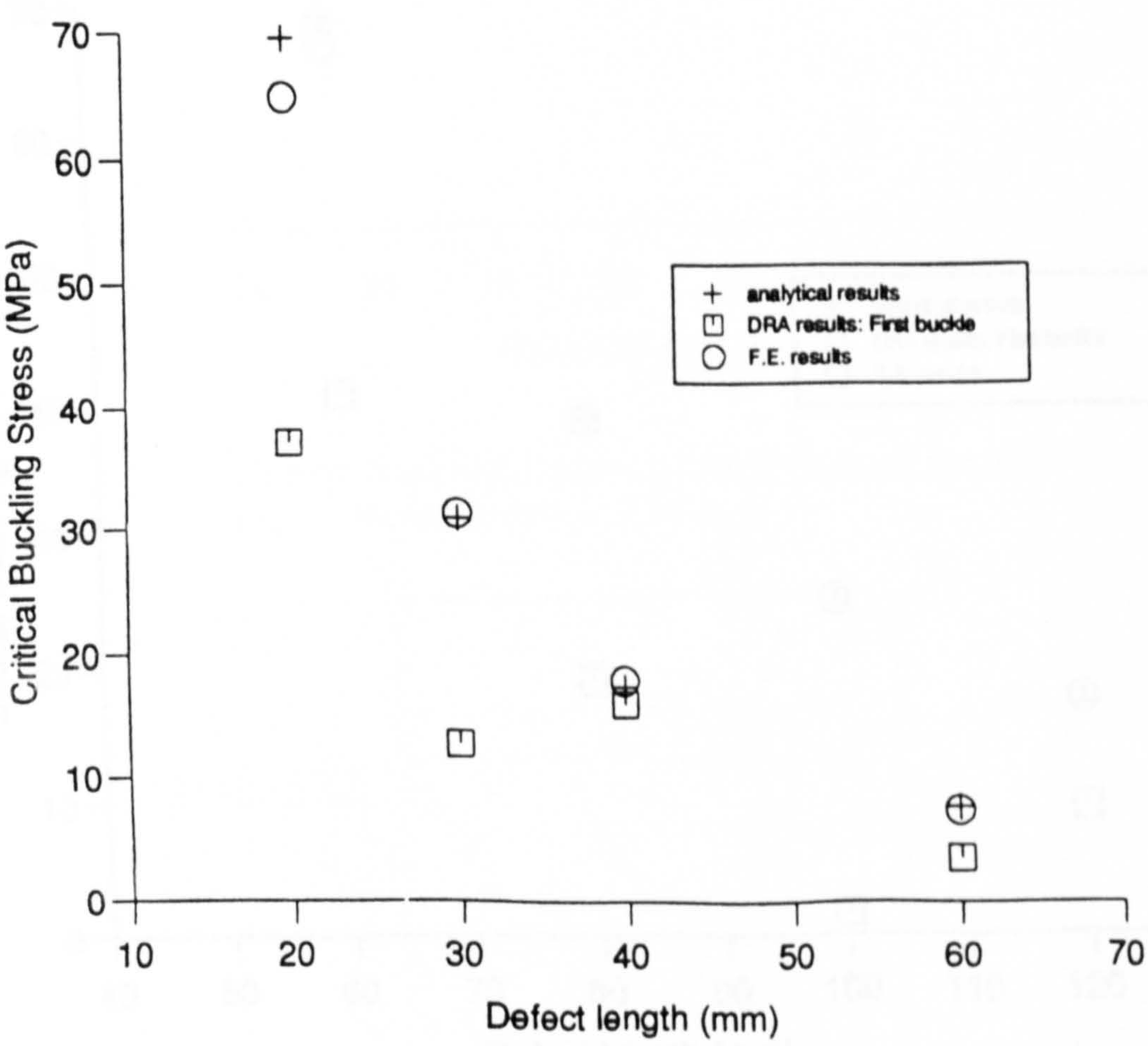

Figure 4.11 Critical Buckling Stress vs. Defect Length for VRT Beams:
(a) Defect Depth = 0.53 mm

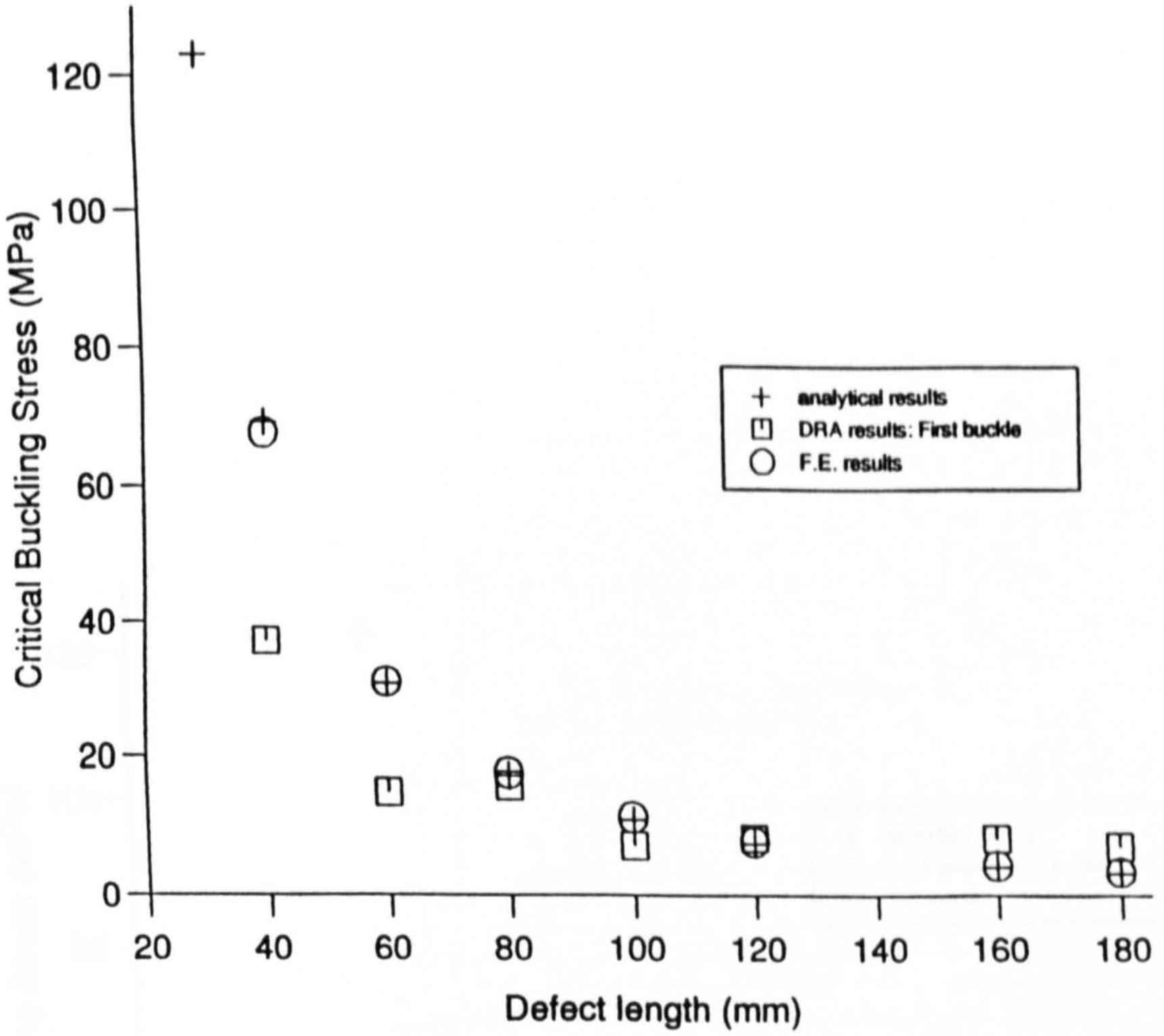

Figure 4.11 Critical Buckling Stress vs. Defect Length for VRT Beams:
(b) Defect Depth = 1.06 mm

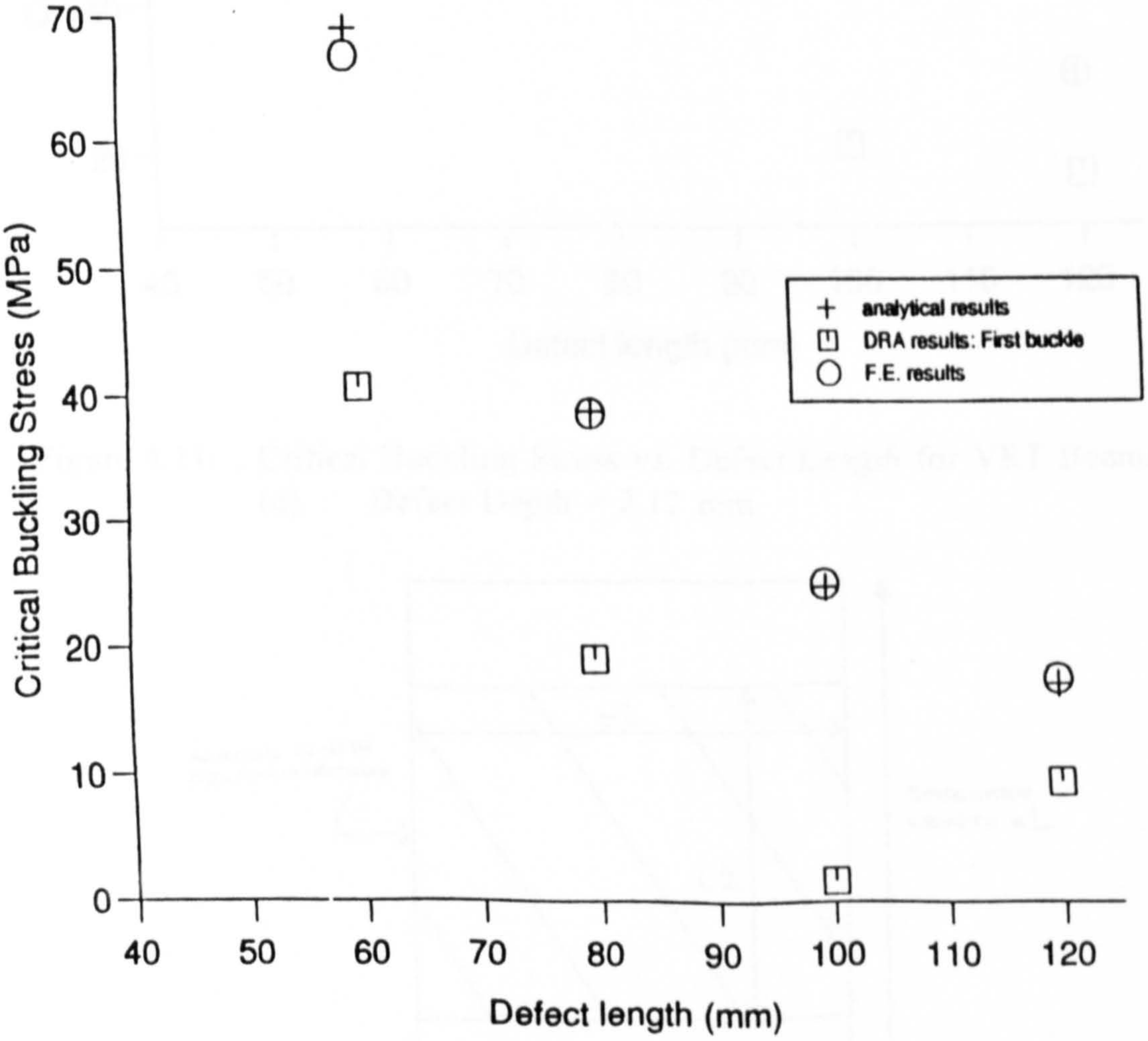

Figure 4.11 Critical Buckling Stress vs. Defect Length for VRT Beams:
(c) Defect Depth = 1.59 mm

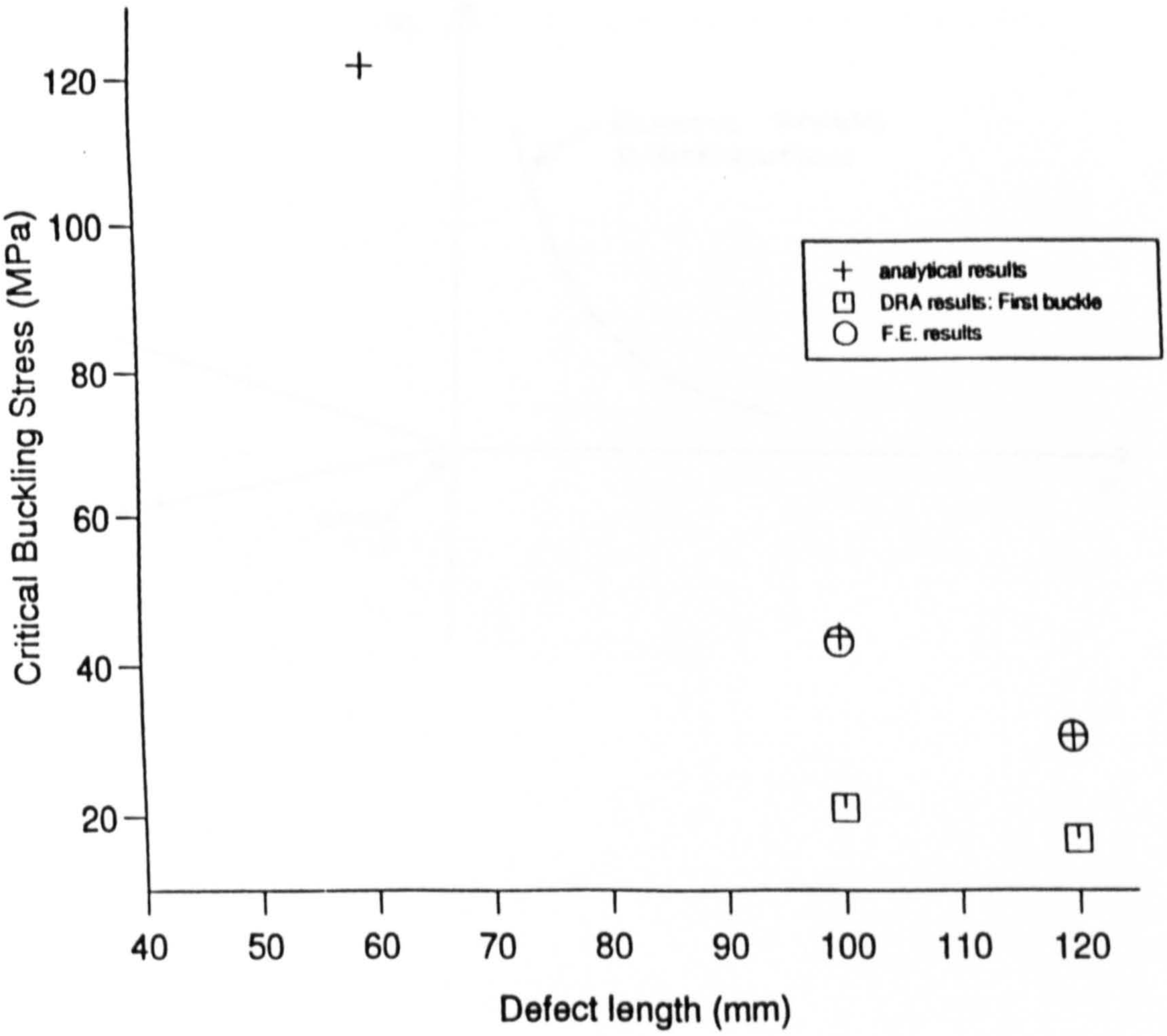

Figure 4.11 Critical Buckling Stress vs. Defect Length for VRT Beams:
(d) Defect Depth = 2.12 mm

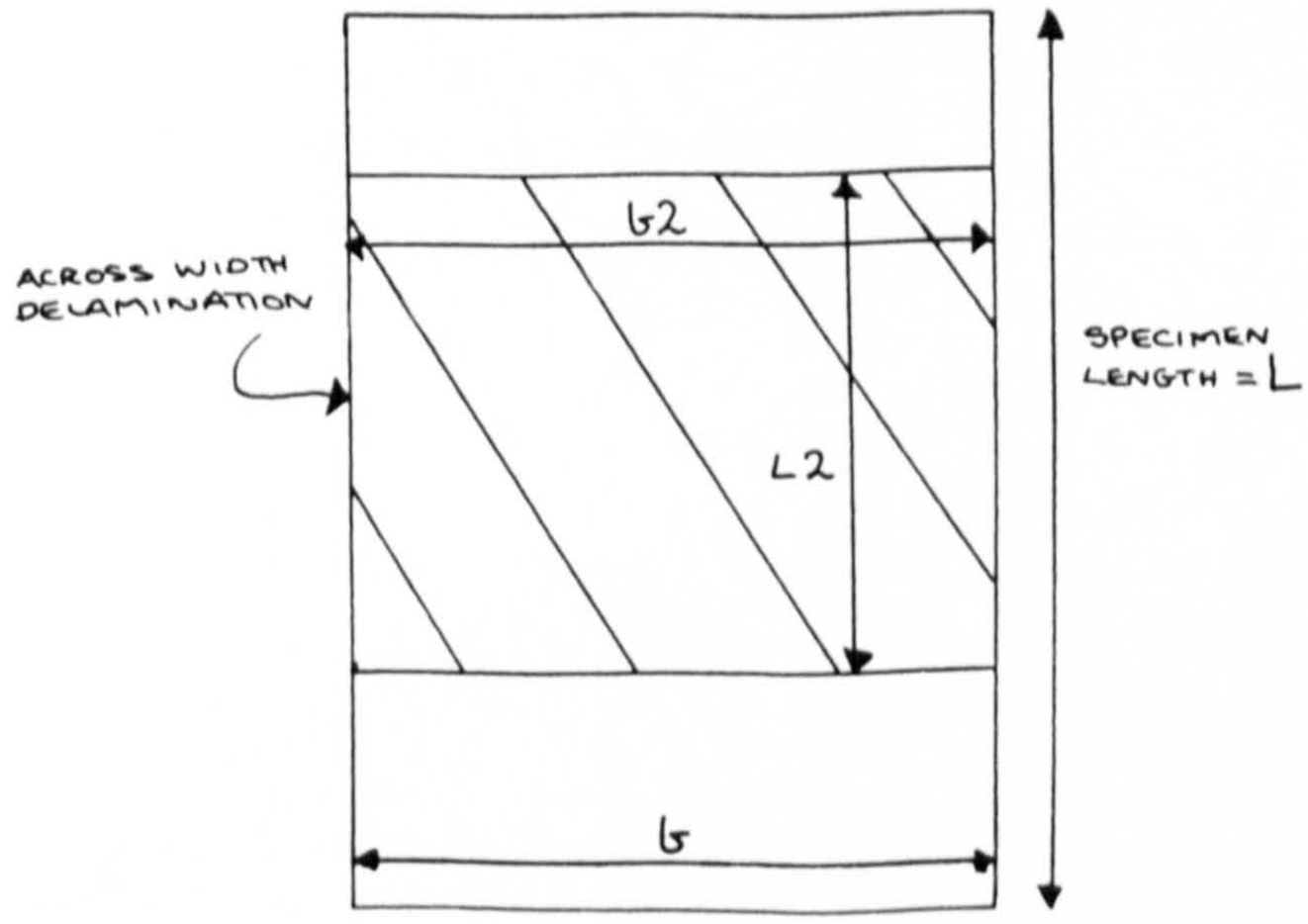

Figure 4.12 Partially Delaminated Beam to Represent Tested Specimens

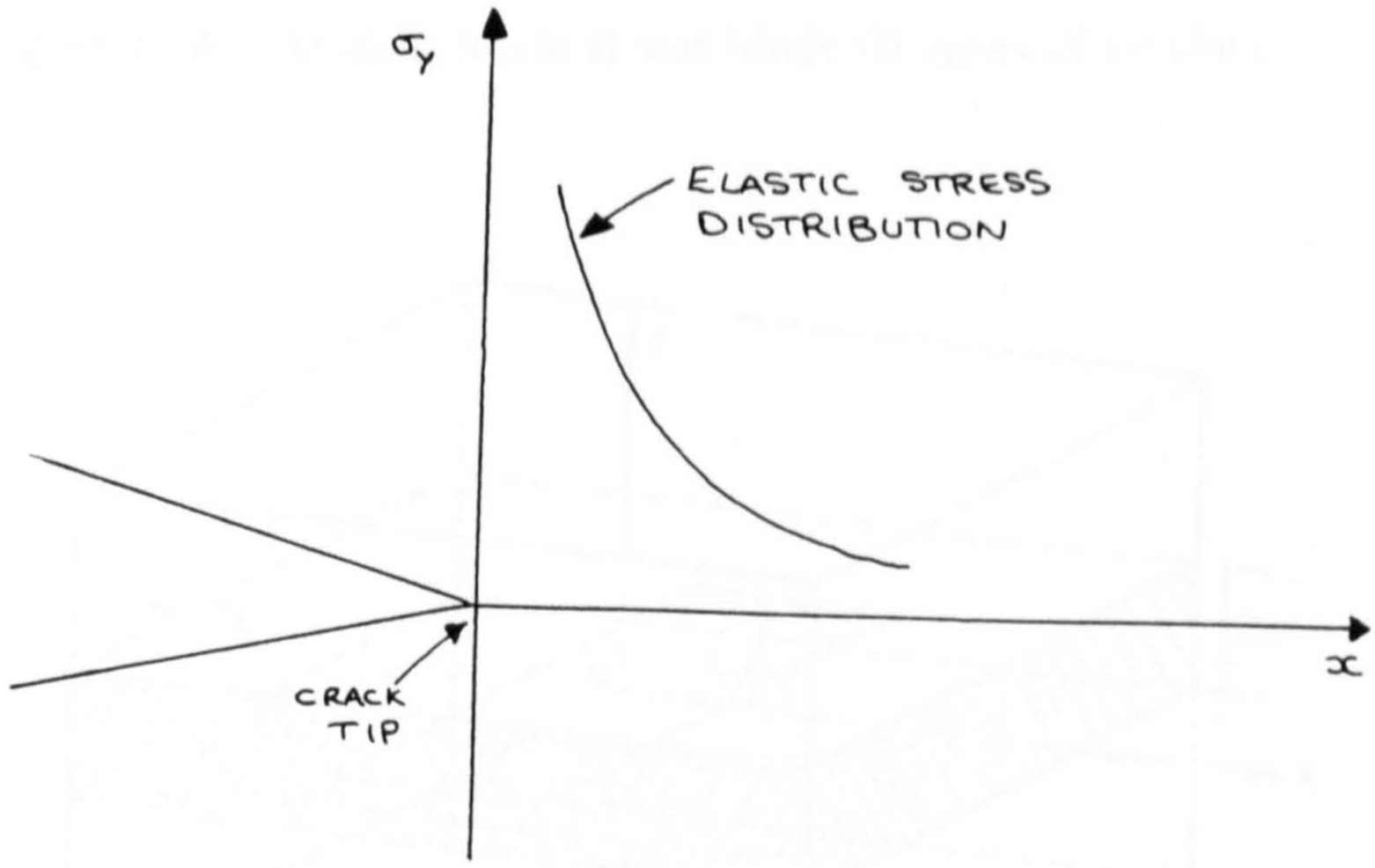

Figure 4.13 Elastic Stress Field at the Crack Tip

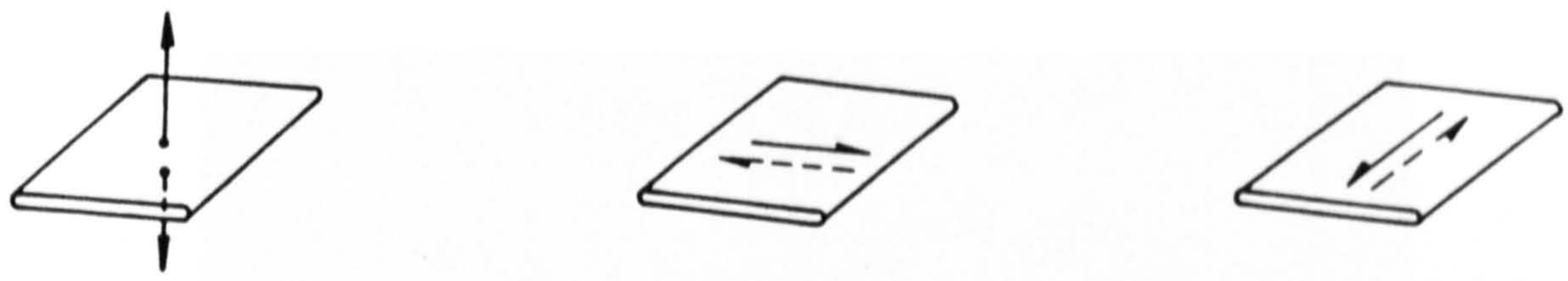

(a) Opening - Mode I (b) Shearing - Mode II (c) Tearing - Mode III

Figure 4.14 Mode I, Mode II and Mode III types of Loading

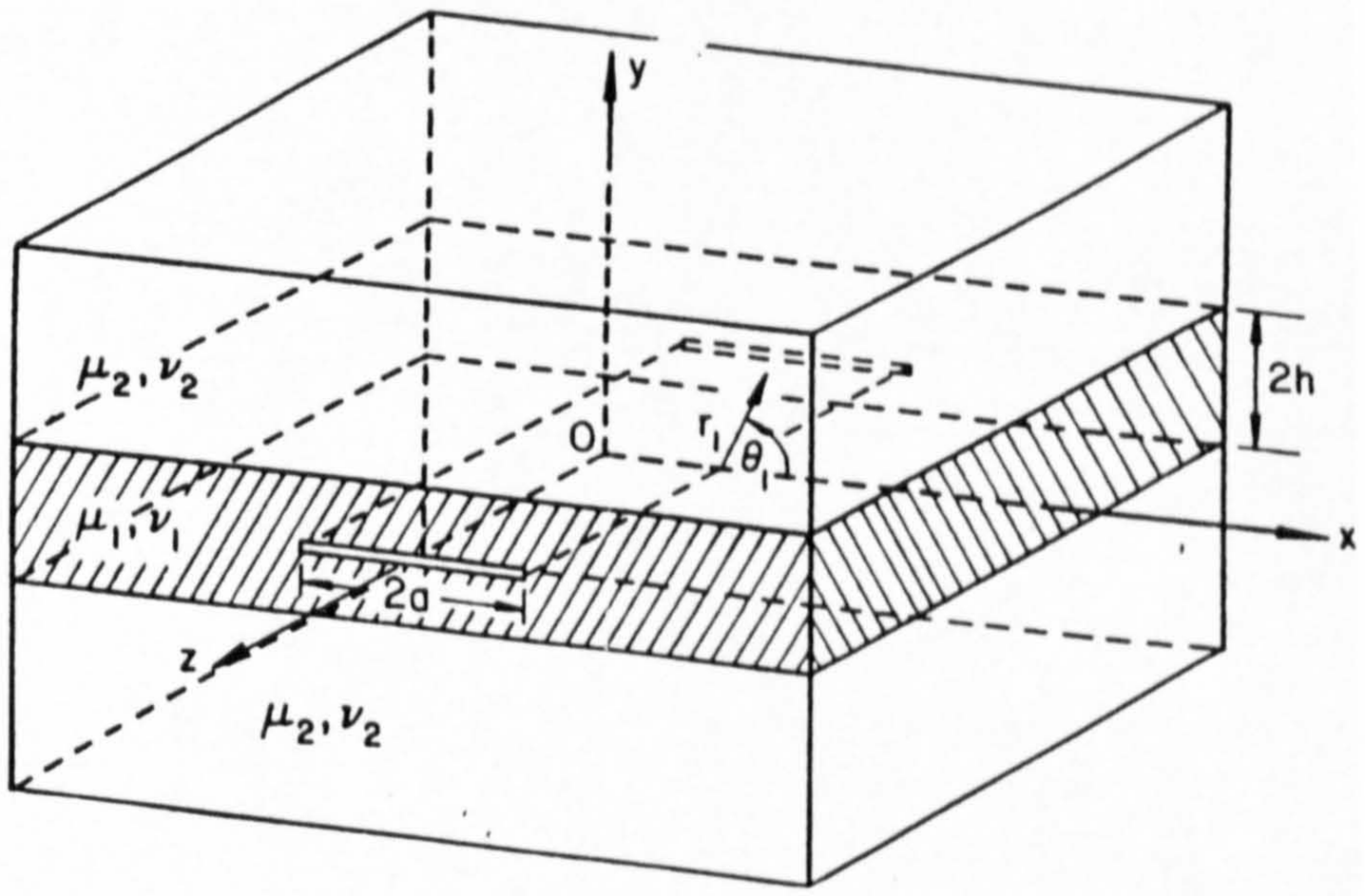

Figure 4.15 Cracked Layer Sandwiched between Two Half-Planes (Taken from Sih & Chen)

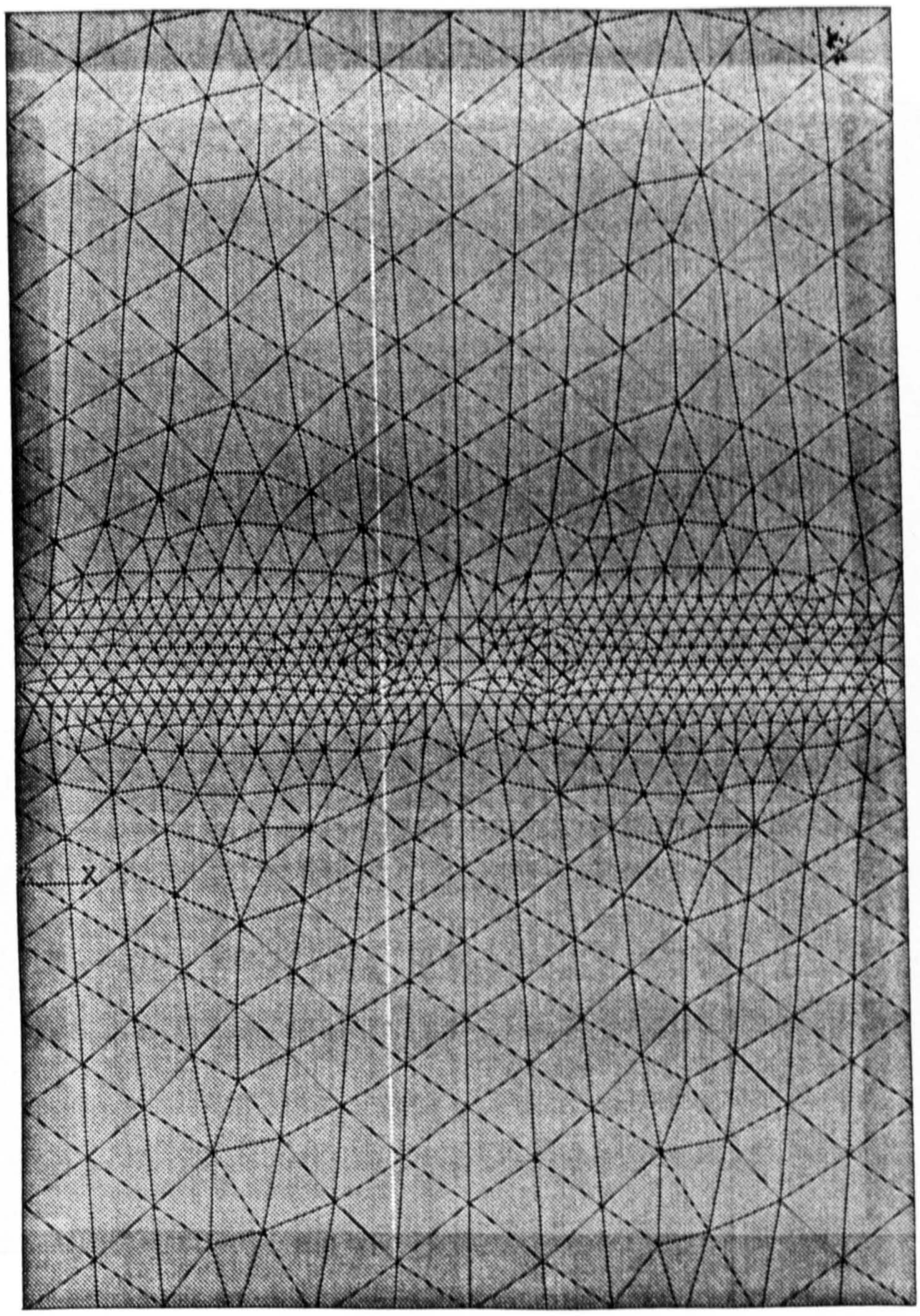

Figure 4.16 Finite Element Model of a Plate Constructed of Layered Materials

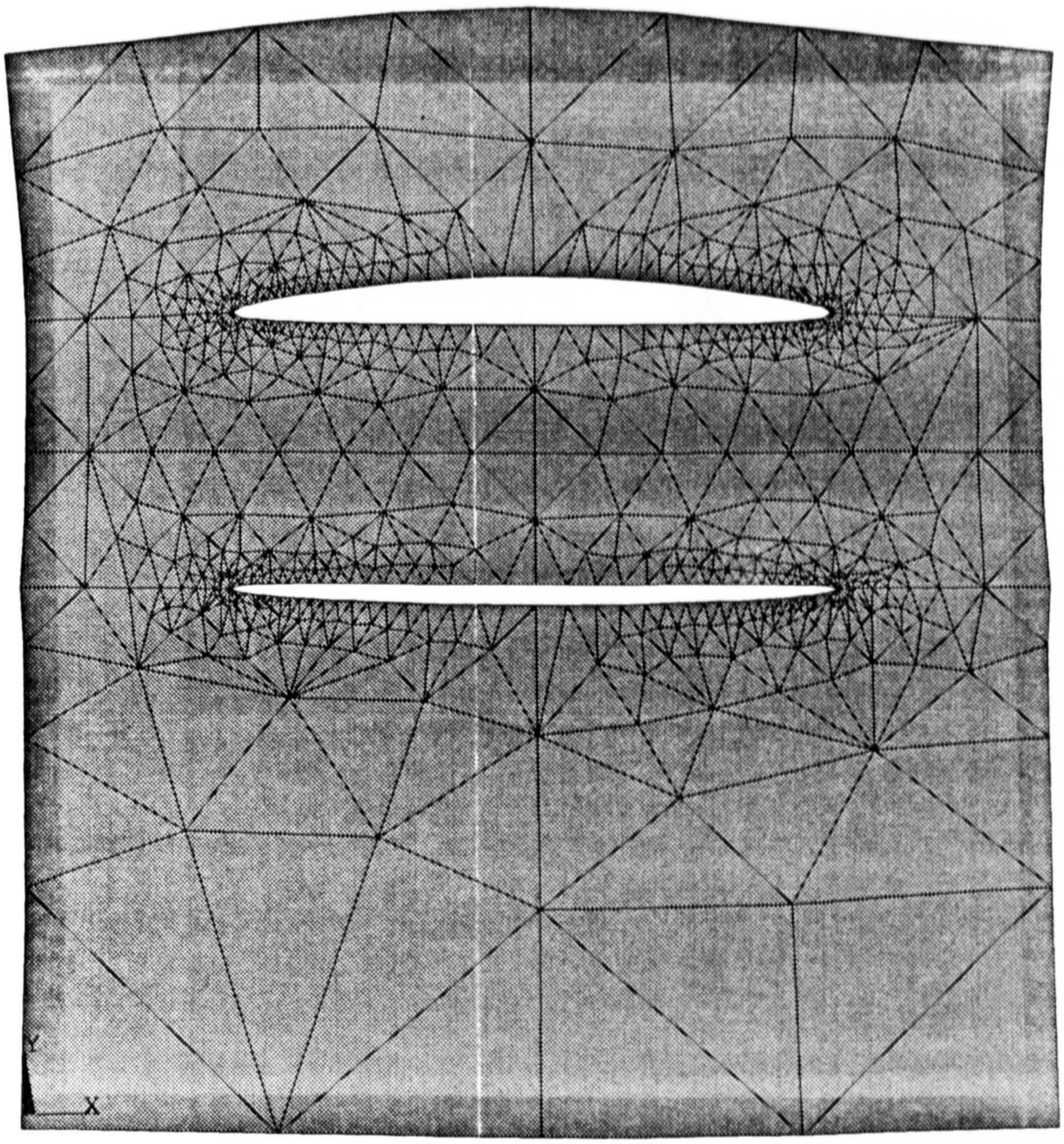

Figure 4.17 Finite Element Model of a Plate with Two Cracks

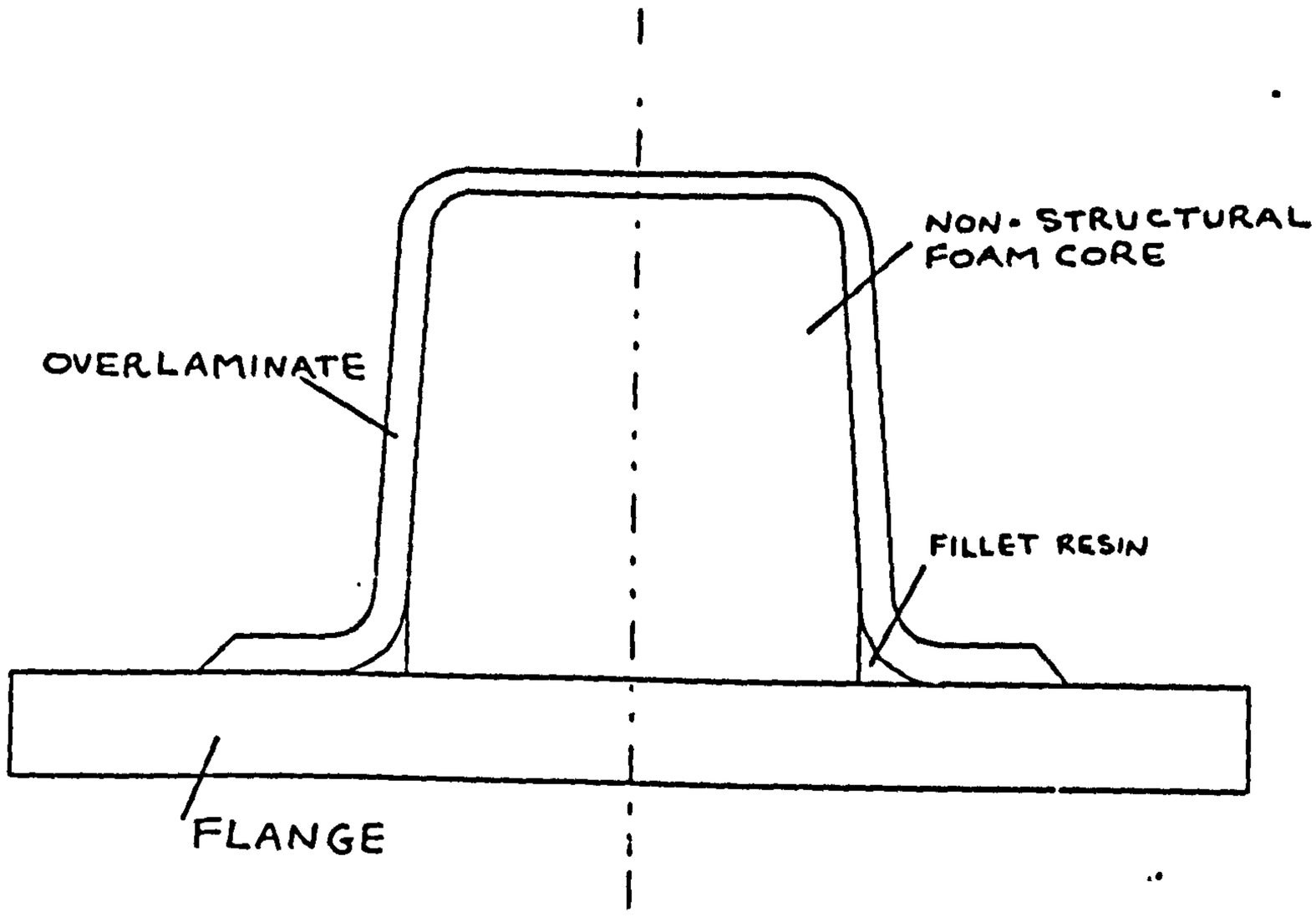

Figure 5.1 Geometry of a Type I Top Hat Stiffener

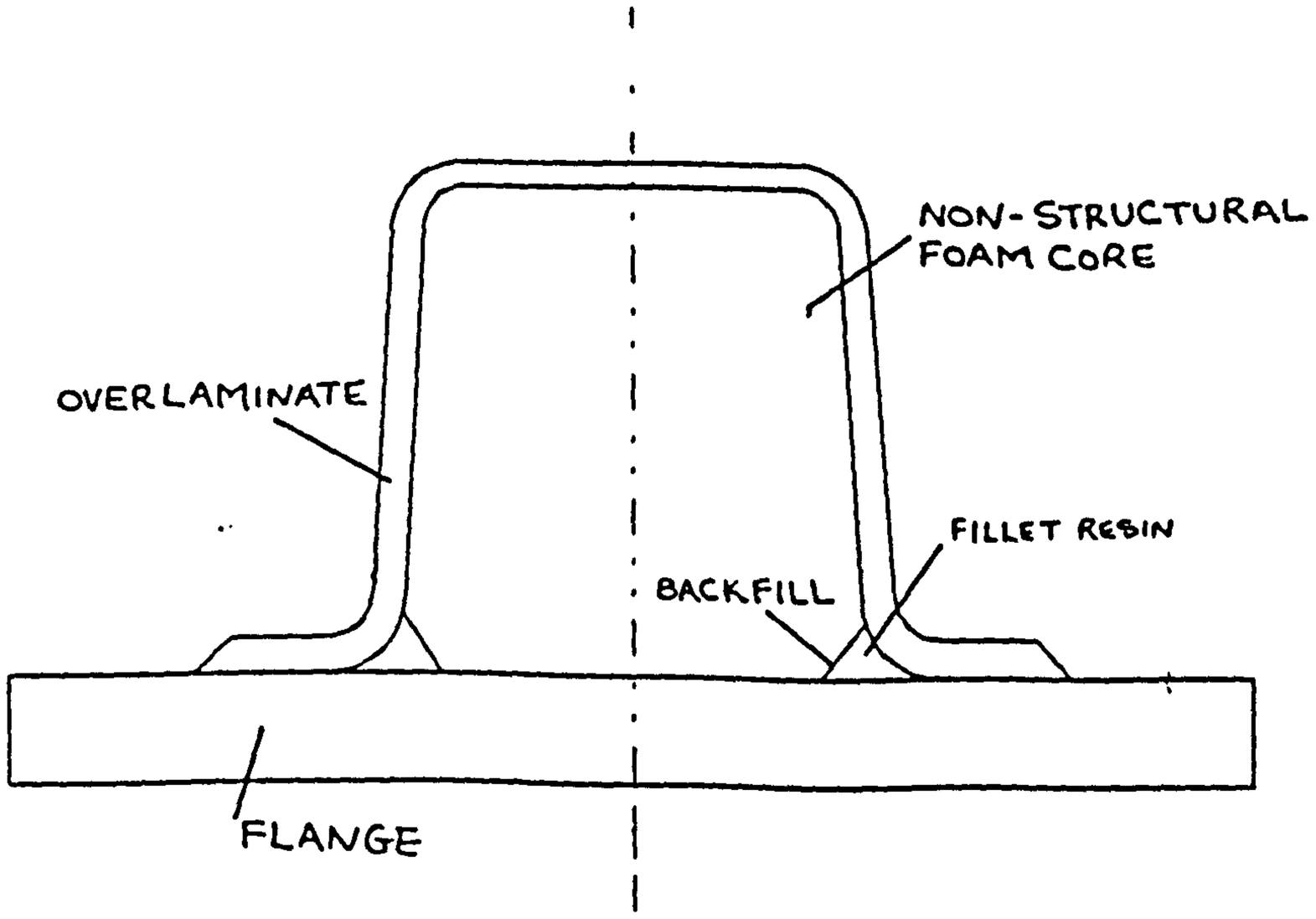

Figure 5.2 Geometry of a Type II Top Hat Stiffener

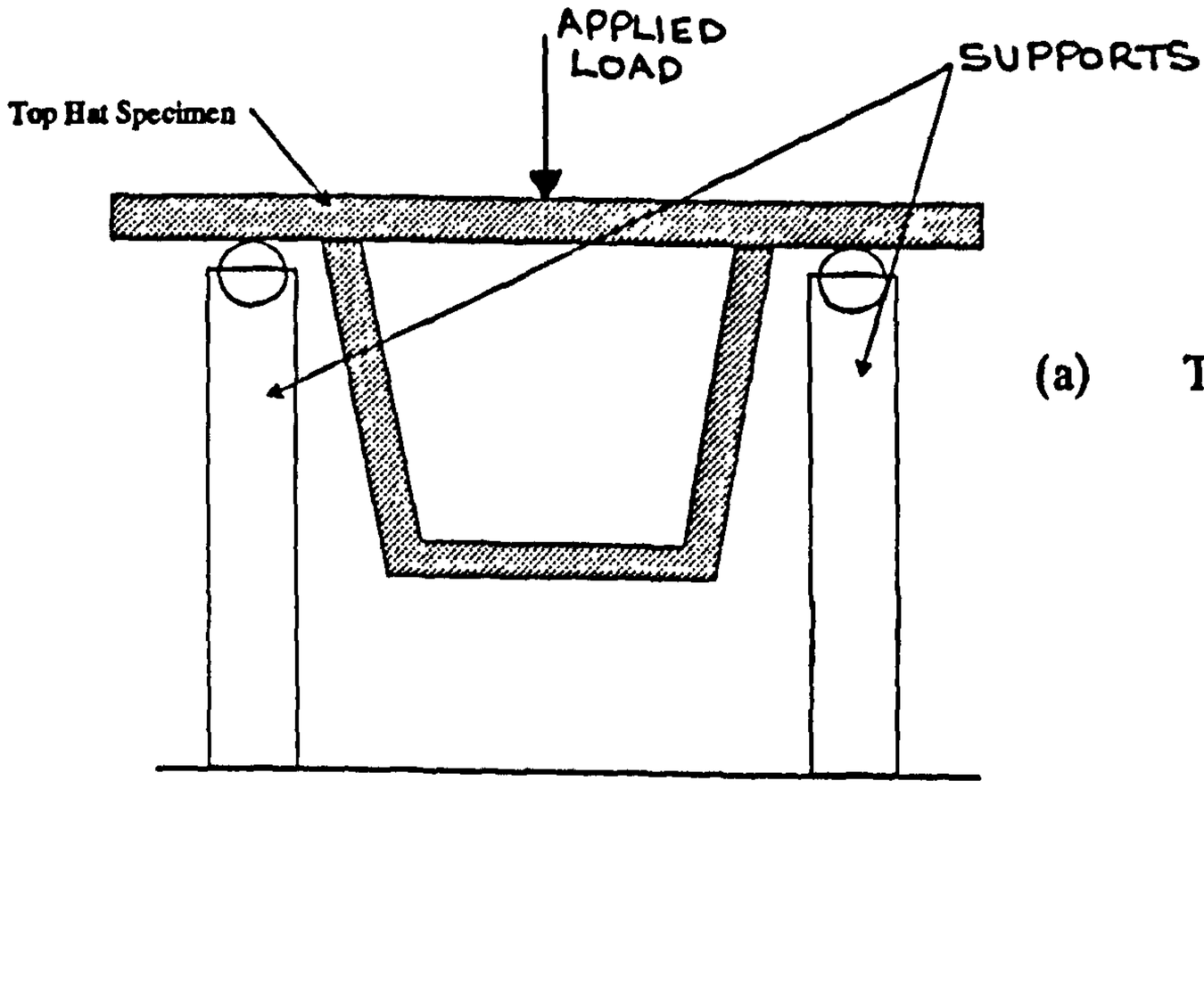

(a) Three Point Bending

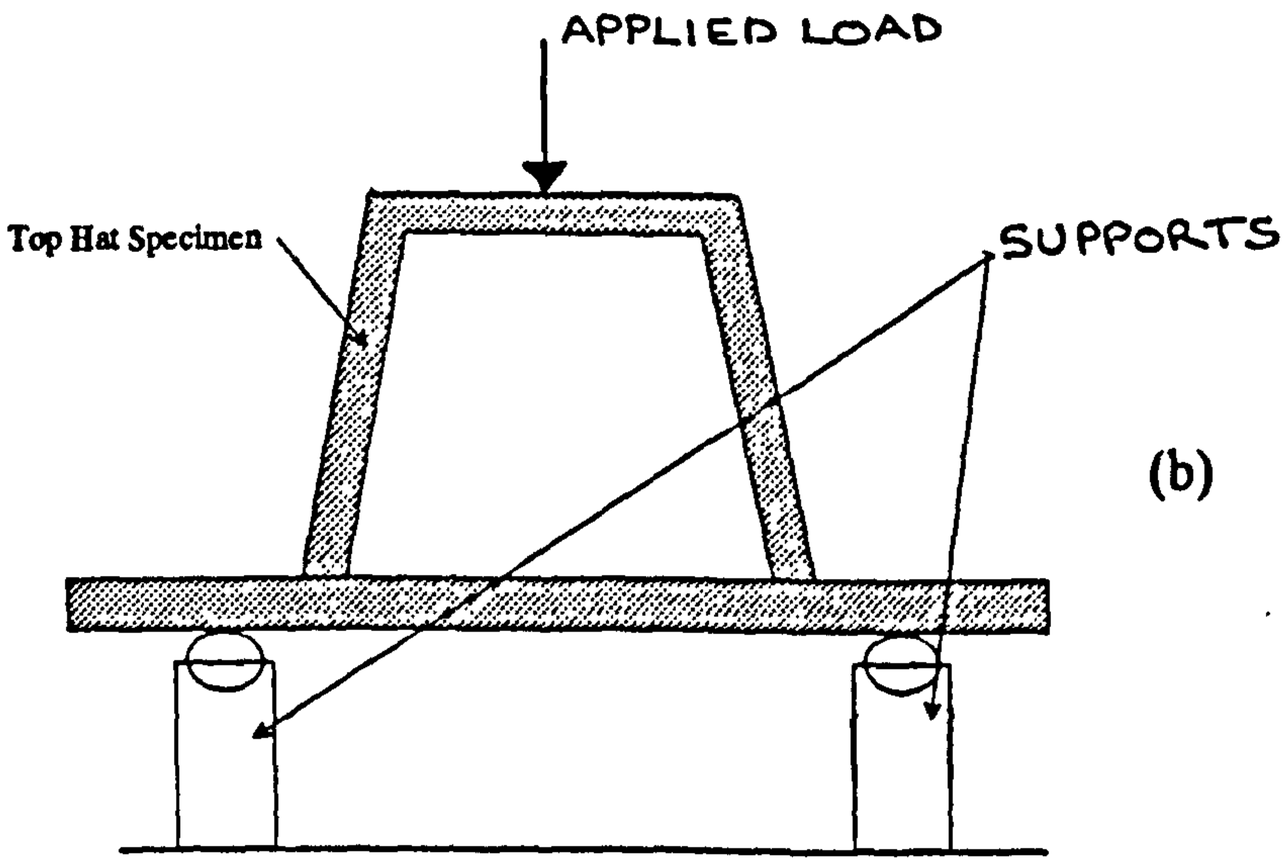

(b) Reverse Bend

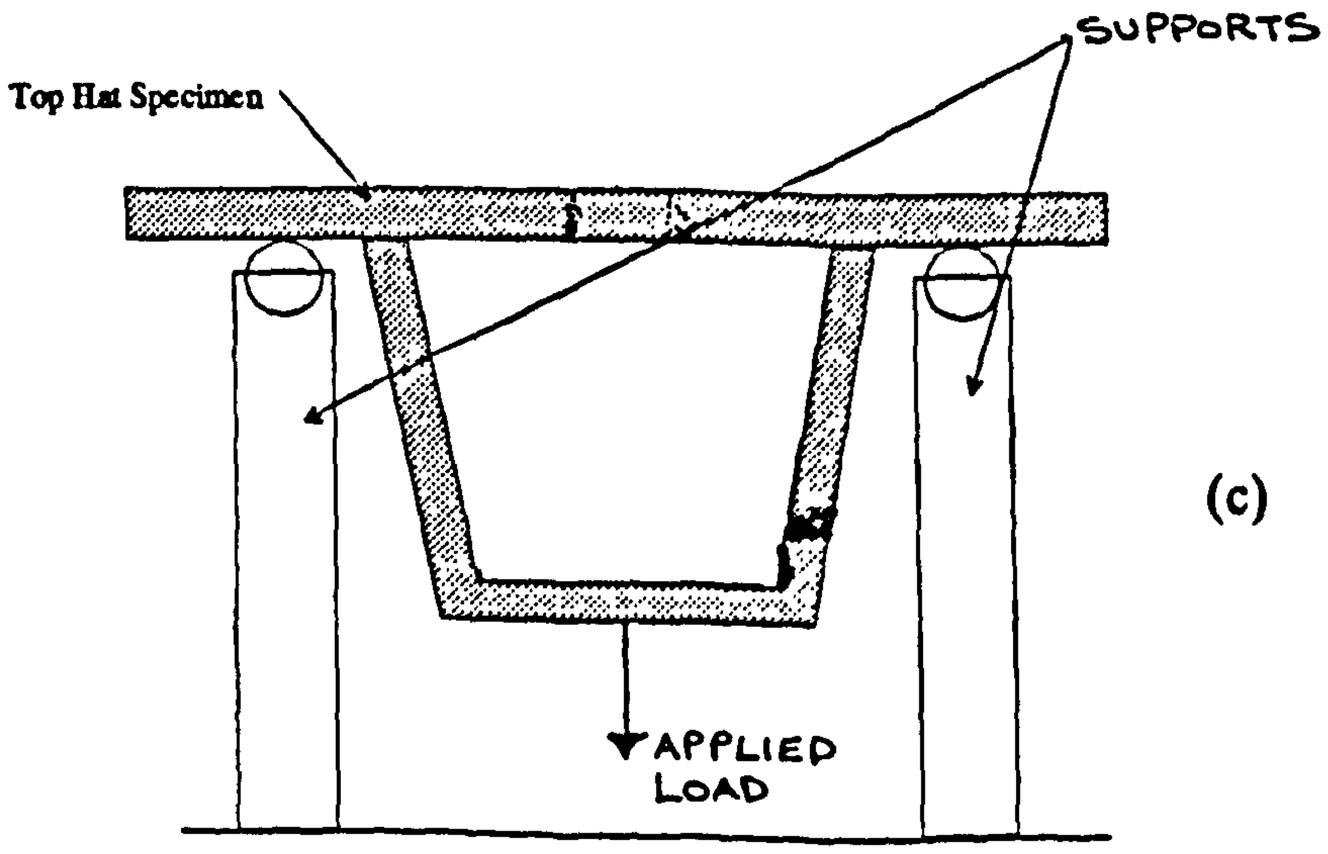

(c) Straight Pull-Off

Figure 5.3 Schematics of the Three Types of Loading Configurations which the Top Hat Stiffeners may be under In-Service :

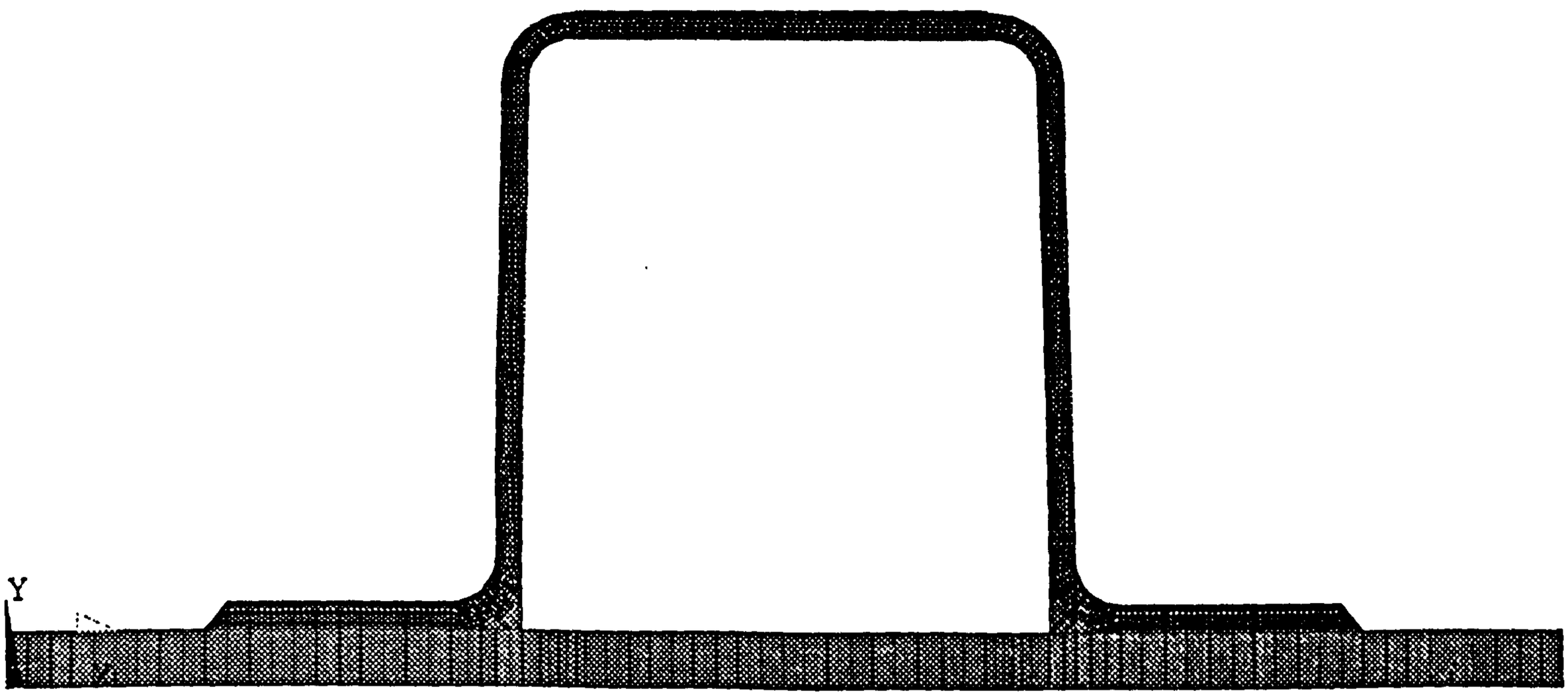

Figure 5.4 Typical Finite Element Representation of a Type I Top Hat Stiffener

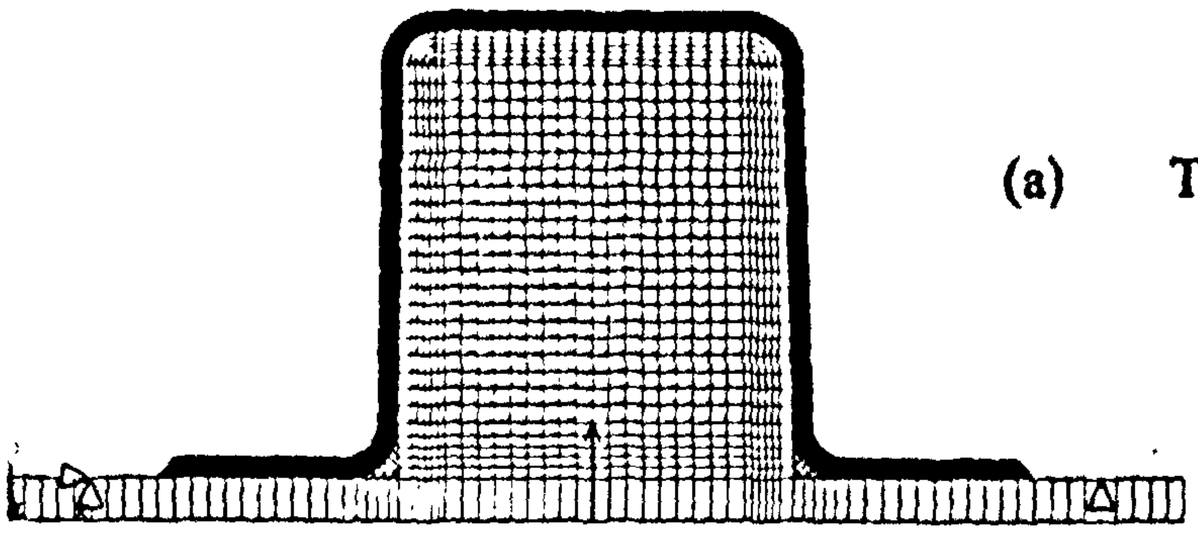

(a) Three Point Bending

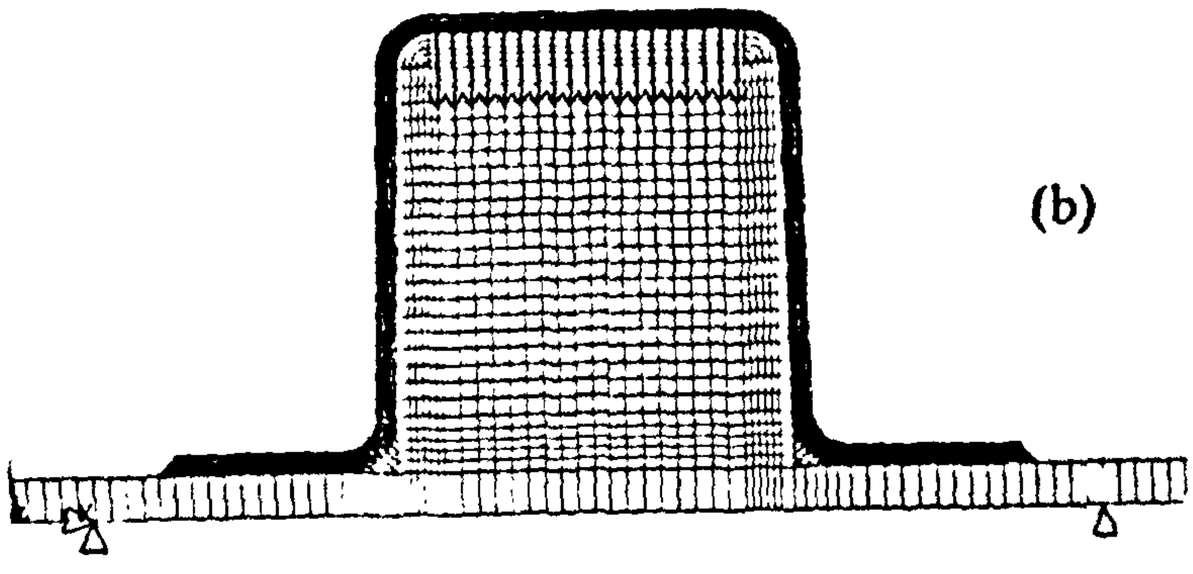

(b) Reverse Bend

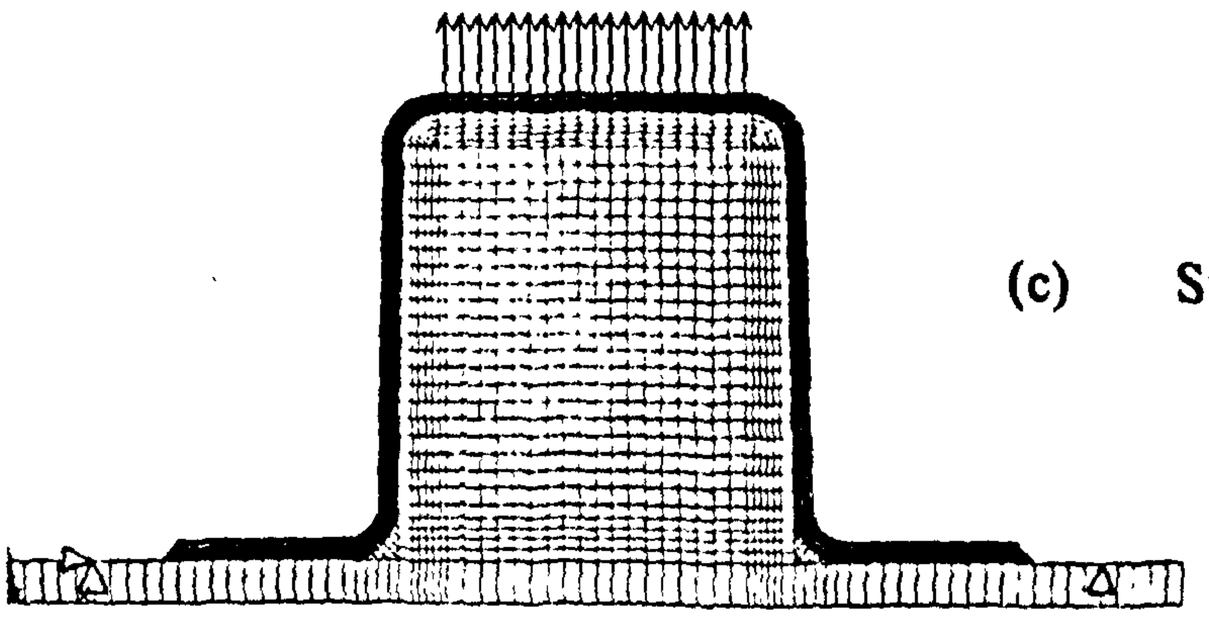

(c) Straight Pull-Off

Figure 5.5 FE Model Representations

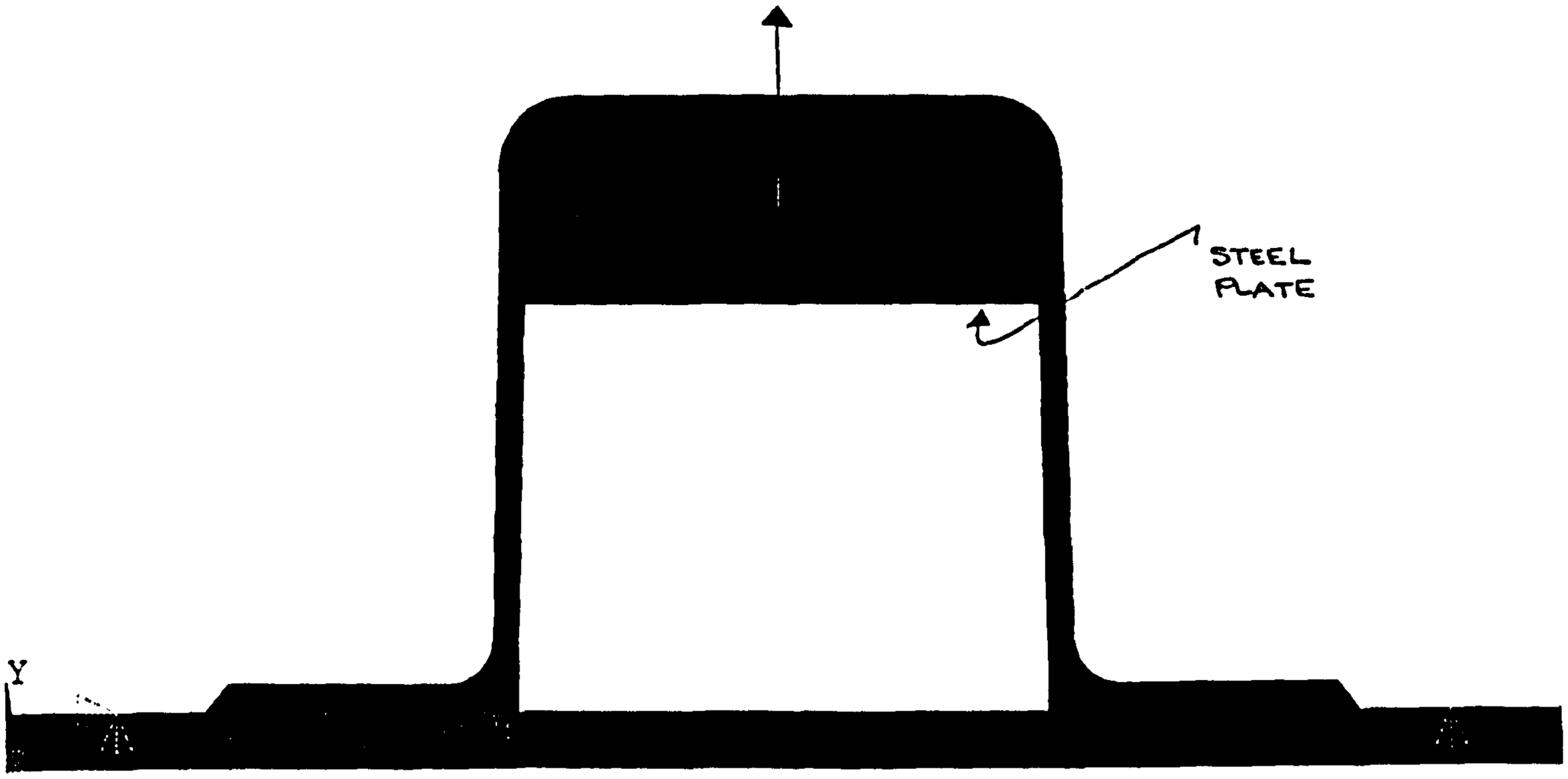

Figure 5.6 Finite Element Model of a Type I Stiffener under a Pull-Off Load which includes the generation of the Steel Plate

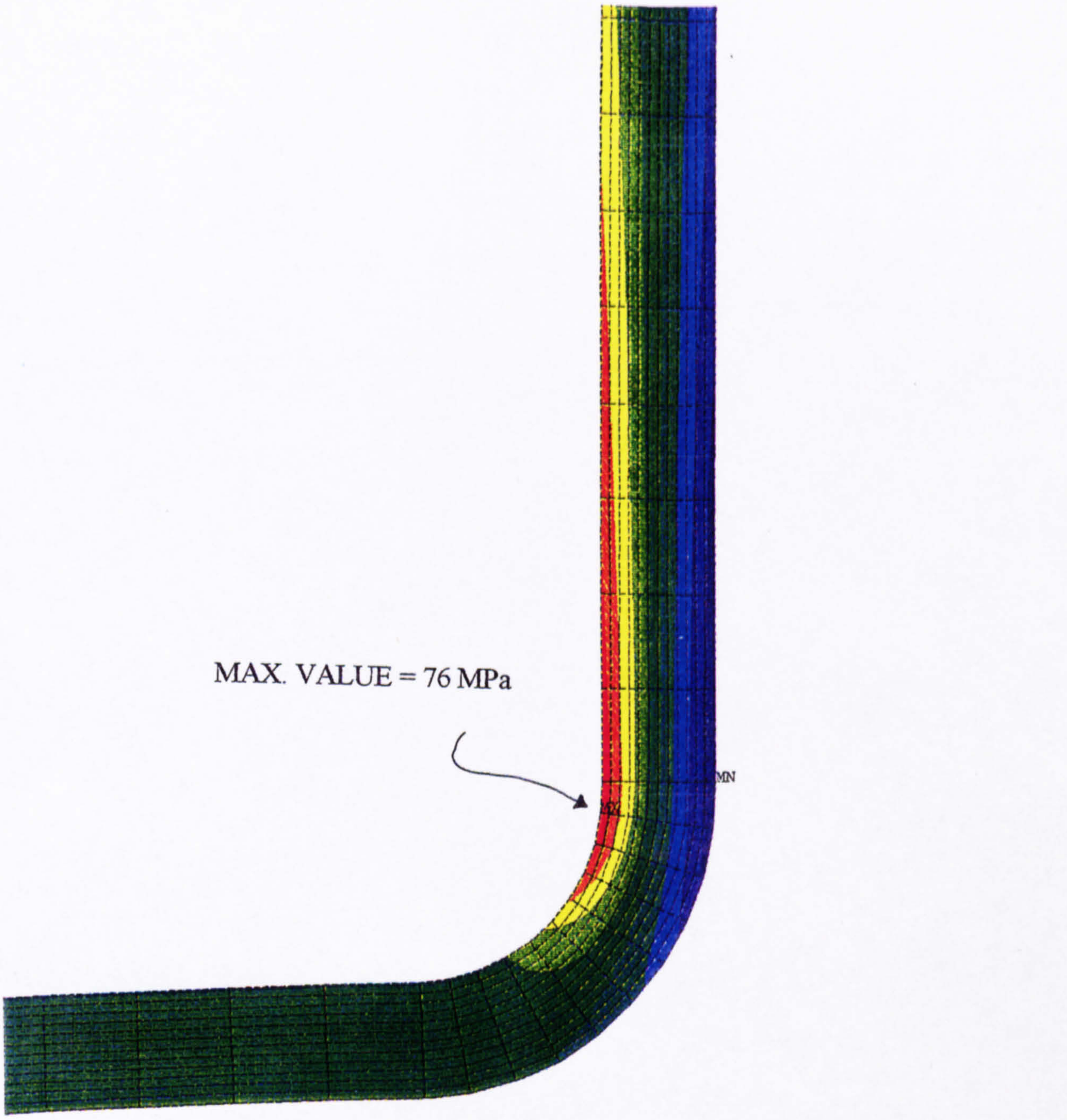

Figure 5.7 Typical Stress Plots for the Type I Stiffener under a Three Point Bending Load of 13.5 kN

(a) Overlaminate Through-Thickness Stress

(b) Flange In-Plane Stress

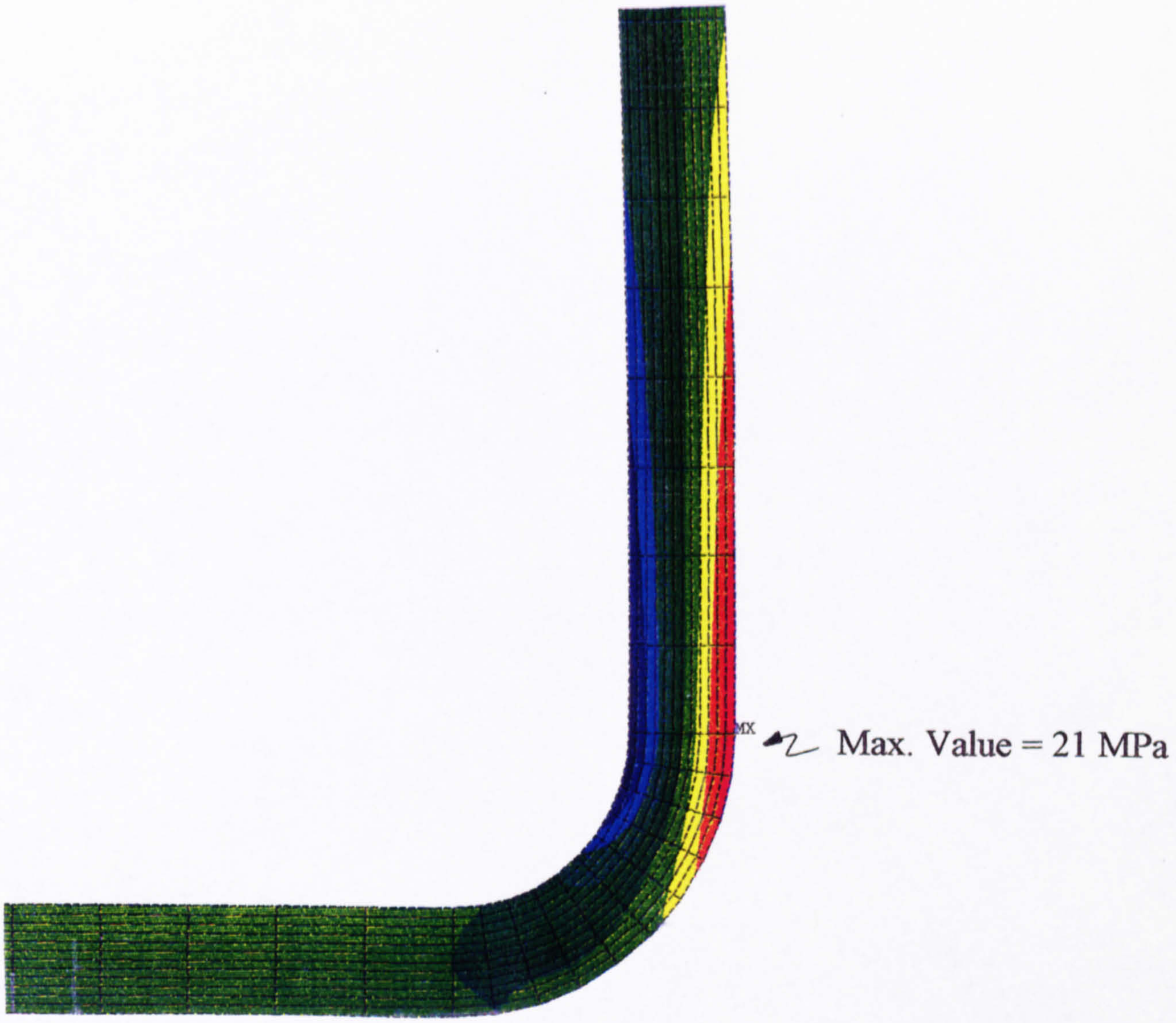

Figure 5.8 Typical Stress Plots for the Type I Stiffener under a Reverse Bending Load of 5 kN

(a) Overlaminate Through-Thickness Stress

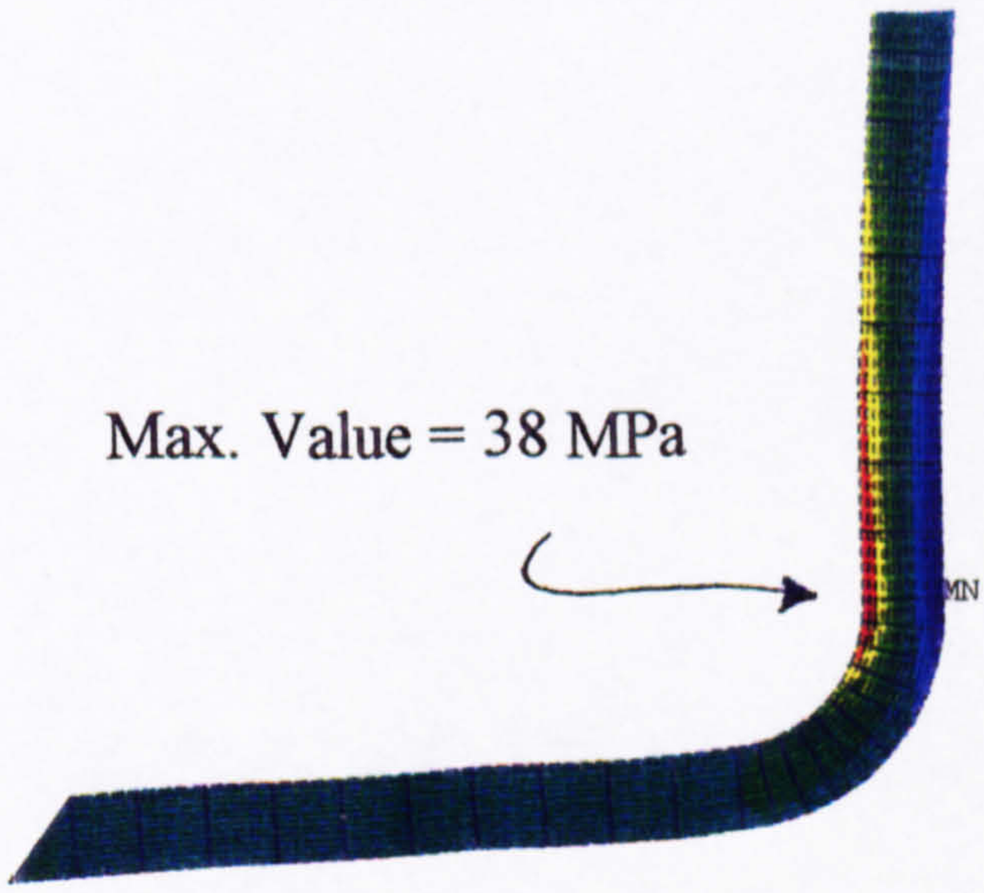

Figure 5.9 Typical Stress Plots for the Type I Stiffener under a Pull-Off Load of 5.5 kN

(a) Overlaminate Through-Thickness Stress

Figure 5.10 Typical Stress Plots for the Type II Stiffener under a Three Point Bending Load of 14.5 kN

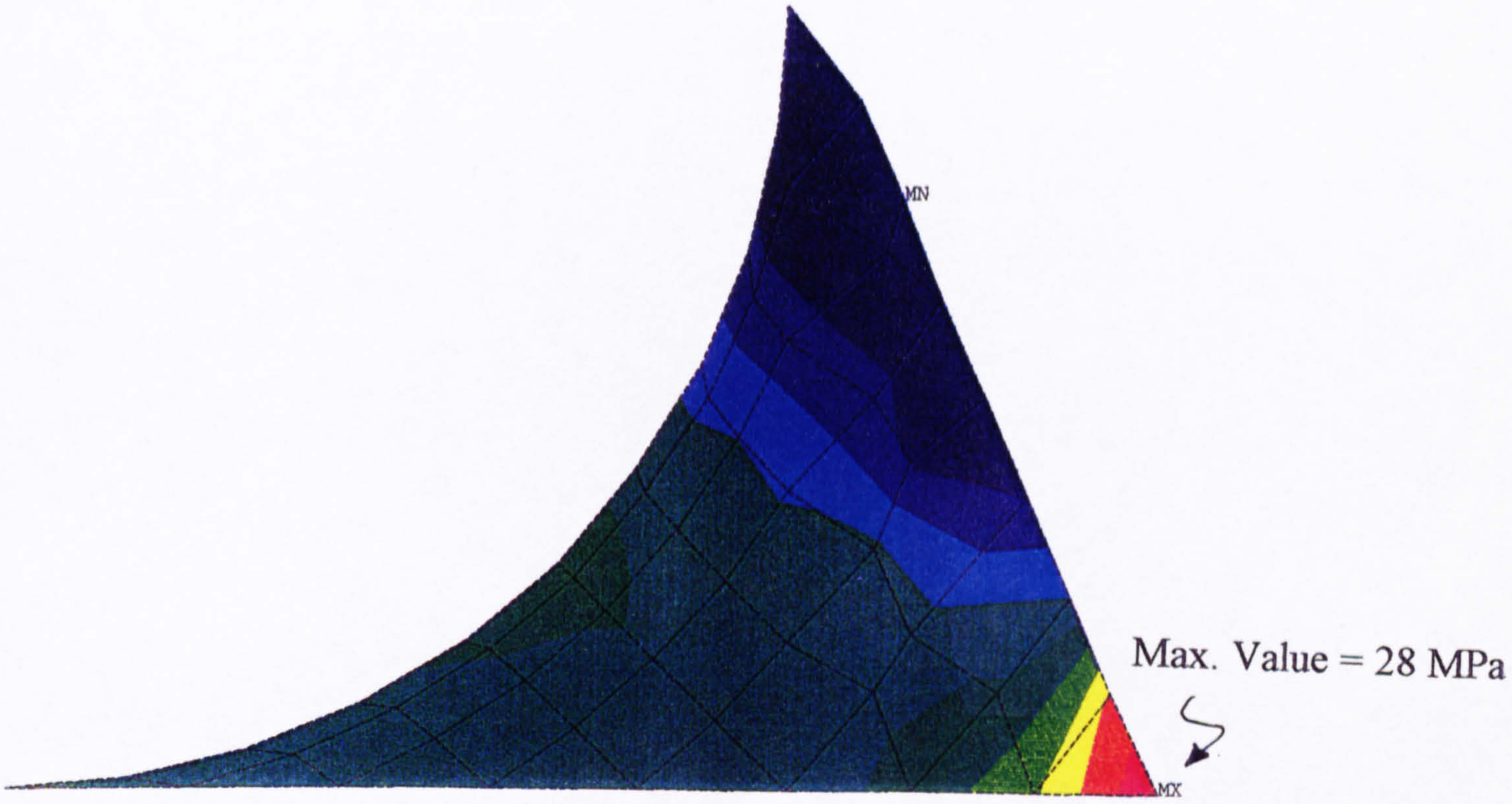

(a) Fillet Principal Stress

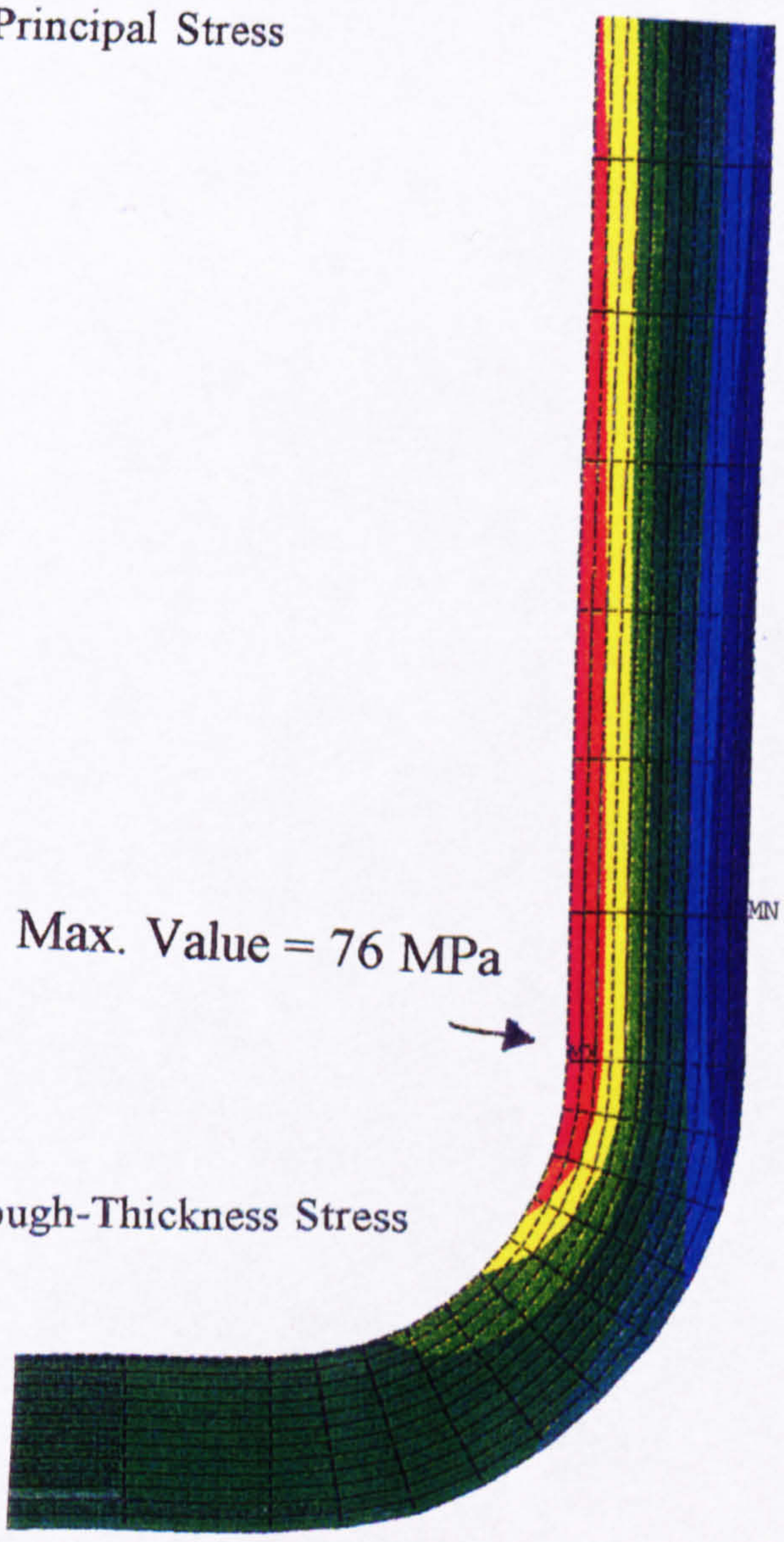

(b) Overlaminate Through-Thickness Stress

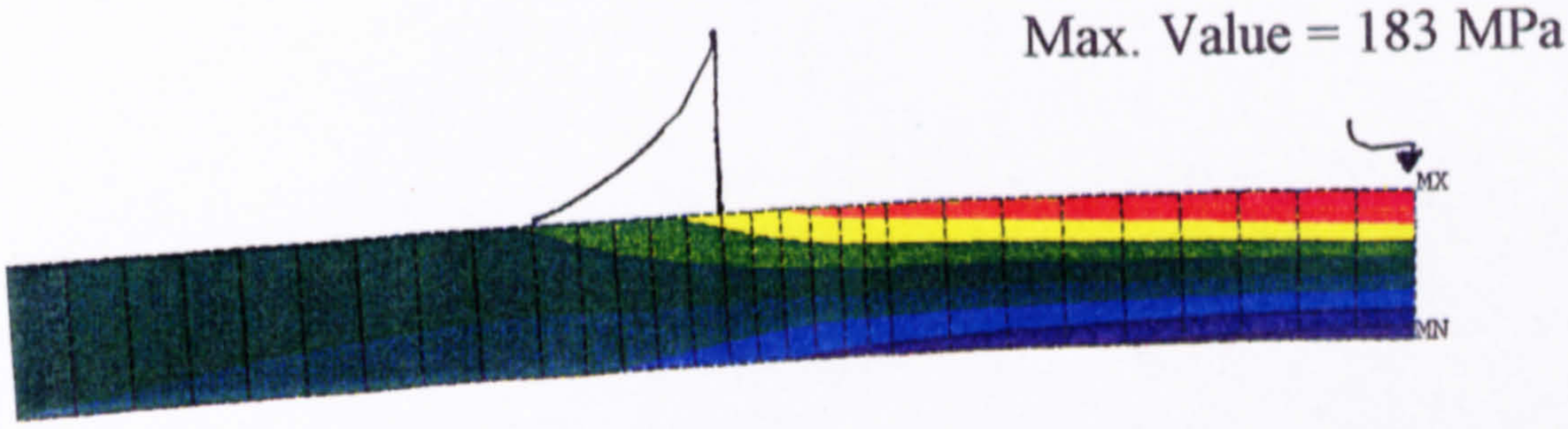

(c) Flange In-Plane Stress

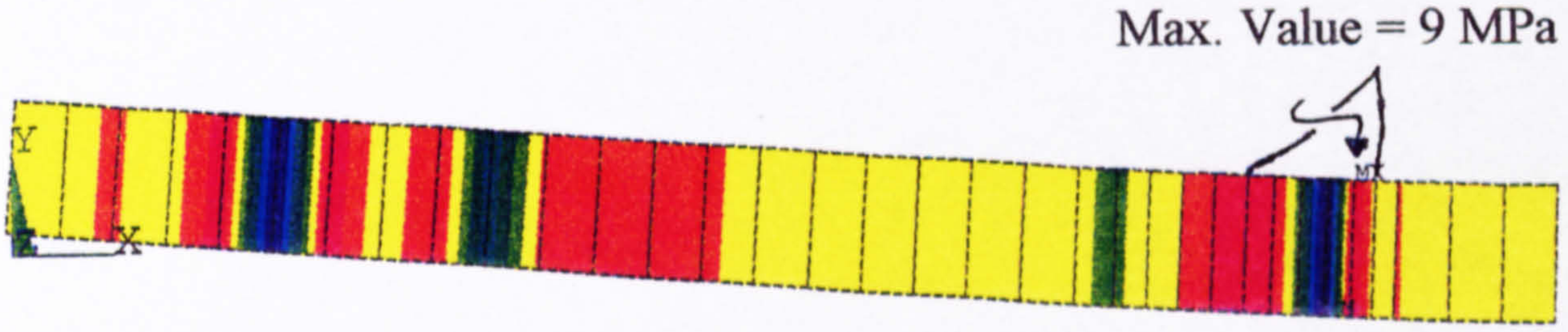

Figure 5.11 Typical Stress Plots for the Type II Stiffener under a Reverse Bending Load of 17 kN

(a) Flange Through-Thickness Stress

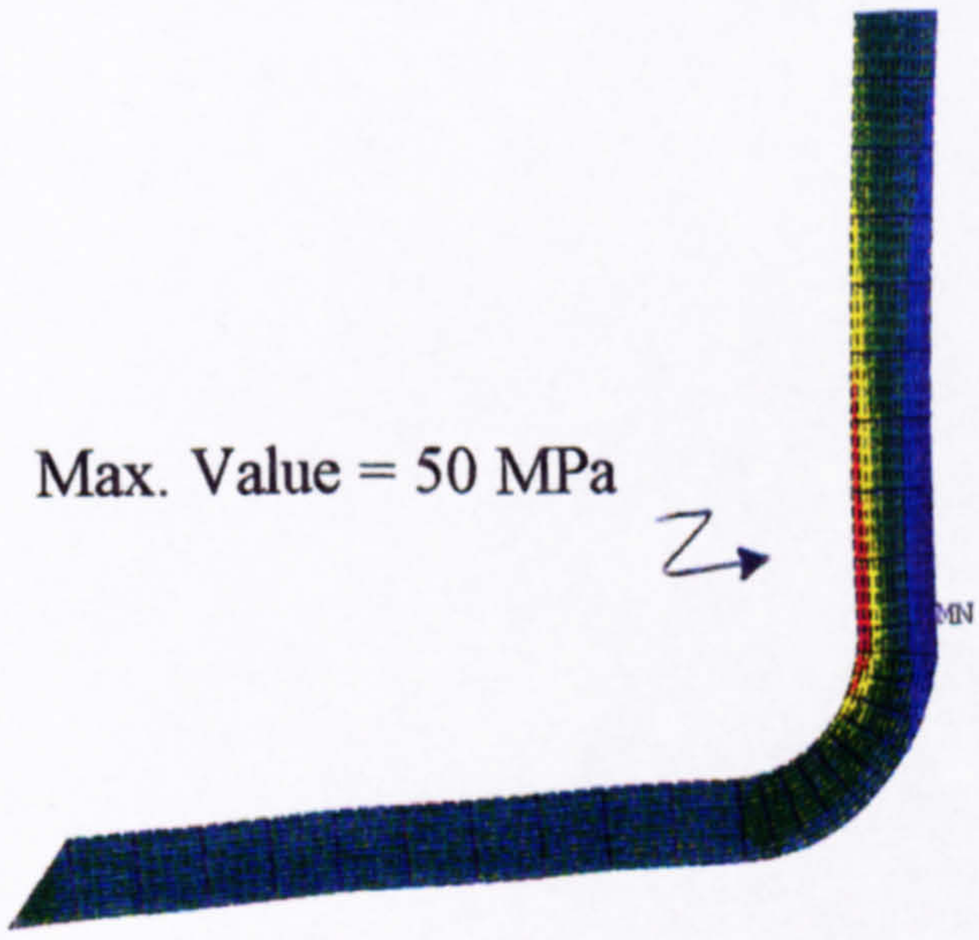

Figure 5.12 Typical Stress Plots for the Type II Stiffener under a Pull-Off Load of 15 kN

(a) Overlaminate Through-Thickness Stress

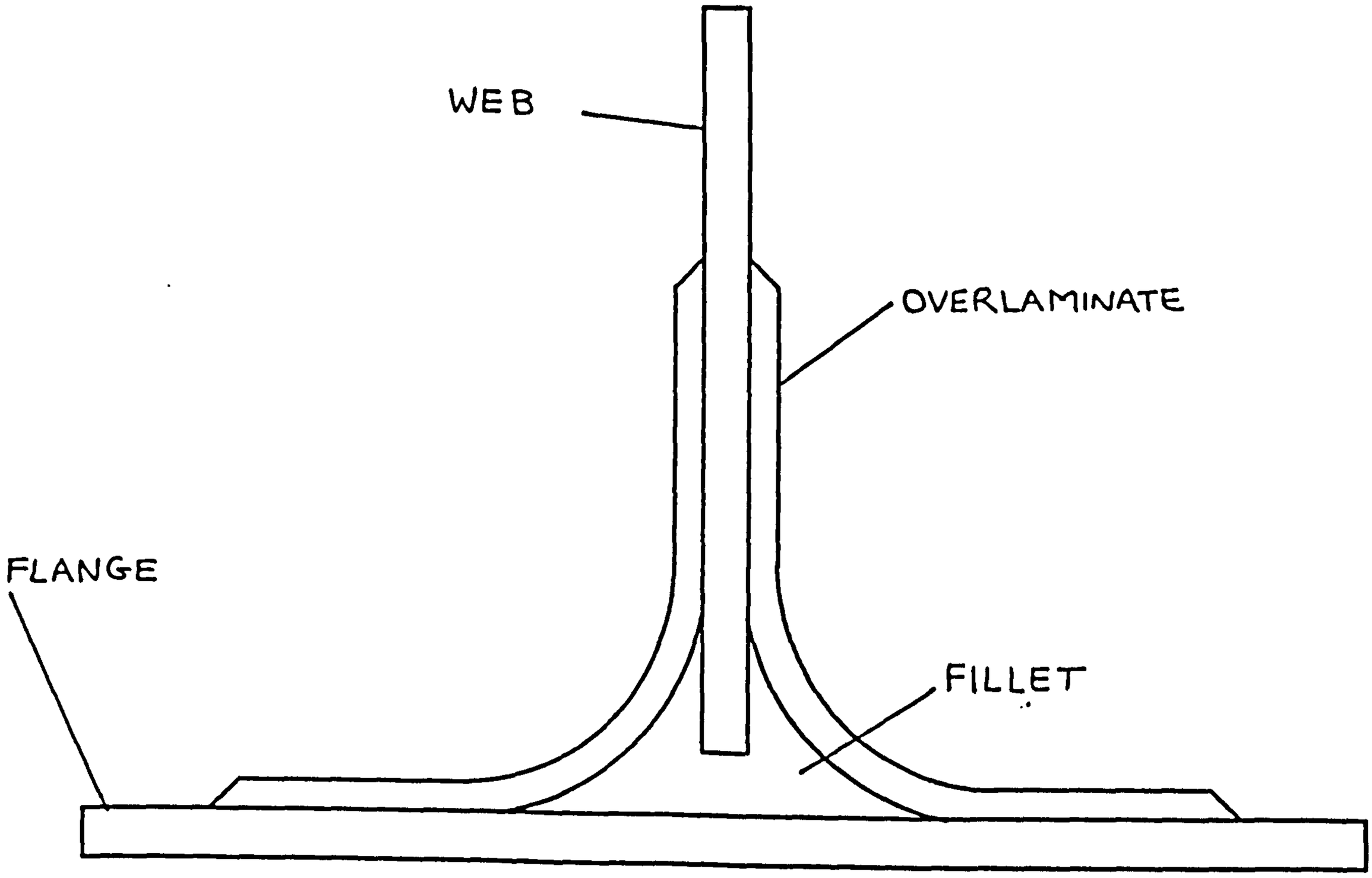

Figure 6.1 Typical Tee Joint Configuration

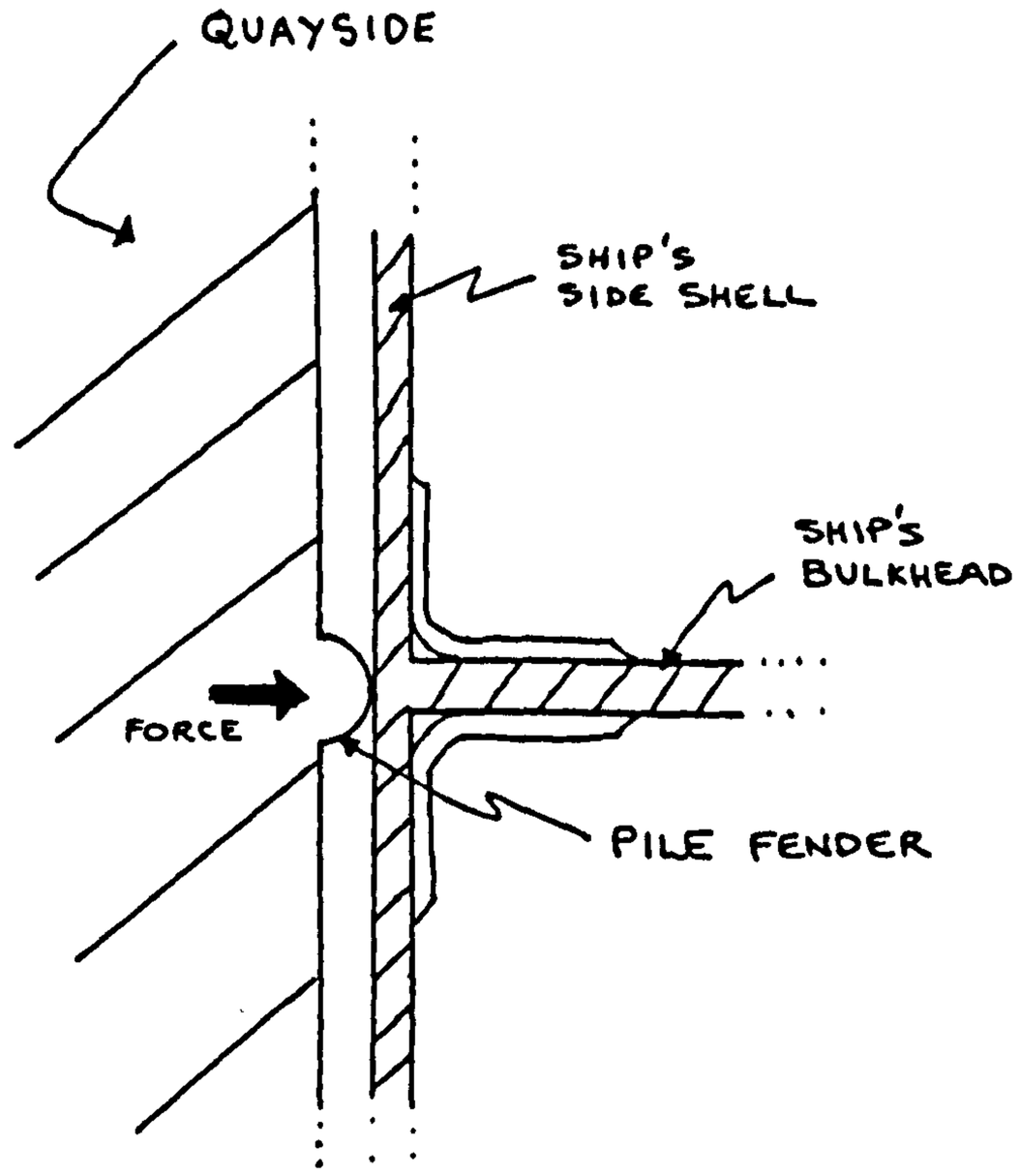

Figure 6.2 Representation of Docking Loads to show the Relevance of a Three Point Bending Load on a Tee Joint

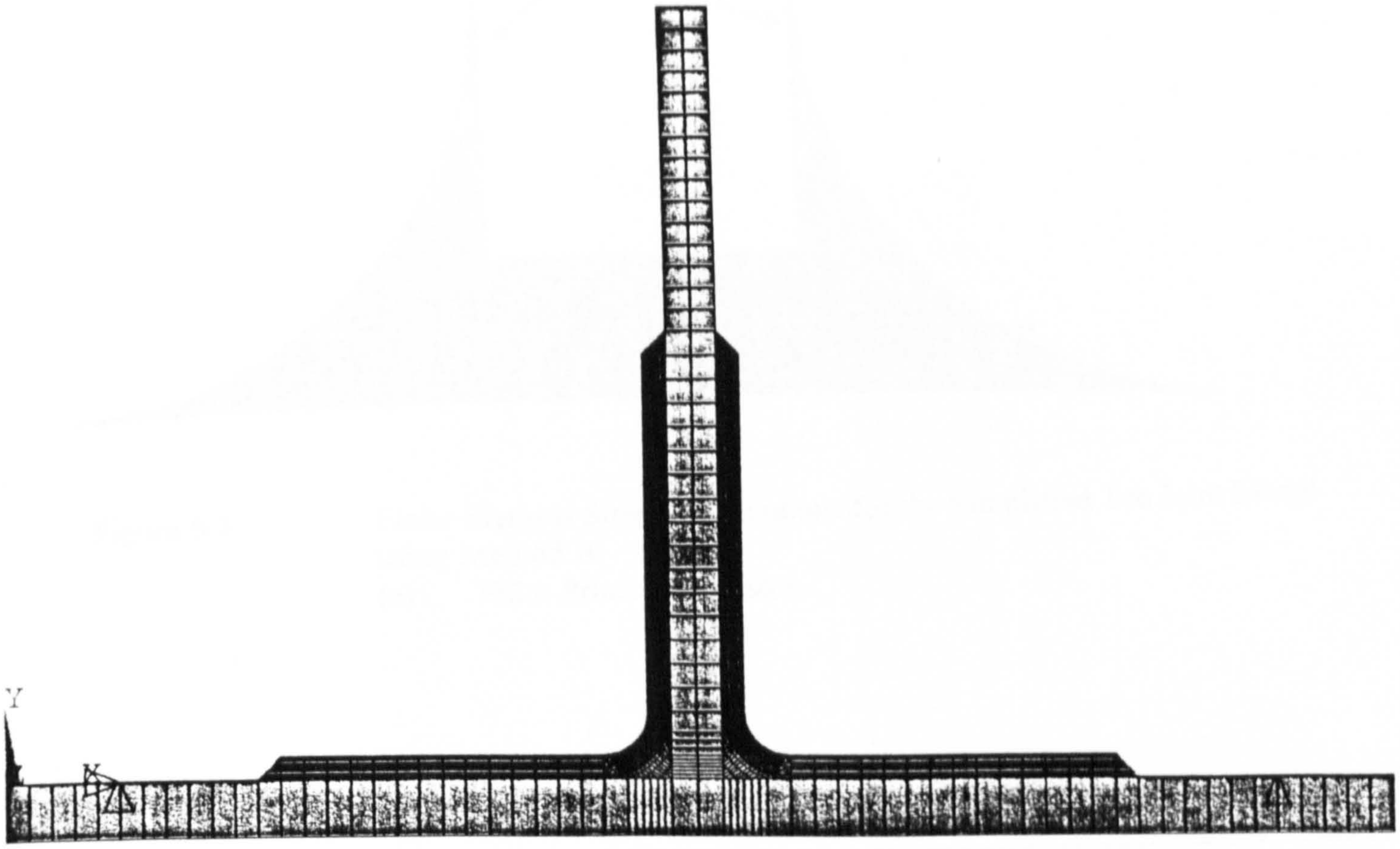

Figure 6.3 Two dimensional Finite Element Model

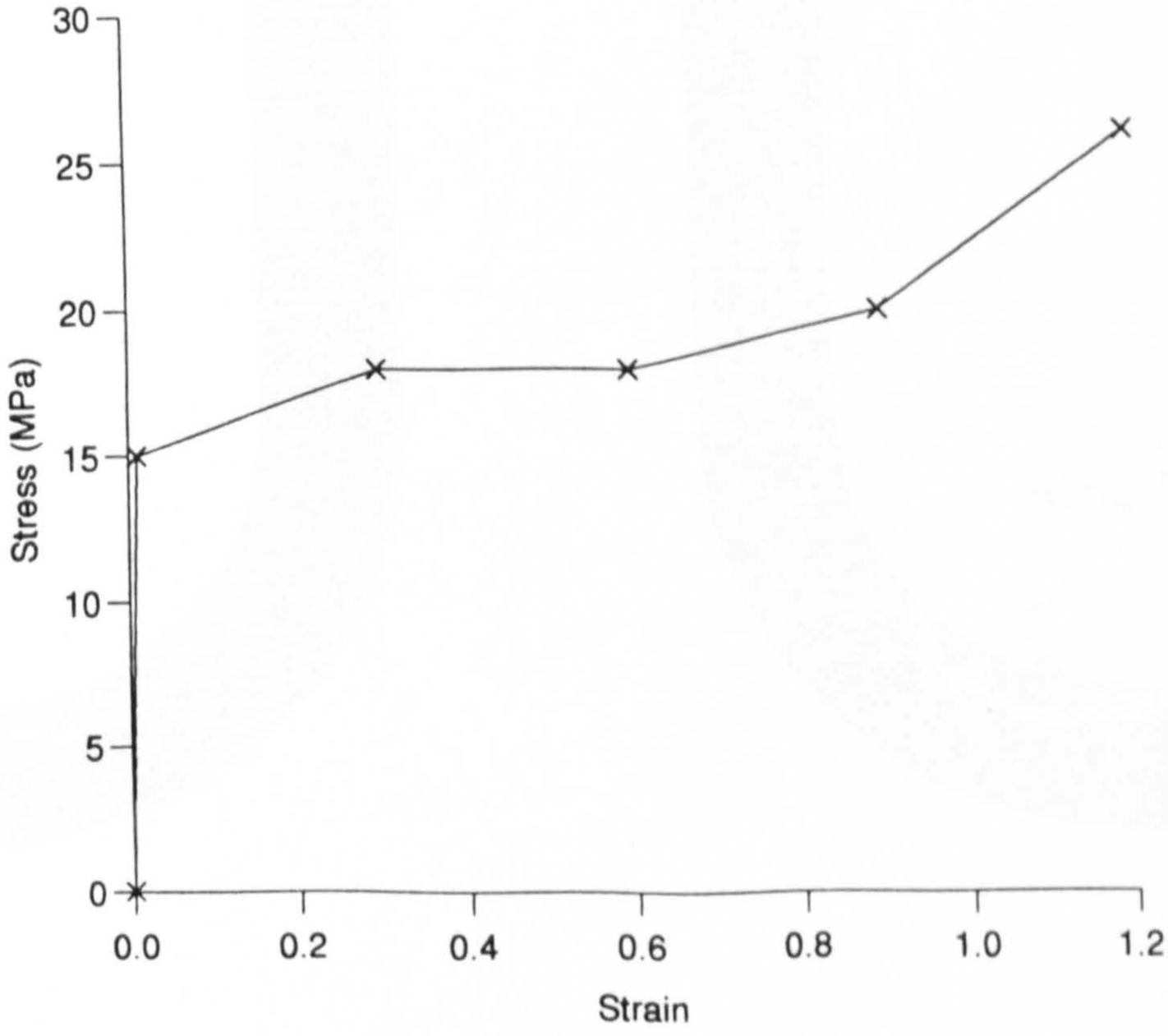

Figure 6.4 Fillet Non-Linear Stress/Strain Curve

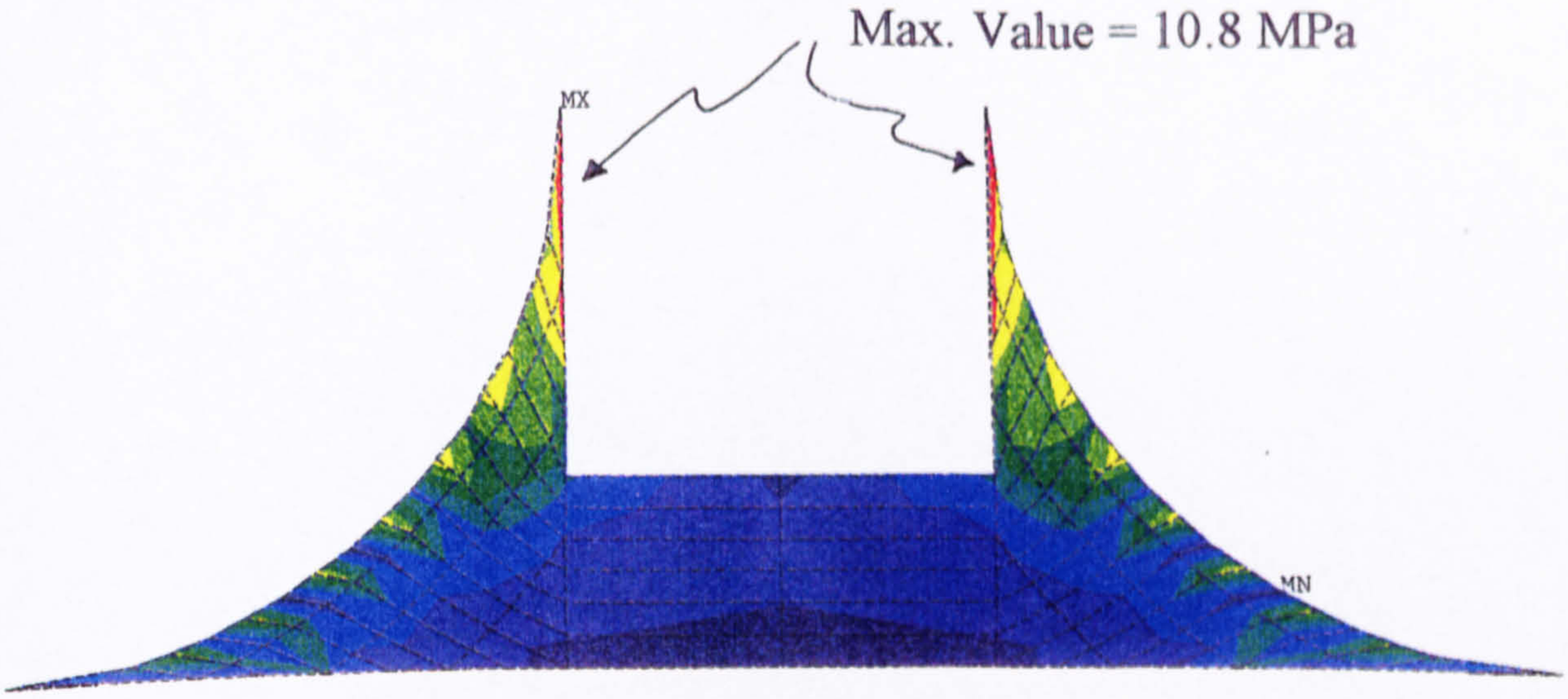

Figure 6.5 Finite Element Stress Distributions for the Simplified Tee Joint Model using Method A:
(a) Fillet Principal Stresses

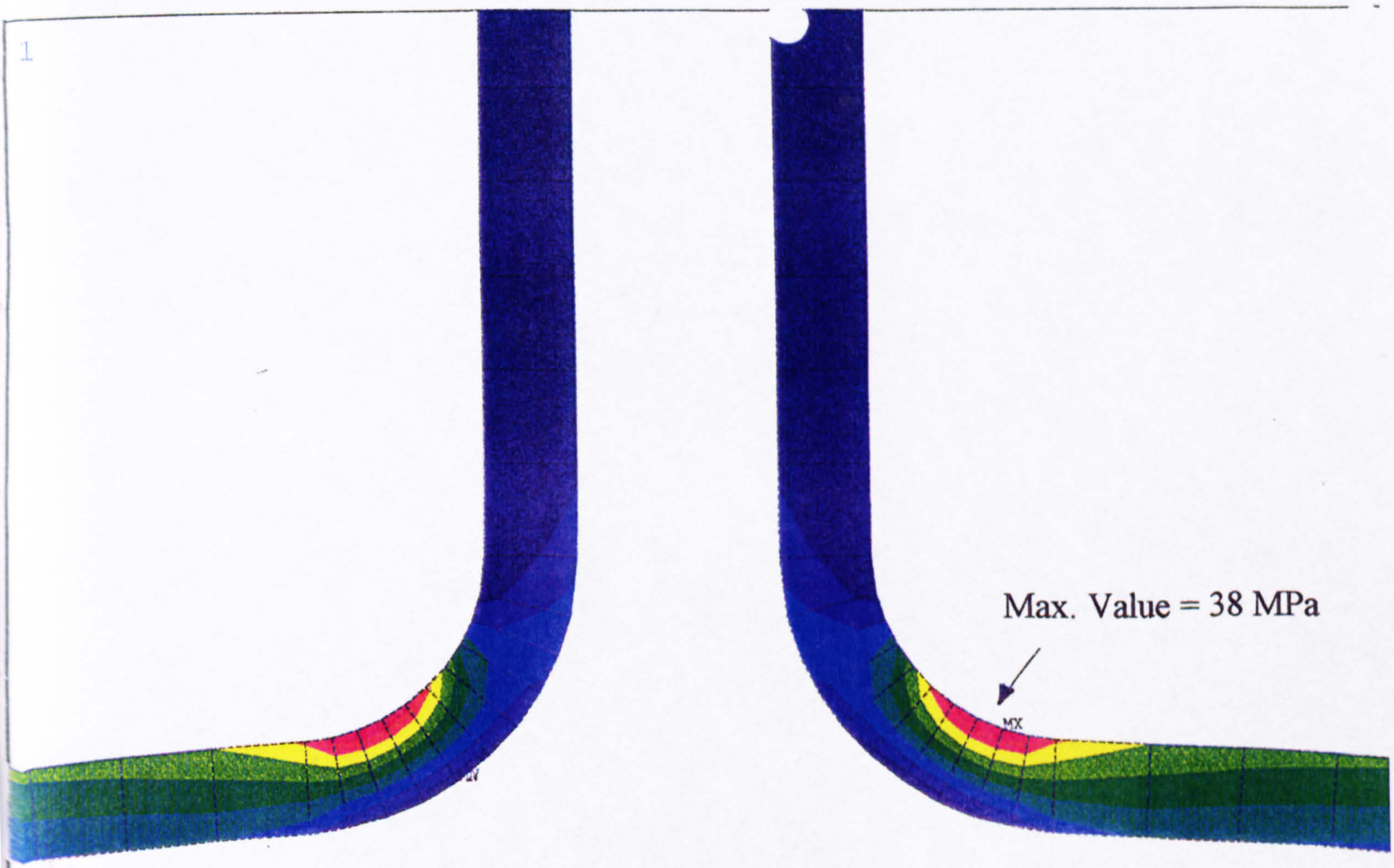

(b) Overlaminate In-Plane Stresses

(c) Overlaminate Through-Thickness Stresses

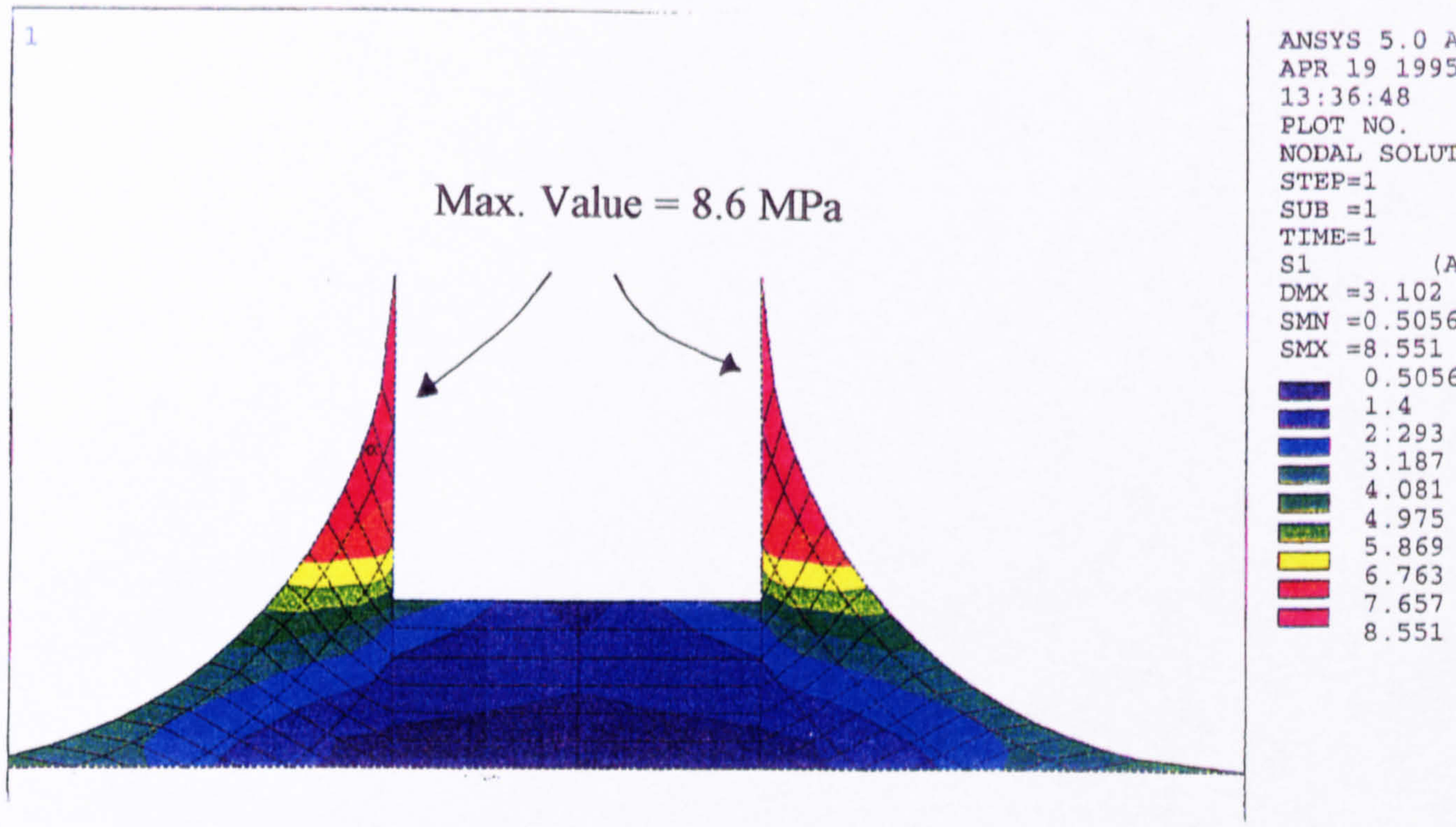

Figure 6.6 Finite Element Stress Distributions for Model 1, the Undamaged Model:

(a) Fillet Principal Stresses

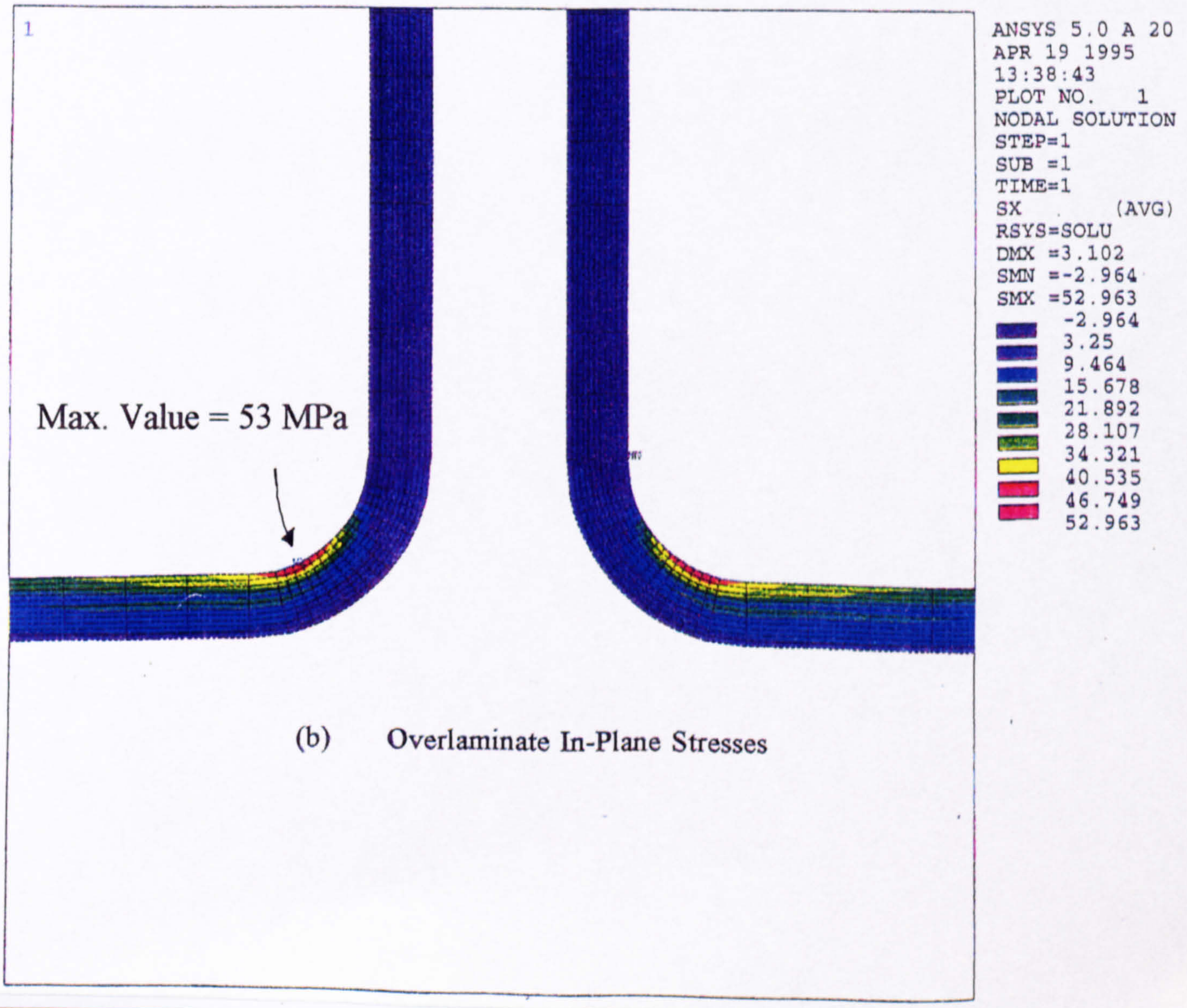

(b) Overlaminate In-Plane Stresses

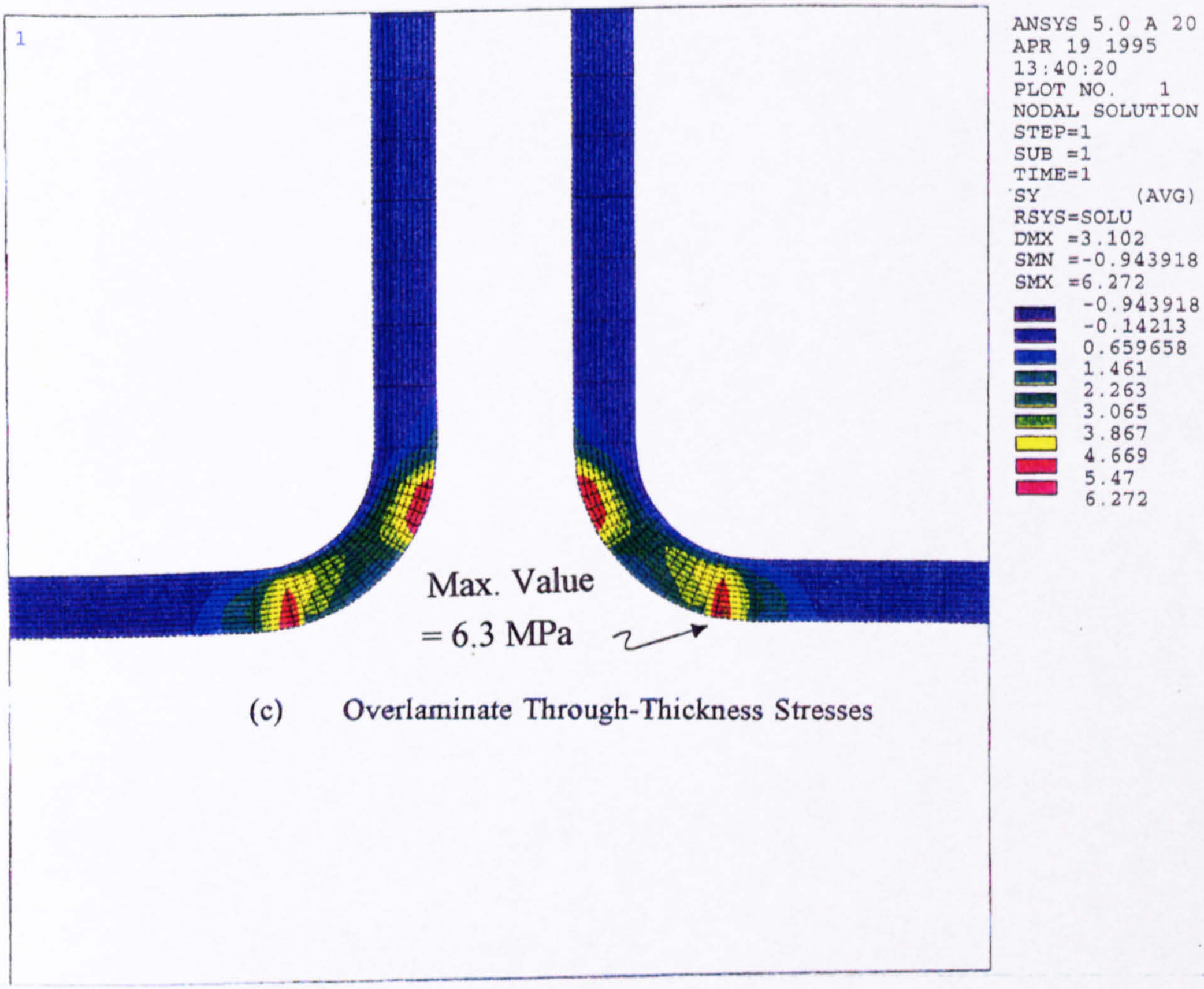

(c) Overlaminate Through-Thickness Stresses

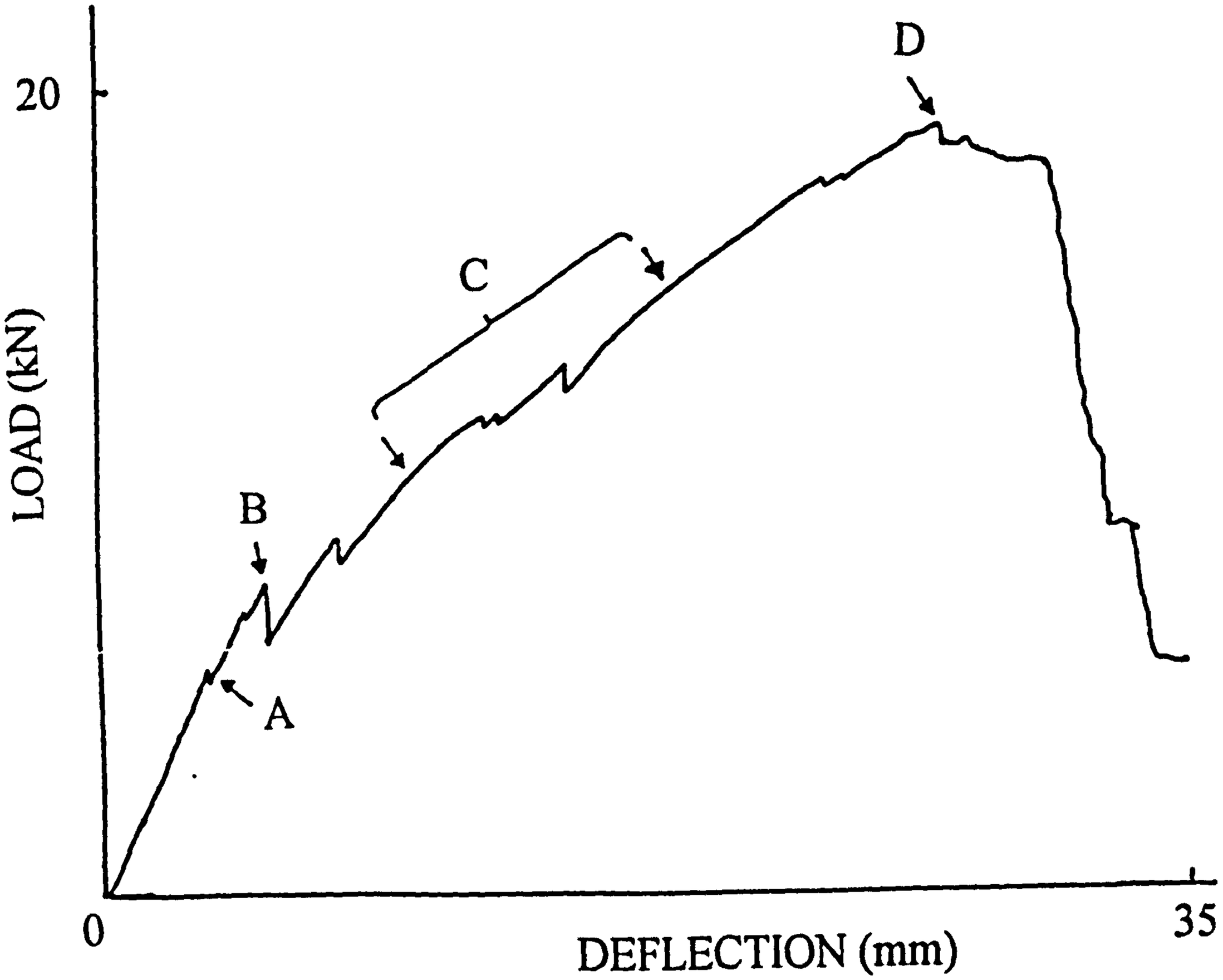

Figure 6.7 Experimental Load/Deflection Curve for a Tee Joint under a Three Point Bending Load

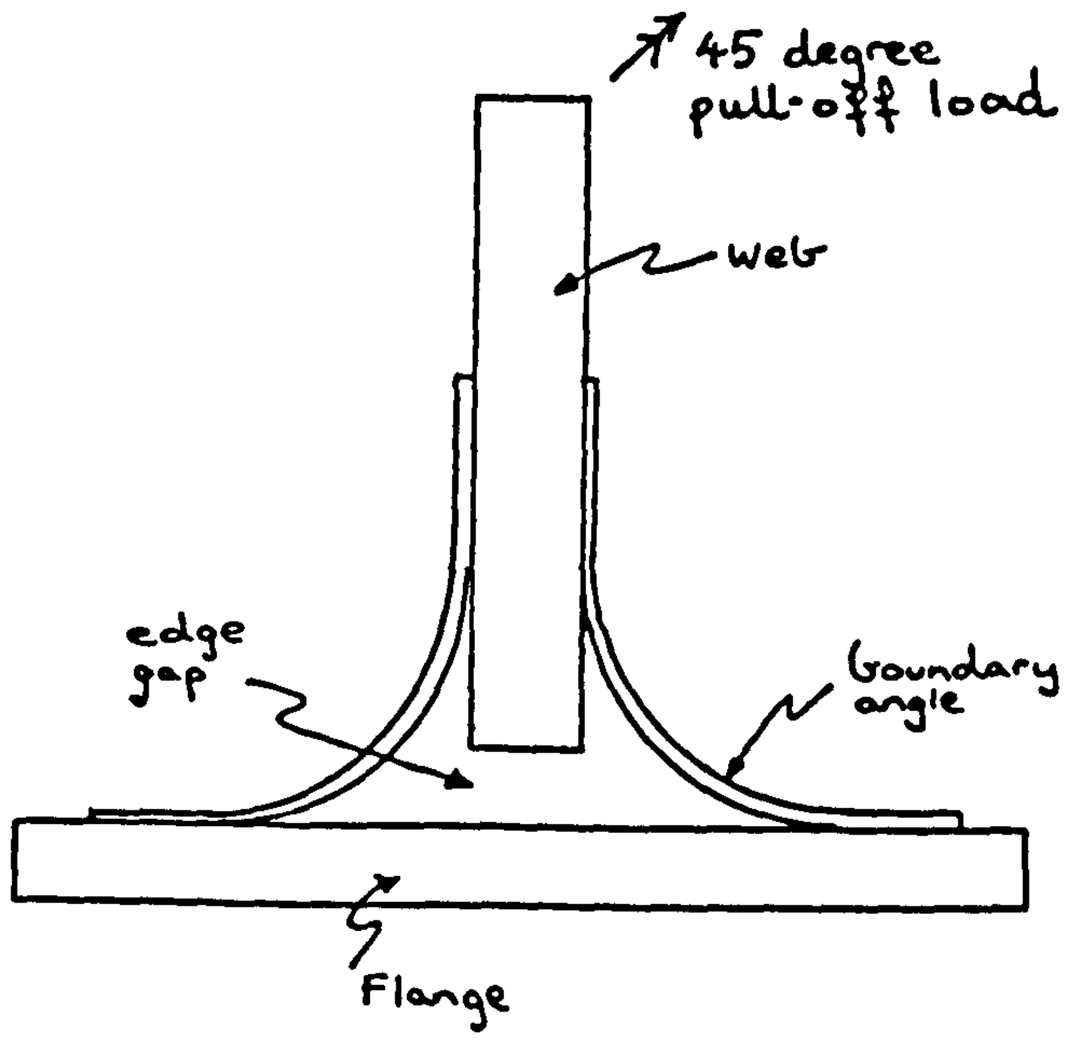

Figure 6.8 Tee Joint under a 45 Degree Pull-Off Load

X : DATA POINT FROM F.E. MODEL

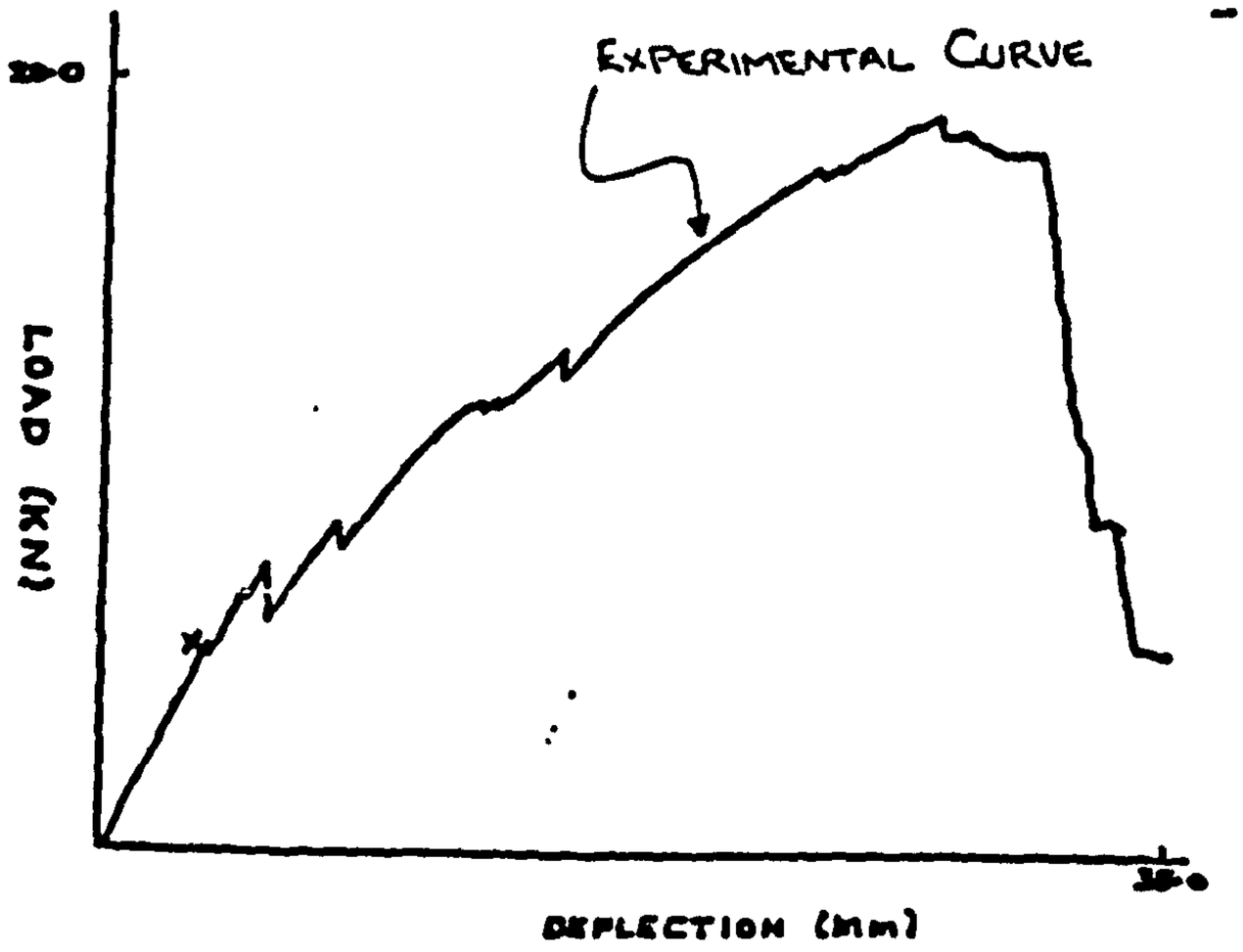

(a) Model 1.

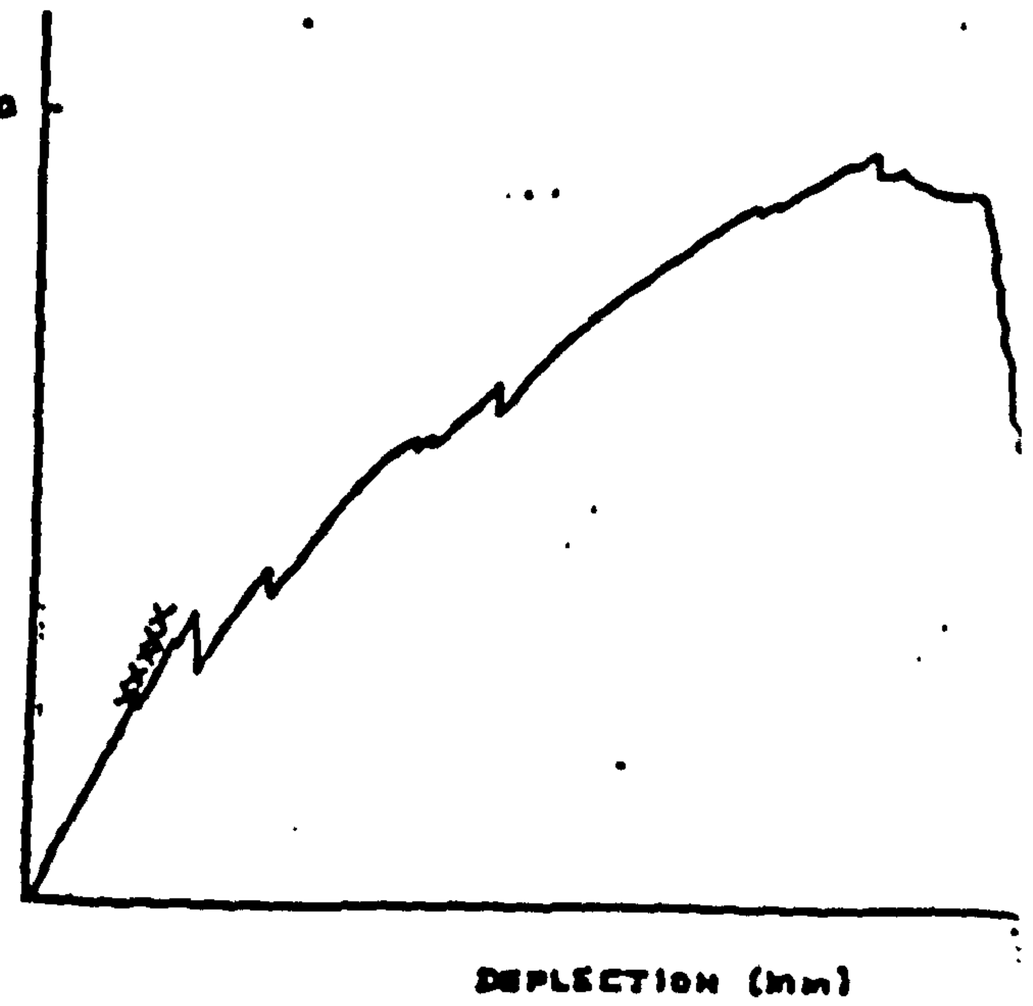

(b) Model 2.

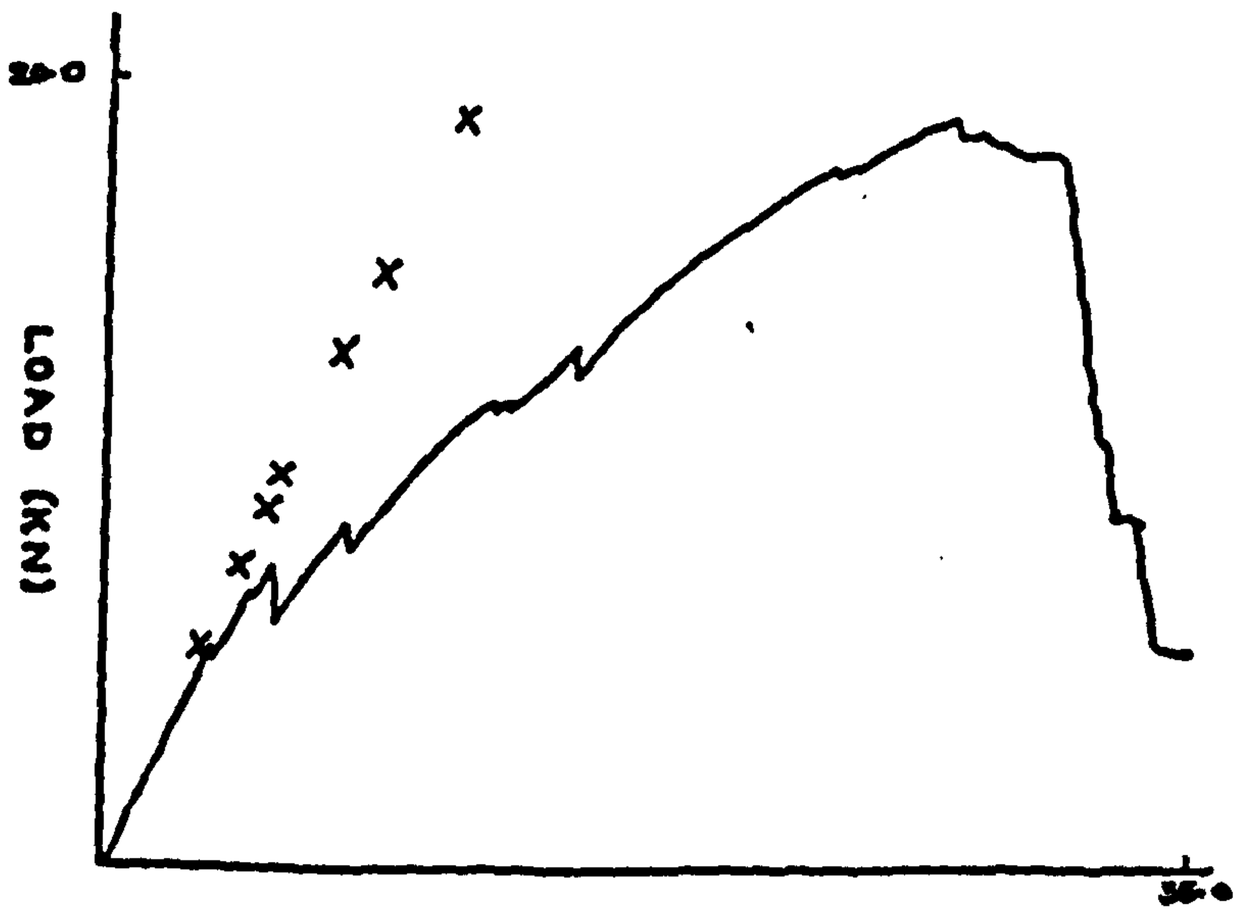

(c) Model 3.

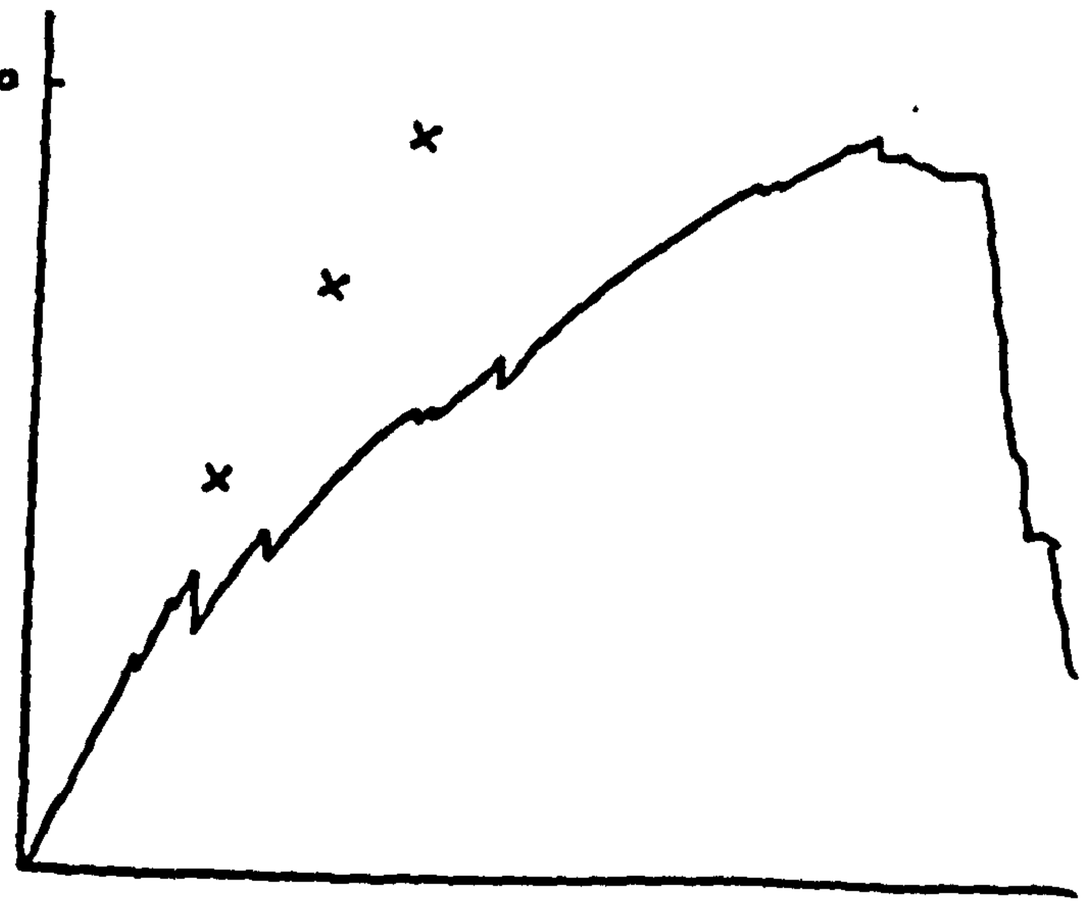

(d) Model 4.

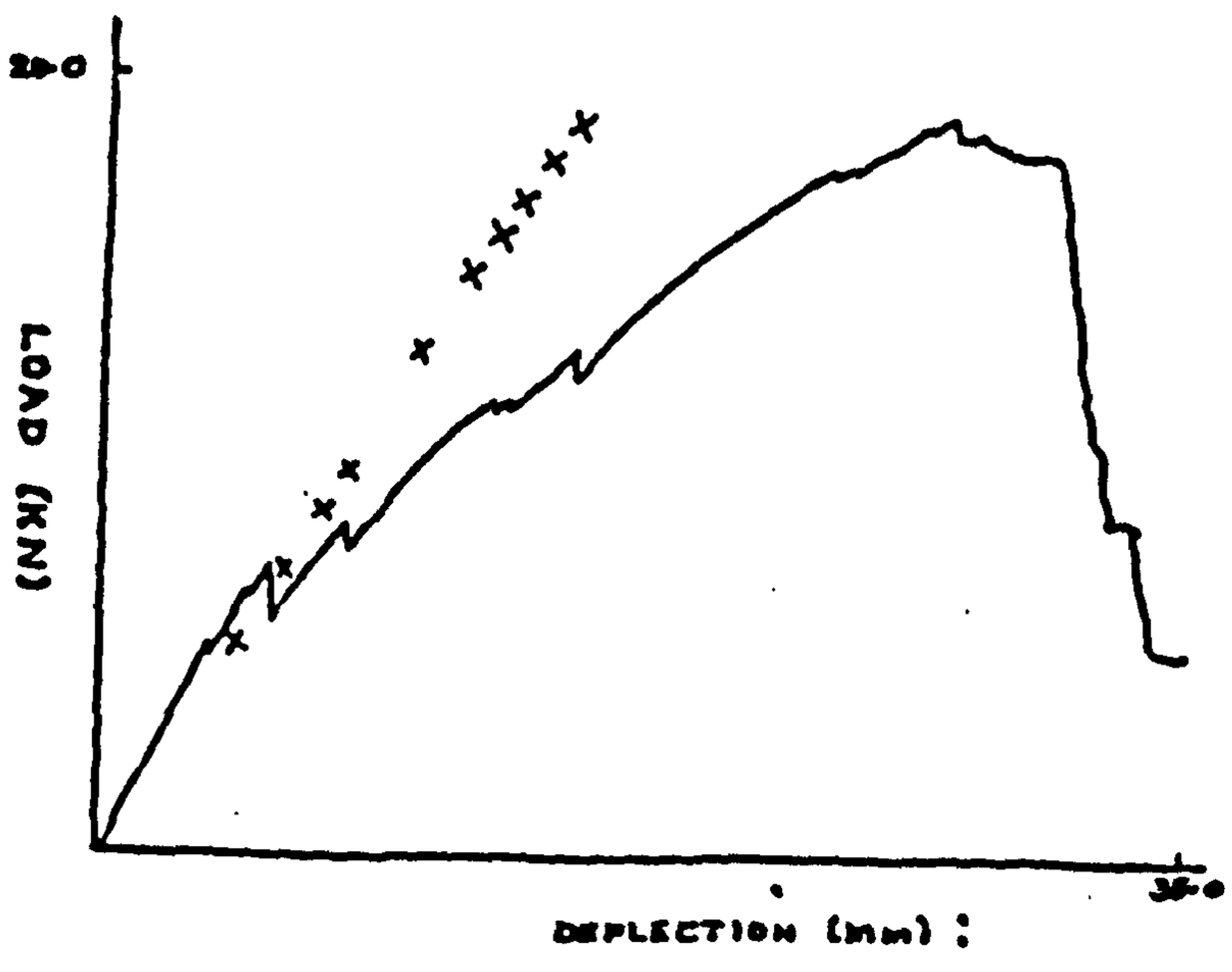

(e) Model 5.

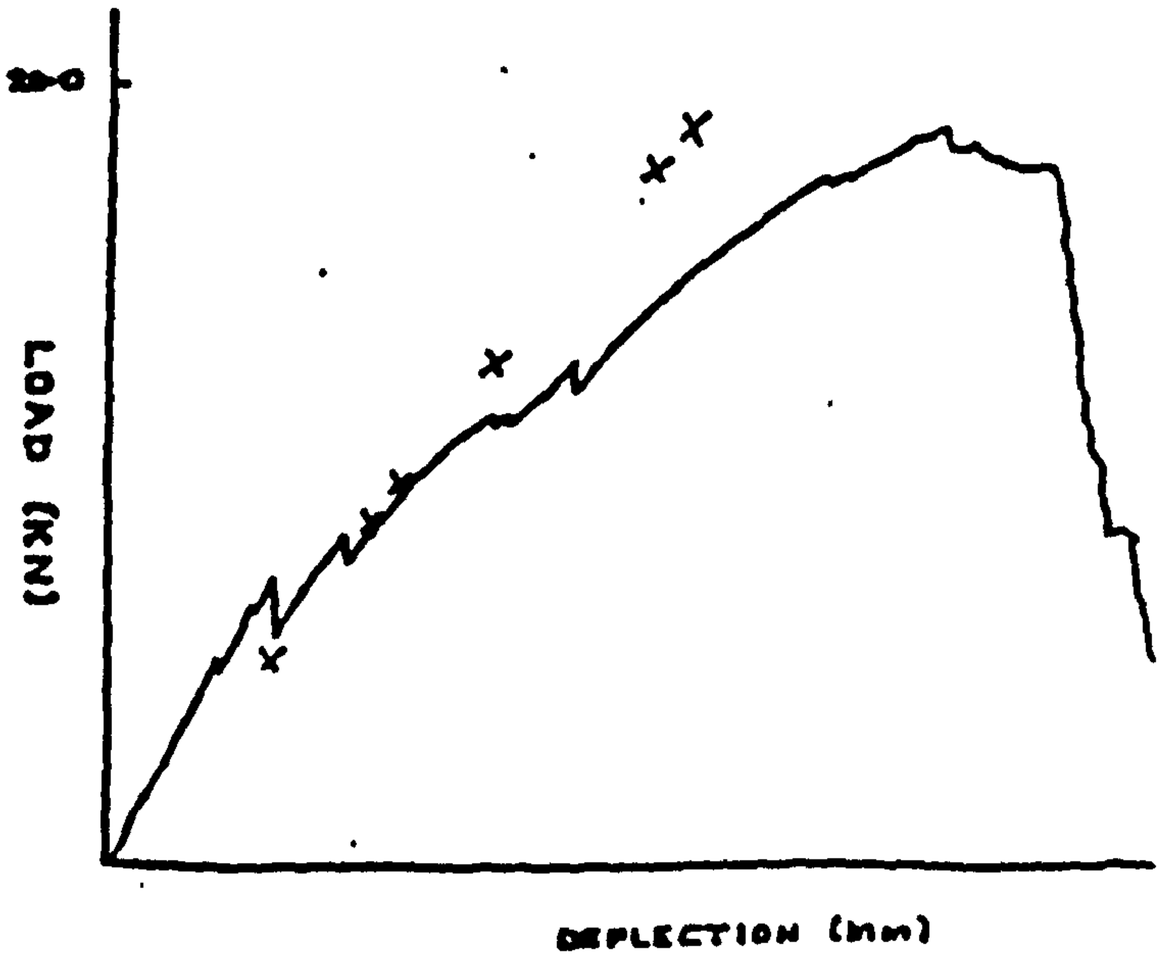

(f) Model 6.

Figure 6.9 Finite Element Load/Deflection Curves:

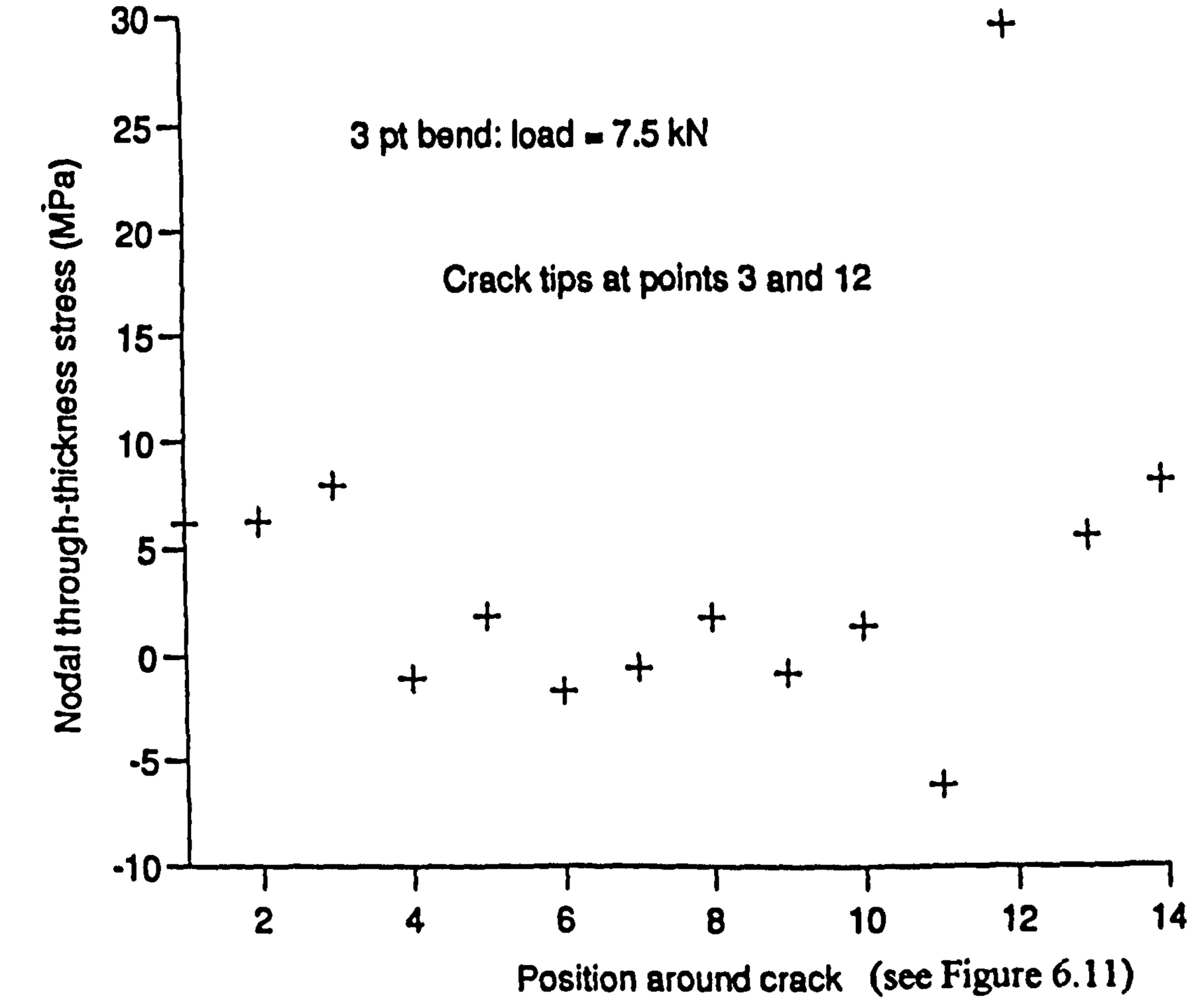

Figure 6.10 Nodal Average Stress Distribution around the radius of the Overlaminate

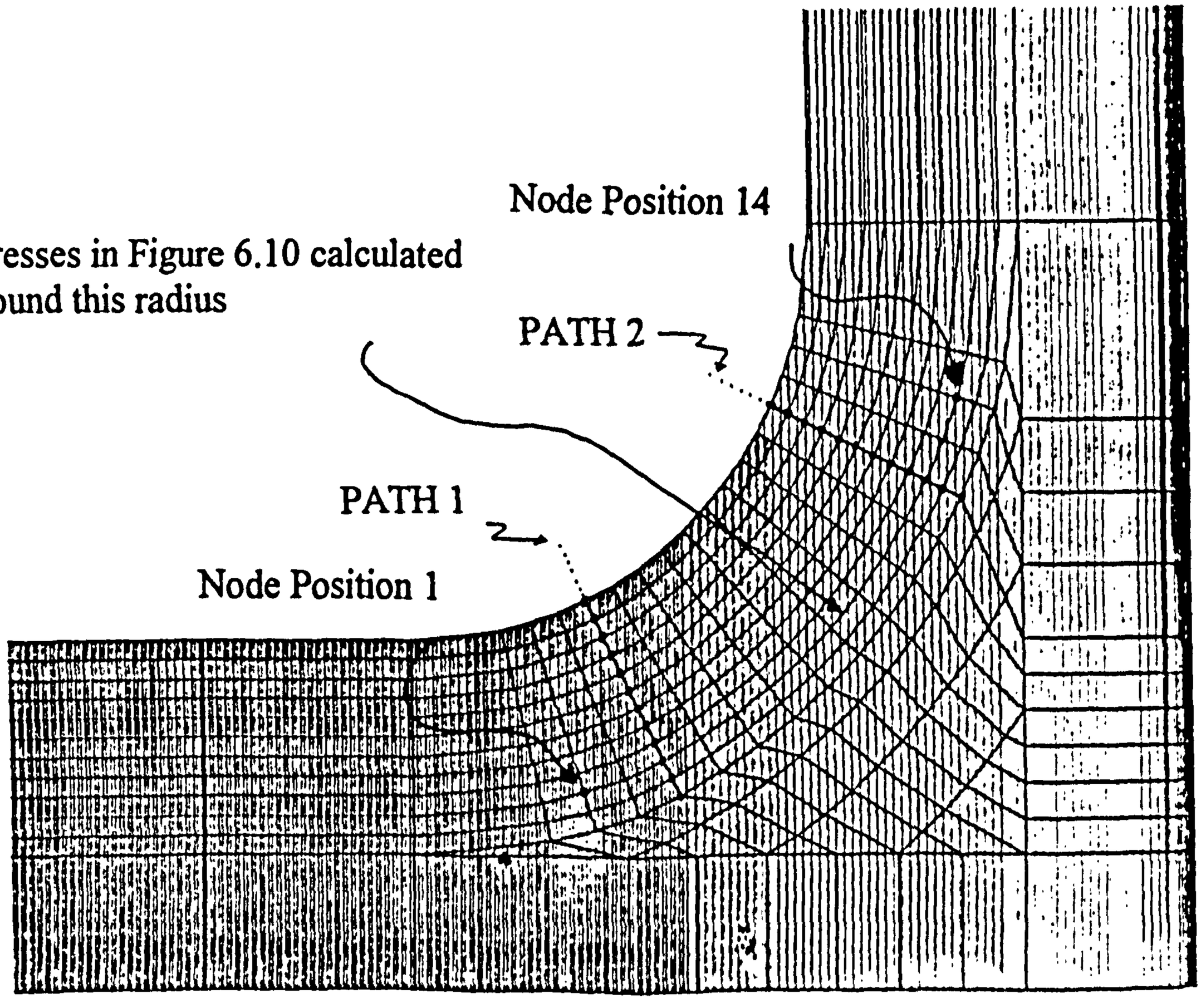

Figure 6.11 Paths through thickness of Overlaminate along which the in-plane and through-thickness stresses are calculated

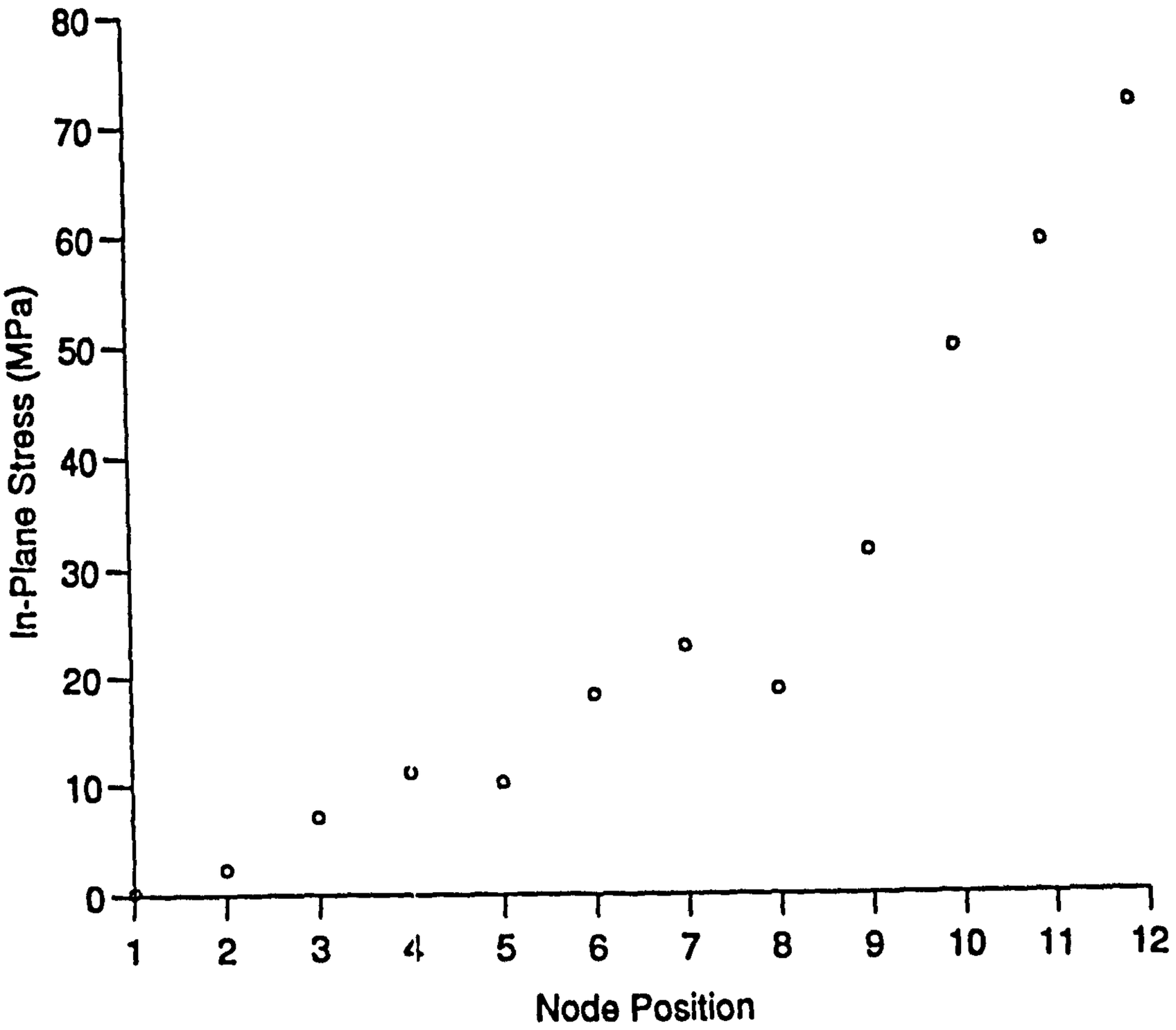

Figure 6.12(a) In-Plane Stress Distribution along Path 1 for Model 1

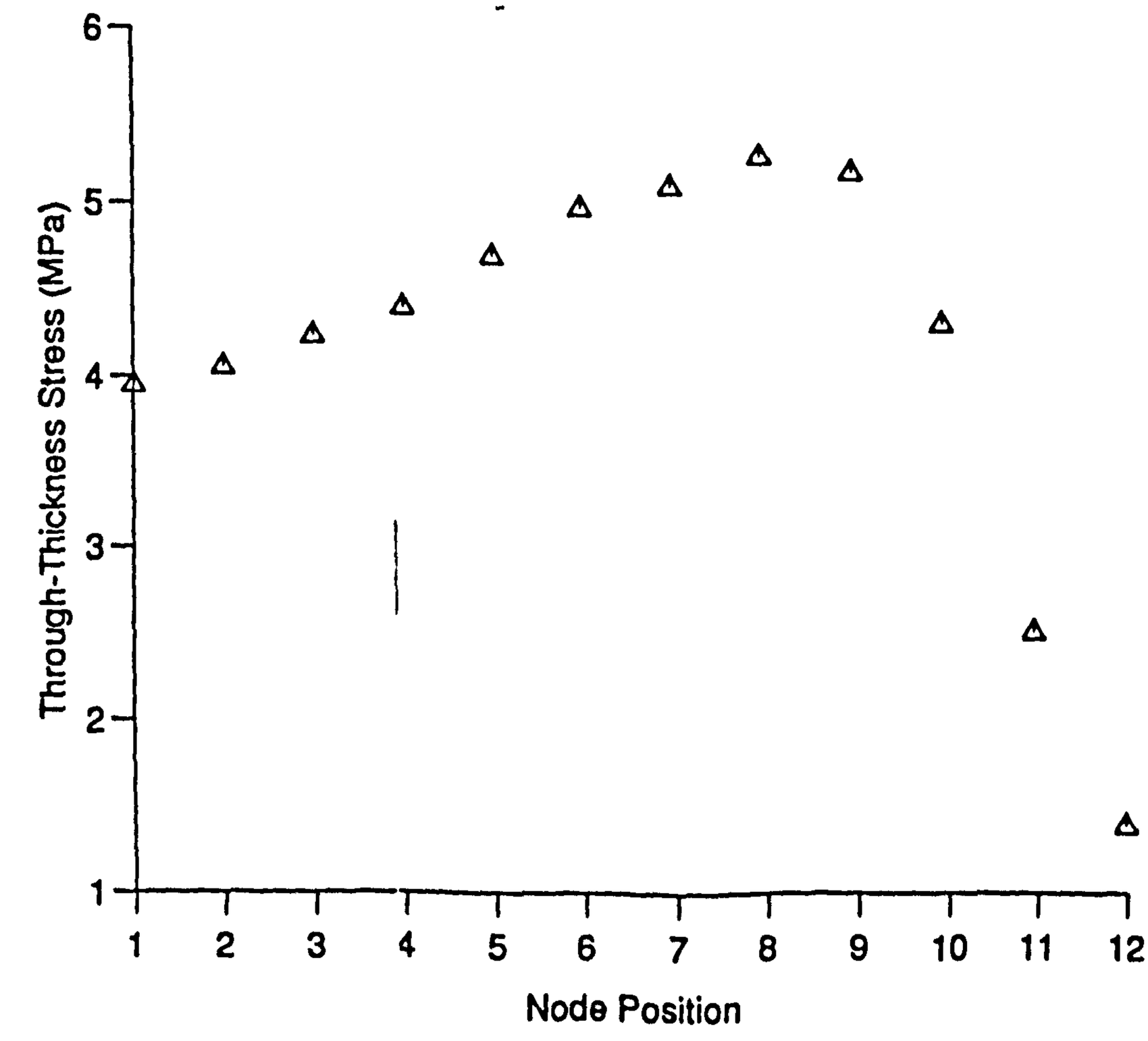

Figure 6.12(b) Through-Thickness Stress Distribution along Path 1 for Model 1

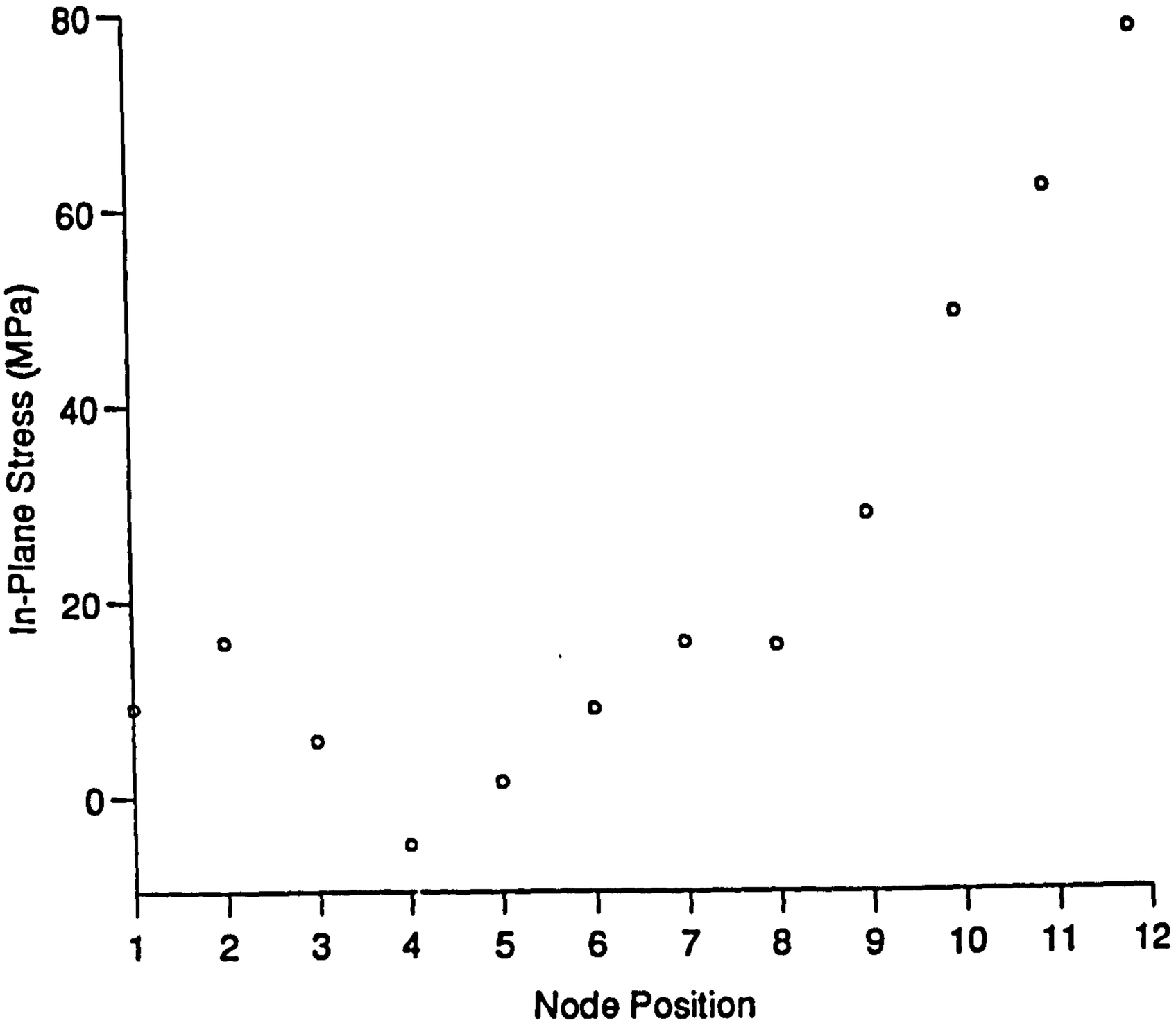

Figure 6.13(a) In-Plane Stress Distribution along Path 1 for Model 3

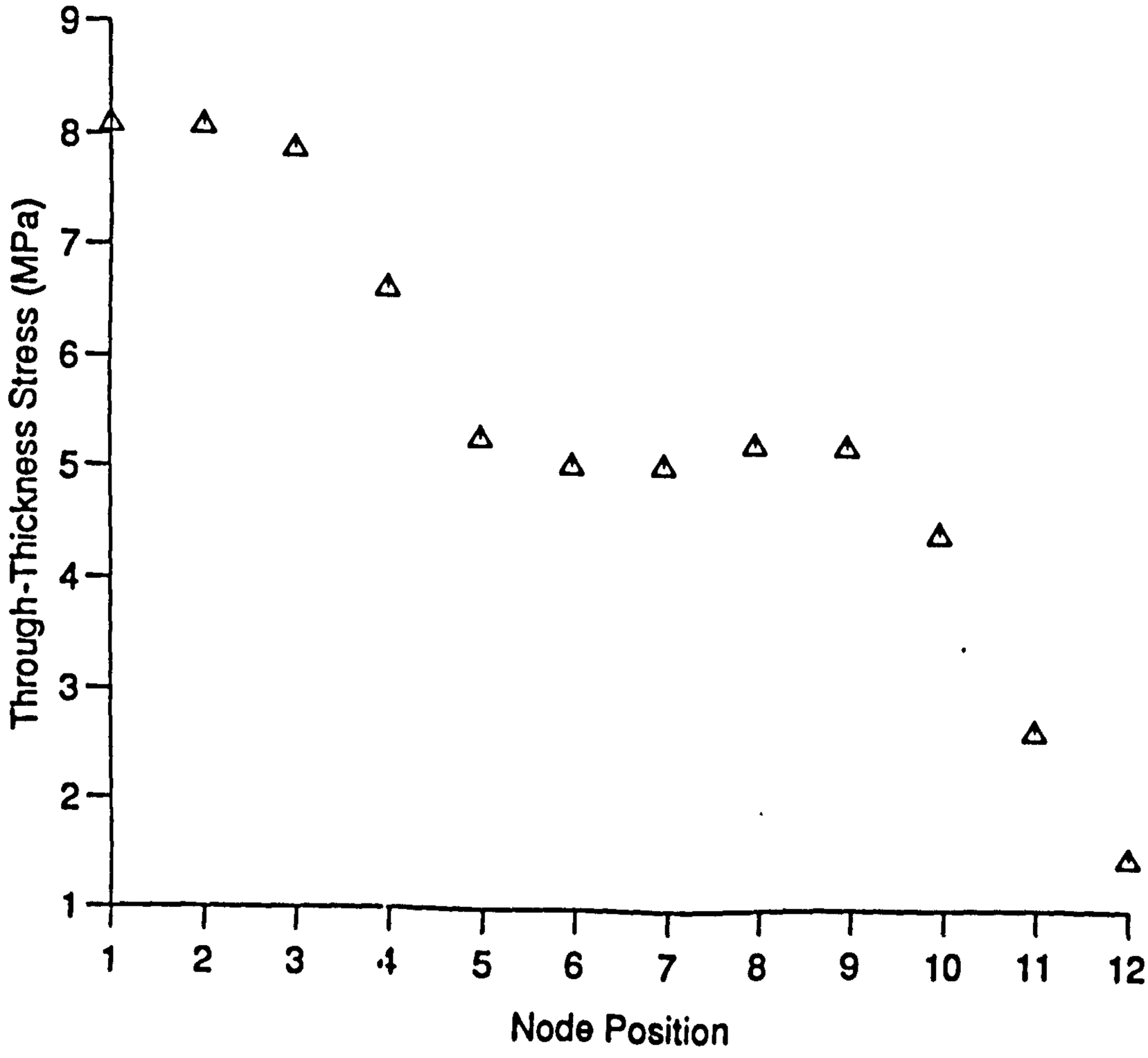

Figure 6.13(b) Through-Thickness Stress Distribution along Path 1 for Model 3

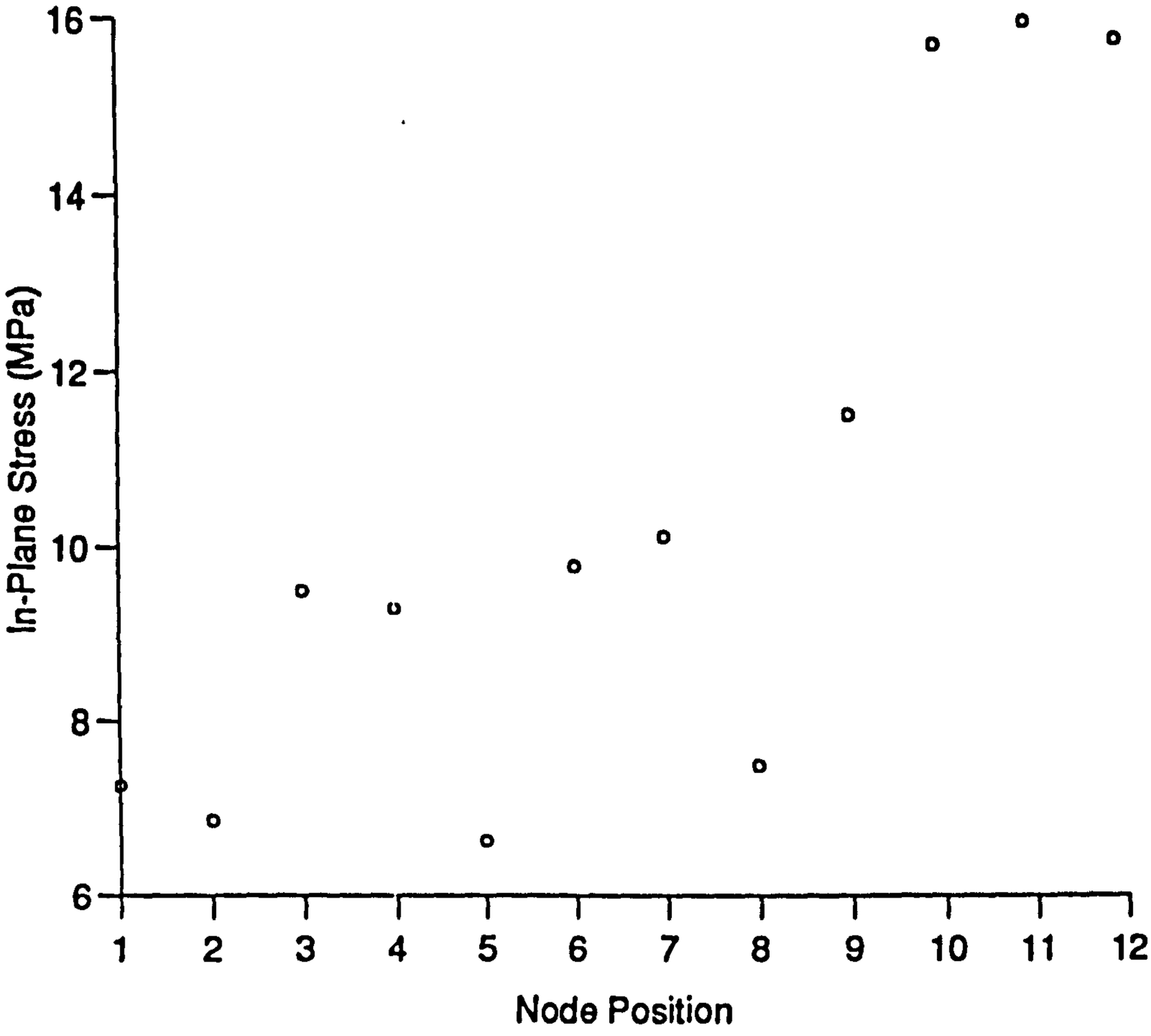

Figure 6.14(a) In-Plane Stress Distribution along Path 2 for Model 1

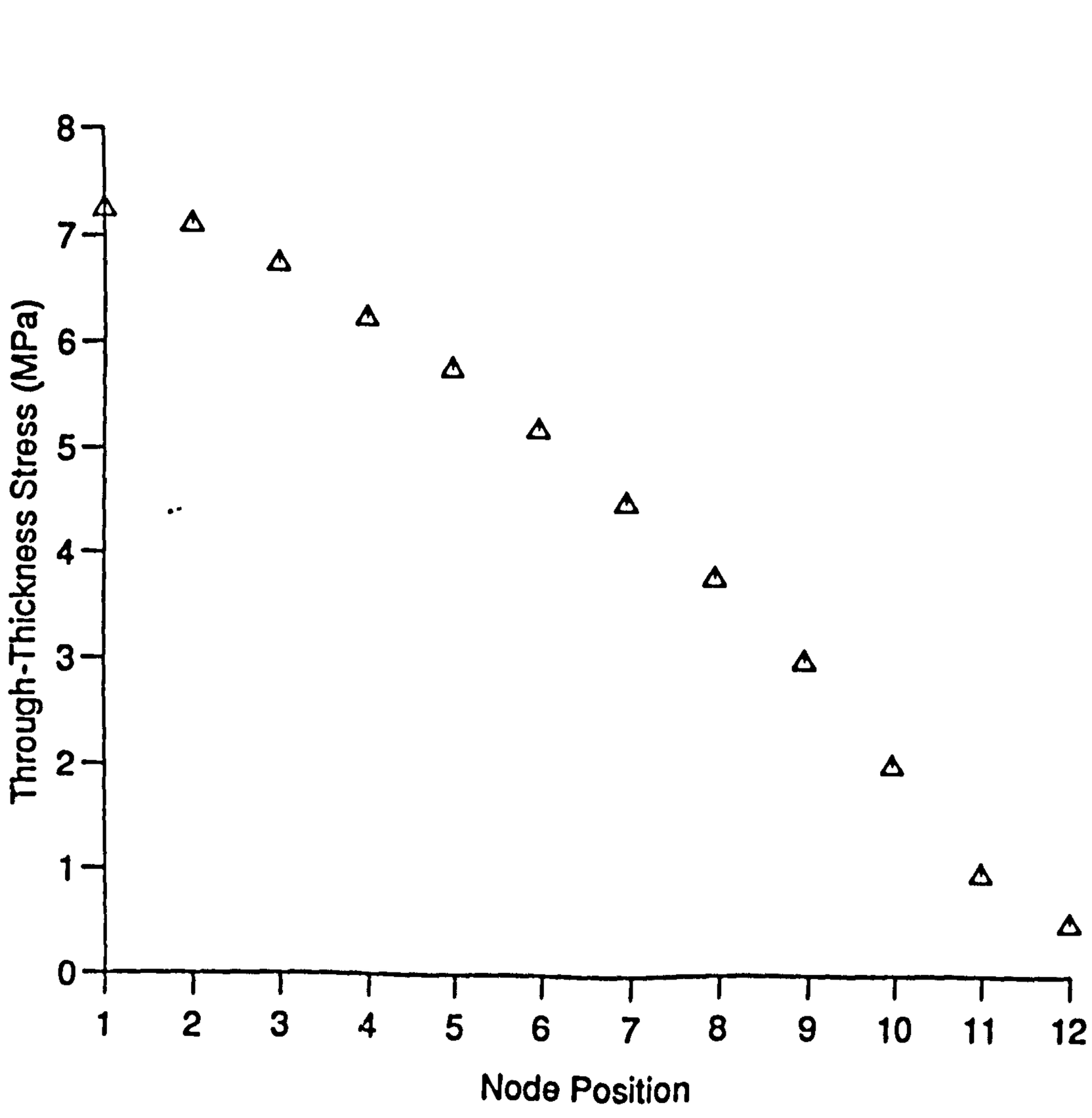

Figure 6.14(b) Through-Thickness Stress Distribution along Path 2 for Model 1

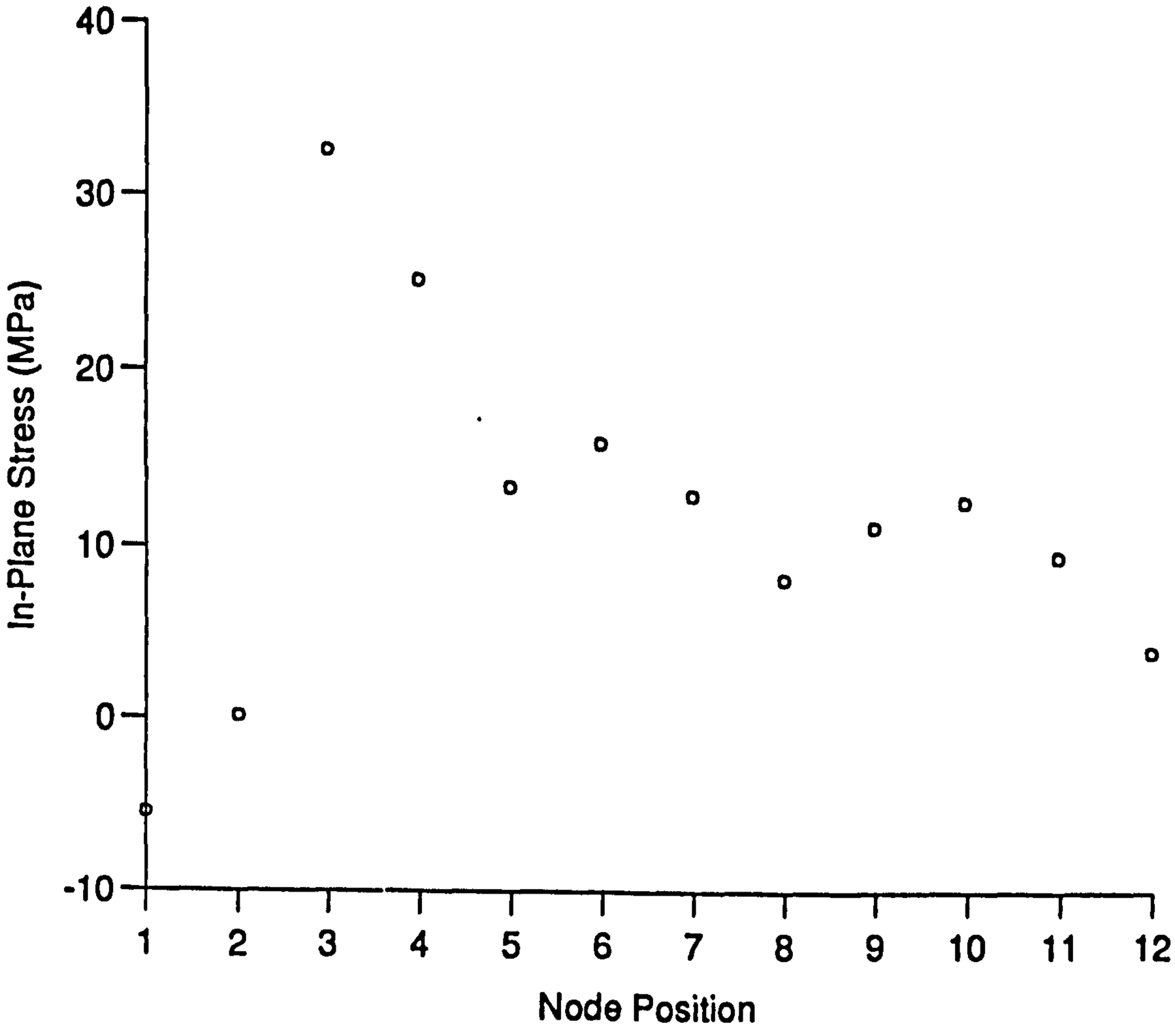

Figure 6.15(a) In-Plane Stress Distribution along Path 2 for Model 3

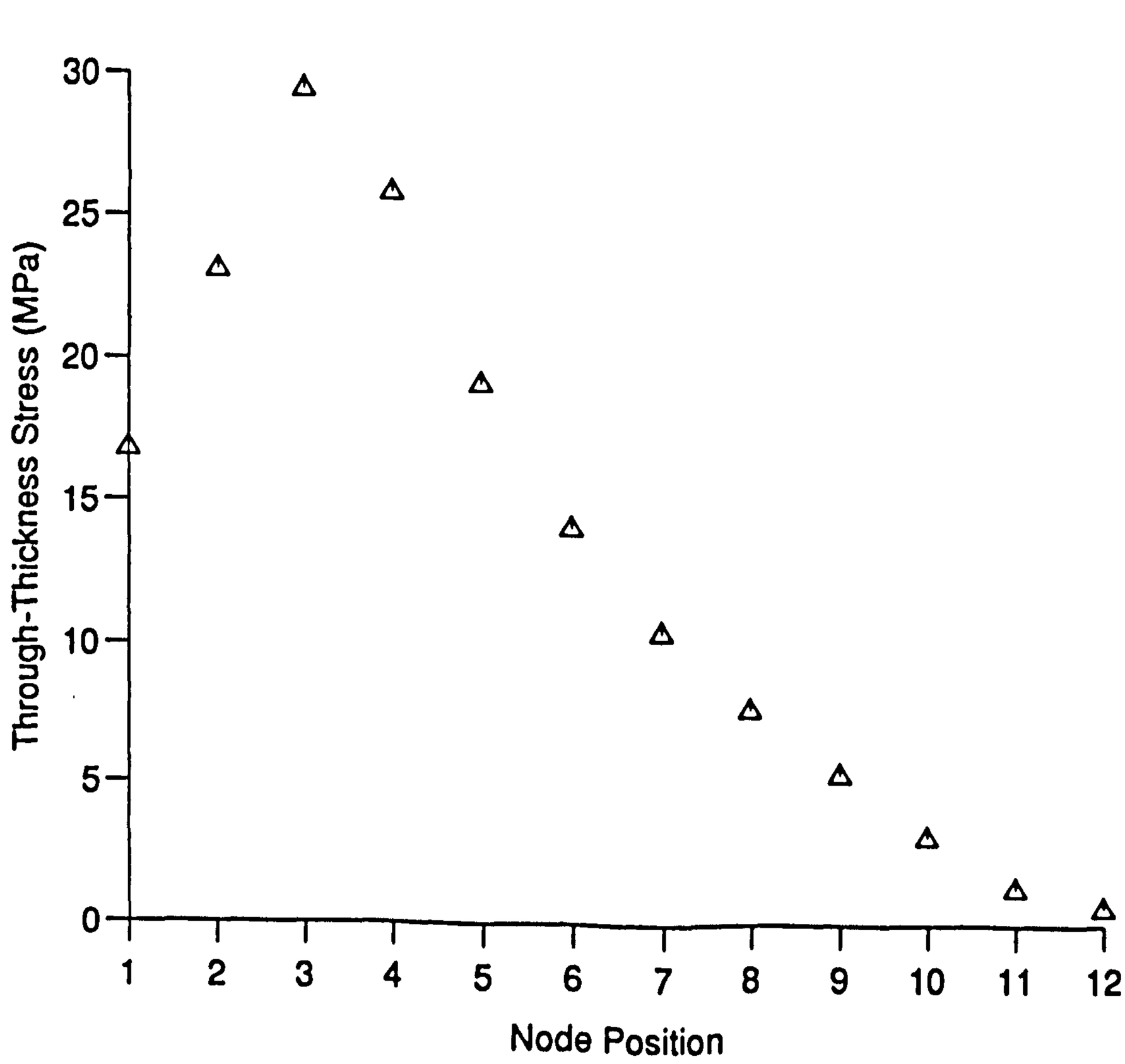

Figure 6.15(b) Through-Thickness Stress Distribution along Path 2 for Model 3

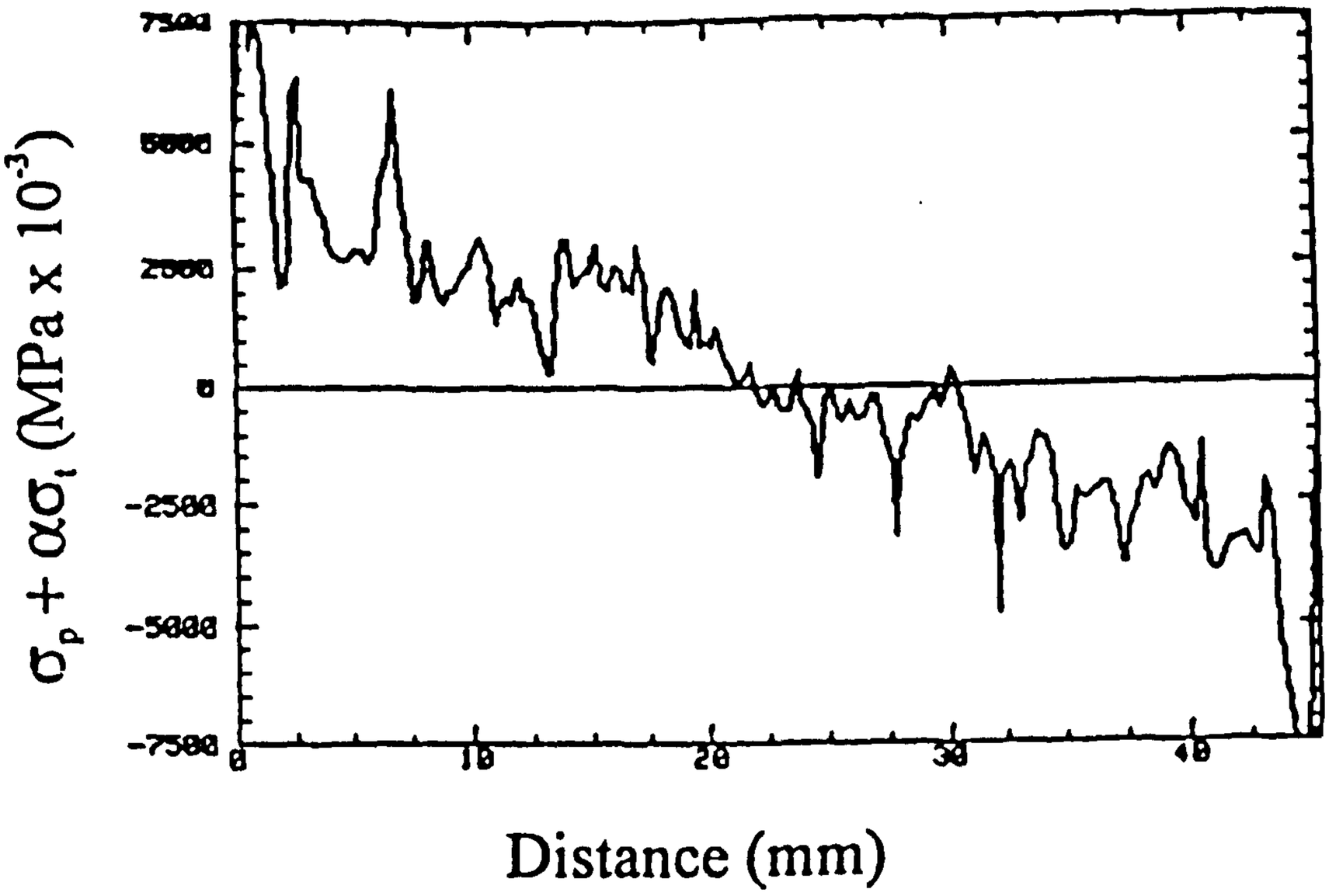

Figure 6.16 Example of a Typical Thermoelasticity Plot (Taken from Dulieu-Smith et. al.)

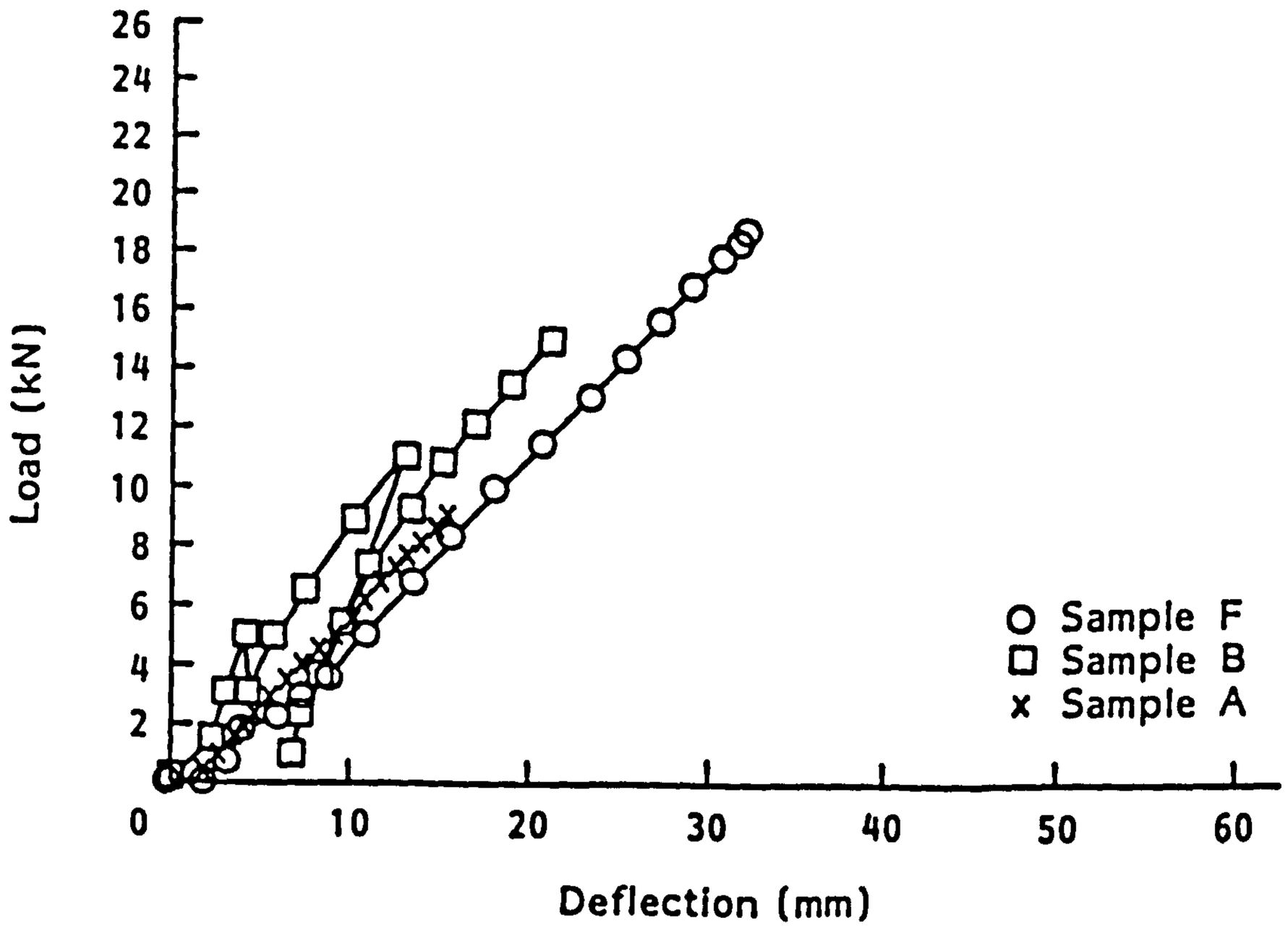

Figure 6.17 Experimental Load/Deflection Curve for a Tee Joint under a 45 Degree Pull-Off Load. (Taken from Shenoi & Hawkins, 1992)

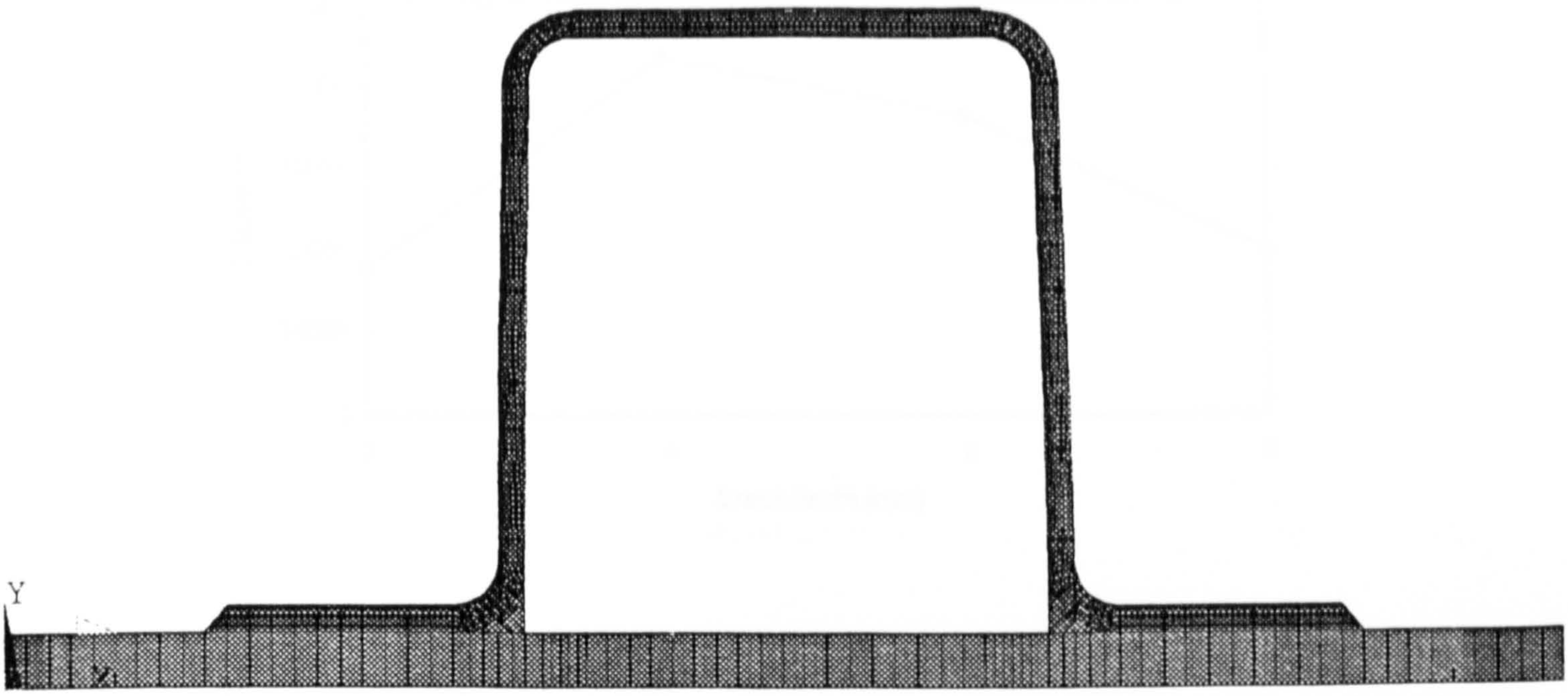

Figure 7.1 Typical FE Model of a Type I Top Hat Stiffener

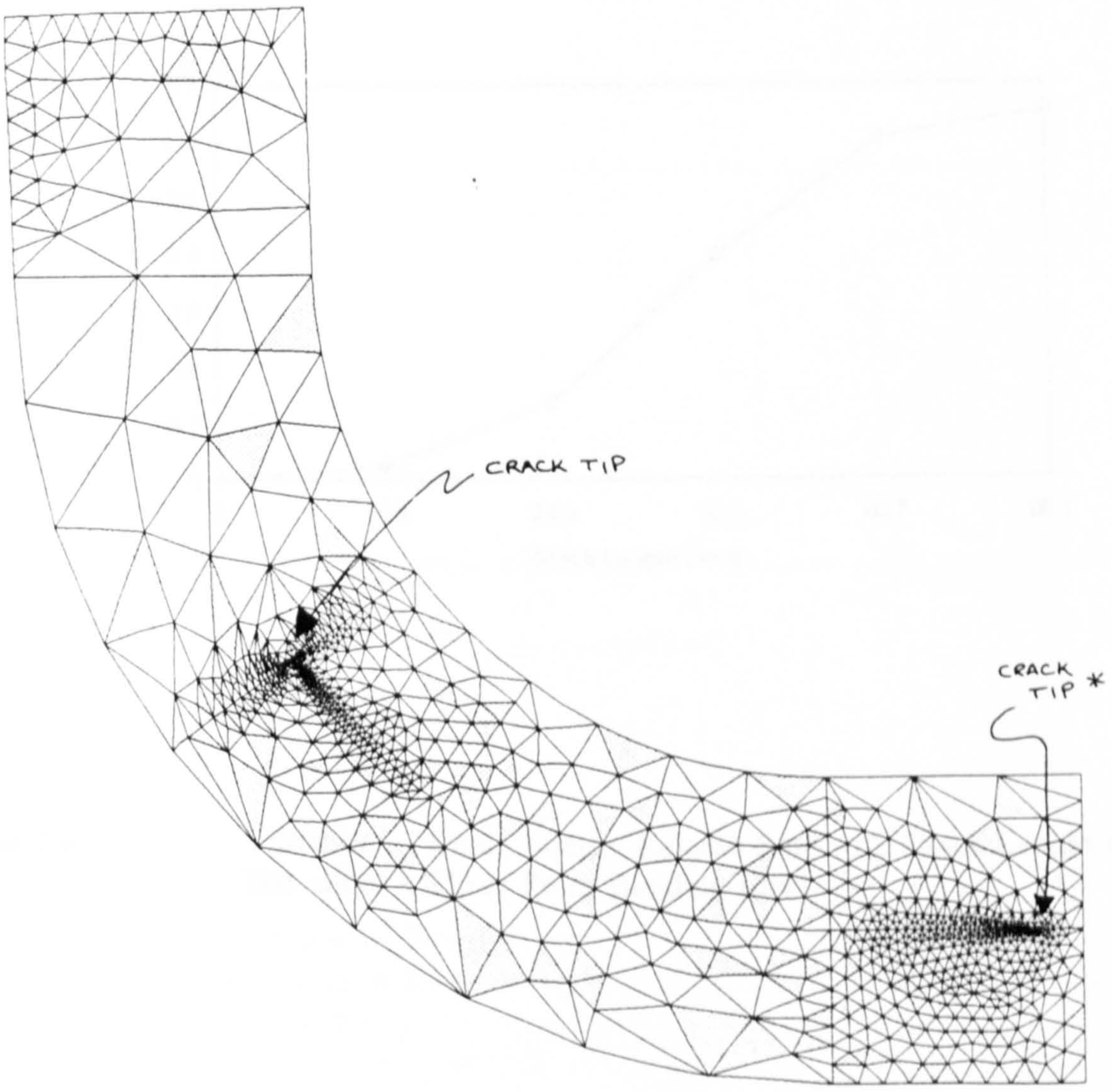

Figure 7.2 Cracked Region of the FE Model

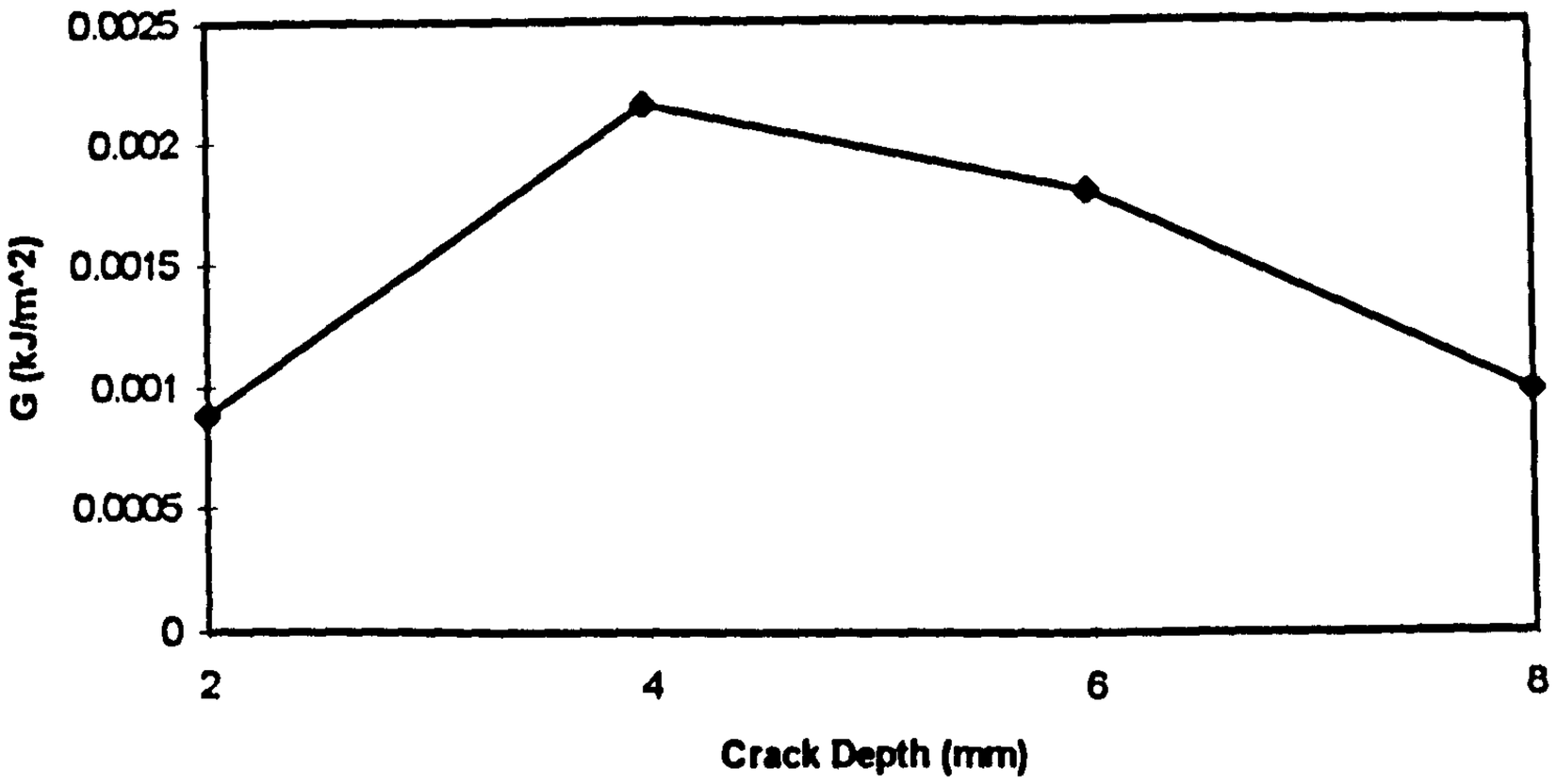

Figure 7.3 Variation of Strain Energy Release Rate with Crack Depth for a Top Hat under a Three Point Bending Load

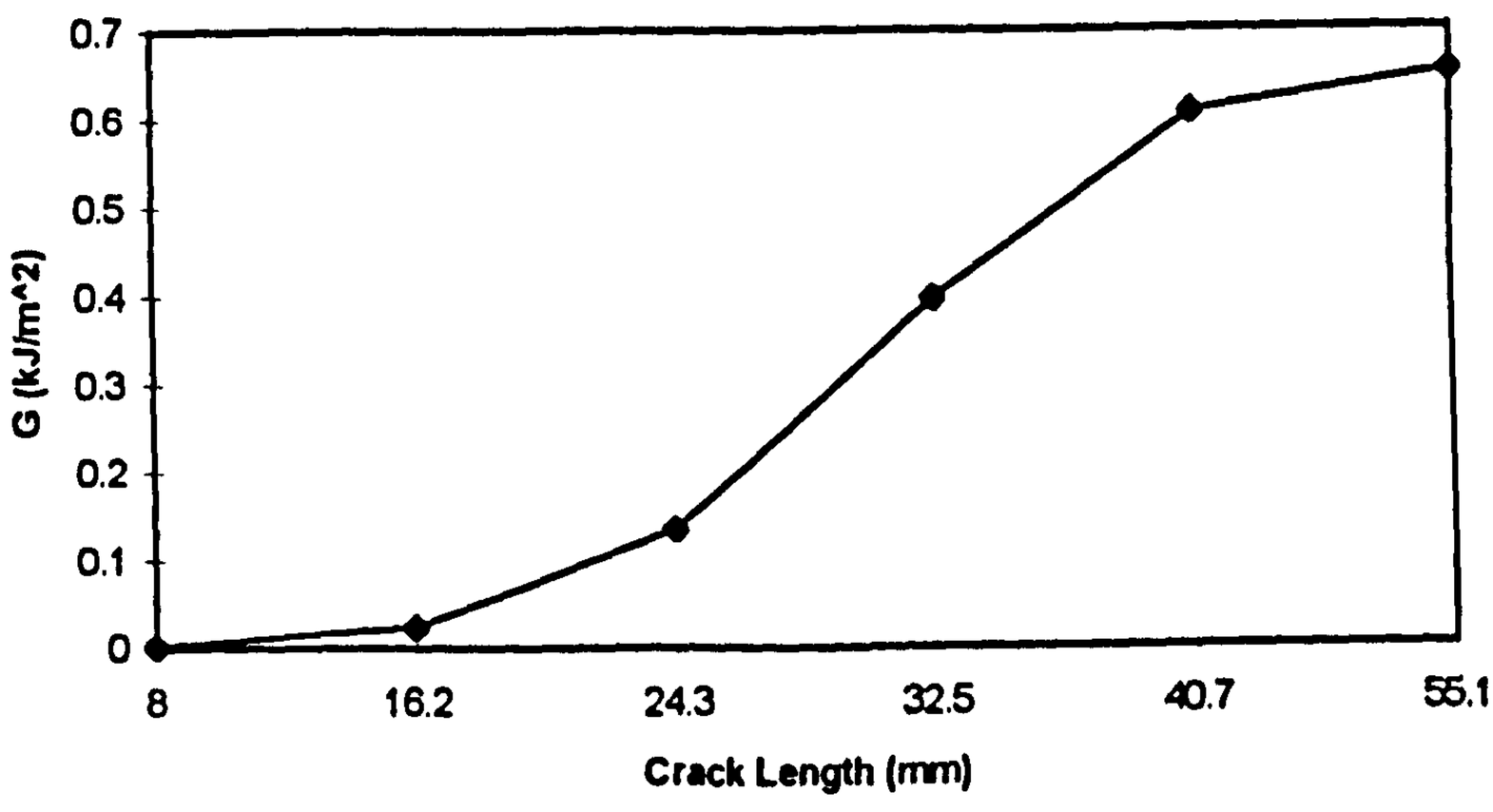

Figure 7.4 Variation of Strain Energy Release Rate with Crack Length for a Top Hat under a Three Point Bending Load

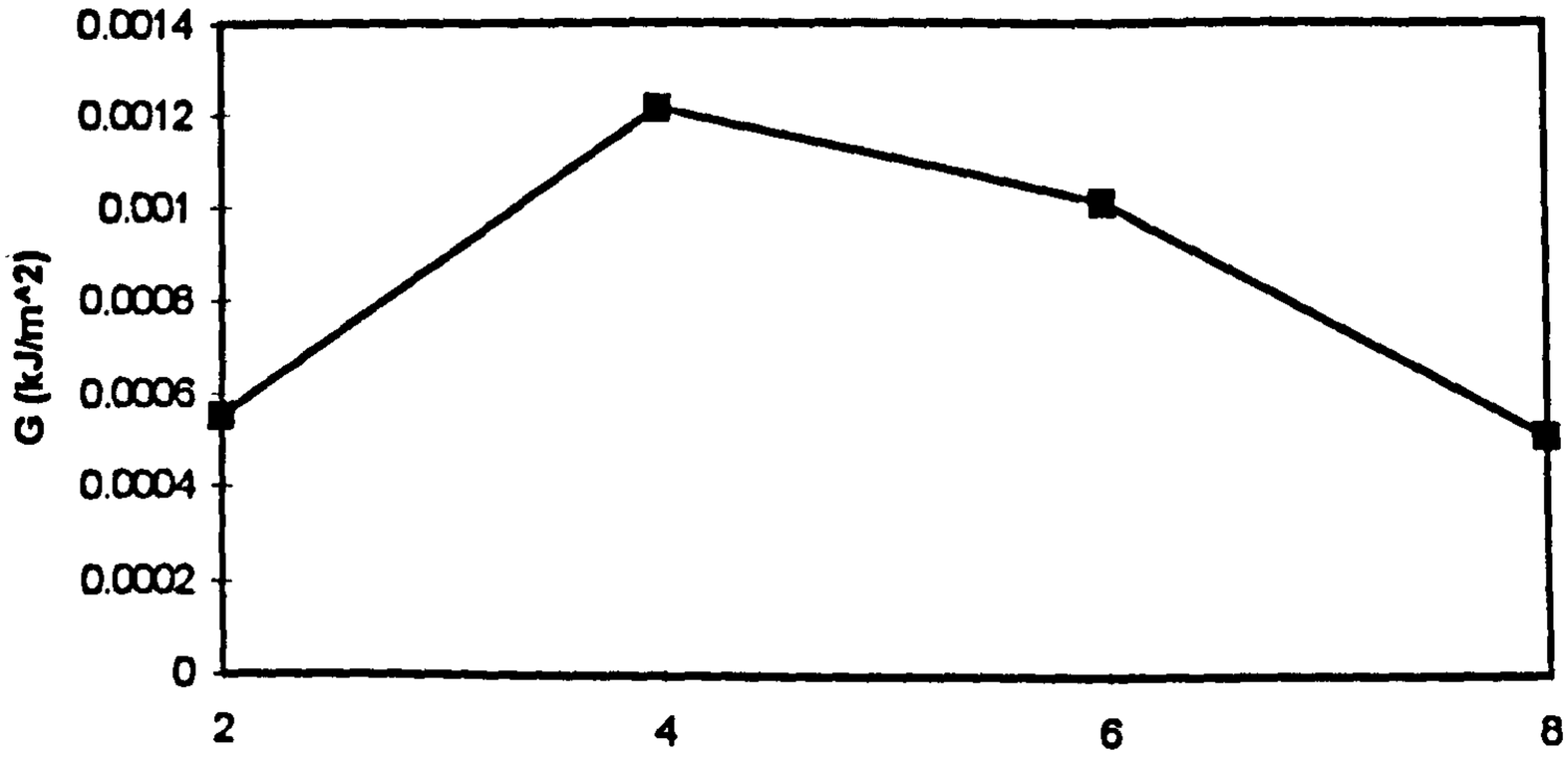

Figure 7.5 Variation of Strain Energy Release Rate with Crack Depth for a Top Hat under a Reverse Bending Load

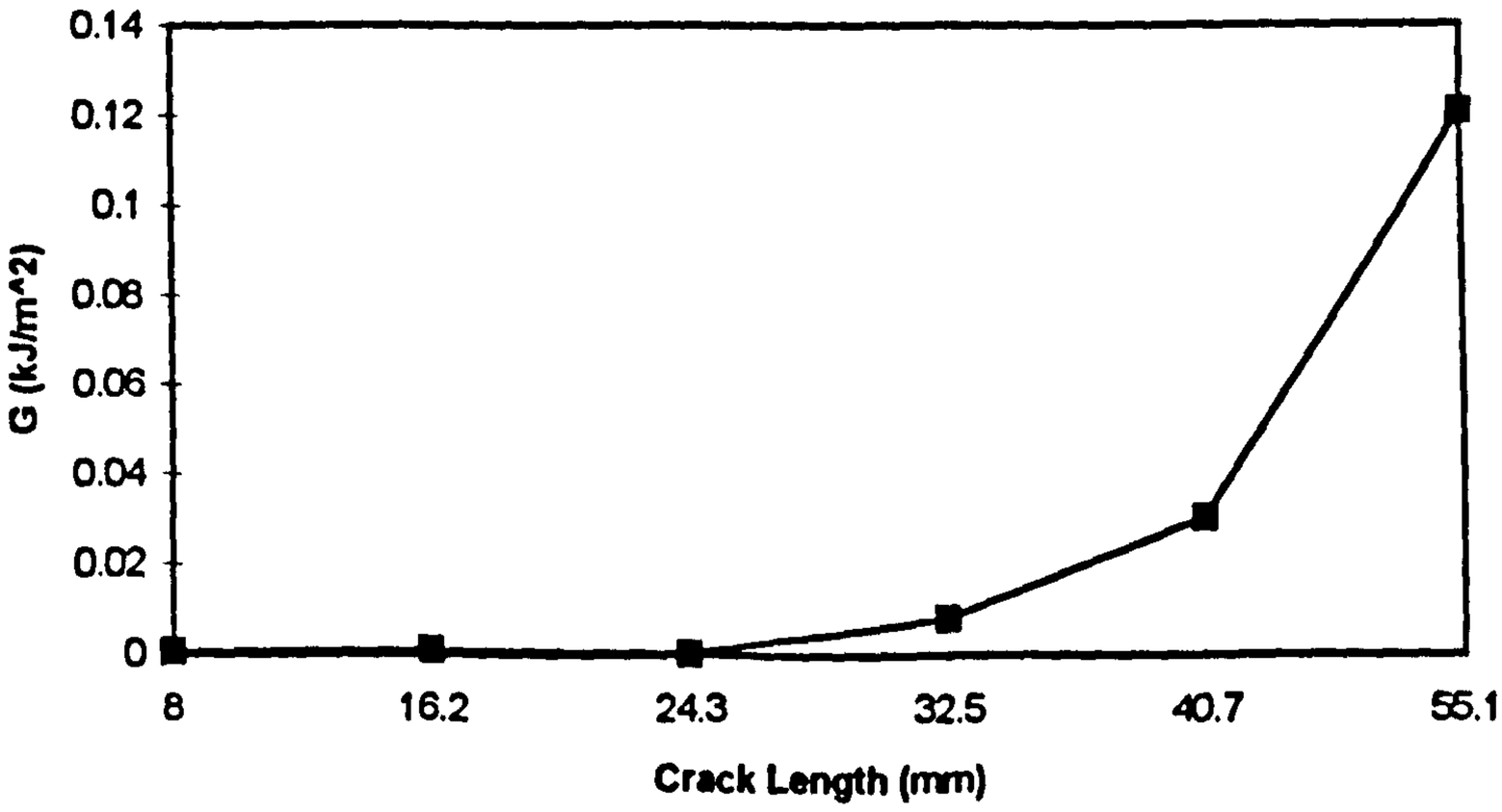

Figure 7.6 Variation of Strain Energy Release Rate with Crack Length for a Top Hat under a Reverse Bending Load

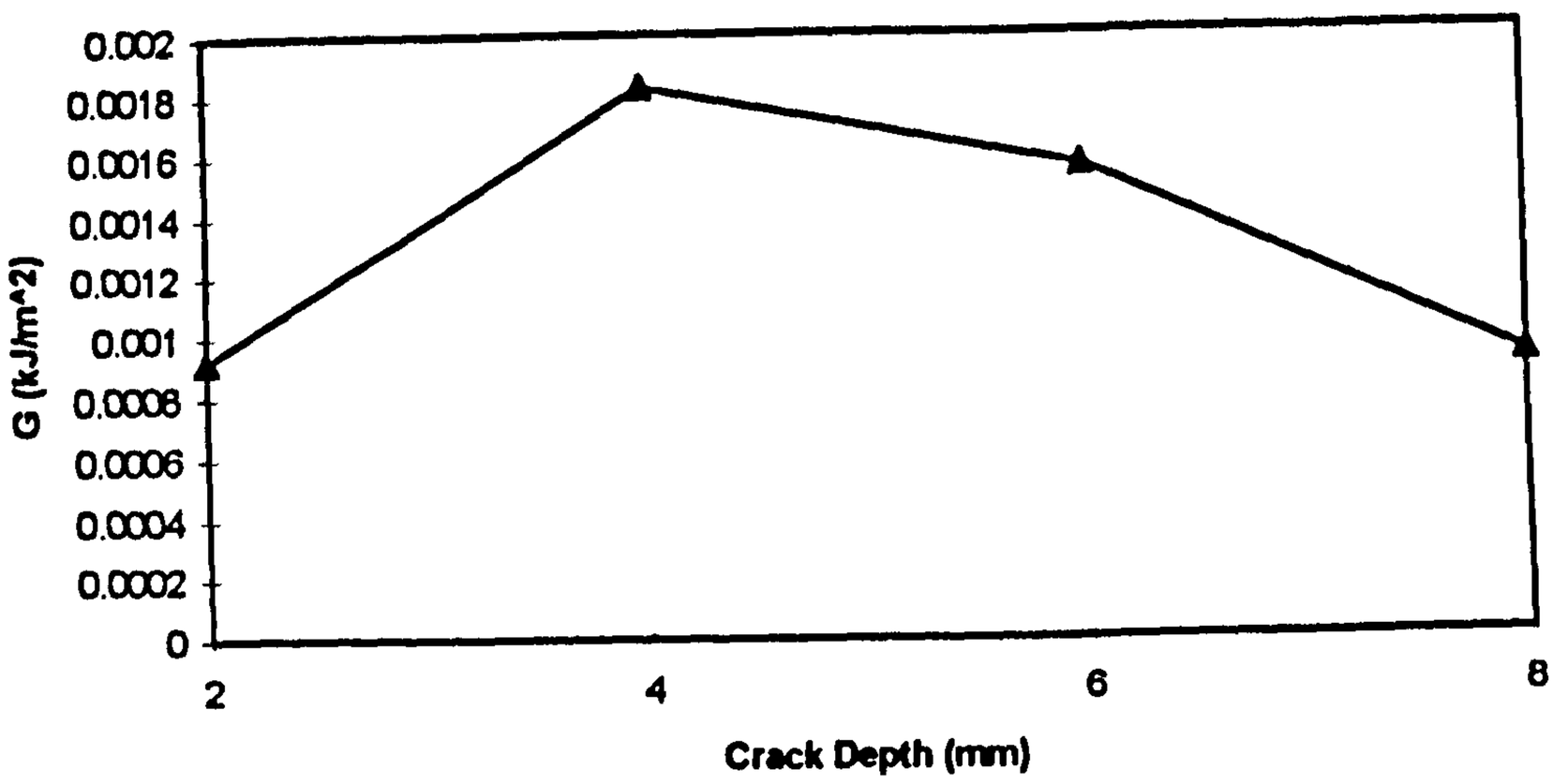

Figure 7.7 Variation of Strain Energy Release Rate with Crack Depth for a Top Hat under a Pull-Off Load

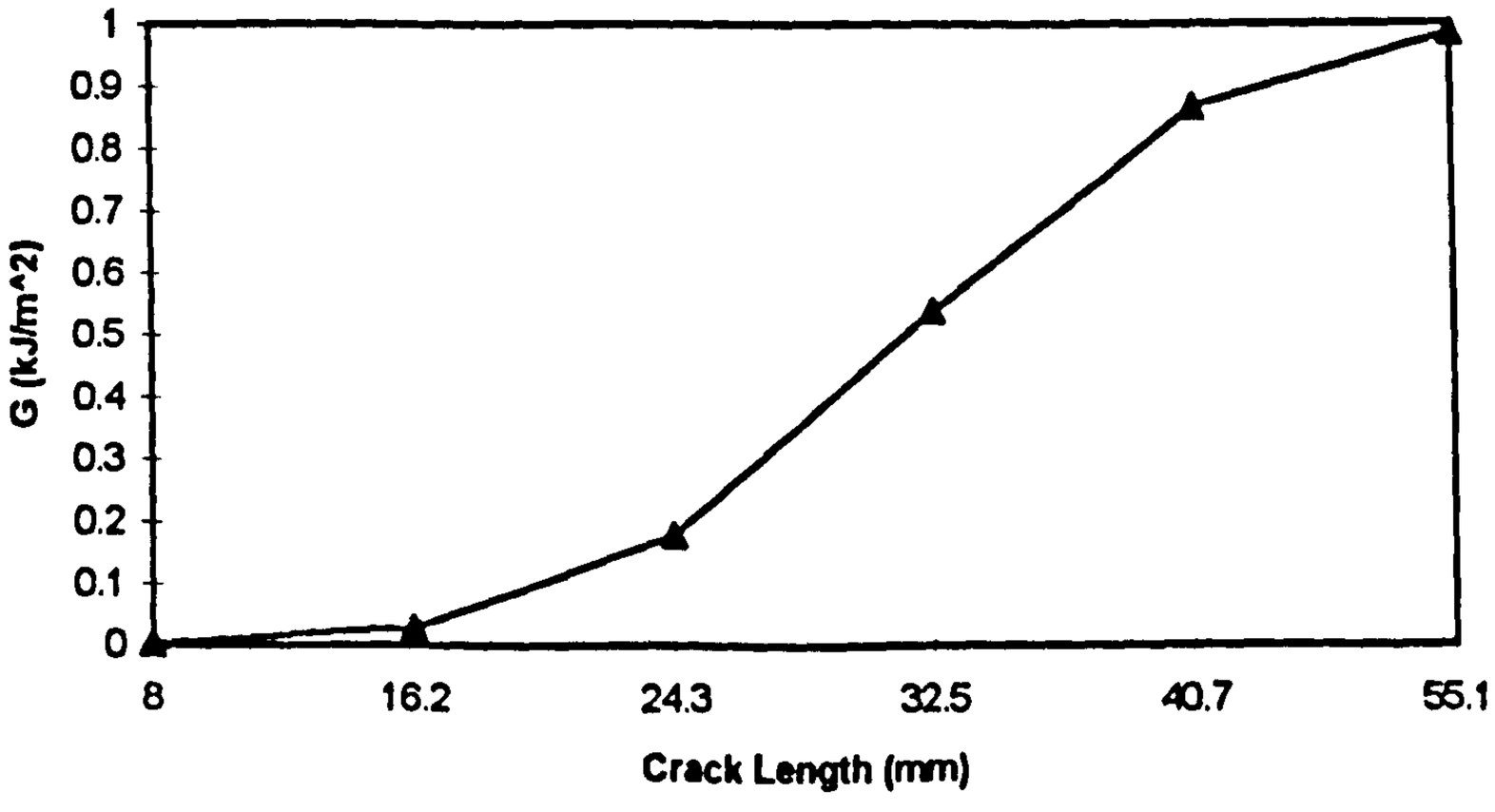

Figure 7.8 Variation of Strain Energy Release Rate with Crack Length for a Top Hat under a Pull-Off Load

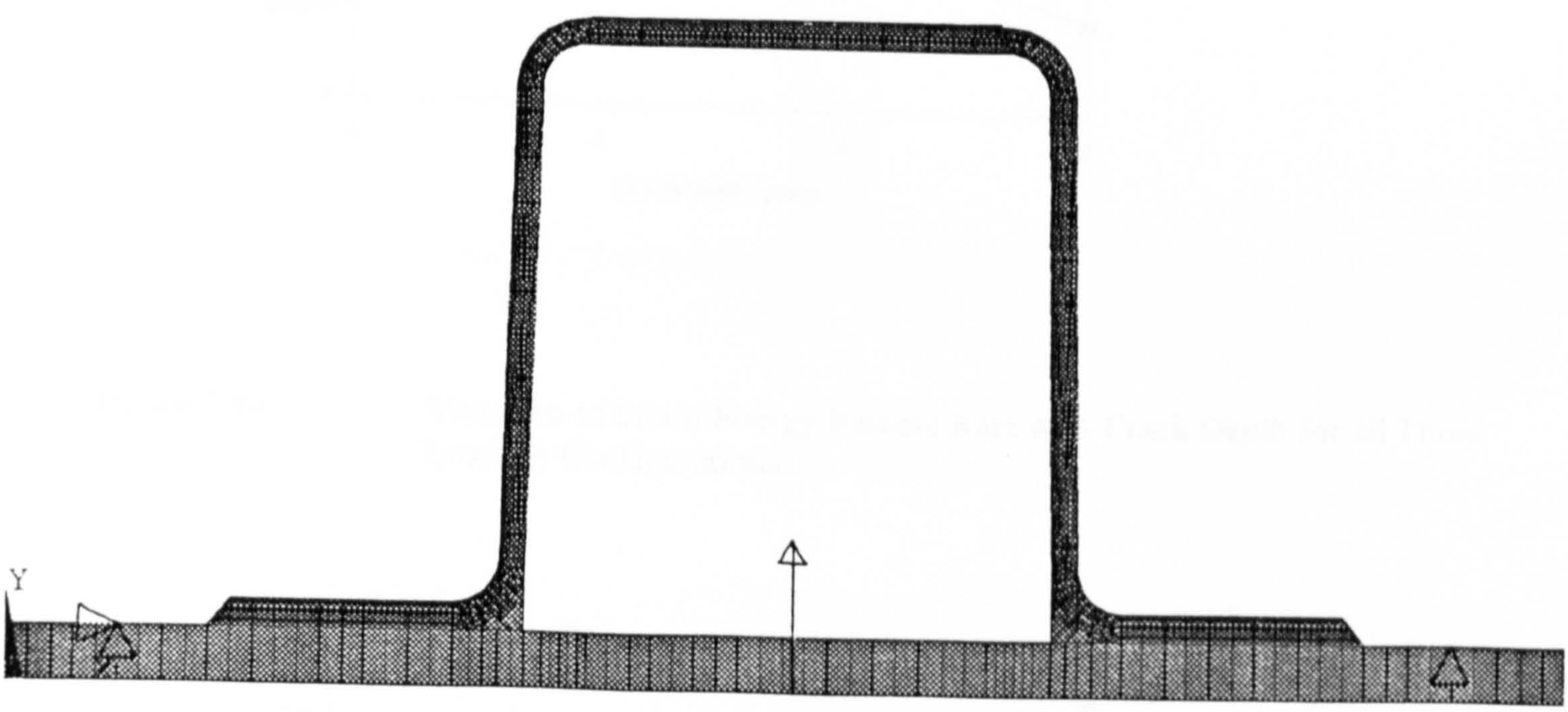

Figure 7.9 FE Representation of a Type I Stiffener under a Typical In-Service Load

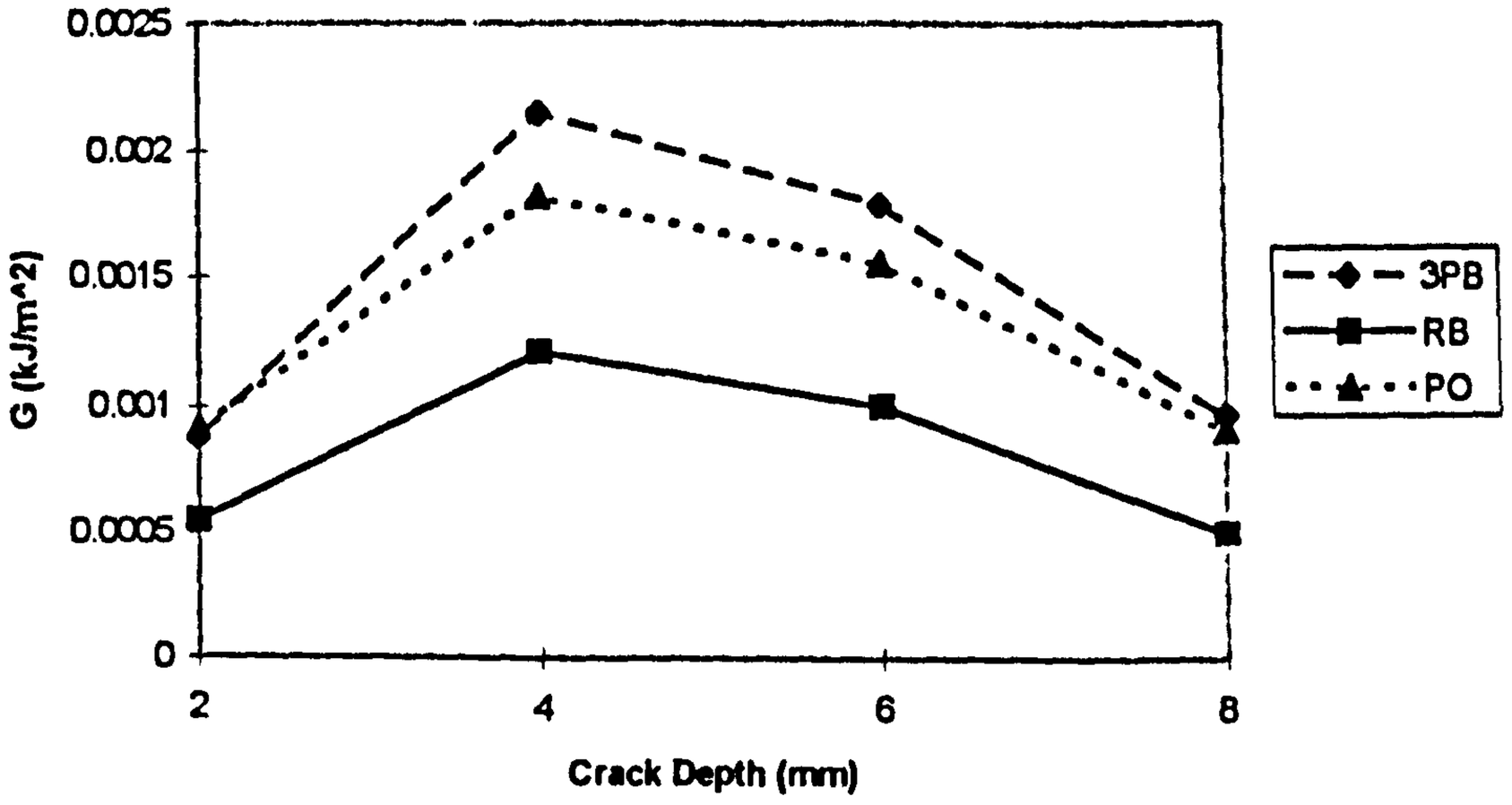

Figure 7.10 Variation of Strain Energy Release Rate with Crack Depth for all Three Loading Configurations

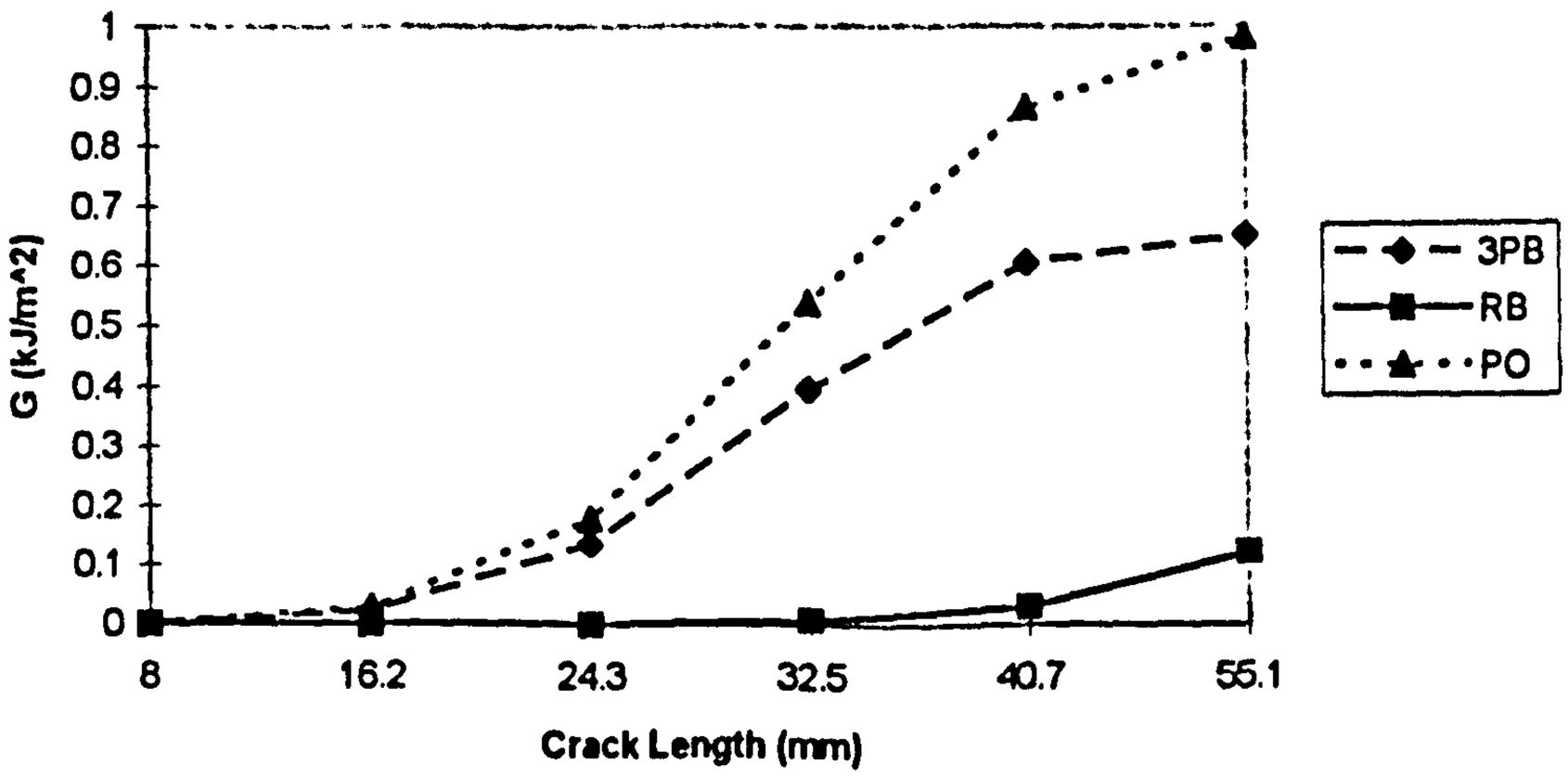

Figure 7.11 Variation of Strain Energy Release Rate with Crack Length for all Three Loading Configurations

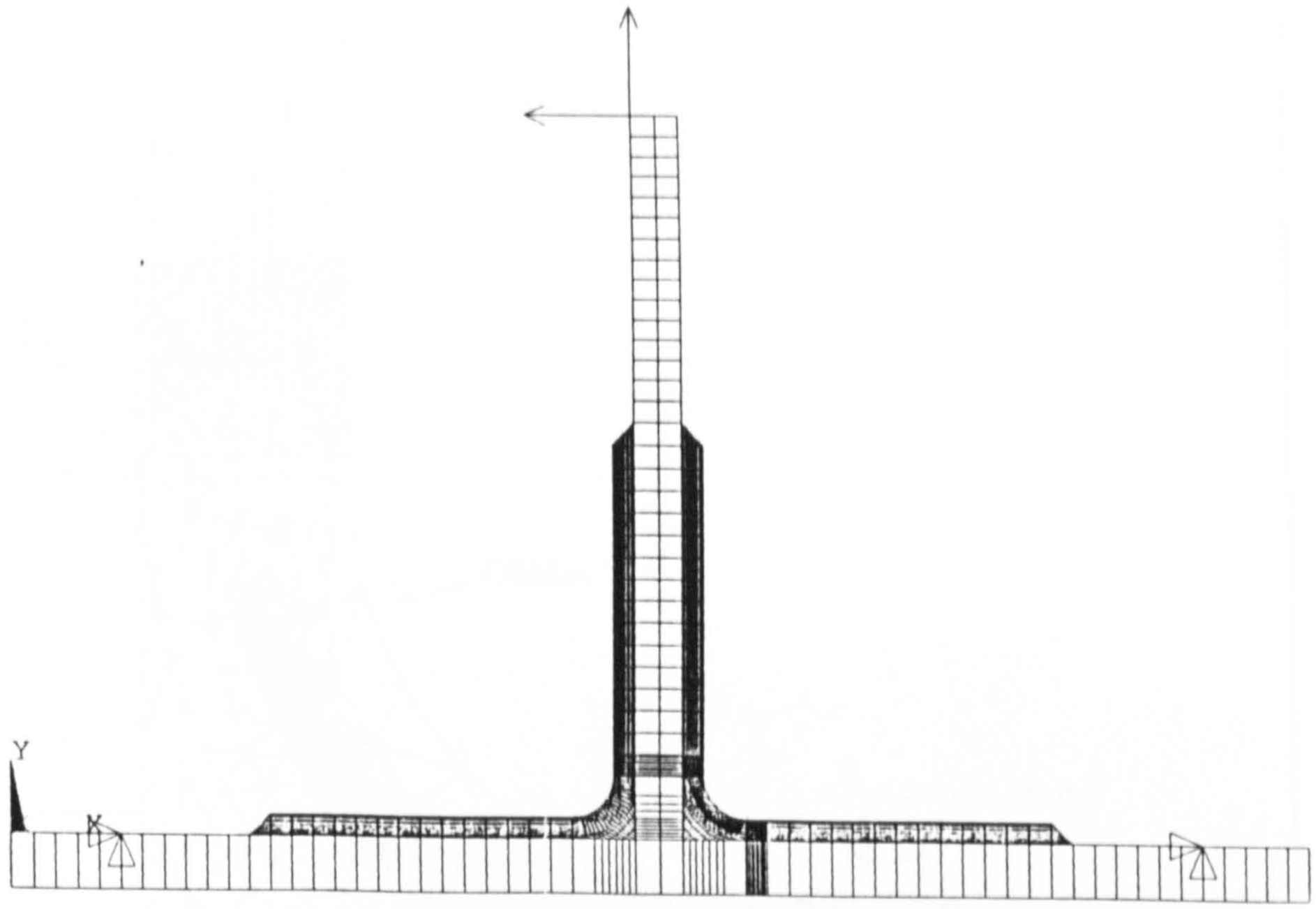

Figure 8.1 Finite Element Model to Represent an Undamaged Tee Joint

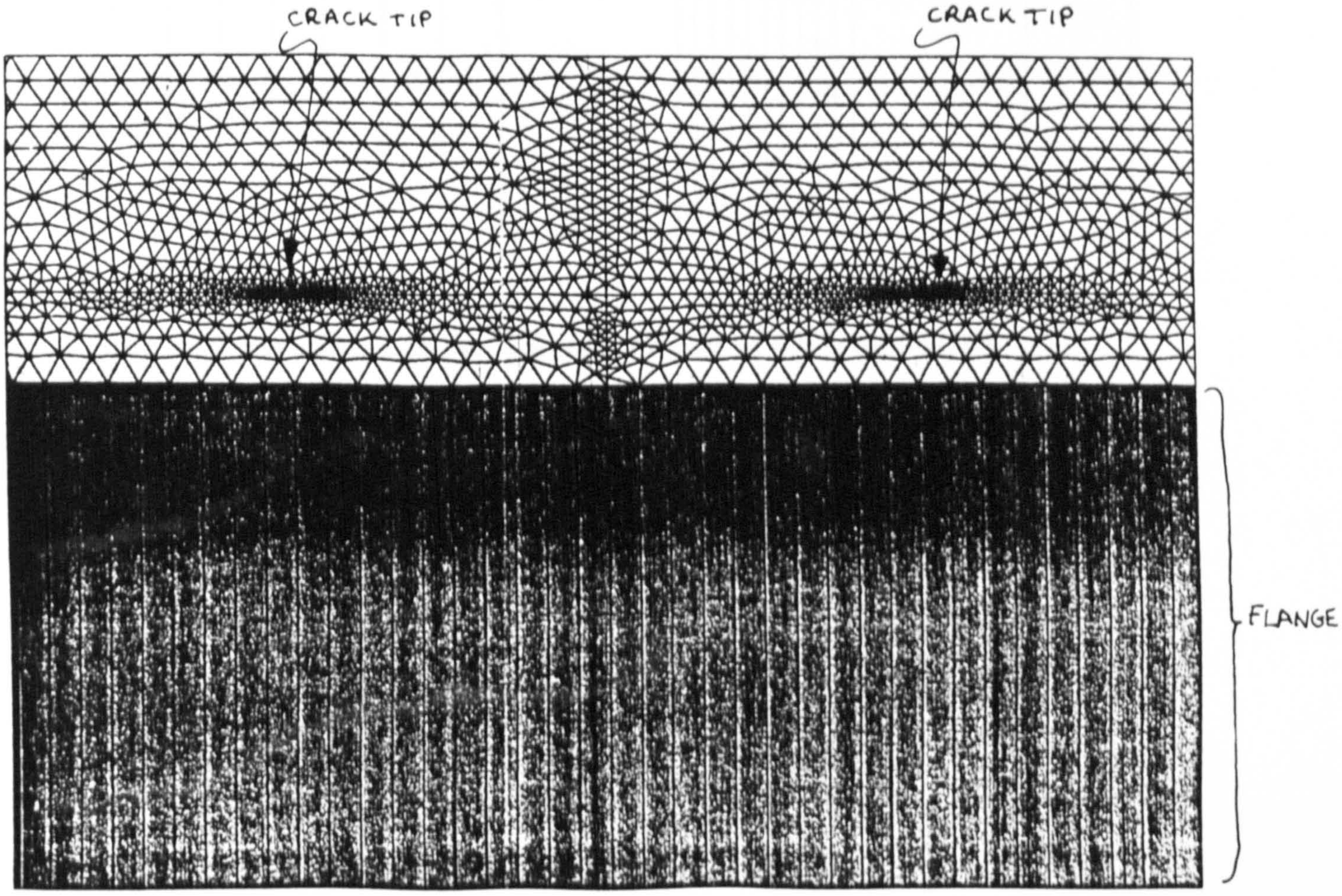

Figure 8.2 Enlarged Regions of the FE Model which contain the Crack :
(a) Straight Crack in Flat Portion of the Overlaminate

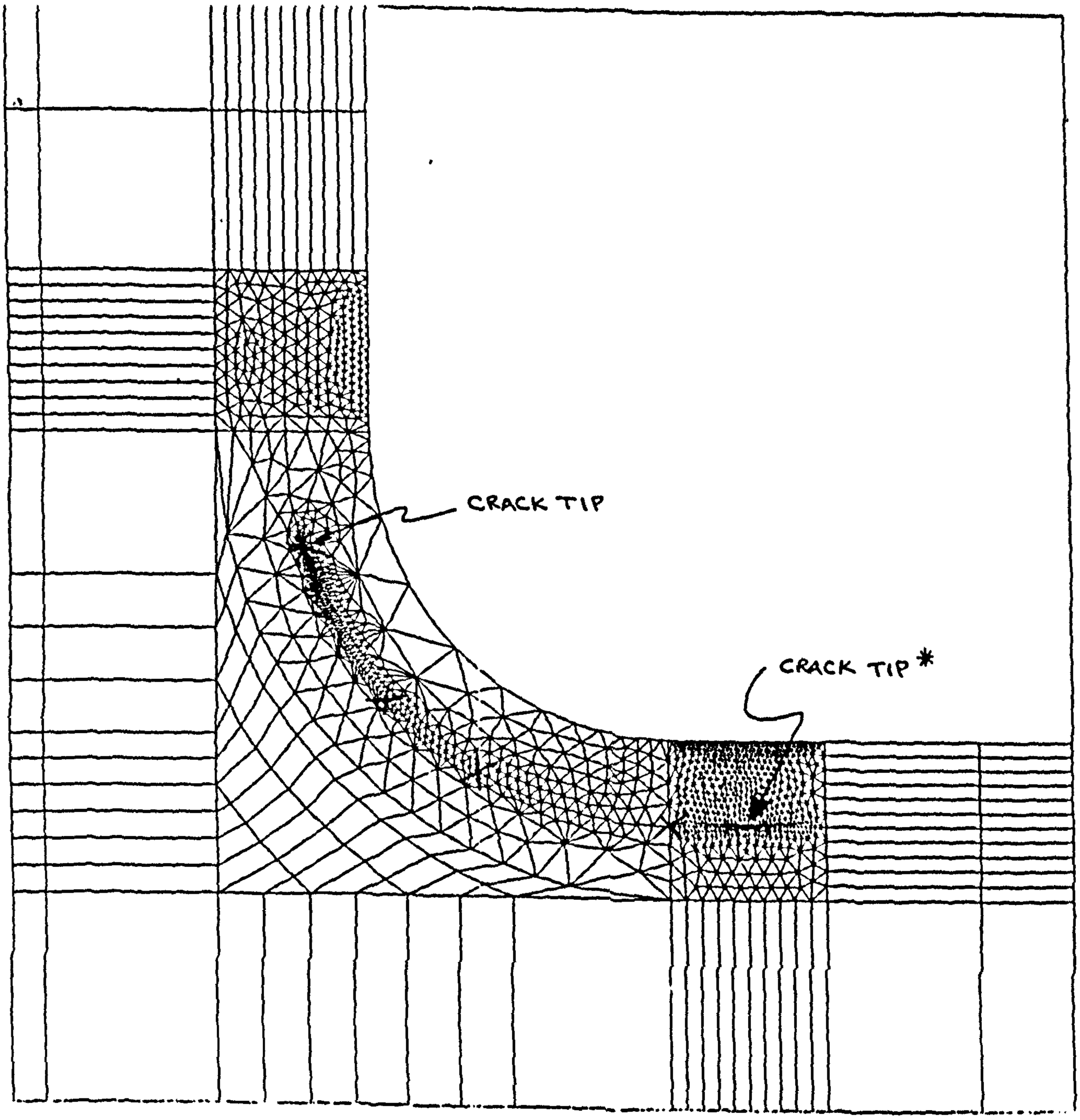

(b) Curved Crack in the Radiused Portion of the Overlaminate

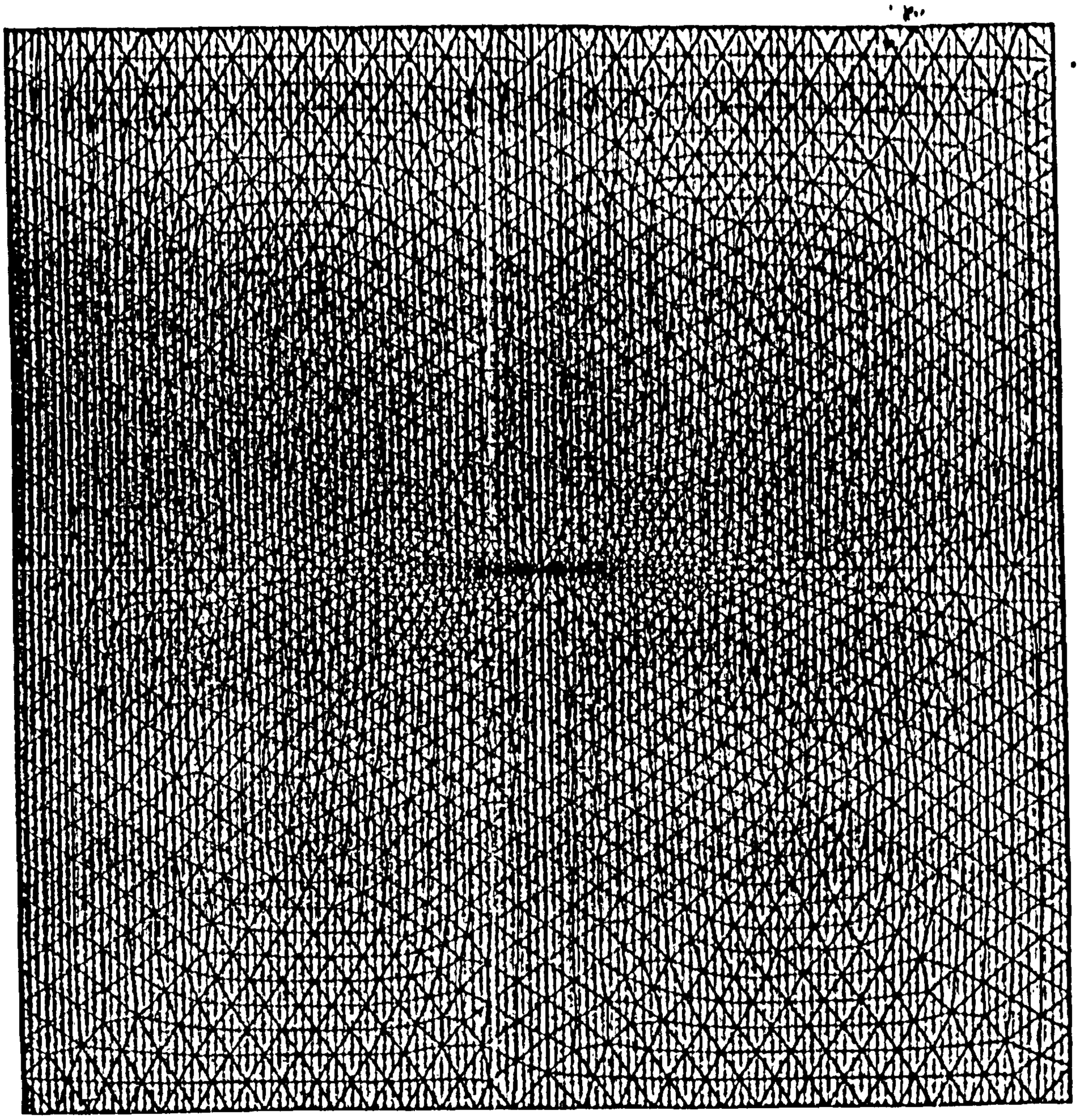

Figure 8.3 Finite Element Model containing a Central Crack

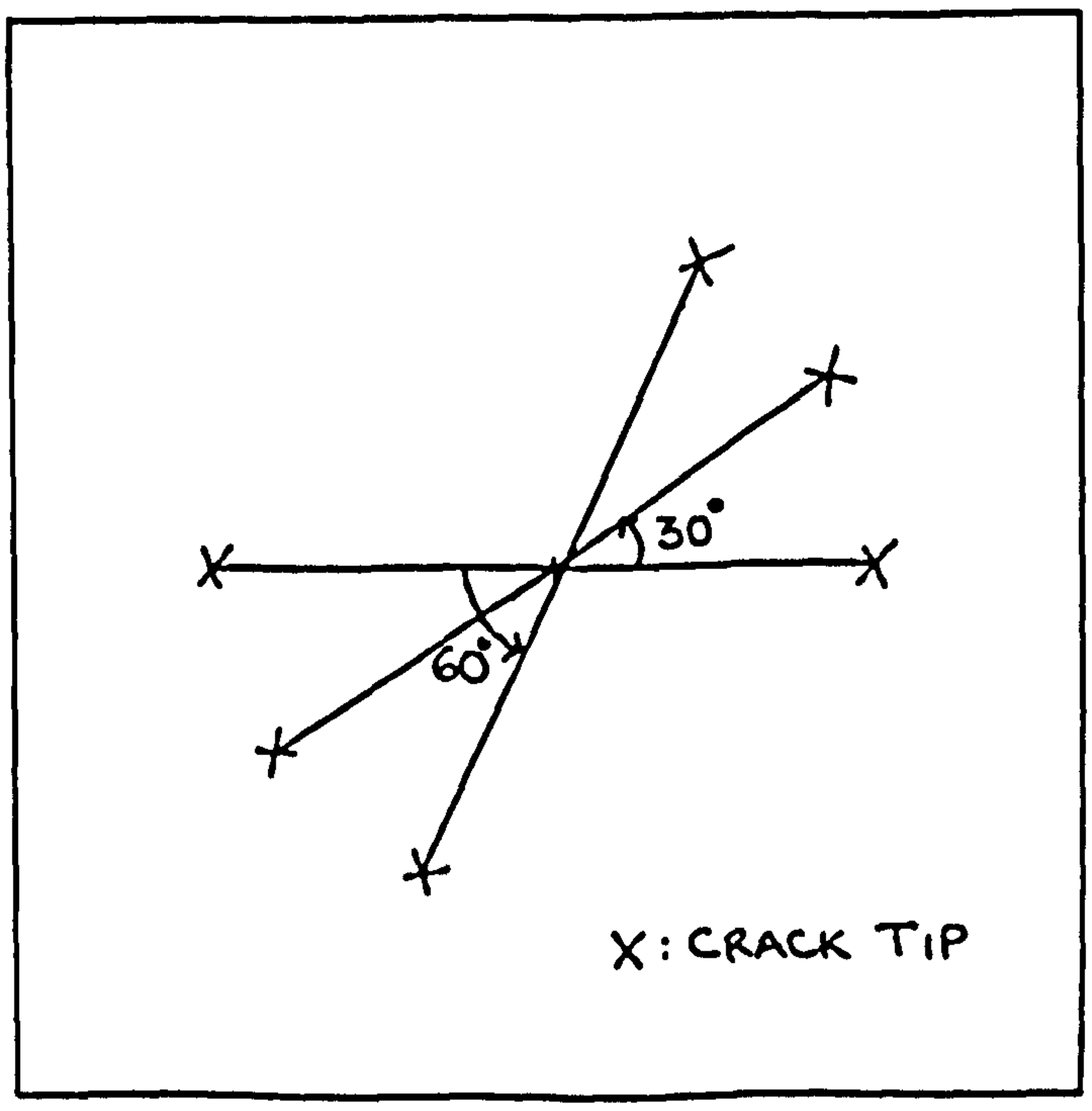

Figure 8.4 Model of plate containing a Central Crack at Three Different Orientations

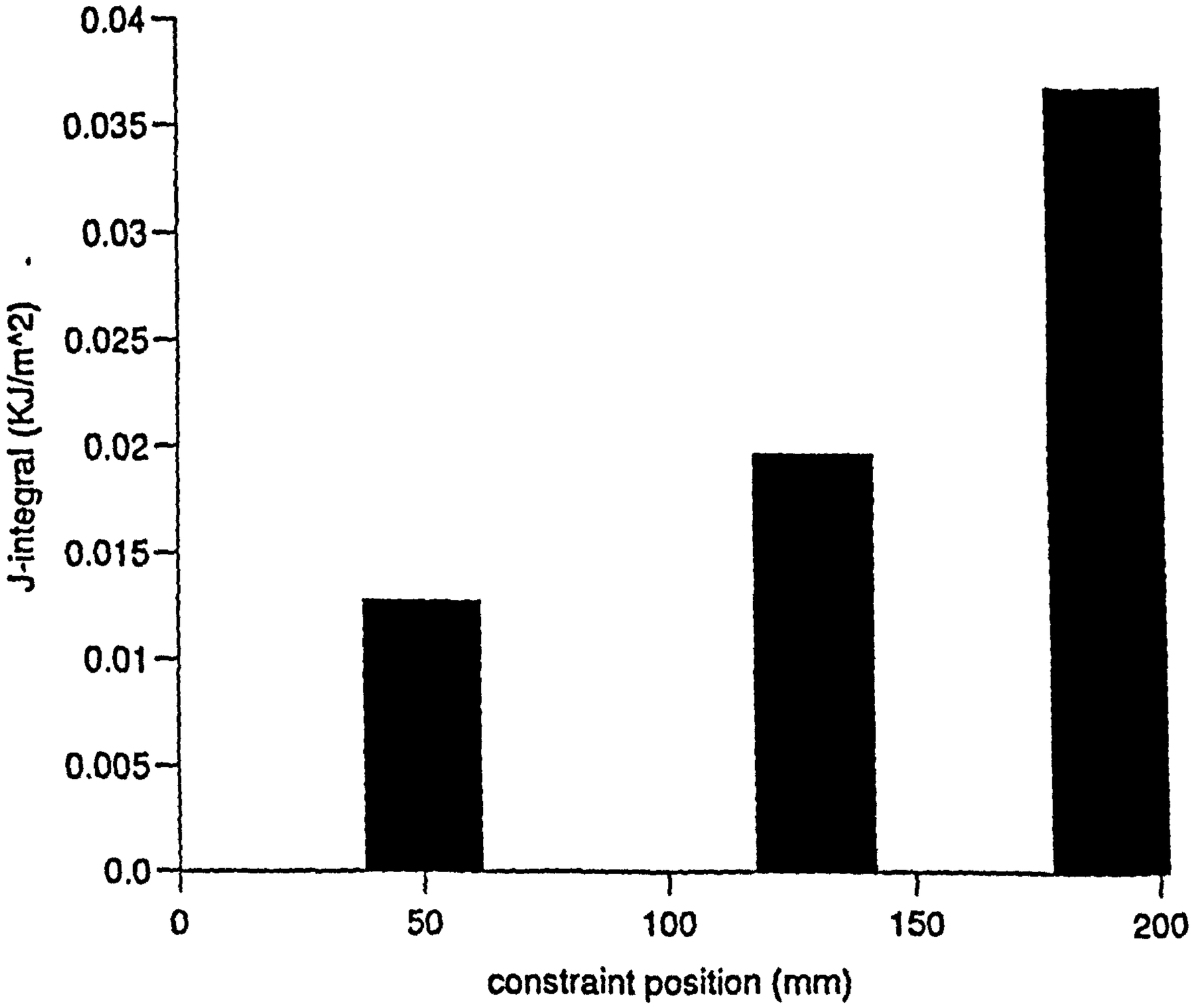

Figure 8.5 J-Integral Values versus Distance of Boundaries from Outside Edge of the Tee Joint Model (Crack Depth = 6 mm, Crack Length = 10 mm)

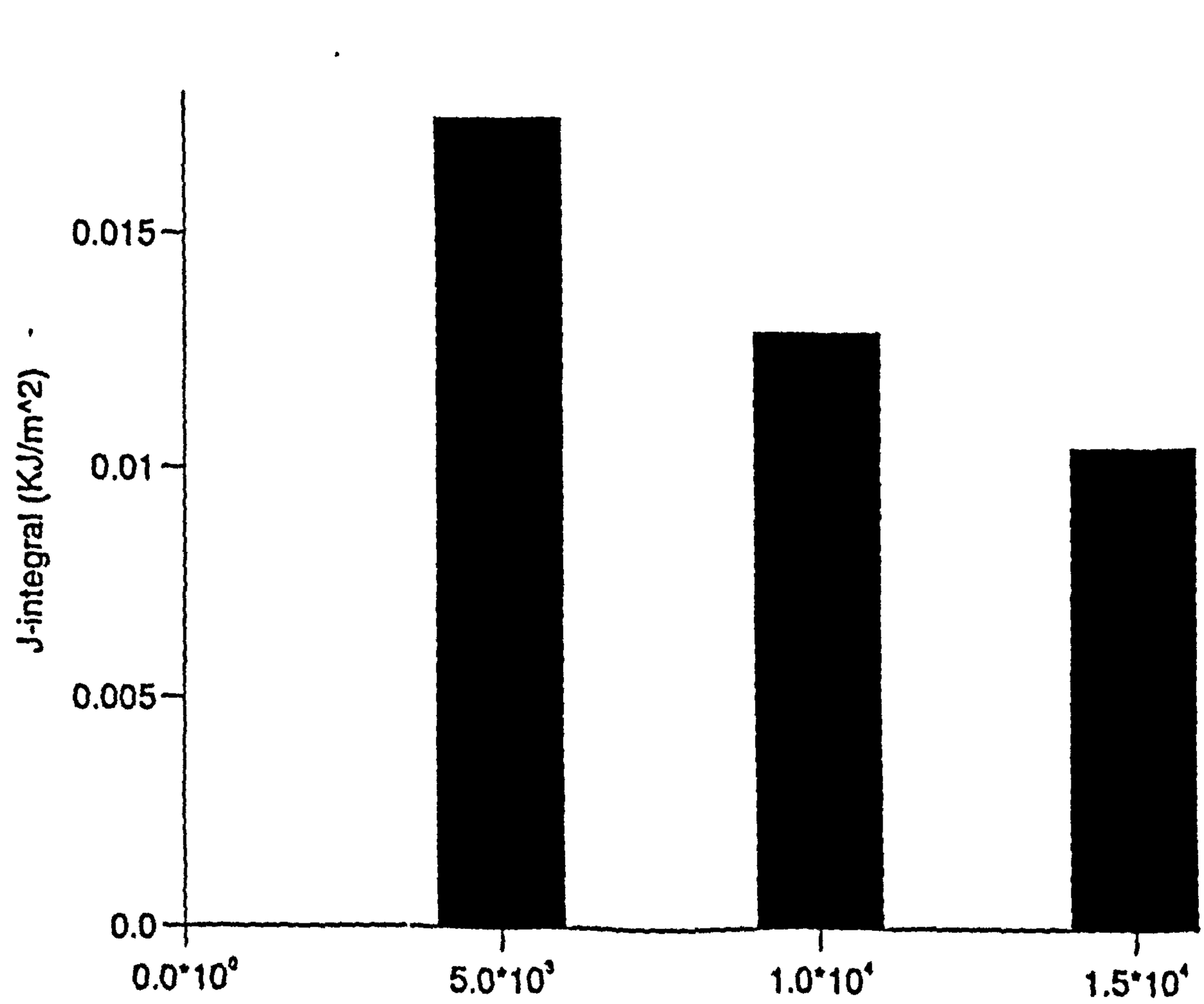

Figure 8.6 J-Integral Values for Different Crack Element Elastic Moduli (Crack Depth = 6 mm, Crack Length = 10 mm)

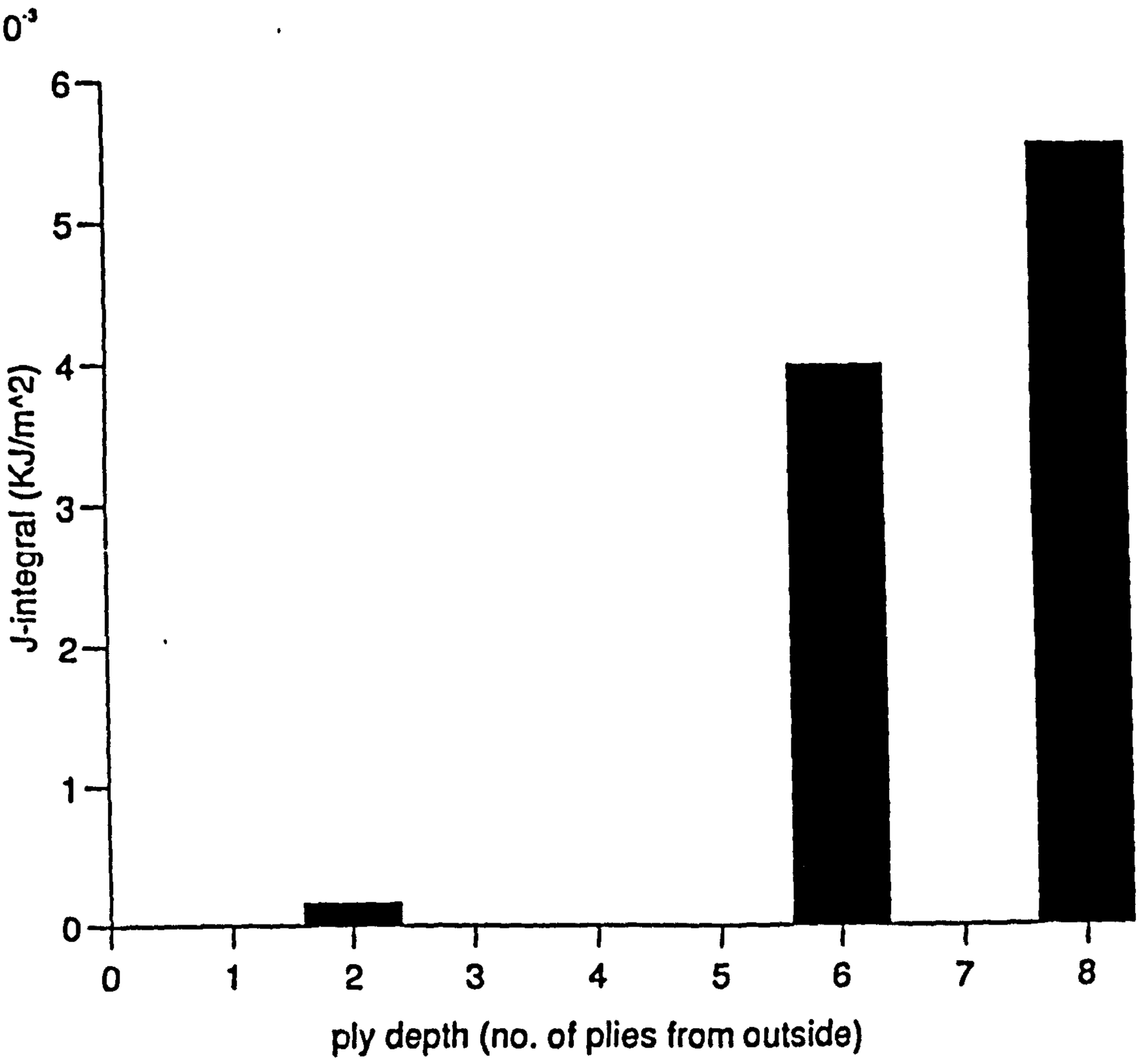

Figure 8.7 J-Integral Values for Different Crack Depths

(a) Straight Crack (Crack Length = 10 mm)

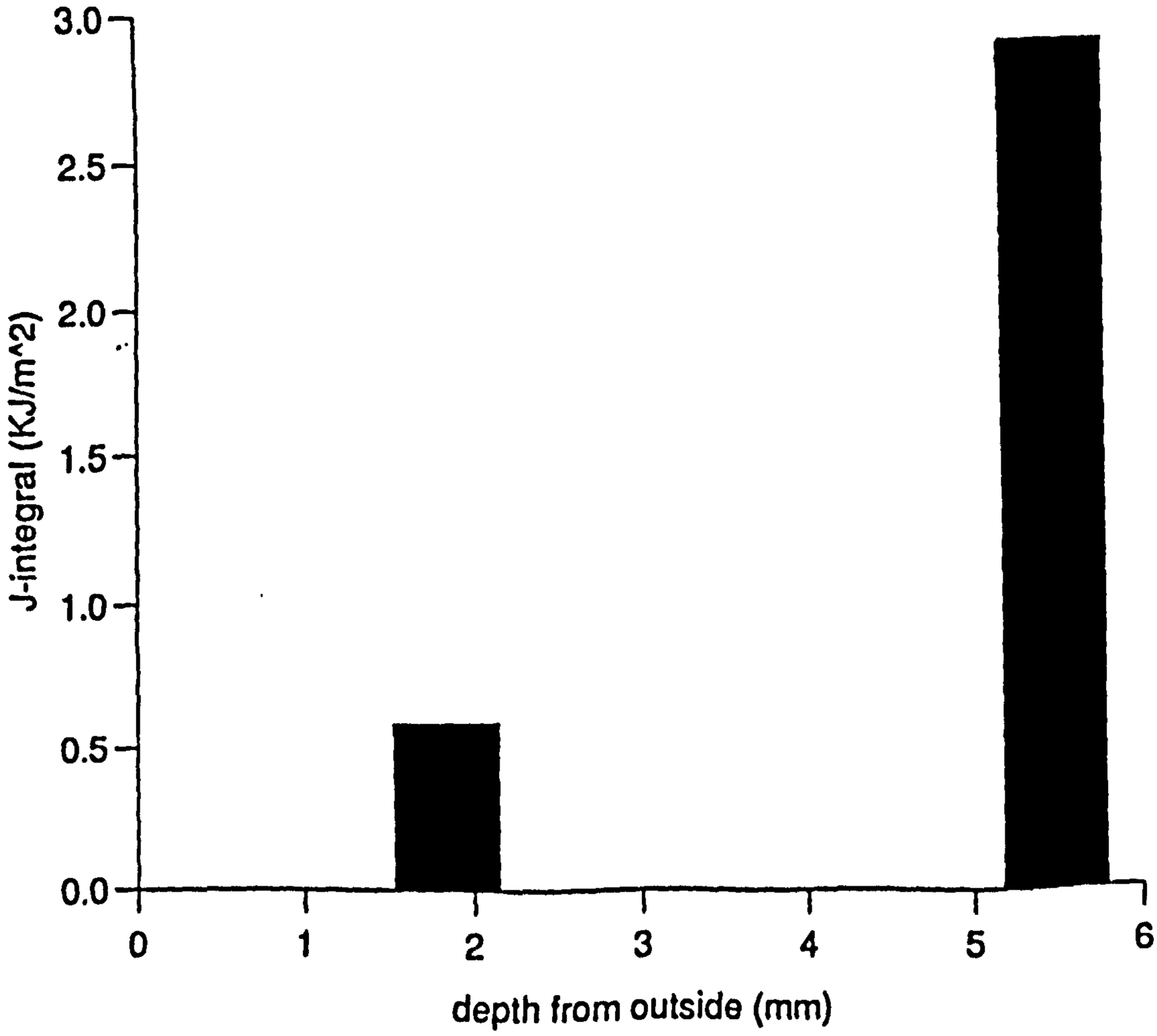

(b) Curved Crack (Crack Length = 36 mm)

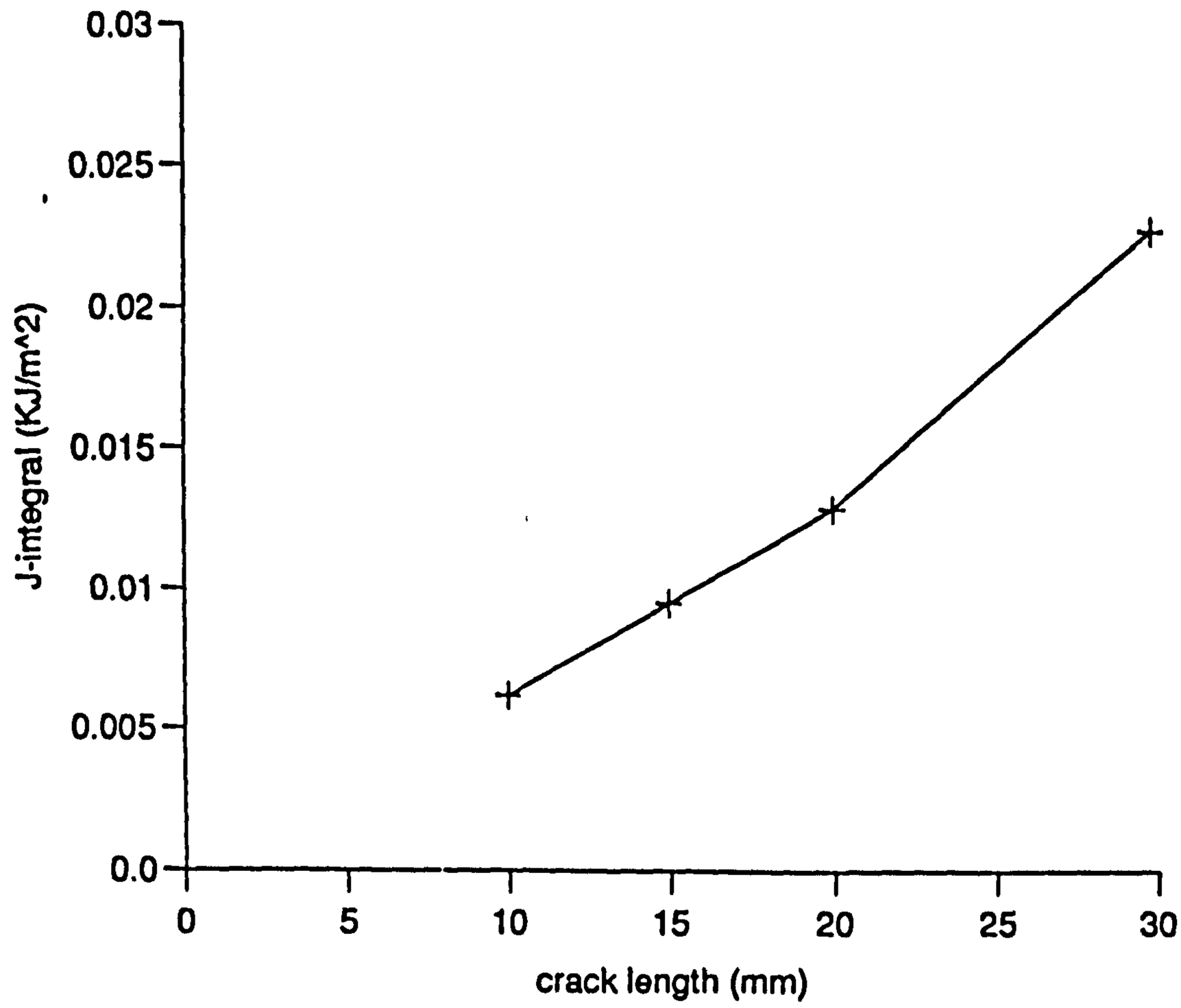

Figure 8.8 J-Integral Values for Straight Cracks of Different Lengths (Crack Depth = 6 mm)

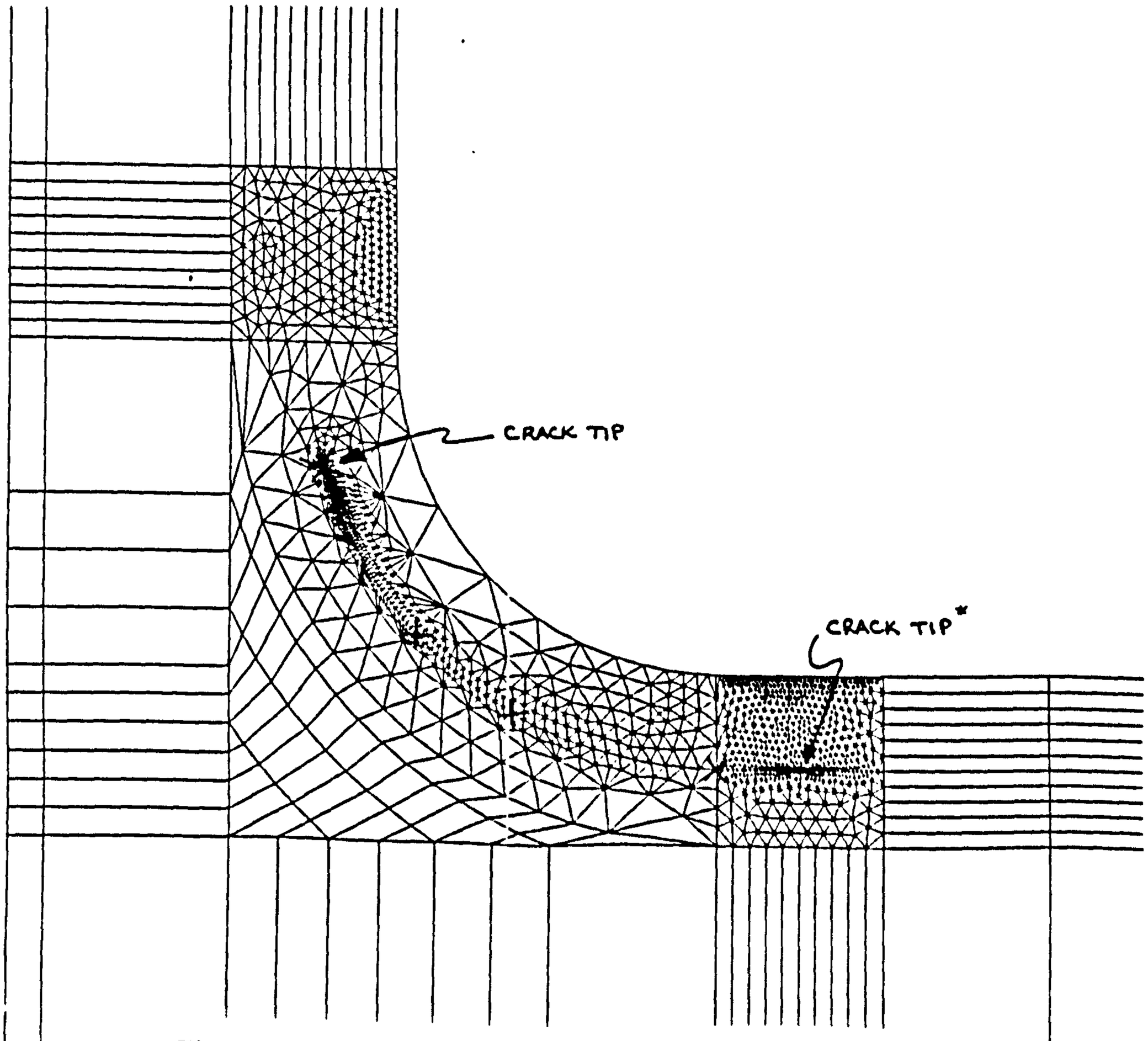

Figure 8.9 Typical FE Mesh Containing a Curved Crack

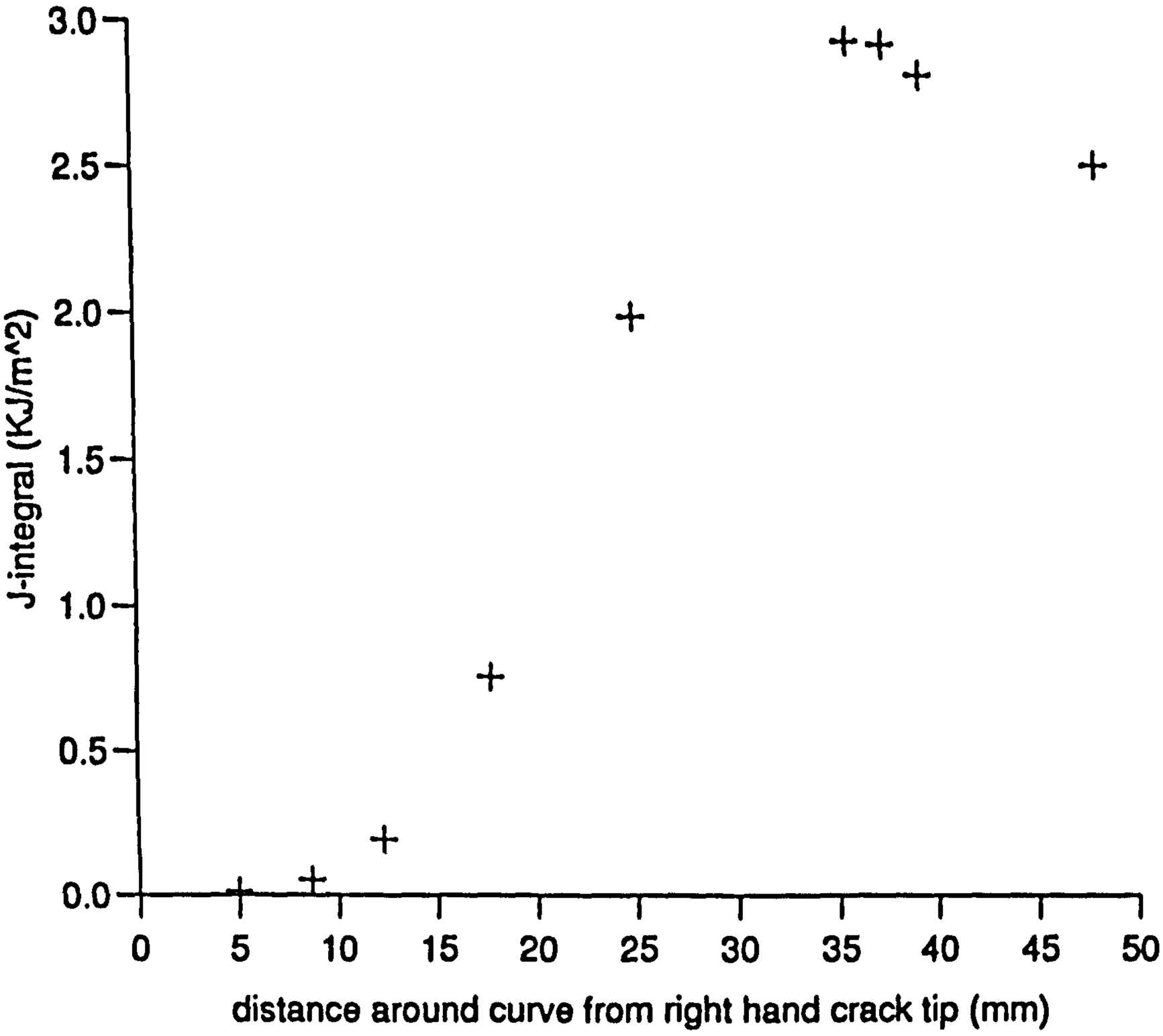

Figure 8.10 J-Integral Values for 9 Curved Crack Lengths (Crack Depth = 6 mm); Values at Right Hand Crack Tip

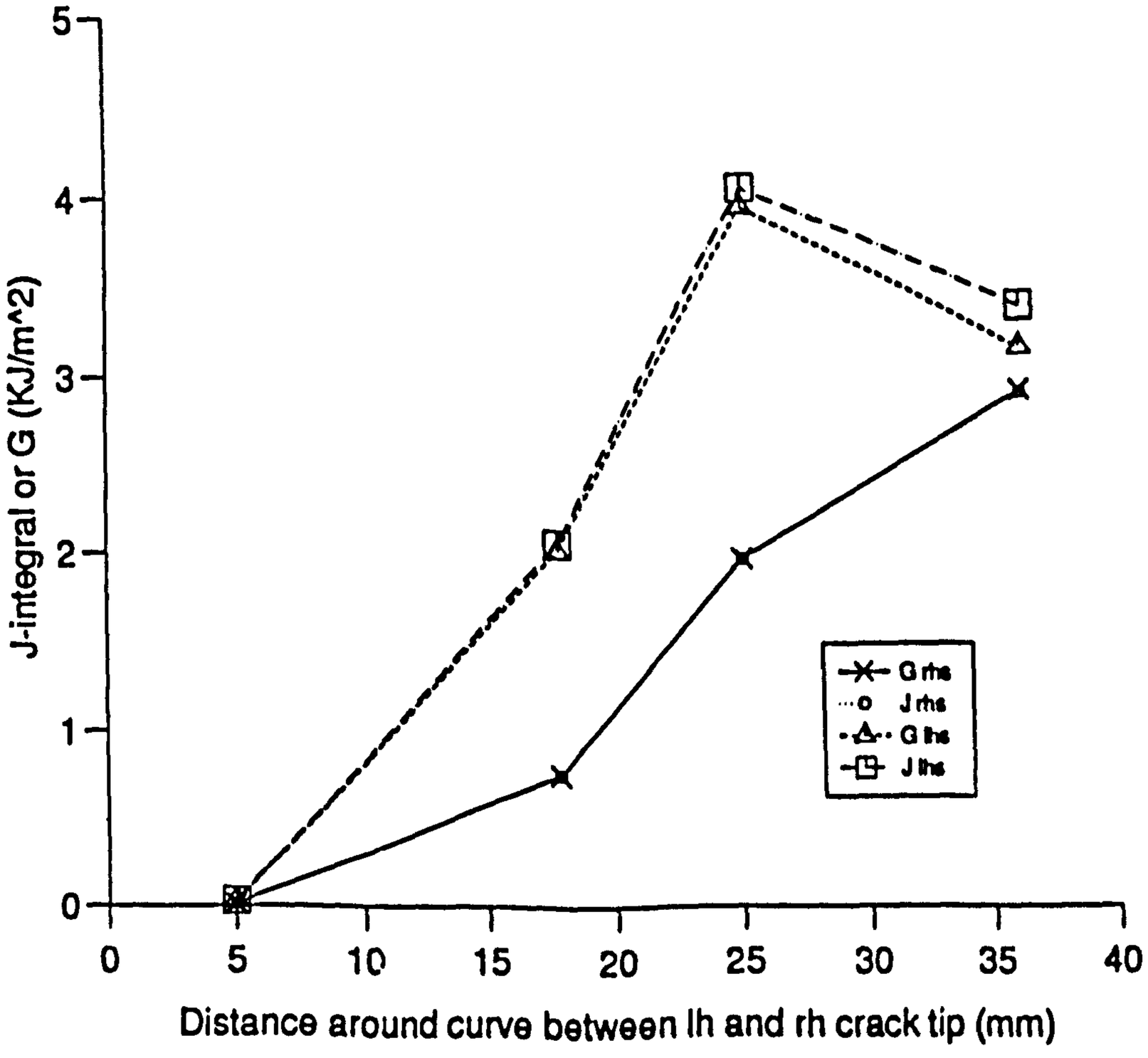

Figure 8.11 J-Integral and Strain Energy Release Rate Values Calculated for Four Crack Lengths at Both Crack Tips

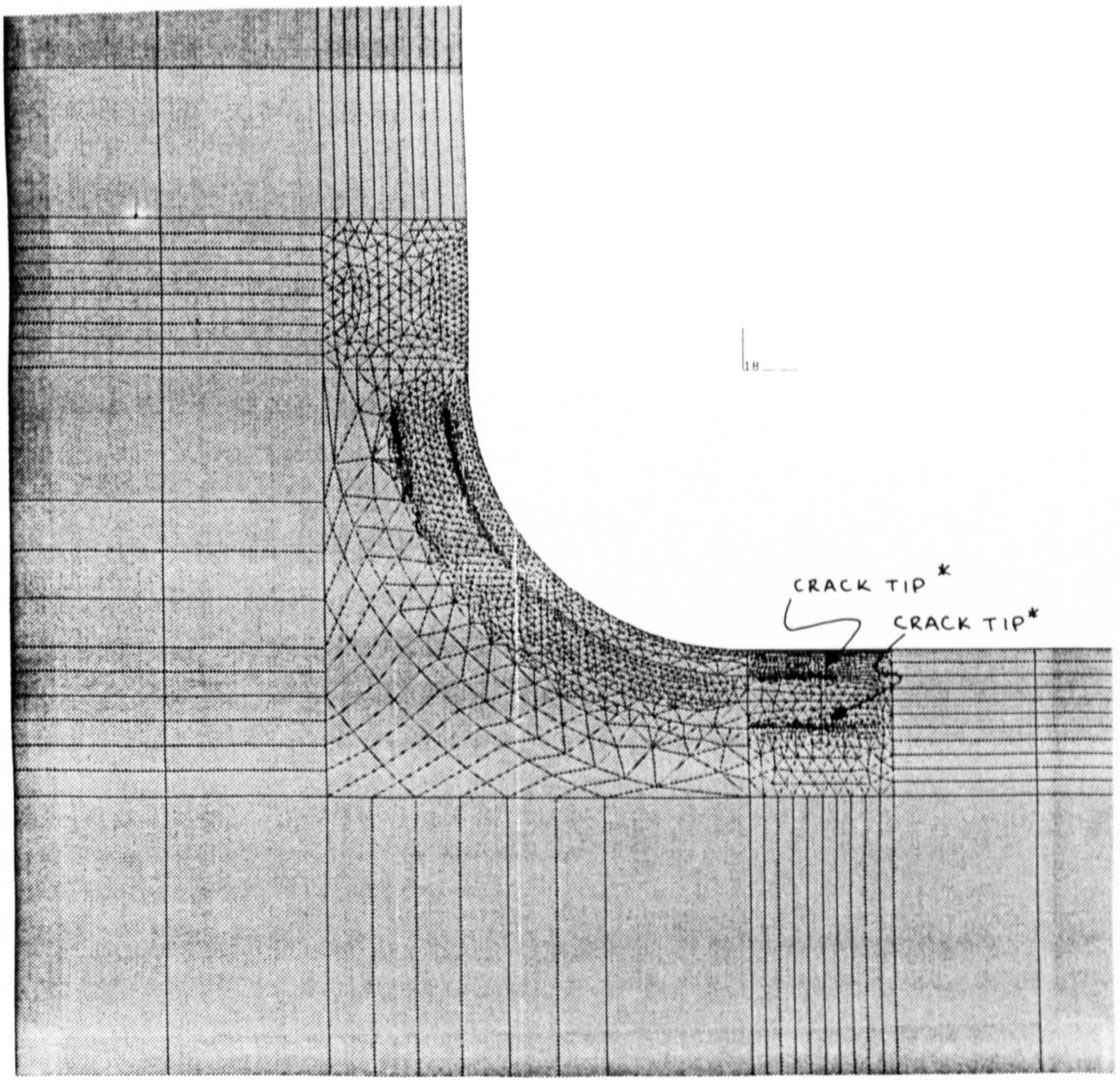

Figure 8.12 FE Model Containing 2 Cracks in the Curved Region of the Overlaminate

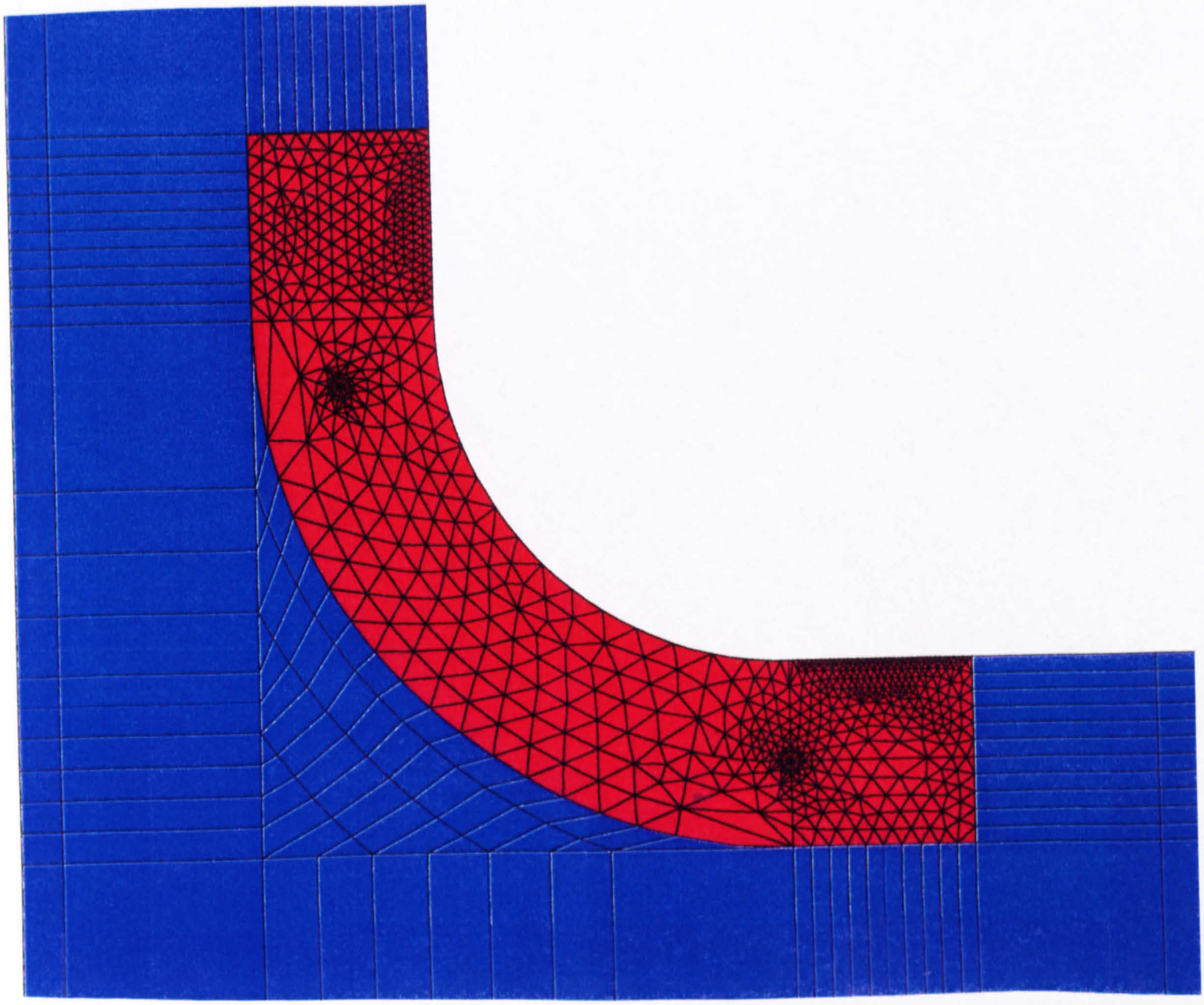

Figure 8.13 FE Model Containing a Curved Crack in the Central Region of the Curved Part of the Overlaminate

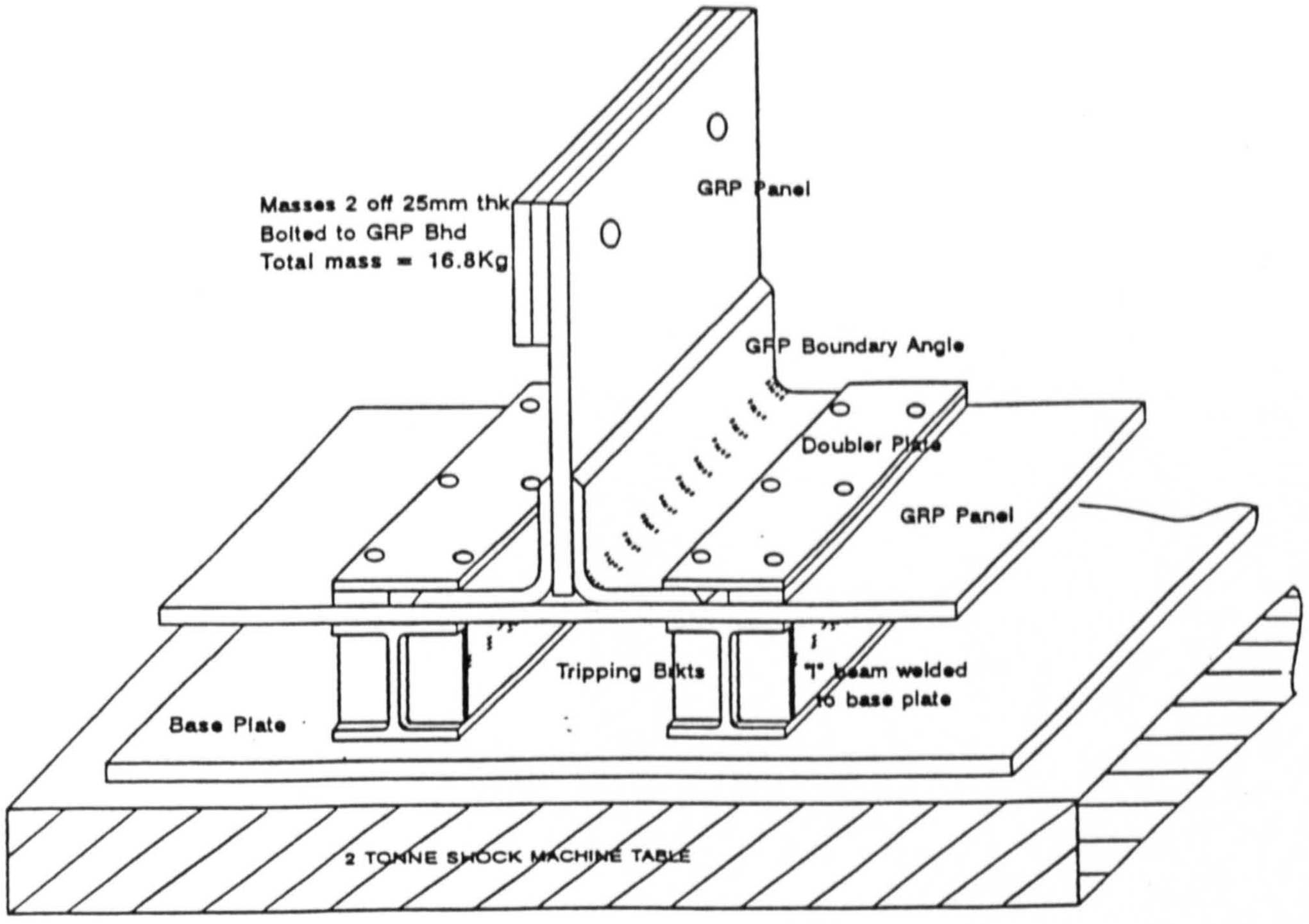

Figure 8.14 Diagram of Shock Tests carried out on Tee Joints (taken from Sumpter)

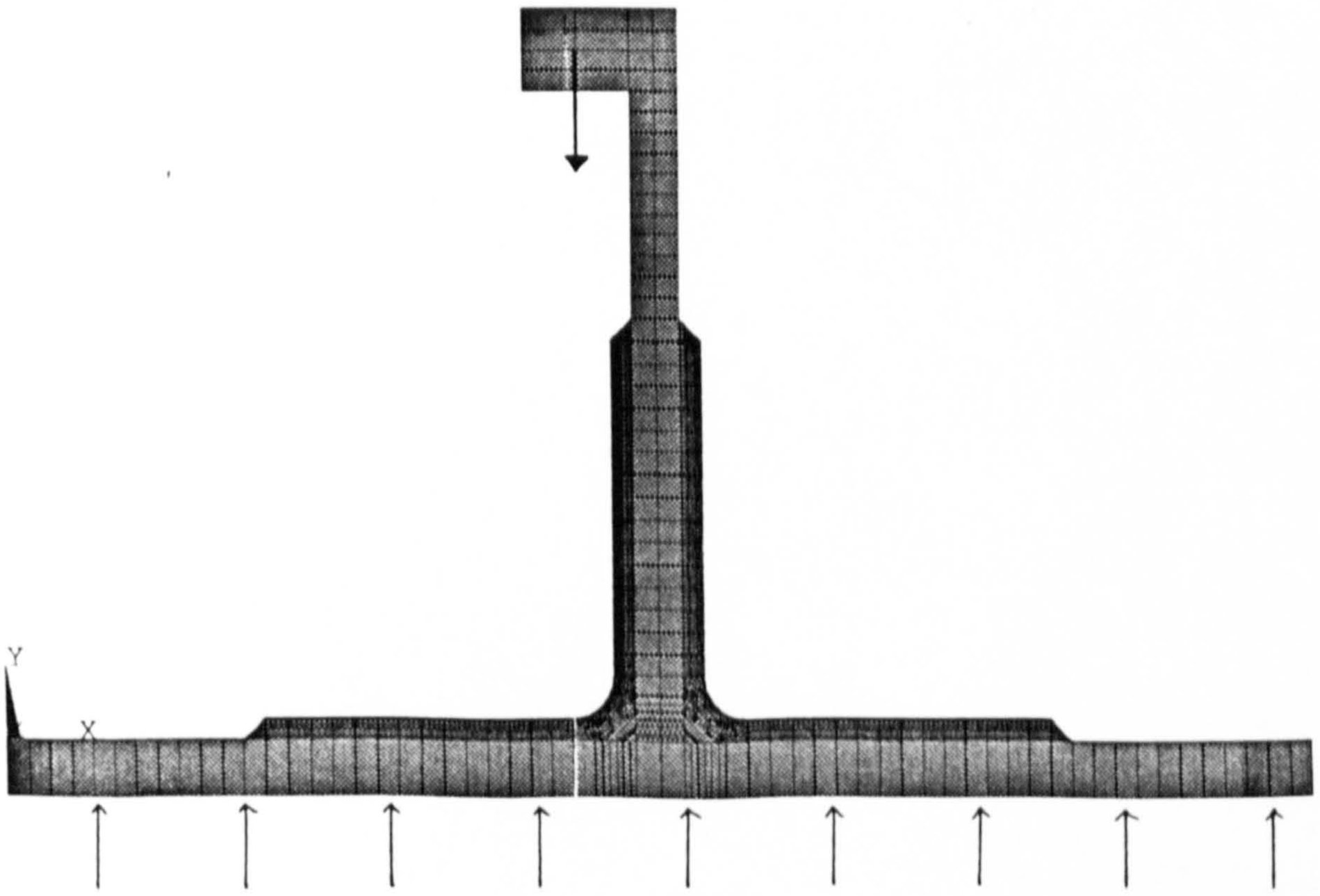

Figure 8.15 FE Representation of Tee Joint with Added Mass

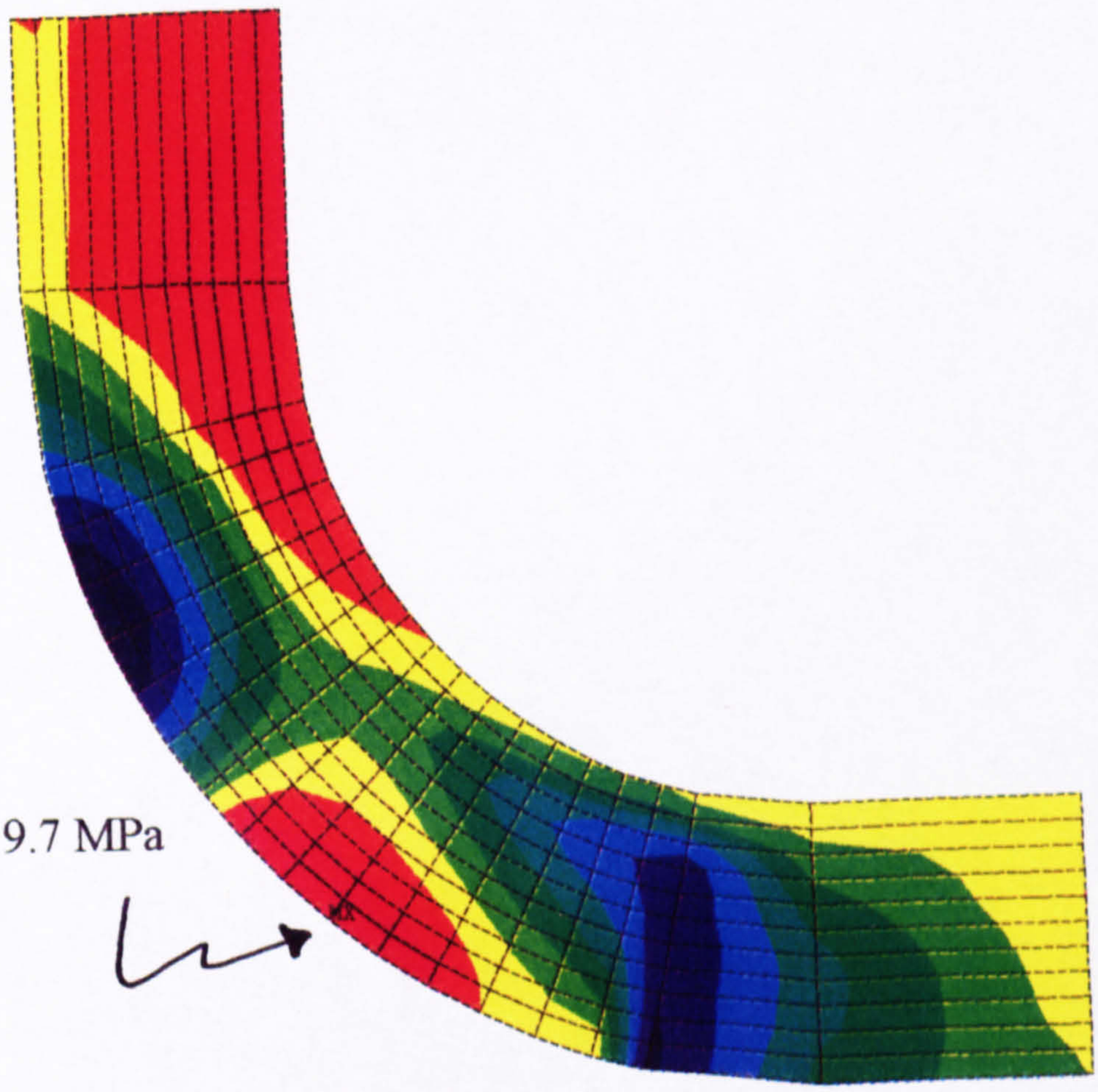

Figure 8.16 FE Generated Through-Thickness Stress Distribution in the Overlaminate under a Simulated Shock Load

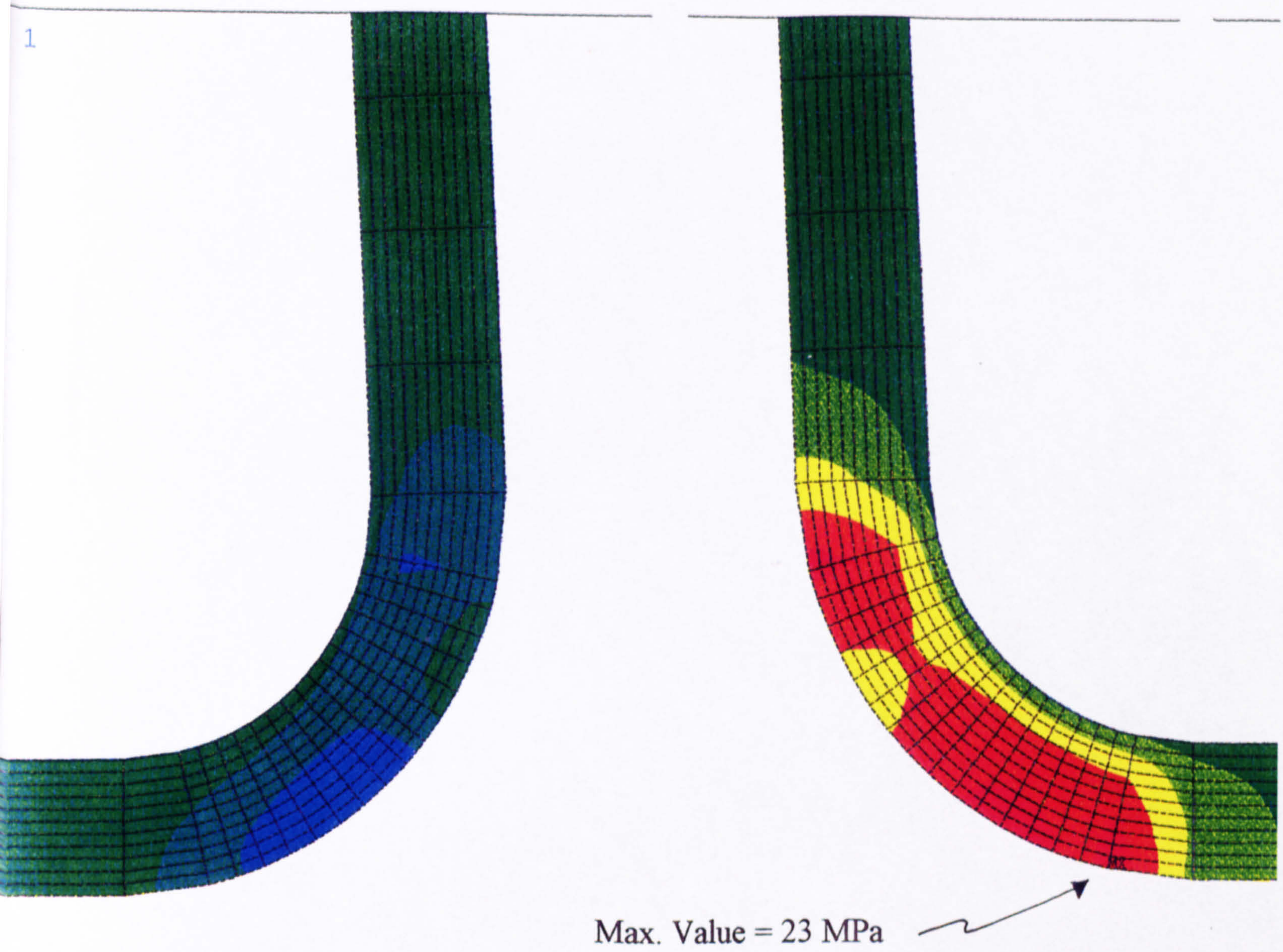

Figure 8.17 Overlaminate Through-Thickness Stress Distribution under a 45 Degree Pull-Off Load

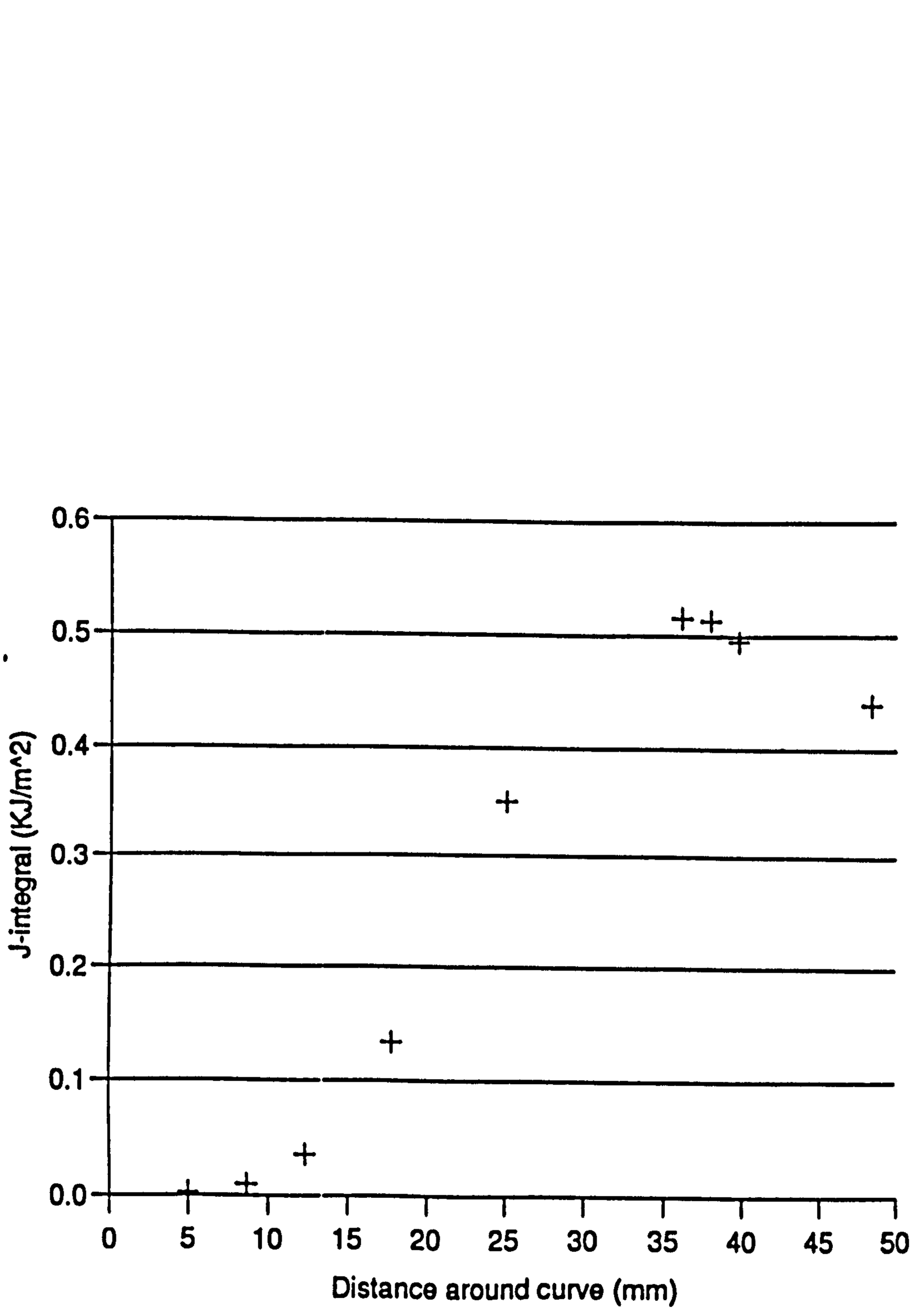

Figure 8.18 J-Integral Values for 9 Curved Crack Lengths Calculated at the Right Hand Crack Tip under a 45 Degree Pull-Off Load of 4.2 kN

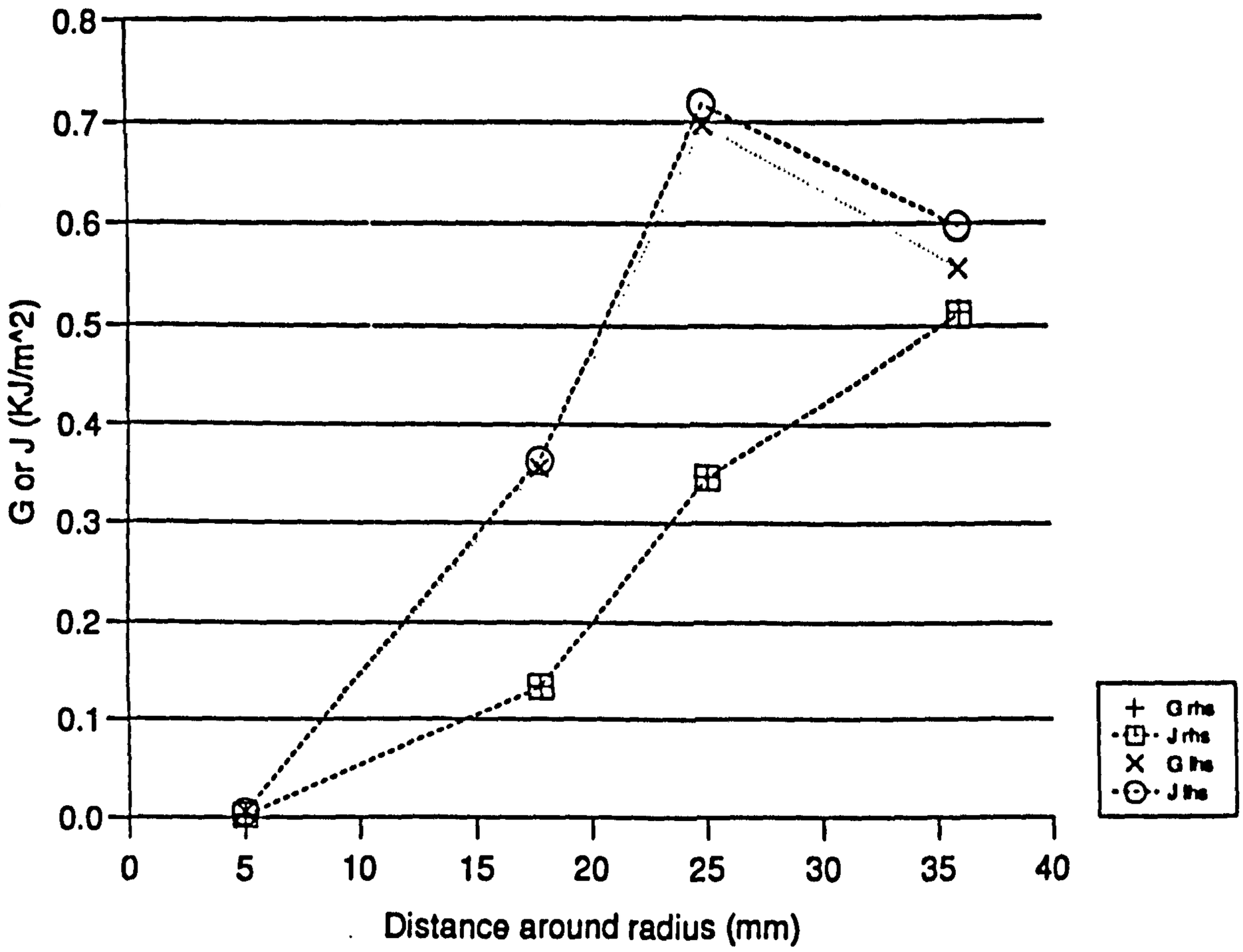

Figure 8.19 J-Integral Values for 4 Curved Crack Lengths Calculated at Both Crack Tips under a 45 Degree Pull-Off Load of 4.2 kN

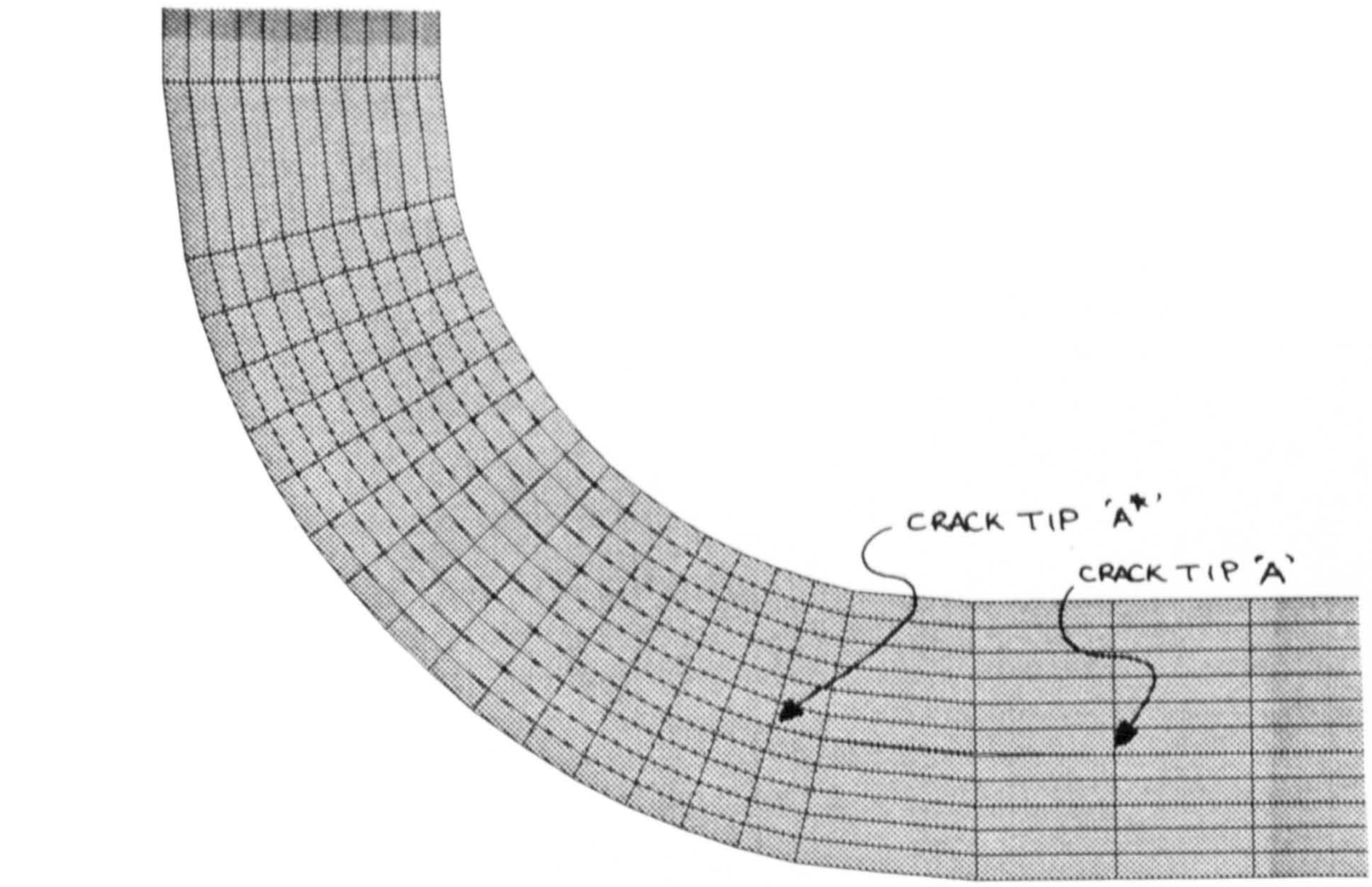

Figure 9.1(a) Finite Element Model (Model (a)) of a Tee Joint Containing One Delamination. (Crack Tips Marked A and A^*)

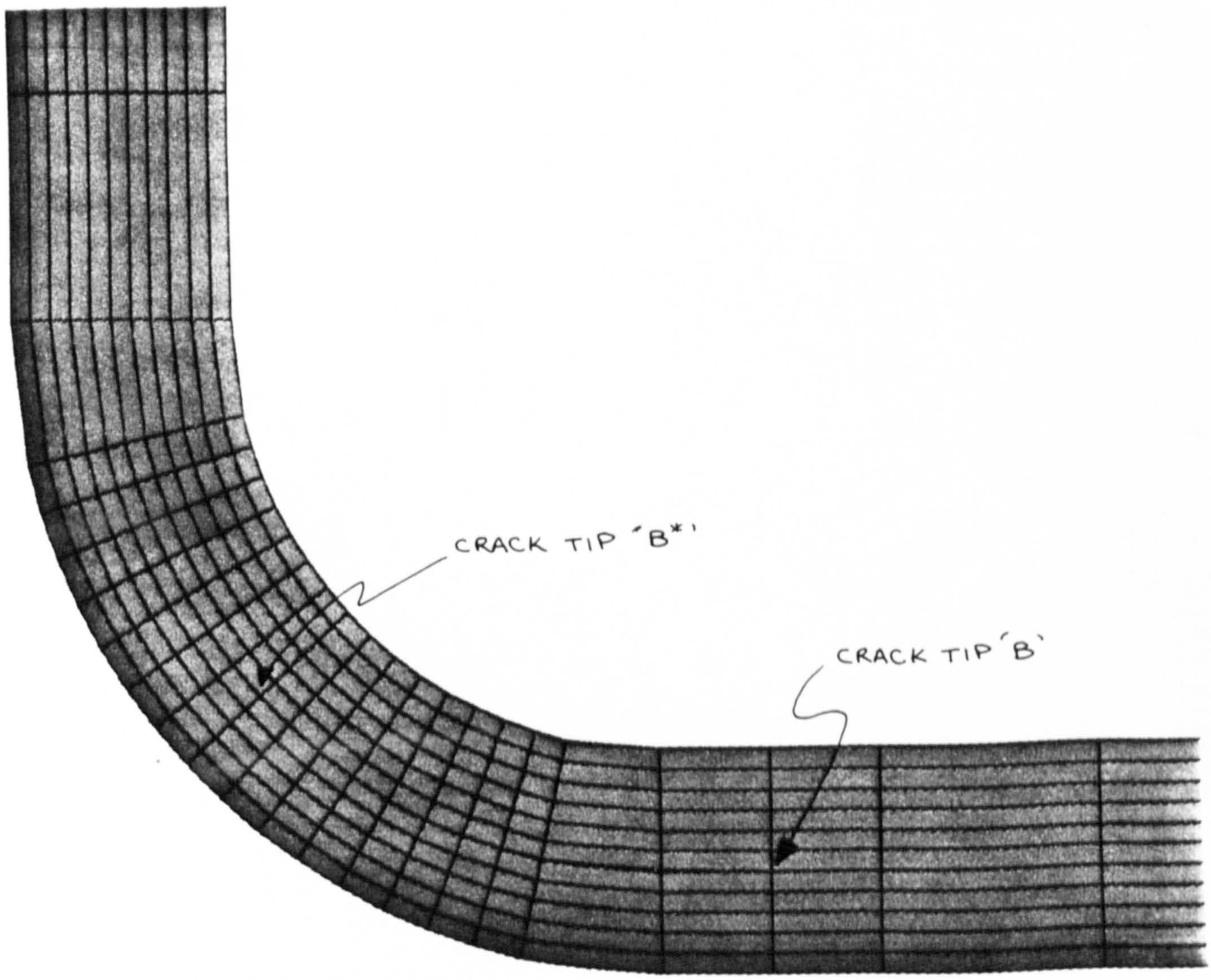

Figure 9.1(b) Finite Element Model (Model (b)) of a Tee Joint Containing One Delamination. (Crack Tips Marked B and B^*)

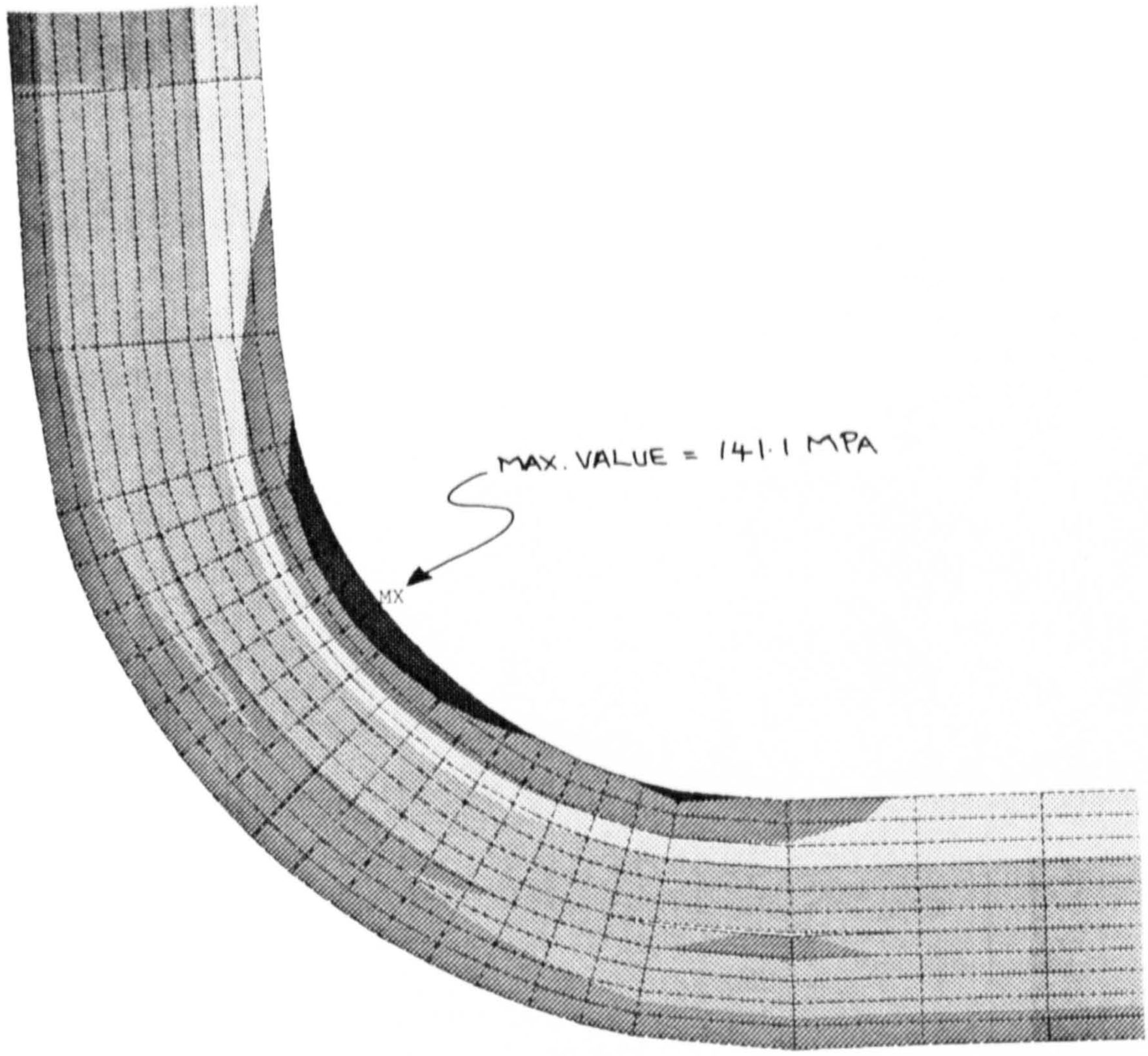

Figure 9.2 Overlaminate In-Plane Stress Distribution for Model (a)

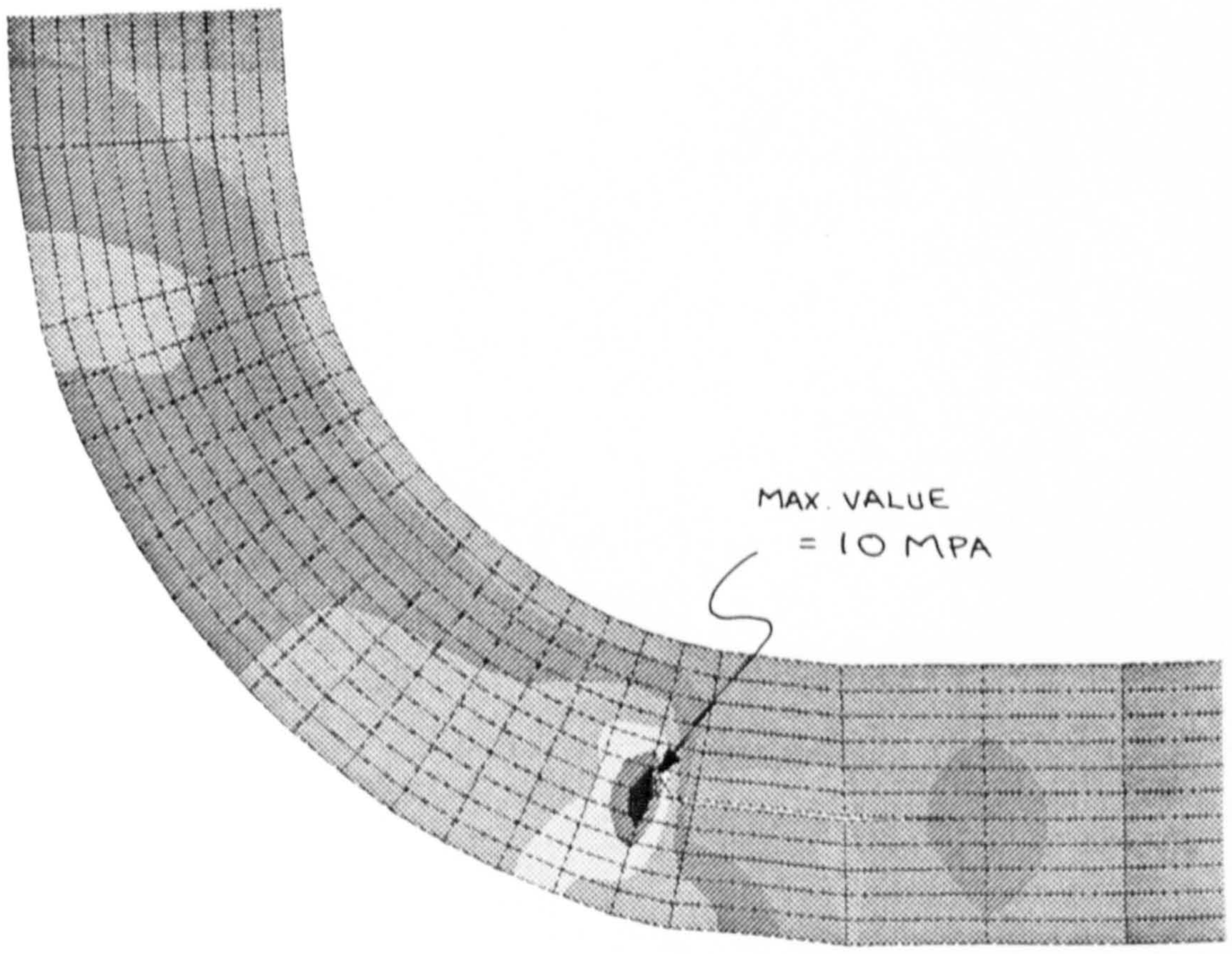

Figure 9.3 Overlaminate Through-Thickness Stress Distribution for Model (a)

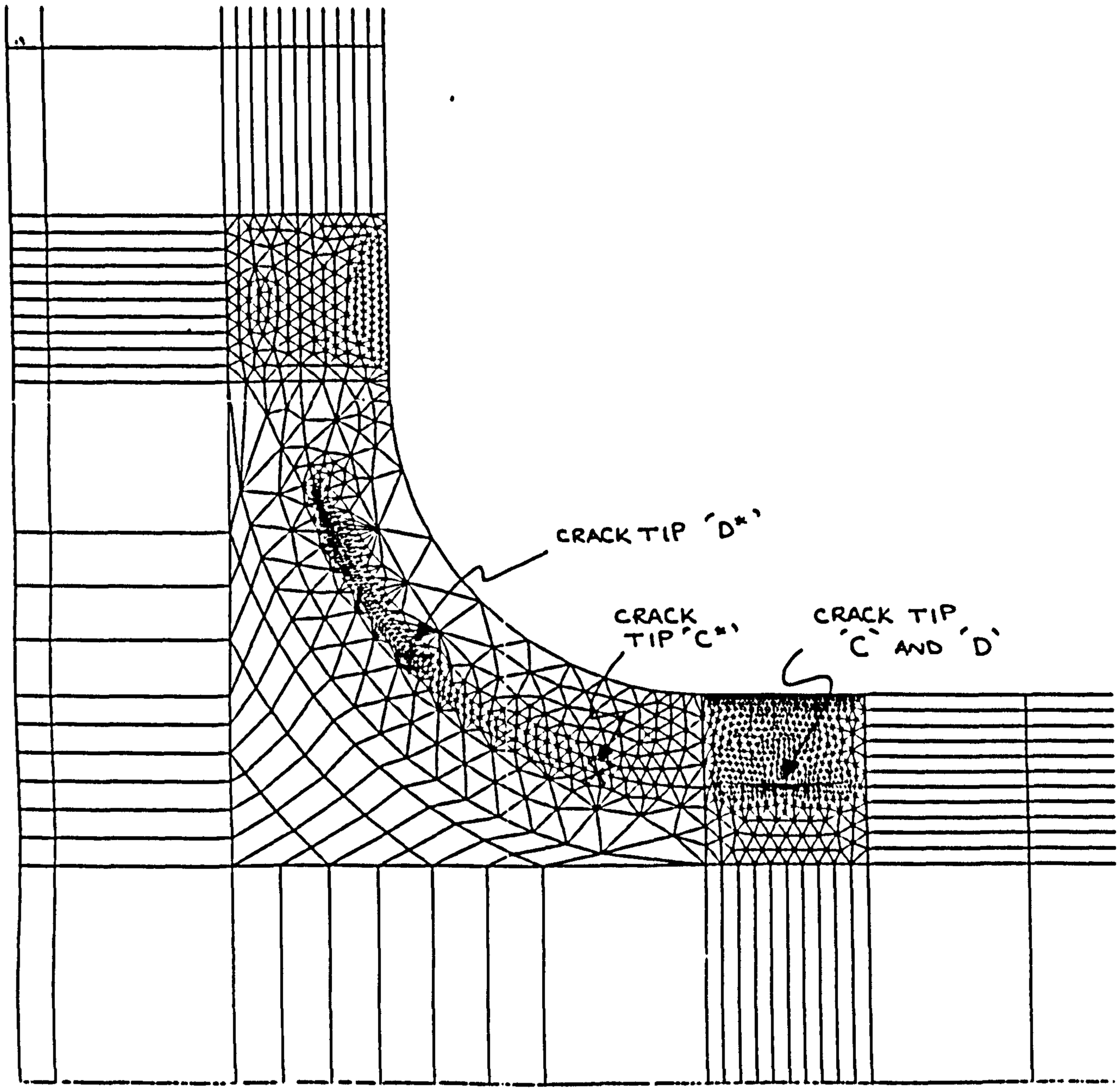

Figure 9.4 Finite Element Model of a Tee Joint Containing Cracks of Two Lengths (Crack Tips Marked C and C*, D and D*)

TABLES

Material	Fibre volume fraction V_f	Specific gravity	Young's modulus E (GPa)	Shear modulus (GPa)	Tensile strength σ_{UT} (MPa)	Compressive strength (MPa)	Shear strength (MPa)	Specific Young's modulus (E/SG)	Specific tensile strength (σ_{UT}/SG)
E-glass polyester (CSM)	0.18	1.5	8	3.0	100	140	75	5.3	67
E-glass polyester (balanced WR)	0.34	1.7	15	3.5	250	210	100	8.8	147
E-glass polyester (unidirectional)	0.43	1.8	30	3.5	750	600		16.7	417
Carbon/epoxy (high-strength balanced fabric)	0.50	1.5	55	12.0	360	300	110	37	240
Carbon/epoxy (high-strength unidirectional)	0.62	1.6	140	15.0	1500	1300		87	937
Kevlar 49/epoxy (unidirectional)	0.62	1.4	50	8.0	1600	230		36	1143

Table 1.1 Typical Mechanical Properties of Selected FRP Laminates (taken from Shenoi & Wellicome)

	Beam Type I	Beam Type II
Gauge Length (mm)	240	240
Width (mm)	50	50
Thickness (mm)	20	12.7
Longitudinal Compressive Modulus (MPa)	18824	29597

Table 4.1 Geometry and Material Properties of Beam Specimens

Number of elements along delamination length	Aspect ratio of elements in delamination region	Critical Stress (MPa) Anal. Results	Critical Stress (MPa) Expt'l Results	Critical Stress (MPa) FE Results	Buckled Shape (FE results)
4	10.0	100.7	71.28	148.64	typical
5	12.5	100.7	71.28	126.78	typical
6	15.0	100.7	71.28	76.47	non-typical
10	25.0	100.7	71.28	7.26	non-typical

Table 4.2 Effect of Number of Elements Modelled along the Delamination Length

Number of elements along delamination length	Aspect ratio of elements in delamination region	Critical Stress (MPa) Anal. Results	Critical Stress (MPa) Expt'l Results	Critical Stress (MPa) FE Results	Buckled Shape (FE results)
1	12.5	104.2	71.28	126.78	typical
2	6.25	104.2	71.28	126.84	typical

Table 4.3 Effect of Number of Elements Modelled across the Width of the Beam Model

Delamination Depth (mm)	Delamination Length (mm)	$E^{\bullet}$ (MPa)	E_P (MPa)
0.53	20	18659	18707
	30	18659	18705
	40	18659	18703
	60	18659	18699
1.06	40	18226	18631
	60	18226	18590
	80	18226	18550
	100	18226	18509
	120	18226	18469
	160	18226	18388
	180	18226	18347
1.59	60	18666	18700
	80	18666	18696
	100	18666	18693
	120	18666	18689
2.12	100	18469	18610
	120	18469	18590

Note : The intact laminate stiffness, E_{LAM} = 18712 MPa in each case
The total laminate thickness is 12.7 mm

Table 4.4 Calculation of laminate stiffness reduction due to partial delamination for the VRT specimens.

Layer Number	Material type	Shear Modulus (MPa)	Poisson's ratio
1	Polyester resin	1320	0.36
2	E-Glass / Polyester & CSM	2750	0.32

Table 4.5 Material Properties of laminate used to represent a resin crack.

Crack Tip	Mode I Stress Intensity Factor (MPa√m)	Mode II Stress Intensity Factor (MPa√m)	Strain Energy Release Rate (kJ/m^2)
Lower Right (model 1)	28.42	0.163	75.82
Lower Left (model 2)	22.24	4.01	47.95
Lower Right (model 2)	22.38	4.03	48.55
Upper Left (model 2)	36.29	9.19	131.6
Upper Right (model 2)	36.29	9.30	131.7

Table 4.6 Calculation of the Strain Energy Release Rate Values for a Square Plate containing Two Straight Cracks

Mode	Max. applied load (MPa)	Non-dimensional stress intensity factor	Critical crack length (mm)
I	7	0.783	66
II	26	0.922	3.00

Table 4.7 Calculation of critical crack lengths for a resin crack

Mode	Crack length (mm)	Non-dimensional stress intensity factor	Applied load at propagation (MPa)
I	10	0.783	18.1
II	10	0.922	15.3

Table 4.8 Calculation of applied loads to cause a 10 mm resin crack to propagate

Material	Location	Property	Value
Polyester/ Woven Roving Glass	Stiffener,Flange and Overlaminate	Ex	13060 MPa
		Ey	7770 MPa
		nuxy	0.25
Urethane Acrylate	Fillet	Ex	1500 MPa
		Ey	1500 MPa
		nuxy	0.25
Core Material		Ex	10^{-6} MPa
		Gxy	10^{-6} MPa
		nuxy	0.25

Table 5.1. Material Properties used in the Finite Element Models

Top Hat Type	Three Point Bending (3PB)		Reverse Bending (RB)		Straight Pull Off (PO)	
	FE (N/mm)	Expt. (N/mm)	FE (N/mm)	Expt. (N/mm)	FE (N/mm)	Expt. (N/mm)
Type I	731.2	696.8	713.0	384.6	620.6	1000
Type II	820.9	740.7	639.1	303.0	639.0	880.0

Table 5.2 Values of Initial Stiffness for Both Types of Top Hat Stiffener

Experimental Stiffness = 342.6 N/mm		
Original FE model Stiffness = 713 N/mm		
Study Carried Out	Value used	FE model Stiffness (N/mm)
A	- 20 %	573.6
B	- 20 %	622.6
C	640 mm	523.9
D	- 40 mm	693.9
E	Second combination	458.4
F	Core Modulus = 10^{-10} MPa	713
G	Includes Fillet Void	712
H	Includes Steel Plate	679

Table 5.3 Results of the Sensitivity Study for the Type I Top Hat under a Reverse Bending Load

Experimental Stiffness = 1000 N/mm		
Original FE model Stiffness = 620.64 N/mm		
Study Carried Out	Value used	FE model Stiffness (N/mm)
A	+ 20 %	742.1
B	+ 20 %	623.2
C	560 mm	734.3
H	Includes Steel Plate	930.0

Table 5.4 Results of the Sensitivity Study for the Type I Top Hat under a Pull-Off Load

Loading Condition	Failure Mode	Type I	Type II
Three Point Bending (3PB)	Initial	Fillet to top hat interface followed by progressive delaminations in curved part of overlaminate	Progressive delaminations in curved part of overlaminate
	Final	Flexural failure of inner surface of flange plate	Flexural failure of inner surface of flange plate
Reverse Bending (RB)	Initial	Through fillet cracking	None
	Final	Flexural failure of outer surface of flange plate	Flexural failure of outer surface of flange plate
Straight Pull Off (PO)	Initial	Fillet Cracking	None
	Final	Failure of one side of top hat interface with flange plate	Failure of one or both sides of top hat interface with flange plate

Table 5.5 Experimental Failure Modes for both types of Top Hat Stiffener

		Stress (M.Pa)									
		Fillet		Overlaminate				Flange			
Test	Load			In-plane		Through-thickness		In-plane		Through-thickness	
	(KN)	Value	Location	Value	Location	Value	Location	Value	Location	Value	Location
Three point bend	13.5	14.81		55.08	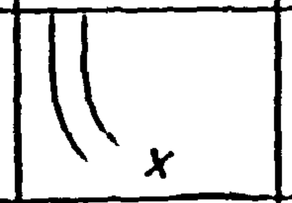	75.95	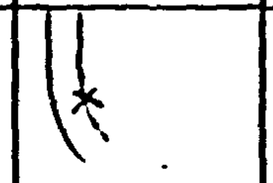	170.52		5.03	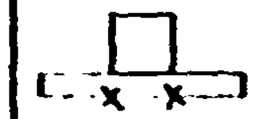
Three point bend	16.5	18.09		67.33	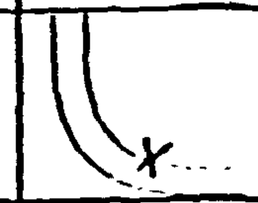	92.83	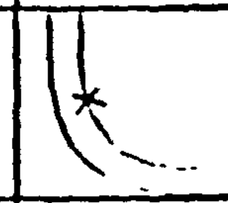	208.42	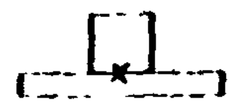	6.15	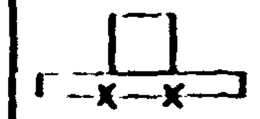
Reverse Bend	5.0	4.80		7.63	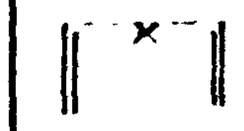	21.31	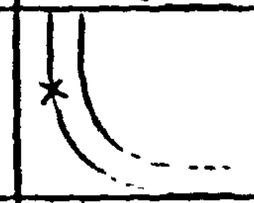	34.56		0.86	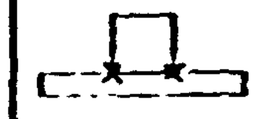
Reverse Bend	14.0	13.44		21.36	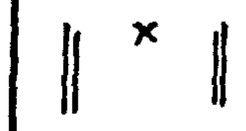	59.67	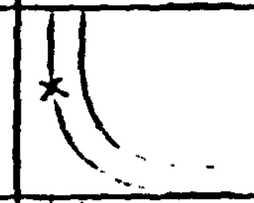	96.77	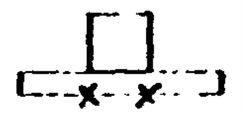	2.41	
Pull-Off	5.5	6.16	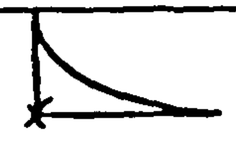	21.77		38.03		34.69		2.18	
Pull-off	7.0	7.84	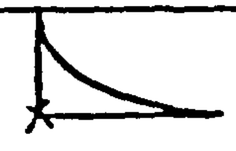	27.71		48.4		44.15		2.77	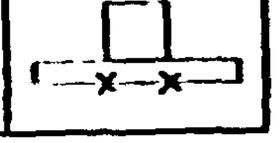

Table 5.6 Locations of Maximum Stresses for the Type I Stiffener

		Stress (M.Pa)									
		Fillet		Overlaminate				Flange			
Test	Load			In-plane		Through-thickness		In-plane		Through-thickness	
	(KN)	Value	Location	Value	Location	Value	Location	Value	Location	Value	Location
Three point bend	12.5	23.76	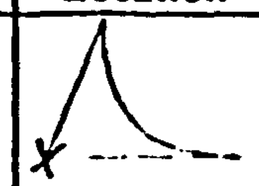	55.42	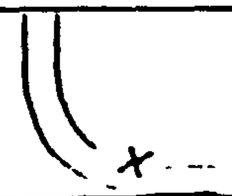	65.87		157.54		6.46	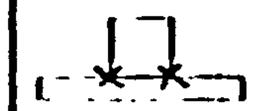
Three point bend	14.5	27.56	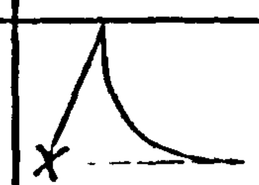	64.28	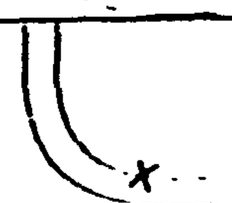	76.41	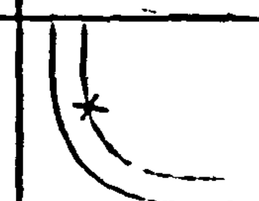	182.75		7.59	
Reverse bend	17.0	5.08		28.80	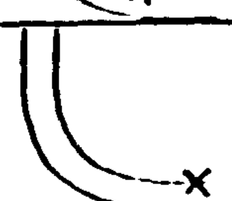	4.74	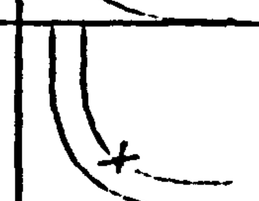	89.89		8.97	
Pull-off	15.0	10.42	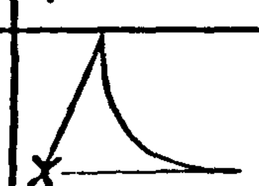	27.35	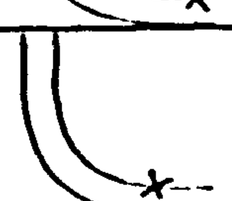	49.68	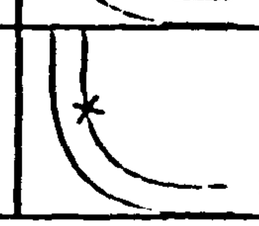	33.16		2.90	

Table 5.7 Locations of Maximum Stresses for the Type II Stiffener

Material	Location	Property	Value
Polyester/ Woven Roving Glass	Web,Flange and Overlaminate	Ex	13060 MPa
		Ey	7770 MPa
		nuxy	0.25
Polyester/CSM	Overlaminate	Ex	6890 MPa
		Ey	7770 MPa
		nuxy	0.25
Urethane Acrylate	Fillet	Ex	1500 MPa
		Ey	1500 MPa
		nuxy	0.25

Table 6.1 Material Properties used in the Finite Element Models

model no.	Load (N)	Max. defl'n (mm)	Max. fillet prin. stress (MPa)	Pos'n	Max. o/lam In-Plane stress (MPa)	Pos'n	Max. o'lam thru-thk. stress (MPa)	Pos'n
1	5500	3.045	8.541		53.10		6.314	
A	5500	3.164	10.79		38.33		6.47	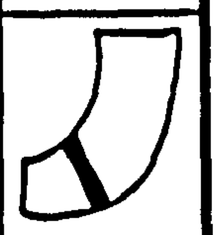
B	5500	3.03	11.26		40.4	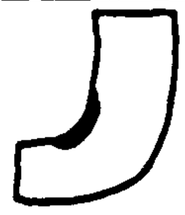	6.74	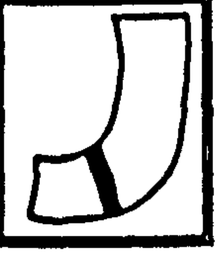

Table 6.2 Comparison of Stresses and Deflections of the two Methods (A and B) used to Calculate the Overlaminate Material Properties

LOAD	DEFL'N	FILLET STRESS S1	POS'N.	O/LAM IN-PLANE STRESS	POS'N.	O/LAM THRO' THICK. STRESS	POS'N
(N)	(mm)	(MPa)		(MPa)		(MPa)	
5500	3.045	8.541		53.10		6.314	

Table 6.3 Stress and Deflection results for Model 1

REFERENCE	LOAD (N)	DESCRIPTION
A	5500	Crack appeared in Fillet
B	7500	First Delamination appeared in Overlaminate
C	10000-15000	Continuing Delamination Development
D	19000	Final Failure : Delaminations present along the overlaminate/web & overlaminate/flange interfaces

Table 6.4 Experimental Failure Patterns

MODEL/EXPT.	LOAD (N)	DEFLECTION (mm)	STIFFNESS (N/mm)
FULL 2D FE MODEL	5500	3.045	1806
EXPERIMENT	5500	3.438	1600

Table 6.5 Validation of Initial Stiffness of 2D FE Model.

LOAD STEP NO.	LOAD (N)	DEFLN (mm)	FILLET σ_P (MPa)	FILLET E_P ($\times 10^{-2}$ MPa)	OVER LAM. $\sigma_{i\text{-}p}$ (MPa)	OVER LAM.$\sigma_{i\text{-}t}$ (MPa)
1	5500	3.045	8.56	0.542	53.07	6.31
3	7600	4.207	11.84	0.750	73.33	8.72
7	13000	7.197	20.25	1.28	125.4	14.92
9	19000	10.52	29.60	1.87	183.3	21.81

Table 6.6 Selection of Deflection and Stress Values including Non-Linear Fillet Material.

LOAD STEP NO.	LOAD (N)	DEFLN (mm)	FILLET σ_P (MPa)
1	5500	3.05	8.57
9	19000	10.56	29.61

Table 6.7 Selection of Deflection and Fillet Stress Results including Non-Linear Fillet Material and Non-Linear Geometry.

LOAD	DEFL'N	FILLET STRESS S1	POS'N.	O/LAM IN-PLANE STRESS	POS'N.	O/LAM THRO' THICK. STRESS	POS'N
(N)	(mm)	(MPa)		(MPa)		(MPa)	
5500	3.045	8.541		53.10		6.314	

Table 6.8 Stress and Deflection results for Model 1

LOAD	DEFL'N	FILLET STRESS S1	POS'N.	O/LAM IN-PLANE STRESS	POS'N.	O/LAM THRO' THICK. STRESS	POS'N
(N)	(mm)	(MPa)		(MPa)		(MPa)	
5500	3.06	8.603		54.00		6.33	
6000	3.339	9.384		58.90		6.90	
6500	3.62	10.198		63.79		7.47	
7000	3.90	10.967		68.68		8.04	
7500	4.18	11.753		73.58		8.61	

Table 6.9 Stress and Deflection results for Model 2

LOAD	DEFL'N	FILLET STRESS S1	POS'N.	O/LAM IN-PLANE STRESS	POS'N.	O/LAM THRO' THICK. STRESS	POS'N
(N)	(mm)	(MPa)		(MPa)		(MPa)	
5500	3.11	10.89		59.09		5.90	
7500	4.25	14.69		80.46		8.05	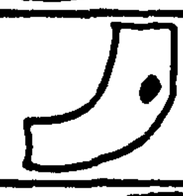
9000	5.10	16.75		96.44		9.66	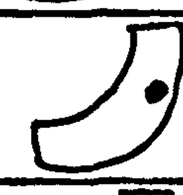
10000	5.68	17.18		107.06		10.73	
13000	7.46	18.16		139.31		13.95	
15000	8.70	18.96		161.49		16.10	
19000	11.39	20.40		211.18		20.39	

Table 6.10 Stress and Deflection results for Model 3

LOAD	DEFL'N	FILLET STRESS S1	POS'N.	O/LAM IN-PLANE STRESS	POS'N.	O/LAM THRO' THICK. STRESS	POS'N
(N)	(mm)	(MPa)		(MPa)		(MPa)	
10000	6.10	19.93	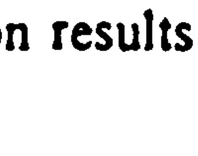	119.8		5.46	
15000	9.40	21.22		180.42		8.20	
19000	12.27	21.41		232.41		10.383	

Table 6.11 Stress and Deflection results for Model 4

LOAD	DEFL'N	FILLET STRESS S1	POS'N.	O/LAM IN-PLANE STRESS	POS'N.	O/LAM THRO' THICK. STRESS	POS'N
(N)	(mm)	(MPa)		(MPa)		(MPa)	
5500	4.26	6.982		77.675		0.524	
7500	5.80	10.544		105.82		0.714	
9000	6.95	11.379		126.89		0.857	
10000	7.72	12.257		140.97		0.953	
13000	10.07	16.304		184.39		1.24	
15000	11.67	17.174		213.77		1.43	
16000	12.49	16.870		228.35		1.52	
17000	13.33	17.481		242.49		1.62	
18000	14.17	17.702		256.03		1.71	
19000	15.02	17.795		268.99		1.81	

Table 6.12 Stress and Deflection results for Model 5

LOAD	DEFL'N	FILLET STRESS S1	POS'N.	O/LAM IN-PLANE STRESS	POS'N.	O/LAM THRO' THICK. STRESS	POS'N
(N)	(mm)	(MPa)		(MPa)		(MPa)	
5500	5.17	11.69		47.62		0.599	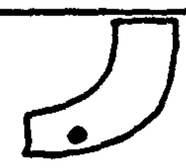
9000	8.50	16.26		79.618		0.981	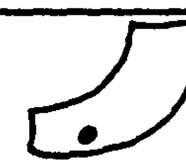
10000	9.47	15.166		89.33		1.09	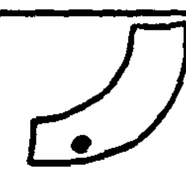
13000	12.45	16.873		119.31		1.42	
15000	14.50	16.941	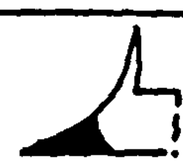	140.27		1.63	
18000	17.60	17.012	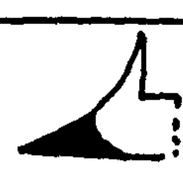	171.76		1.96	
19000	18.64	17.057		182.24		2.07	

Table 6.13 Stress and Deflection results for Model 6

Material Changed	Property changed	Old value / New value	Deflection (mm)	Fillet S_P (MPa)	O/Lam S_{i-p} (MPa)	O/Lam S_{t-t} (MPa)
-	Base Model	-	3.045	8.56	53.07	6.31
Fillet	E	1500/500 MPa	3.25	8.32	59.92	7.81
Fillet	E	1500/2500 MPa	2.98	8.95	50.74	6.37
Fillet	E	1500/3500 MPa	2.94	9.04	49.63	6.29
Poly/WR	υ_{xy}	0.25/0.15	3.15	8.69	54.37	6.16
Poly/WR	υ_{xy}	0.25/0.35	2.89	8.40	51.70	6.21

Table 6.14 Effect of changing the Assumed Material Properties in the FE Model 1 for a load of 5500 N

MODEL NO.	LOAD (N)	MATERIAL CHANGED	E_{ip} (MPa)	E_{t-t} (MPa)	DEFL'N (mm)
3	7500	-	CSM:6890 WR:13060	CSM:7770 WR:7770	4.246
3	7500	CSM	3445	7770	4.251
3	7500	CSM	6530	3885	4.252
3	7500	WR	6530	7770	4.252

Table 6.15 Effect of Reducing Material Propeties of Elements Adjacent to Delamination.

MODEL NO.	LOAD (N)	LOCATION OF VOID(S)	FILLET MAX. PRINCIPAL STRESS (MPa)	FILLET MAX. PRINCIPAL STRAIN (%)
1	5500	NONE	8.56	0.54
1	5500		8.56	0.54
1	5500		14.25	0.80
1	5500		14.32	0.8
1	5500		9.32	0.6
1	5500		11.66	0.67
1	5500		10.31	0.564
1	5500		10.52	0.565
1	5500		8.81	0.56
1	5500		8.55	0.543

Table 6.16 Effect of Voidage on the Maximum Fillet Principal Stress

Material	Location	Property	Value
Polyester/ Woven Roving Glass	Stiffener, Flange and Overlaminate	Ex	13060 MPa
		Ey	7770 MPa
		nuxy	0.25
Urethane Acrylate	Fillet	Ex	1500 MPa
		Ey	1500 MPa
		nuxy	0.25
Core Material		Ex	10^{-6} MPa
		Gxy	10^{-6} MPa
		nuxy	0.25
Crack Elements	Cracked Region	E	10000 MPa
		nu	0.25

Table 7.1. Material Properties used in the Finite Element Models

Material	Location	Property	Value
Polyester/ Woven Roving Glass	Web,Flange and Overlaminate	Ex	13060 MPa
		Ey	7770 MPa
		nuxy	0.25
Polyester/CSM	Overlaminate	Ex	6890 MPa
		Ey	7770 MPa
		nuxy	0.25
Urethane Acrylate	Fillet	Ex	1500 MPa
		Ey	1500 MPa
		nuxy	0.25
Crack Elements	Cracked Region	E	10000 MPa
		nu	0.25

Table 8.1 Material Properties used in the Finite Element Models.

G (analytical) kJ/m^2	G (finite element) kJ/m^2	J-integral (finite element) kJ/m^2
4712	4003	4085

Table 8.2 Verification of the J-Integral.

Angle of orientation (degrees)	G at left hand tip (kJ/m^2)	J at left hand tip (kJ/m^2)	G at right hand tip (kJ/m^2)	J at right hand tip (kJ/m^2)
0	3.098	3.000	3.048	3.306
30	3.152	3.172	3.132	3.230
60	2.839	2.981	2.823	2.947

Table 8.3 J-Integral and G values calculated for cracks at three orientations.

	45 Degree Pull Off Load	Three Point Bending
Elastic Modulus, E (MPa)	10000	10000
Poisson's Ratio, NU	0.25	0.25
Supports	Clamped	Clamped
Crack Length (mm)	10	10
Crack Depth (no. of plies from outer surface)	8	8
Applied Load (N)	5000	5000
Constraint Position from LH and RH edges of Joint model (mm)	50	50
J-Integral (kJ/m^2) $\times 10^{-3}$	1.46	0.643

Table 8.4 Effect of Loading Condition on the J-integral.

	Clamped Boundaries	Simple Supports
Elastic Modulus, E (MPa)	10000	10000
Poisson's Ratio, NU	0.25	0.25
Applied Load Configuration	45 Degree Pull Off Load	45 Degree Pull Off Load
Crack Length (mm)	10	10
Crack Depth (no. of plies from outer surface)	8	8
Applied Load (N)	5000	5000
Constraint Position from LH and RH edges of Joint model (mm)	190	190
J-Integral (kJ/m^2) $\times 10^{-3}$	36.9	36.7

Table 8.5 Effect of Boundary Condition on the J-integral.

Crack Tip	Mode I Stress Intensity Factor (MPa√m)	Mode II Stress Intensity Factor (MPa√m)	Strain Energy Release Rate (kJ/m^2)
Lower right (model 1)	5.51	0.26	2.82
Lower right (model 2)	3.33	0.18	1.04
Upper right (model 2)	0.71	2.38	0.58

Table 8.6 Mode I and Mode II Stress Intensity Factors and Strain Energy Release Rates for Two Curved Overlaminate Cracks.

APPENDICES

APPENDIX 2A. FRACTURE MECHANICS CRITERIA - A REVIEW

2A.1 Introduction

The first steps towards the analysis of fracture - dominated problems was taken by Griffith in 1920 who analysed the propagation of brittle cracks in glass. Griffith derived the concept that an existing crack will propagate if the total energy of the system is lowered. He assumed that a simple energy balance exists consisting of a decrease in the elastic strain energy stored within the stressed body as the crack extends which is counteracted by the energy required to create the new crack surfaces. A couple of decades later, Irwin pointed out that the energy balance must be between the stored strain energy and the surface energy plus the work done in plastic deformation. Irwin also recognised that the energy required to form new crack surfaces is generally insignificant compared with the work done in plastic deformation in the case of ductile materials. He defined a material property, G, the strain energy release rate, as the total energy absorbed during cracking per unit increase in crack length and per unit thickness.

A paper by Irwin discusses the application of fracture mechanical concepts to large welded structures. He came to the conclusion that if the nominal stress in a structure of mild steel plates never exceeds 30,000 psi then a crack which forms and extends into a plate of the structure should not go unstable until it has developed to a length of 4 inches. The critical crack length for a stress of 15,000 psi would be four times as large. It is this type of damage tolerance calculations which are required for composite materials used in the marine industry.

Owing to the complexity of certain structures used in the construction of ships such as tee joint connections and top hat stiffeners it is not possible to entirely use analytical techniques to calculate damage tolerance levels. It is, however, possible to combine numerical analyses such as finite element modelling along with analytical techniques to calculate fracture mechanics criteria to yield critical crack lengths, for example. The paragraphs which follow discuss the fracture mechanics criteria which have been used in the analysis of isotropic plates (Chapter 4), top hat stiffeners (Chapter 7) and tee joints (Chapter 8).

2A.2 Linear-Elastic Fracture Mechanics (LEFM)

2A.2.1 Elastic Stress Field Approach.

From linear elastic theory, Irwin developed the stress intensity approach. In the region of the crack tip, the stress intensity factor, K, can determine the magnitude of the elastic stresses. The value of K, shown in Equation 2A.1 depends upon the magnitude of the applied stress, σ, the length of the crack, 2a and a parameter which depends upon the crack and specimen geometry, f(a/W) where W is the specimen width.

$$K = \sigma\sqrt{\pi a}\ f\left(\frac{a}{W}\right) \qquad (2A.1)$$

Irwin proved that the achievement of a critical stress intensity factor, K_C, is exactly equivalent to the Griffith-Irwin balance approach which requires the achievement of a stored elastic strain equal to G_C. For tensile loading, the relationships between K_C and G_C is given in Equation 2A.2a for plane stress and Equation 2A.2b for plane strain.

$$G_c = \frac{K_c^2}{E} \qquad plane\ stress \qquad (2A.2a)$$

$$G_c = \frac{K_c^2}{E}(1-\nu^2) \qquad plane\ strain \qquad (2A.2b)$$

All stress systems in the vicinity of the crack may be derived from three modes of loading, (a) mode I which is the opening mode, (b) mode II which is the sliding mode and (c) mode III which is the tearing mode. The mode I elastic stress field equations can be expressed in terms of principal stresses which are in turn written in polar coordinates (Ewalds & Wanhill). Similar expressions for modes II and III can also be written.

The elastic stress field equations mentioned earlier are only valid for an infinite plate. The factor f(a/W) in Equation 2A.1 takes into account finite specimen geometry where a is half the crack length and W is the specimen width. A number of numerical approximations are available, an example which is given in Equation 2A.3 is accurate to 0.3 % for $a/W < 0.35$ and is found to be the most accurate approximation.

$$f\left(\frac{a}{W}\right) = \sqrt{\sec\left(\frac{\pi a}{W}\right)} \qquad (2A.3)$$

2A.2.2 Energy Balance Approach

The Griffith energy balance approach states that the total energy content, U, of an elastic, remotely loaded cracked plate can be written by Equation 2A.4 where U_O is the elastic energy content of the uncracked plate (a constant), U_a is the change in the elastic strain energy caused by introducing the crack in the plate, U_γ is the change in elastic surface energy caused by the formation of the crack surfaces and F is the work performed by external forces.

$$U = U_O + U_a + U_\gamma - F \qquad (2A.4)$$

Crack instability will occur as soon as U is no longer increasing with increasing crack length, i.e when dU/da = 0. By rearranging Equation 2A.4 and noting that U_O is a constant then we can write Equation 2A.5.

$$\frac{d}{da}(F - U_a) \geq \frac{dU_\gamma}{da} \qquad (2A.5)$$

The left hand part represents the energy given to the body by the external work per unit crack extension. $dF/da - dU_a/da$ is the amount of energy that remains available for the crack tip to propagate. The right hand part of Equation 2A.5 represents the elastic surface energy of the crack surfaces. This is the energy required for the crack to grow.

The elastic strain energy required to open the crack can be written as in Equations 2A.6a and 2A.6b where E is the Young's modulus, a is half the crack length and σ is the remotely applied stress.

$$U_a = \frac{\pi\sigma^2 a^2}{E} \qquad \textit{plane stress} \qquad (2A.6a)$$

$$U_a = (1-\nu^2)\frac{\pi\sigma^2 a^2}{E} \qquad \textit{plane strain} \qquad (2A.6b)$$

It can be shown that $dU_a/da = G$ and, therefore, for mode I (opening mode), expressions for the mode I strain energy release rate, G_I, can be written in terms of the mode I stress intensity factor, K_I, from Equations 2A.6a and 2A.6b and Equation 2A.1 for f(a/W) = 1 (infinite plate) as shown in Equations 2A.7a and 2A.7b.

$$G = \frac{K_I^2}{E} \qquad \textit{plane stress} \tag{2A.7a}$$

$$G_I = \frac{K_I^2}{E}(1-\nu^2) \qquad \textit{plane strain} \tag{2A.7b}$$

The strain energy release rate, G can be considered to be the amount of energy which is available for crack extension and can be written in terms of the three stress intensity factors for mixed mode behaviour:

$$G = \frac{(K_I^2 + K_{II}^2)(\kappa+1)}{8\mu} + \frac{K_{III}^2}{2\mu} \tag{2A.8}$$

where:

K_I	is the mode I stress intensity factor
K_{II}	is the mode II stress intensity factor
K_{III}	is the mode III stress intensity factor
μ	is the material shear modulus
κ	is the conversion factor between conditions of plane strain and plane stress. Equals $3-4\upsilon$ for plane strain conditions
υ	is the material Poisson's ratio

For the case where only modes I and II are applicable, mode III is assumed to give a negligible contribution to the strain energy release rate and hence the strain energy release rate can be calculated from:

$$G = \frac{(K_I^2 + K_{II}^2)(\kappa+1)}{8\mu} \tag{2A.9}$$

2A.3 Elastic-Plastic Fracture Mechanics (EPFM)

The use of linear elastic fracture mechanics (LEFM) may not always be applicable, for

example in the case of ductile materials where the crack tip plastic zone is too large. It is therefore necessary to identify alternative parameters to analyse EPFM problems.

2A.3.1 The J-integral

The J-integral approach was first introduced by Rice and is based on an energy balance as with the strain energy release rate, G, in the case of LEFM. Consider Equation 2A.4 given above which remains valid as long as the material behaviour remains elastic, it need not necessarily be linear. An important consequence of this is that this nonlinear elastic behaviour can be used to represent the plastic behaviour of a material. One restriction of its use, however, requires that no unloading occurs in any part of the body. This is because in actual plastic behaviour, the plastic part of the deformation is irrecoverable. Hence the nonlinear equivalent to the LEFM parameter, G can be given as J, the J-integral.

The J-integral is a path independent line integral which measures the magnitude of the singular stresses and strains near a crack tip:

$$J = \int_{\Gamma} W dy - \int_{\Gamma} t_i \frac{\delta u_i}{\delta x} ds \qquad (2A.10)$$

where:

	Γ	is any path surrounding the crack tip
	W	is strain energy density (strain energy per unit volume)
	t_x	is the traction vector along x-axis ($\sigma_x n_x + \sigma_{xy} n_y$)
	t_y	is the traction vector along y-axis ($\sigma_y n_y + \sigma_{xy} n_x$)
	σ	is the component stress
	n	is the unit outer normal vector to path Γ
	u	is the displacement vector
	s	is the distance along path Γ

The J-integral approach may be used for nonlinear elastic materials and thus can be used in a wider variety of problems than the strain energy release rate, G which is only valid in the case of linear elastic behaviour.

For linear elastic materials, the J-integral is related to the stress intensity factors in a similar manner as the strain energy release rate (Equations 2A.8 and 2A.9). i.e for linear elastic materials, J = G. A crack will propagate if the calculated value of the strain

energy release rate (or J-integral) is greater than or equal to the material critical strain energy release rate.

APPENDIX 2B. ANALYSIS OF WOVEN LAMINATES

2B.1 One-Dimensional Mosaic Models

Ishikawa and Chou (1983) derived a one-dimensional analytical model to derive the elastic moduli upper and lower bounds of a woven fabric composite. This model does not take into account the fibre continuity or the undulation which naturally occurs in these type of laminates. Classical laminate plate theory has been adopted as the basis of this model leading to simple closed form solutions for the upper and lower bounds. The woven fabric is assumed to be comprised of a series of cross-ply laminates. Figure 2B.1 shows the idealisation of the mosaic model in the case of an eight-harness satin weave. i.e a fill thread is woven with every eighth warp thread and a warp thread is woven with every eighth fill thread. Two one-dimensional models give rise to the upper and lower bounds these being the parallel and series models respectively. The sections of the cross-ply laminates are either in parallel or series. This is shown in Figure 2B.2.

The parallel model assumes a state of constant strain (iso-strain) in the laminate midplane. An applied average membrane stress is applied to the laminate. Equations 2B.1 give the upper bounds of the stiffness constants of the woven fabric, A_{ij}^{Mp}, B_{ij}^{Mp} and D_{ij}^{Mp} based on the parallel mosaic model.

$$A_{ij}^{Mp} = A_{ij} \,, \qquad B_{ij}^{Mp} = \left(1-\frac{2}{n_g}\right) B_{ij} \,, \qquad D_{ij}^{Mp} = D_{ij} \tag{2B.1}$$

The stiffness constants, A_{ij}, B_{ij} and D_{ij} are calculated from the basic laminate where the top layer is the fill threads. n_g dictates the type of weave present in the laminate. For plain weave, $n_g = 2$, twill weave $n_g = 3$ and for satin weave, $n_g = 4$ (four-harness) or $n_g = 8$ (eight-harness).

The series model assumes that the disturbance of stress and strain near the interface of the woven region is negligible. If an in-plane force in the longitudinal direction is applied to the laminate, the iso-stress condition leads to Equations 2B.2 for the upper bounds of the composite compliance constants, a_{ij}^{Ms}, b_{ij}^{Ms} and d_{ij}^{Ms} and hence the lower bounds of the composite stiffness constants.

$$a_{ij}^{Ms} = a_{ij} \,, \qquad b_{ij}^{Ms} = \left(1-\frac{2}{n_g}\right) b_{ij} \,, \qquad d_{ij}^{Ms} = d_{ij} \tag{2B.2}$$

where: a_{ij}, b_{ij} and d_{ij} are the compliance constants which relate to the average

where superscripts M, F and W represent the matrix, fill thread and warp thread respectively. The local stiffness of the fill yarn, $Q_{ij}^{F}(\theta)$ depends upon the local fill angle to the x-axis. Thus, the effective elastic moduli depend upon the value of the fill angle (Lekhnitskii). If the fill angle exists then the effective elastic moduli in the x-direction are reduced.

This model only considers a one-dimensional strip of laminate and is, therefore not suitable for calculating non-axis constants. In addition, the fibre undulation model is inadequate for calculating the elastic constants for satin weave fabrics.

The averaged in-plane compliance constants for the woven laminate under a uniformly applied in-plane stress resultant are given for the FUM by Equations 2B.4.

$$a_{ij}^{FUM} = \left(1-\frac{2a_u}{n_g a}\right)a_{ij} + \frac{2}{n_g a}\int_{a_0}^{a_2} a_{ij}(x)\ dx$$

$$b_{ij}^{FUM} = \left(1-\frac{2}{n_g}\right)b_{ij} + \frac{2}{n_g a}\int_{a_0}^{a_2} b_{ij}(x)\ dx$$

$$d_{ij}^{FUM} = \left(1-\frac{2a_u}{n_g a}\right)d_{ij} + \frac{2}{n_g a}\int_{a_0}^{a_2} d_{ij}(x)\ dx \qquad (2B.4)$$

The compliance constants are obtained numerically from Equations 2B.4. Finally, the stiffness constants are obtained by the inversion of Equations 2B.4.

2B.3 Analysis of First Knee Behaviour of Woven Composites

The tensile stress-strain behaviour of woven roving composites, on a macroscopic level exhibits distinctive knee points. It is reported in Kimpara et. al. that the first knee occurs at a relatively low stress level. The internal failure mechanism is due to failure in the weft roving followed by the accumulation of matrix cracks between the filaments in the weft rovings transverse to the applied load.

A series of finite element models were analysed which represent a two dimensional

idealisation of a glass/polyester woven roving composites each containing elements representing the warp, weft yarns and the matrix. The stresses and strains were computed for each element under a prescribed uniform displacement until the critical value of principal matrix strain (2 %) was reached. The rigidity of the element(s) which are deemed to have failed is then reduced to 1 %. This procedure is repeated to yield a stress strain curve from which a series of Young's moduli can be computed which mirror the rigidity loss due to the knee behaviour. The decrease in rigidity around the first knee is quoted to be 25 % which is consistent with the actual behaviour of FRP.

Ishikawa and Chou (1982 b) uses an analytical approach to calculate the stress/strain behaviour of a plain weave glass/polyester composite. It is assumed that classical laminate theory is applicable in this case. The reduced stiffness of the warp threads which are transverse to the load in this case, is represented by reducing the Q_{ij}s except Q_{22} by a factor of 1/100. This is so as to represent the stiffness reduction due to transverse cracking. Two predictions for the stress/strain behaviour have been made, the first assuming bending-free conditions and the second allowing bending to take place. The bending-free condition compares extremely well with the FE result from Ishikawa and Chou (1982 b). In plain weave composites, the local bending is constrained by the adjacent interlaced regions hence the bending-free condition is the most likely condition to exist.

2B.4 Bridging Model for Satin Weaves

The fibre undulation model discussed above is effective for plain weave fabrics since there are no straight thread regions surrounding the woven regions in the plain weave laminate. This is shown in Figure 2B.4. In satin weaves, however, where $n_g \geq 4$, the woven regions are separated from each other by straight thread regions. This is shown in Figure 2B.5. These straight regions have higher in-plane stiffnesses than the woven regions due to the lack of undulation. Thus the straight regions have the effect of carrying higher loads causing load transfer by bridging. Figure 2B.6 shows the concept of the bridging model. Equations 2B.5 give rise to the averaged compliance constants for a satin weave plate based in the bridging model.

$$a_{ij}^{B} = \frac{1}{\sqrt{n_g}} [2a_{ij} + (\sqrt{n_g}-2)\, a_{ij}^{FUM}]$$

$$b_{ij}^{B} = \frac{1}{\sqrt{n_g}} [2b_{ij} + (\sqrt{n_g}-2)\, b_{ij}^{FUM}]$$

$$d_{ij}^{B} = \frac{1}{\sqrt{n_g}} [2d_{ij} + (\sqrt{n_g}-2)\, d_{ij}^{FUM}] \qquad \text{(2B.5)}$$

The stiffness constants can then be obtained by inverting Equations 2B.5.

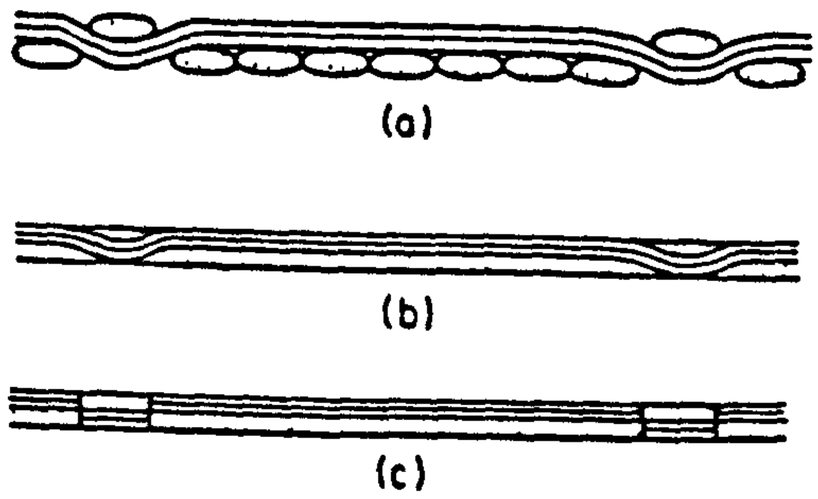

Figure 2B.1 Idealisation of the Mosaic model :
(a) cross-sectional view of a woven fabric before resin impregnation
(b) woven fabric composite
(c) idealisation of the mosaic model
(taken from Ishikawa & Chou)

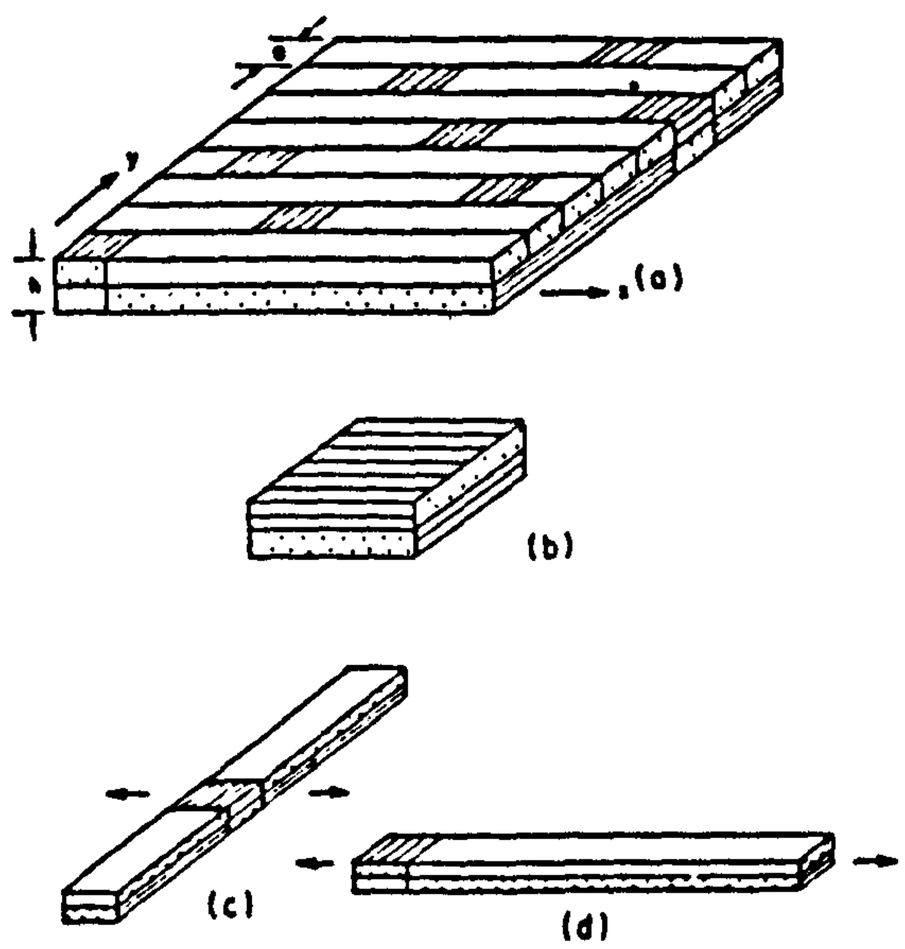

Figure 2B.2 Mosaic model of :
(a) repeating region in an eighth harness satin composite
(b) a basic cross-ply laminate
(c) parallel model
(d) series model (taken from Ishikawa & Chou)

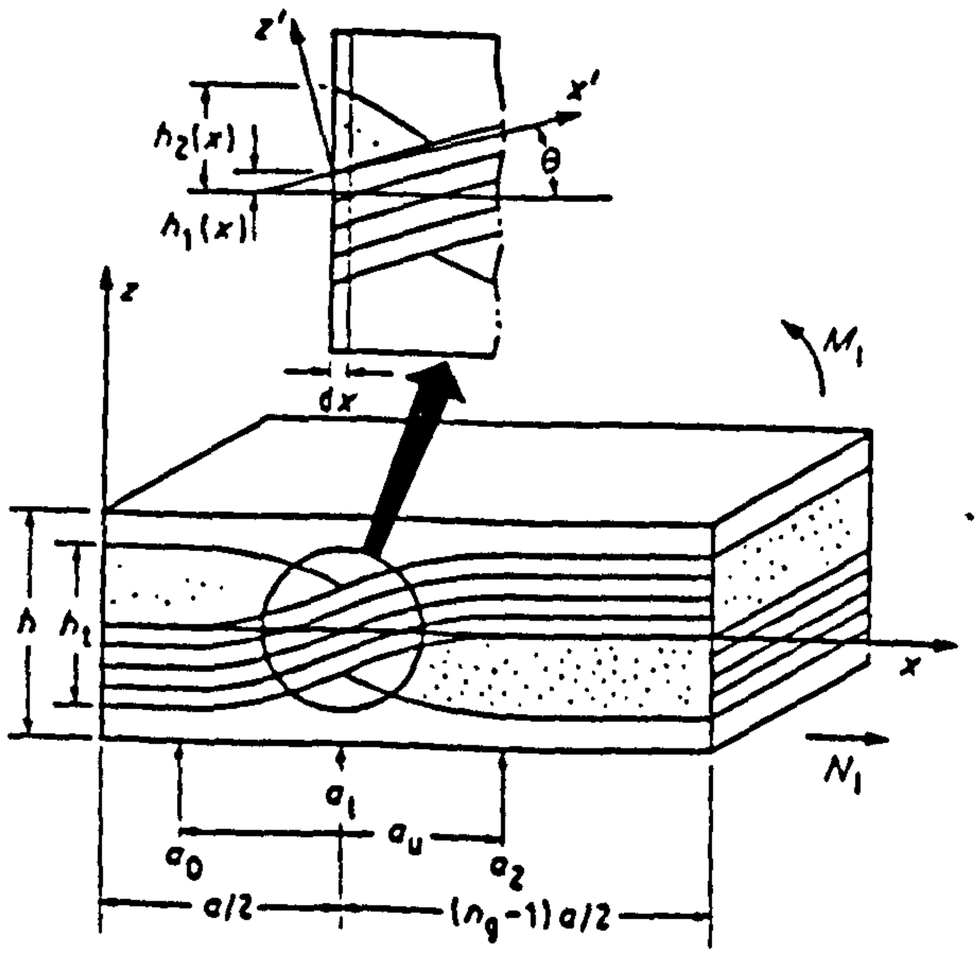

Figure 2B.3 Geometry used in the Fibre Undulation Model
(taken from Ishikawa & Chou)

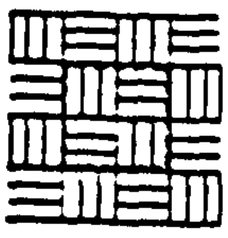

Figure 2B.4 Regions in a Plain Weave Laminate
(taken from Ishikawa & Chou)

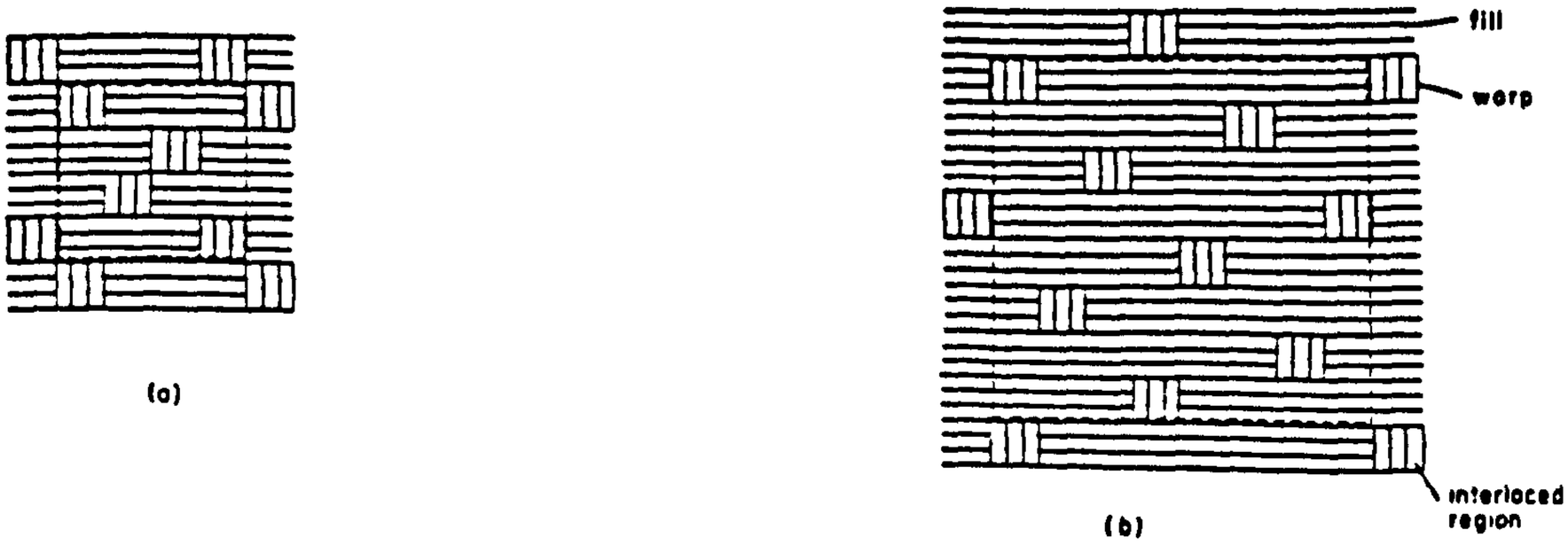

Figure 2B.5 Straight Thread Regions within Satin Weaves :
(a) four harness satin
(b) eight harness satin
(taken from Ishikawa & Chou)

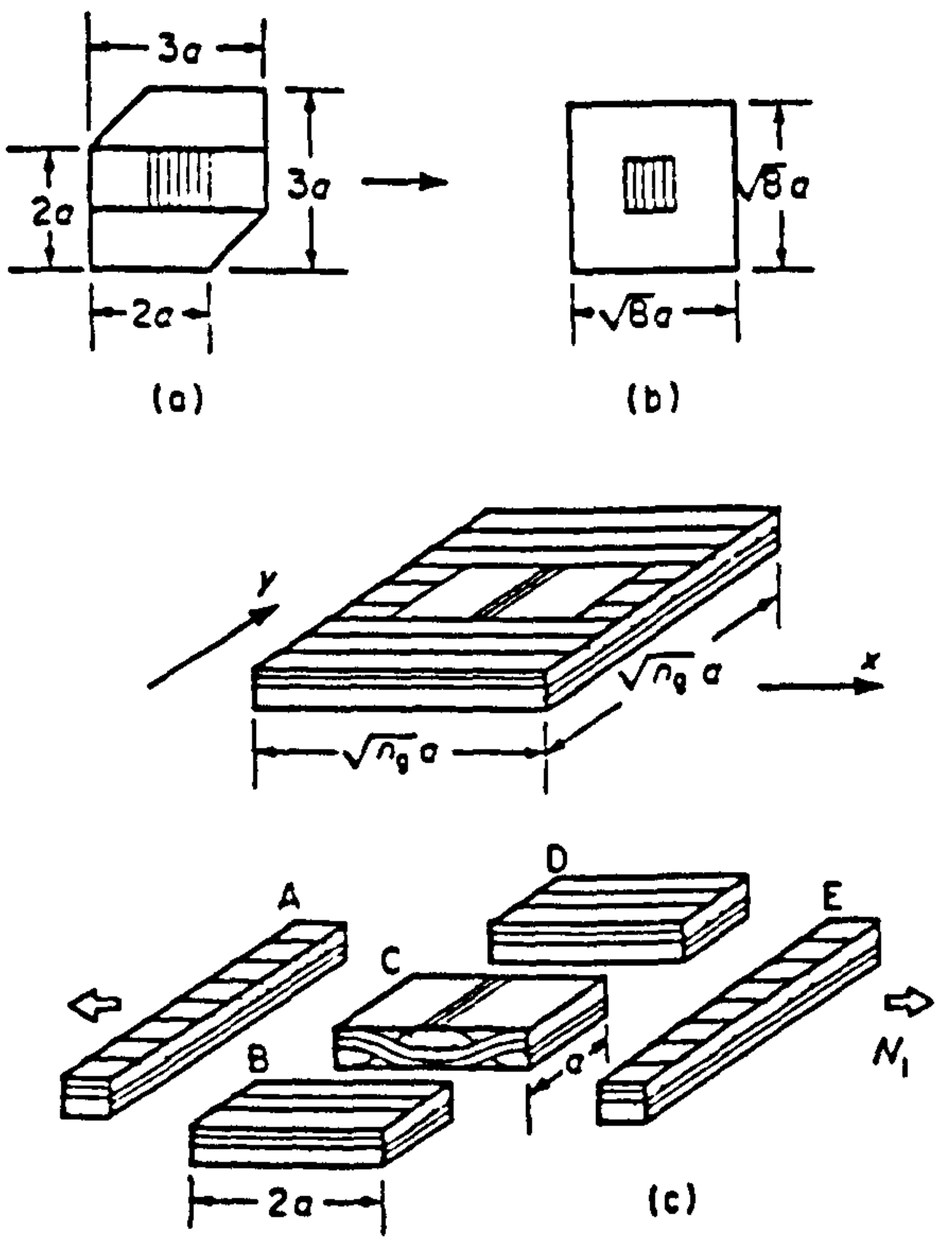

Figure 2B.6 Concept of the Bridging Model :
(a) shape of the repeating unit of an 8 harness satin weave
(b) modified shape for the repeating unit
(c) idealisation for the bridging model
(taken from Ishikawa & Chou)

APPENDIX 4A. DERIVATION OF LAMINATE CONSTITUTIVE EQUATIONS.

For an orthotropic material, Generalised Hooke's law yields the Equation 4A.1 which relates the strain components to the stress components via the compliance matrix. The inverse of the compliance matrix is the stiffness matrix whose elements are the material stiffness constants.

$$\varepsilon_i = \sum_{j=1}^{6} S_{ij}\sigma_j \qquad (4A.1)$$

Classical laminate theory (CLT) assumes plane stress conditions within all the laminae constituting the laminate. If we consider the diagram in Figure 4A.1, and let the x_1x_2 plane represent the plane of plane stress, then σ_3, σ_4 and σ_5 are equal to zero. Thus, Equation 4A.2 can be written to represent the plane stress components.

$$\begin{bmatrix}\sigma_1\\ \sigma_2\\ \sigma_6\end{bmatrix}_k = \begin{bmatrix}Q_{11} & Q_{12} & 0\\ Q_{12} & Q_{22} & 0\\ 0 & 0 & Q_{66}\end{bmatrix}_k \begin{bmatrix}\varepsilon_1\\ \varepsilon_2\\ \varepsilon_6\end{bmatrix}_k \quad \equiv \quad [\,\sigma\,]_k = [\,Q\,]_k\,[\,\varepsilon\,]_k \qquad (4A.2)$$

where the elements Q_{ij} are the reduced stiffness constants for plane stress.

For the laminate shown in Figure 4A.2 with a coordinate system x,y,z, the mid-plane of each lamina k has principal material directions, $(x_1)_k$ and $(y_1)_k$. If the x- and y-axes in that plane are rotated through an angle θ_k and are denoted by $(\bar{x}_1)_k$ and $(\bar{y}_1)_k$ then the reduced stiffness matrix with respect to the principal directions of the laminate can be denoted by $[Q]_k$ the elements of which are given in Shenoi & Wellicome. Equation 4A.3 represents the lamina stress-strain relations with respect to the principal directions of the laminate.

$$[\,\bar{\sigma}\,]_k = [\,\bar{Q}\,]_k\,[\,\bar{\varepsilon}\,]_k \qquad (4A.3)$$

Equation 4A.4 represents the in-plane strain vector of each lamina k as a function of the distance from the laminate midplane to the lamina midplane, z.

$$\{\,\bar{\varepsilon}\,\}_k = \{\,\varepsilon^o\,\} + z\,\{\,\kappa\,\} \quad ; \quad z_{k-1} < z < z_k \qquad (4A.4)$$

By substituting Equation 4A.4 into Equation 4A.3, the stress-strain variation in a lamina k with respect to the principal directions of the laminate can be given by Equation 4A.5.

$$\begin{Bmatrix} \overline{\sigma_x} \\ \overline{\sigma_y} \\ \overline{\tau_{xy}} \end{Bmatrix}_k = \begin{bmatrix} \overline{Q}_{11} & \overline{Q}_{12} & \overline{Q}_{16} \\ \overline{Q}_{12} & \overline{Q}_{22} & \overline{Q}_{26} \\ \overline{Q}_{16} & \overline{Q}_{26} & \overline{Q}_{66} \end{bmatrix}_k \begin{Bmatrix} \epsilon^0{}_x \\ \epsilon^0{}_y \\ \gamma^0{}_{xy} \end{Bmatrix} + z \begin{bmatrix} \overline{Q}_{11} & \overline{Q}_{12} & \overline{Q}_{16} \\ \overline{Q}_{12} & \overline{Q}_{22} & \overline{Q}_{26} \\ \overline{Q}_{16} & \overline{Q}_{26} & \overline{Q}_{66} \end{bmatrix}_k \begin{Bmatrix} k_x \\ k_y \\ k_{xy} \end{Bmatrix} \qquad (4A.5)$$

where: Q_{11}, Q_{12}, Q_{22} and Q_{66} are elements of the k_{th} lamina reduced stiffness matrix and can be found in Shenoi & Wellicome.

To define the forces and moments applied to a rectangular section of the plate as shown in Figure 4A.2, the stresses must be integrated over the thickness of the plate, thus giving equations for the resultant forces per unit edge length:

$$\{ N \} = \sum_{k=1}^{n} \int_{z_{k-1}}^{z_k} \{ \overline{\sigma} \}_k \, dz \qquad (4A.6)$$

The variation in normal stress in the thickness direction (z), corresponds to a bending moment per unit length, M_x. The remaining stress components, σ_x and σ_{xy} each give rise to bending moment M_y and twisting moment M_{xy}.

$$\{ M \} = \sum_{k=1}^{n} \int_{z_{k-1}}^{z_k} \{ \overline{\sigma} \}_k \, z \, dz \qquad (4A.7)$$

Since the stress distribution through the laminate thickness is discontinuous at the laminae interfaces, the integration of stresses over the whole thickness to determine the laminate stiffness matrices [A], [B] and [D] must be replaced by integrals over the individual laminae which are then summed. Hence, from a knowledge of the laminate construction the elements of the [A], [B] and [D] matrices can be calculated from Equations 4A.8 and the reduced laminate stiffness matrix.

$$A_{ij} = \sum_{k=1}^{n} [\overline{Q}_{ij}]_k \, (z_k - z_{k-1})$$

$$B_{ij} = \frac{1}{2} \sum_{k=1}^{n} [\overline{Q}_{ij}]_k \, (z_k^2 - z_{k-1}^2)$$

$$D_{ij} = \frac{1}{3} \sum_{k=1}^{n} [\overline{Q}_{ij}]_k \, (z_k^3 - z_{k-1}^3) \qquad (4A.8)$$

where: i,j = 1,2,6

Equations 4A.8 can be combined to yield the load-strain relations of the laminate according to CLT.

$$\begin{bmatrix} \{ N \} \\ \{ M \} \end{bmatrix} = \begin{bmatrix} [A] & [B] \\ [B] & [D] \end{bmatrix} \begin{bmatrix} \{ \varepsilon^{o} \} \\ \{ \kappa \} \end{bmatrix} \tag{4A.9}$$

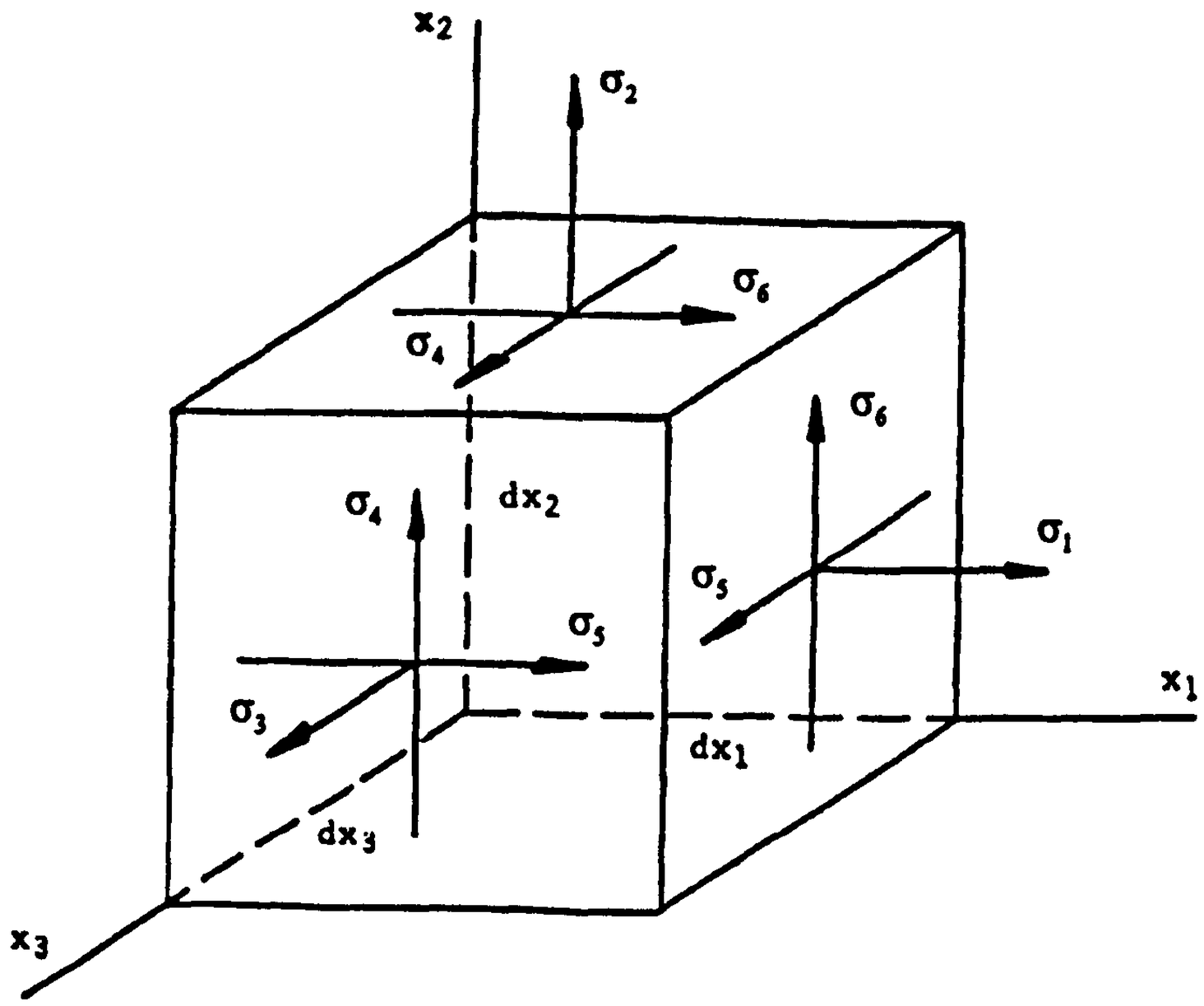

Figure 4A.1 Diagram of Positive Stress Direction Convention and Coordinate System (taken from Shenoi & Wellicome)

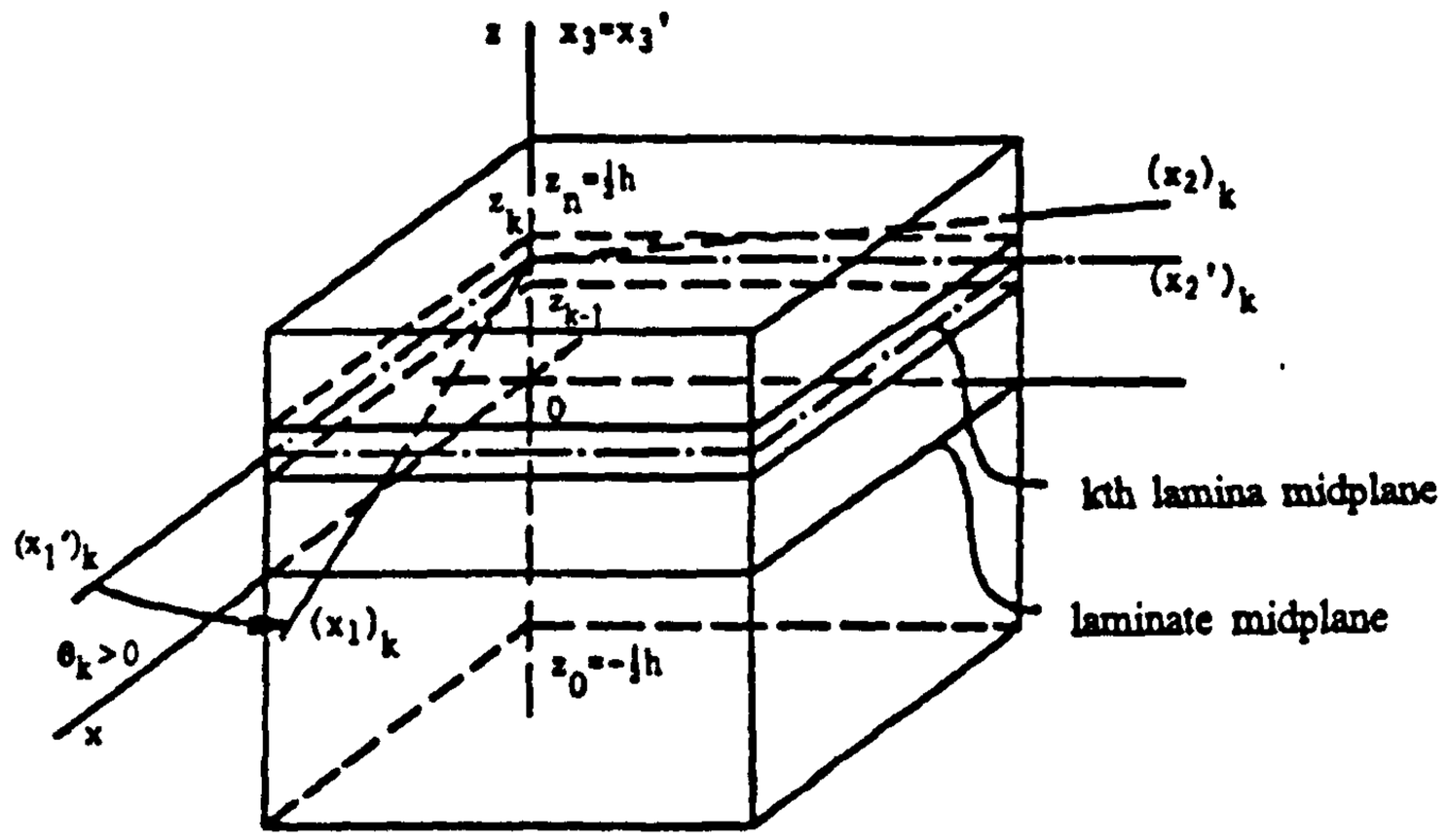

Figure 4A.2 Laminate and Laminae Coordinate Systems
(taken from Shenoi & Wellicome)

APPENDIX 4B. CALCULATION OF LAMINATE ELASTIC MODULI

The laminate stiffness matrix which was derived in Appendix 4A can be written as

$$\begin{bmatrix} \{N\} \\ \{M\} \end{bmatrix} = \begin{bmatrix} [A] & [B] \\ [B] & [D] \end{bmatrix} \begin{bmatrix} \{\epsilon^0\} \\ \{\kappa\} \end{bmatrix} \tag{4B.1}$$

where: [A] is the in-plane stiffness matrix

[B] is the coupling stiffness matrix

[D] is the flexural stiffness matrix

$\{\epsilon^0\}$ is the in-plane strains vector.

$\{\kappa\}$ is the plate curvatures vector.

{N} is the in-plane forces vector.

{M} is the edge moments vector.

Equation 4B.1 must now be inverted in order to give the laminate compliance matrix. This is given in Equation 4B.2.

$$\left[\begin{array}{c} [\epsilon^0] \\ \hline [\kappa] \end{array}\right] = \left[\begin{array}{c|c} [a] & [b] \\ \hline [c] & [d] \end{array}\right] \left[\begin{array}{c} [N] \\ \hline [M] \end{array}\right] \tag{4B.2}$$

where: [a] is the in-plane compliance matrix.

[b] is the coupling compliance matrix.

[d] is the flexural compliance matrix.

and

$$[a] = [A]^{-1} - [b][B][A]^{-1}$$

$$[b] = -[A]^{-1}[B][d]$$

$$[d] = ([D] - [B][A]^{-1}[B])^{-1}$$

The coupling effects due to the coupling matrix [B] can be avoided if the laminate is constructed symmetrically with respect to its midplane, for which the laminate coupling matrix [B] equals zero. As a result, a uniaxial in-plane force will not cause bending or twisting. If N_x , the force per unit length in the x-direction is the only non-zero force then Equation 4B.2 can be re-written as:

$$\epsilon^0_x = a_{11} N_x \tag{4B.3}$$

N_x is shown graphically in Figure 4B.1. Now, N_x is related to the direct in-plane stress in the x-direction, averaged across the laminate thickness, t as in Equation 4B.4.

$$\overline{\sigma_x} = \frac{N_x}{t} \tag{4B.4}$$

Substituting Equation 4B.4 into Equation 4B.3 yields:

$$\epsilon_x^0 = a_{11}\,\overline{\sigma_x}\,t \tag{4B.5}$$

Now the stiffness E_x^0 can be written as :

$$E_x^0 = \frac{\overline{\sigma_x}}{\epsilon_x^0} \tag{4B.6}$$

Rearranging 4B.5 and substituting into 4B.6 gives the following equation for the stiffness of an arbitrary composite laminate, E_x

$$E_x = \frac{1}{a_{11}\,t} \tag{4B.7}$$

where: a_{11} is the first element of the in-plane compliance matrix [a].
t is the laminate thickness

also, for laminate with n plies

$$A_{ij} = \sum_{k=1}^{n} [Q'_{ij}]_k \,(z_k - z_{k-1})$$

$$B_{ij} = \frac{1}{2} \sum_{k=1}^{n} [Q'_{ij}]_k \,(z_k^2 - z_{k-1}^2)$$

$$D_{ij} = \frac{1}{3} \sum_{k=1}^{n} [Q'_{ij}]_k \,(z_k^3 - z_{k-1}^3) \tag{4B.8}$$

where:

$[Q'_{ij}]_k$ is the reduced stiffness matrix for each ply k.

For a symmetric laminate, the coupling matrix [B] is equal to zero and Equation 4B.7 can be re-written as:

$$E_x = \frac{1}{X_{11}\ t} \qquad (4B.9)$$

where: X_{11} is the first element in the matrix $[A]^{-1}$.

Also, the other engineering constants can be yielded from Equations 4B.10.

$$E_y = \frac{1}{a_{22}\ h} \quad ; \quad \nu_{xy} = -\frac{a_{21}}{a_{11}} \quad ; \quad G_{xy} = \frac{1}{a_{66}\ h} \qquad (4B.10)$$

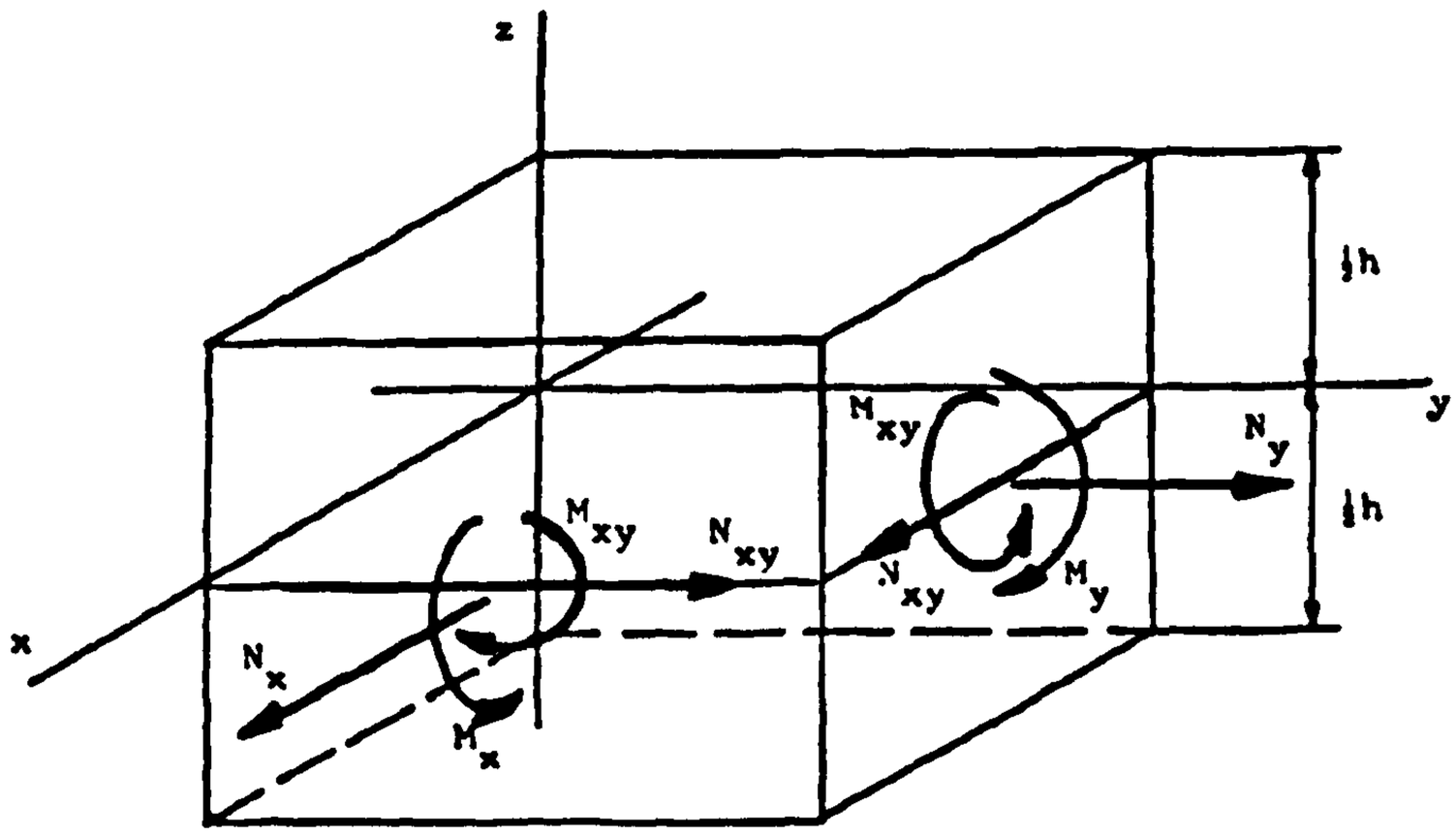

Figure 4B.1 Forces and Moments per Unit Length acting in the Laminate (taken from Shenoi & Wellicome)

APPENDIX 4C DERIVATION OF WOVEN LAMINATE RELATIONS.

The analysis which is described here is restricted to the analysis of plain weave type fabric laminates. The warp and fill material are assumed to be the same. It is first necessary to discuss the analysis of one lamina. The extension to laminates shall then be discussed.

Consider a unit cell of a plain weave lamina such as the one shown diagrammatically in Figure 4C.1. The unit cell is divided into sections depending on the nature of the weave along both the x- and y-axes. These sections are distinguished by a_{1-5} along the x-axis and b_{1-5} along the y-axis. The exact location of these sections along the x-axis is dependent upon the width of the warp yarn (a_w), the gap between two adjacent warp yarns (g_w) and the undulation length of the fill yarn (u_f).

Figure 4C.2 shows the side DC of the unit cell. The shape functions $hy_1(y)$ and $hy_2(y)$ define the yarn configuration across the y-axis. The undulation is assumed sinusoidal in form. Figure 4C.3 shows the side AD of the unit cell. The shape functions $hx_1(x,y)$, $hx_2(x,y)$ and $hx_3(x,y)$ define the yarn configuration. These shape functions depend upon both the x and y location within the unit cell.

The shape functions defining the yarns along the x-axis are defined in Equations 4C.1.

$$hx_1(x,y) = -\left[1-\sin\left\{(x-a_3)\ \frac{\pi}{u_f-g_w}\right\}\right]\left(\frac{hy_2(y)\ +\ hy_1(y)}{2}\right\} + hy_2(y)$$

$$a_3 \le x \le a_5$$

$$hx_1(x,y) = hy_2(y) \qquad a_5 \le x \le (a_w+g_w)$$

$$hx_2(x,y) = -\ [h_w-hy_1(y)-(h_f-hx_1(a_4,y))]\cos\left\{(x-a_5)\frac{\pi}{u_f}\right\}$$

$$-\ (h_f-hx_1(a_4,y)) \qquad a_4 \le x \le a_5$$

$$hx_2(x,y) = hy_1(y) - h_w \qquad a_5 \le x \le (a_w+g_w)$$

(4C.1)

where: h_f is the maximum fill yarn thickness

h_w is the maximum warp yarn thickness

In addition, the local angles of the warp and fill yarns to the global coordinate axes must be defined. Equation 4C.2 gives the local angle between the warp yarn and the global coordinate system, $\theta_w(y)$ and the local angle of the fill yarn to the global coordinate system, $\theta_f(x,y)$.

$$\theta_w(y) = \tan^{-1}\left(\frac{dhy_1(y)}{dy}\right) \; ; \; \theta_f(x,y) = \tan^{-1}\left(\frac{dhx_1(x,y)}{dx}\right)$$

(4C.2)

Classical laminate theory in Appendix 4A gives equations for the in-plane, coupling and flexural matrices (Equation 4A.8) which must be adapted to take into account the different regions within the woven lamina. For example, in the region where $0 \le x \le a_3$ and $0 \le y \le b_3$, the in-plane matrix can be defined by Equation 4C.3.

$$A_{ij}(x,y) = \int_{-\frac{h}{2}}^{hx_3(x,y)} Q_{ij}^{M}\, dz + \int_{hx_3(x,y)}^{hx_1(x,y)} Q_{ij}^{F}(x,y)\, dz + \int_{hx_1(x,y)}^{hx_2(x,y)} Q_{ij}^{W}(x,y)\, dz + \int_{hx_2(x,y)}^{\frac{h}{2}} Q_{ij}^{M}\, dz$$

(4C.3)

Equations 4C.4 give the resulting equations for the in-plane, coupling and flexural matrices for the woven lamina.

$$\begin{aligned} A_{ij}(x,y) = \quad & Q_{ij}^{M}\,[hx_3(x,y) + h - hx_2(x,y)] \\ & + Q_{ij}^{W}(x,y)[hx_2(x,y) - hx_1(x,y)] \\ & + Q_{ij}^{F}(x,y)[hx_1(x,y) - hx_3(x,y)] \end{aligned}$$

$$\begin{aligned} B_{ij}(x,y) = \quad & 1/2\; Q_{ij}^{M}\,[hx_3(x,y)^2 - hx_2(x,y)^2] \\ & + 1/2\; Q_{ij}^{W}(x,y)[hx_2(x,y)^2 - hx_1(x,y)^2] \\ & + 1/2\; Q_{ij}^{F}(x,y)[hx_1(x,y)^2 - hx_3(x,y)^2] \end{aligned}$$

$$D_{ij}(x,y) = \quad 1/3\ Q_{ij}^{M}\,[hx_3(x,y)^3 + h^3/4 - hx_2(x,y)^3] + 1/3\ Q_{ij}^{W}(x,y)[hx_2(x,y)^3 - hx_1(x,y)^3] + 1/3\ Q_{ij}^{F}(x,y)[hx_1(x,y)^3 - hx_3(x,y)^3] \qquad (4C.4)$$

The composite cylinder assemblage model or CCA (Naik) gives simple closed-form analytical expressions or close bound solutions for the effective composite moduli. The fibre and the matrix are assumed to be transversely isotropic (Lekhnitskii). The CCA model yields values for the elastic constants in the principal material directions of a unidirectional lamina. Due to the inherent undulations in the fill and warp yarns, these elastic moduli must be adapted. They need to incorporate a dependence on the local angles of the fill and warp yarns to the global coordinate system. It is assumed that the woven fabric lamina is subjected to a uniform in-plane loading along the x-axis. Infinitesimal pieces of a section parallel to AD (Figure 4C.3) are in series with respect to the loading condition and are assumed to be under constant stress. Alternatively, all infinitesimal pieces of sections parallel to DC (Figure 4C.2) are in parallel with respect to the loading condition and the mid-plane strains of these pieces are the assumed to be the same.

An assemblage of infinitesimal pieces of a section along the loading direction under iso-stress is described as a SERIES model. An assemblage of infinitesimal pieces of a section across the loading direction under iso-strain is described as a PARALLEL model.

A Series-Parallel model is such that all the infinitesimal pieces of a section along the loading direction are first assembled with an iso-stress condition and then with an iso-strain condition. A Parallel-Series model is such that all the infinitesimal pieces of a section across the loading direction are first assembled with an iso-strain condition and then with an iso-stress condition.

In the case of the Series-Parallel model, for a uniformly applied in-plane stress resultant for sections along the loading direction, the average in-plane compliance constants can be calculated from Equation 4C.5.

$$\bar{a}^{s}_{ij}(y)\,,\bar{b}^{s}_{ij}(y)\,,\bar{d}^{s}_{ij}(y) = \frac{1}{a_w + g_w}\int_0^{a_w + g_w} a_{ij}(x,y)\,,b_{ij}(x,y)\,,d_{ij}(x,y)\ dx \qquad (4C.5)$$

For a plain weave lamina, the average coupling compliance, $\bar{b}_{ij}^{s}(y)$ becomes zero since the lamina is symmetrical with respect to its mid-plain. The average in-plane stiffness constants $\bar{A}_{ij}^{s}(y)$, $\bar{B}_{ij}^{s}(y)$ and $\bar{D}_{ij}^{s}(y)$ can be obtained by inverting the average in-plane compliance constants given in Equation 4C.5. The average in-plane stiffness constants of the unit cell of woven fabric lamina can then be found by integrating the in-plane stiffness constants of all sections along the Y-axis with an iso-strain condition using Equation 4C.6.

$$\bar{A}_{ij}^{sp}, \bar{B}_{ij}^{sp}, \bar{D}_{ij}^{sp} = \frac{1}{a_w+g_w} \int_0^{a_f+g_f} \bar{A}_{ij}^{s}(y), \bar{B}_{ij}^{s}(y), \bar{D}_{ij}^{s}(y) \qquad (4C.6)$$

$\bar{A}_{ij}^{sp}$, $\bar{B}_{ij}^{sp}$ and $\bar{D}_{ij}^{sp}$ are the average in-plane stiffness constants obtained by the series-parallel (SP) model. $\bar{B}_{ij}^{sp}$ equals zero for a plain weave. The elastic moduli of the woven laminate can be obtained using the same method as for unidirectional laminates which has been discussed in Appendix 4B.

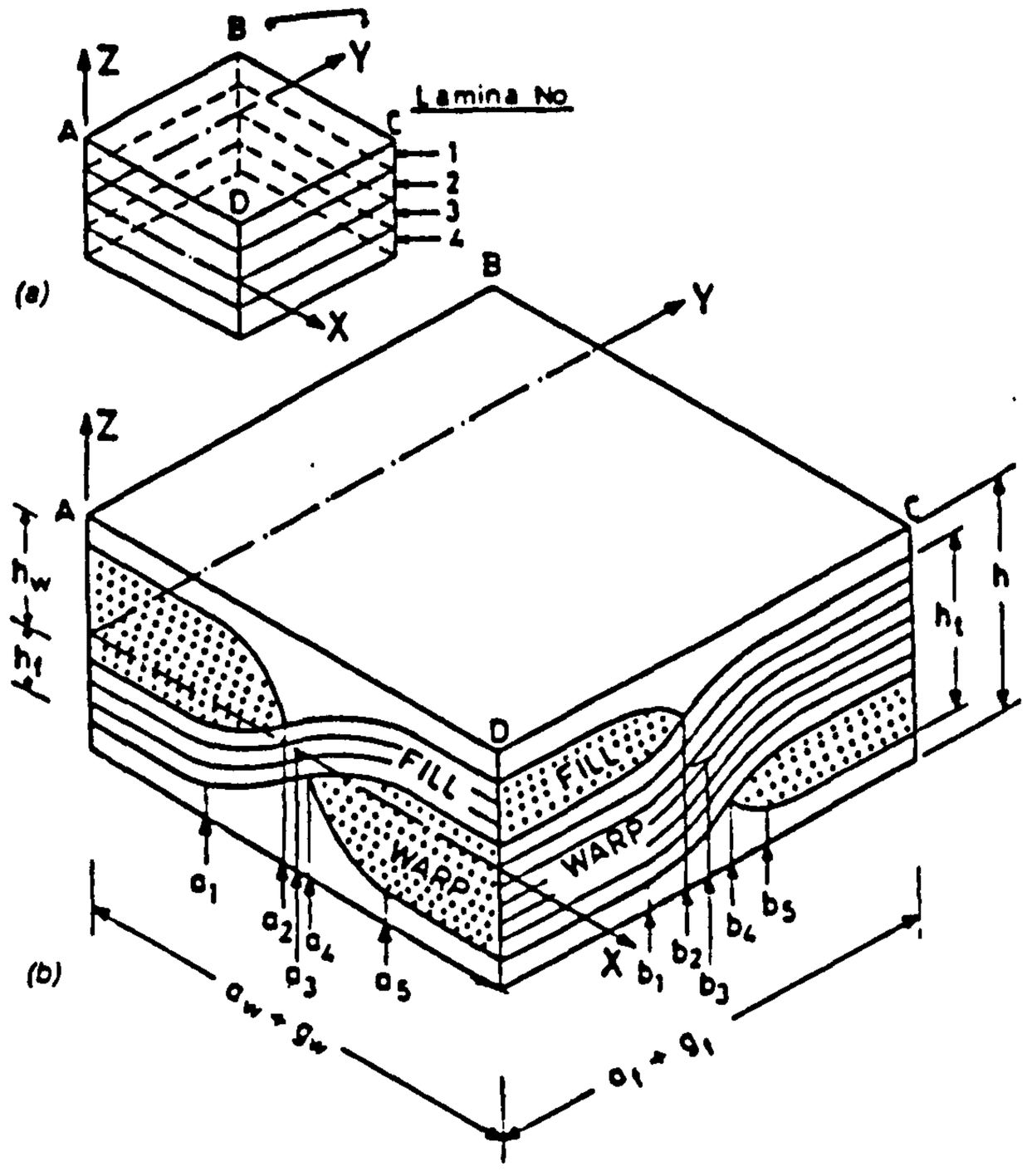

Figure 4C.1 Unit Cell of a Woven Laminate
(taken from Shembekar & Nash)

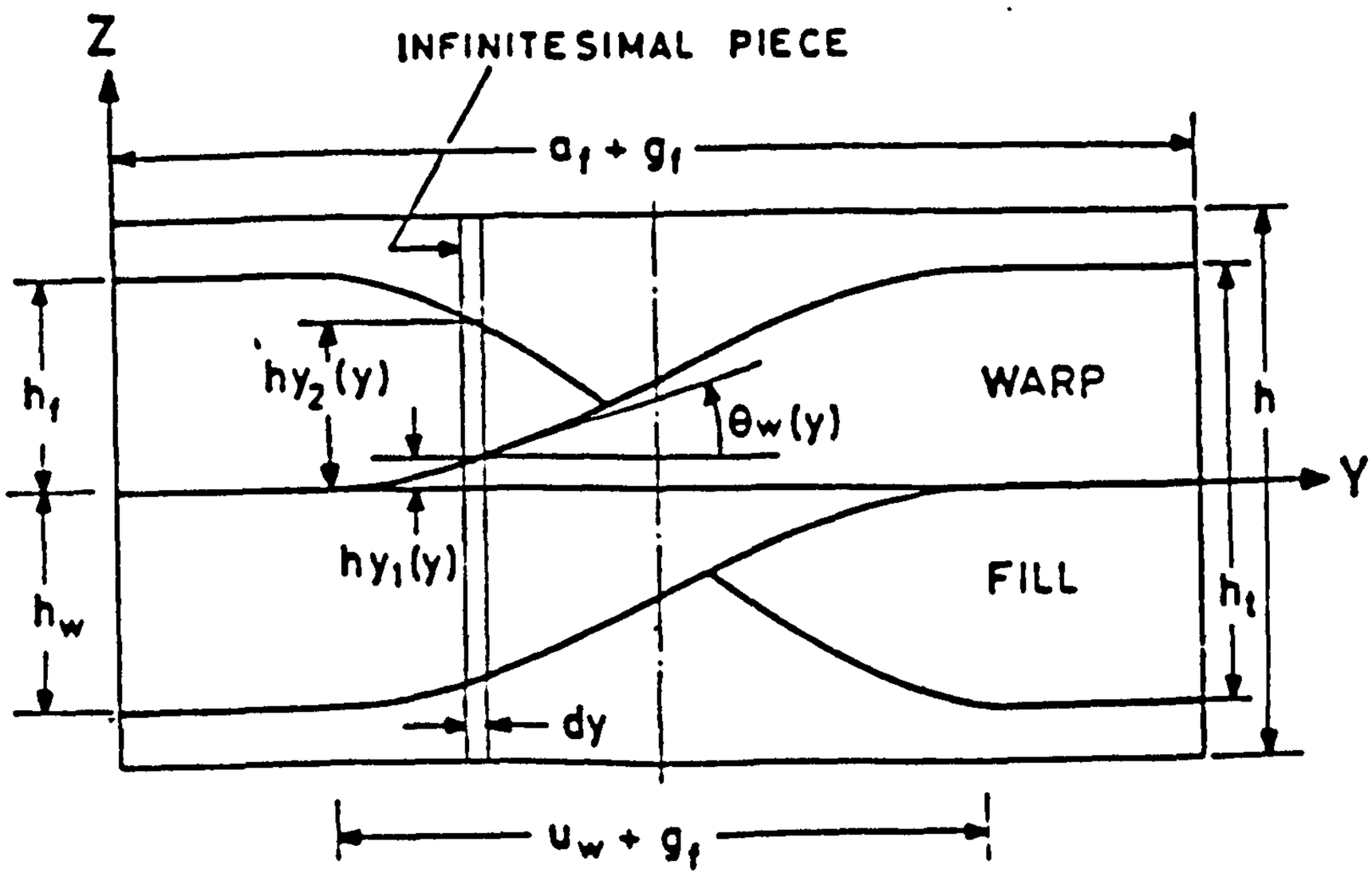

Figure 4C.2 Side DC of the Unit Cell
(taken from Shembekar & Nash)

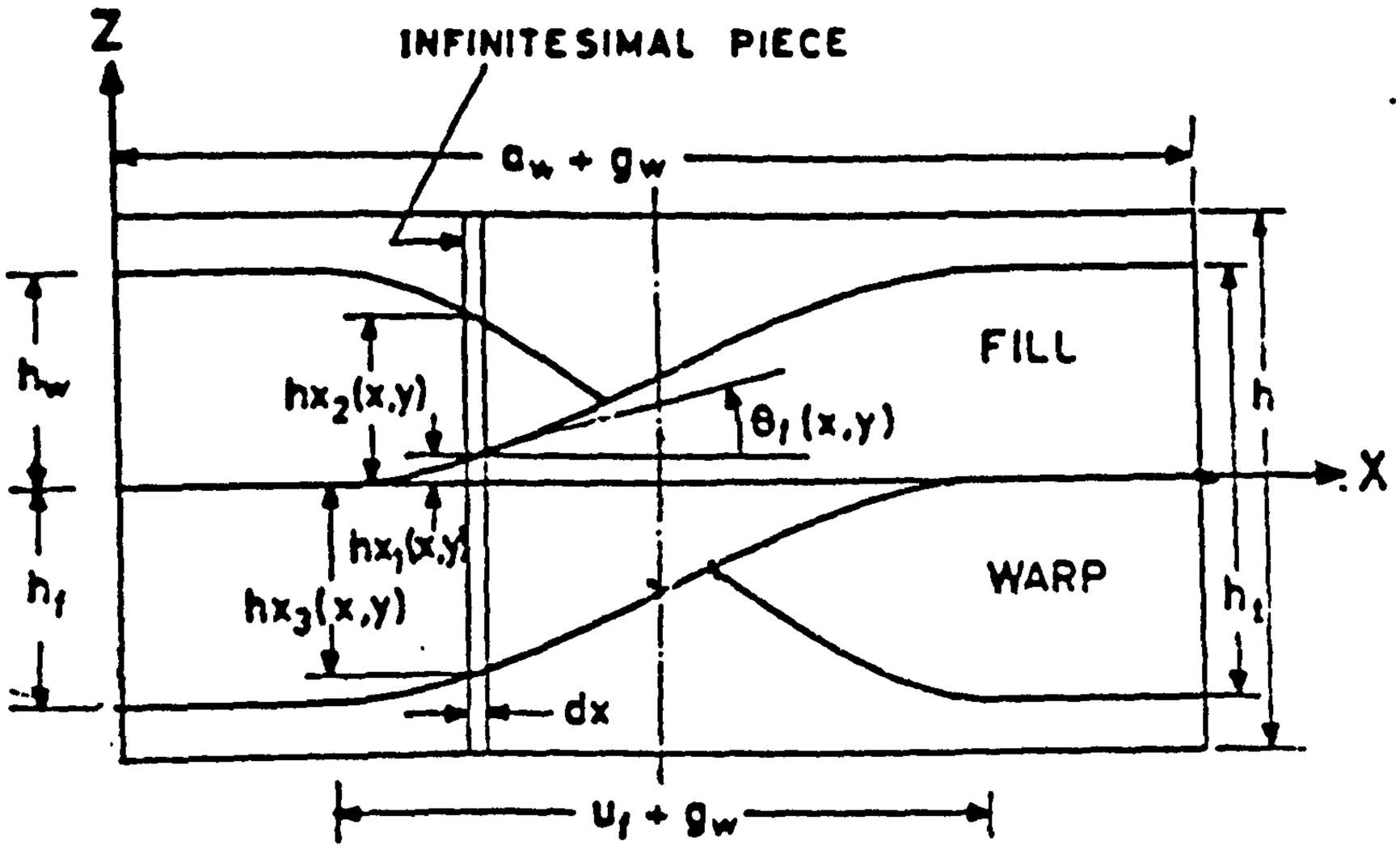

Figure 4C.3 Side AD of the Unit Cell
(taken from Shembekar & Nash)

APPENDIX 4D. LAMINA STIFFNESS MATRICES FOR CHOPPED STRAND MAT LAMINAE.

Chopped Strand Mat laminates have a random fibre orientation. The isotropic in-plane moduli may be derived from the moduli of aligned short-fibre composites. The following equations give values of E, the Young's modulus and G, the shear modulus:

$$E = \frac{3}{8} E_{cL} + \frac{5}{8} E_{cT} \quad ; \quad G = \frac{1}{8} E_{cL} + \frac{1}{4} E_{cT} \qquad (4D.1)$$

where: E_{cL} is the longitudinal modulus of a unidirectional composite of the same material

E_{cT} is the transverse modulus of a unidirectional composite of the same material

The Poisson's ratio, υ, can be calculated from $\upsilon = (E/2G) - 1$.

Now, the stiffness matrix [Q] can be calculated as:

$$Q_{11} = Q_{22} = E/(1-\upsilon^2)$$
$$Q_{12} = Q_{21} = E\upsilon/(1-\upsilon^2)$$
$$Q_{33} = G$$
$$Q_{13} = Q_{23} = Q_{31} = Q_{32} = 0 \qquad (4D.2)$$

The in-plane stiffness matrix [A], the coupling stiffness matrix [B] and the flexural stiffness matrix [D] can now be determined for the CSM lamina using Equations 4A.8 and replacing with the stiffness matrix [Q] whose elements are given above .

APPENDIX 4E. CALCULATION OF STIFFNESS OF A COMPLETELY DELAMINATED LAMINATE.

In the case of multiphase materials with n phases the following relationship holds:

$$E = \sum_{i=1}^{n} E_i V_i \qquad (4E.1)$$

where: E is the total elastic modulus of the multiphase material.

E_i is the modulus of phase number i.

V_i is the volume fraction of phase number i.

Since the volume fraction is proportional to the thickness ratio (thickness of one phase

to total laminate thickness), Equation 4E.1 can be written as:

$$E = \frac{1}{t} \sum_{i=1}^{n} E_i \; t_i \qquad (4E.2)$$

where: t is the total laminate thickness.

t_i is the thickness of phase number i.

If we assume that the laminate completely delaminates, as shown in Figure 4E.1, then we can assume that each sublaminate caused by the complete delaminations can be treated as a "phase j" in the above equations (O'Brien,1982). Re-writing Equation 4E.2 we have:

$$E^* = \frac{\sum_{j=1}^{n} E_j \; t_j}{t} \qquad (4E.3)$$

where: E^* is the stiffness of a completely delaminated laminate.

E_j is the stiffness of sublaminate number j.

t_j is the thickness of sublaminate number j.

t is the total laminate thickness.

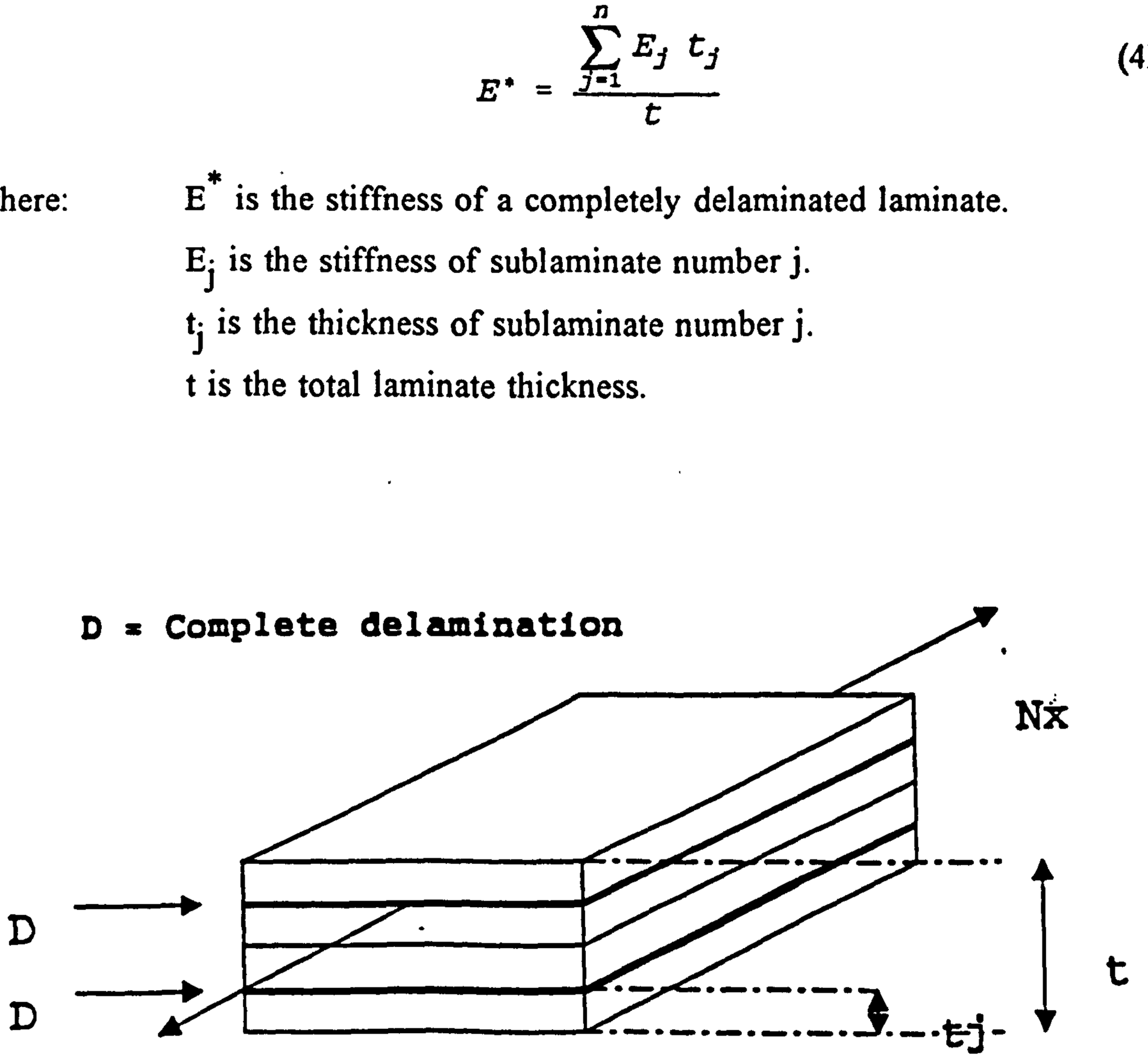

Figure 4E.1 Completely Delaminated Laminate

APPENDIX 4F. CALCULATION OF STIFFNESS OF A PARTIALLY DELAMINATED LAMINATE.

O'Brien, 1982 developed an equation for the stiffness of a partially delaminated laminate, E_p. Figure 4F.1 shows a laminate of width 2b with equal-sized delaminated strips width a along both edges. Assuming that each of the three parts of the laminate can be treated as three phases, an equation for E_p can be formulated as in Equation 4F.1.

$$E_p = \frac{E_{LAM}(2b-2a) + E^*a + E^*a}{2b} \qquad (4F.1)$$

where: E_{LAM} is the stiffness of a laminate with no delaminations
E^* is the stiffness of a completely delaminated laminate

Rearranging Equation 4F.1 yields a relationship for a partially delaminated laminate.

$$E_p = \frac{a}{b}\ [E^*-E_{LAM}] + E_{LAM} \qquad (4F.2)$$

A more general form of Equation 4F.2 can be derived, if it is assumed that the laminate stiffness loss and delamination size are related by Equation 4F.3:

$$\frac{E - E_{LAM}}{E^* - E_{LAM}} = \frac{A}{A^*} \qquad (4F.3)$$

where: A is the delaminated area
A^* is the total interfacial area

Rearranging Equation 4F.3 gives:

$$E = (E^* - E_{LAM})\frac{A}{A^*} + E_{LAM} \qquad (4F.4)$$

of which Equation 4F.2 is a special case when $a/b = A/A^*$

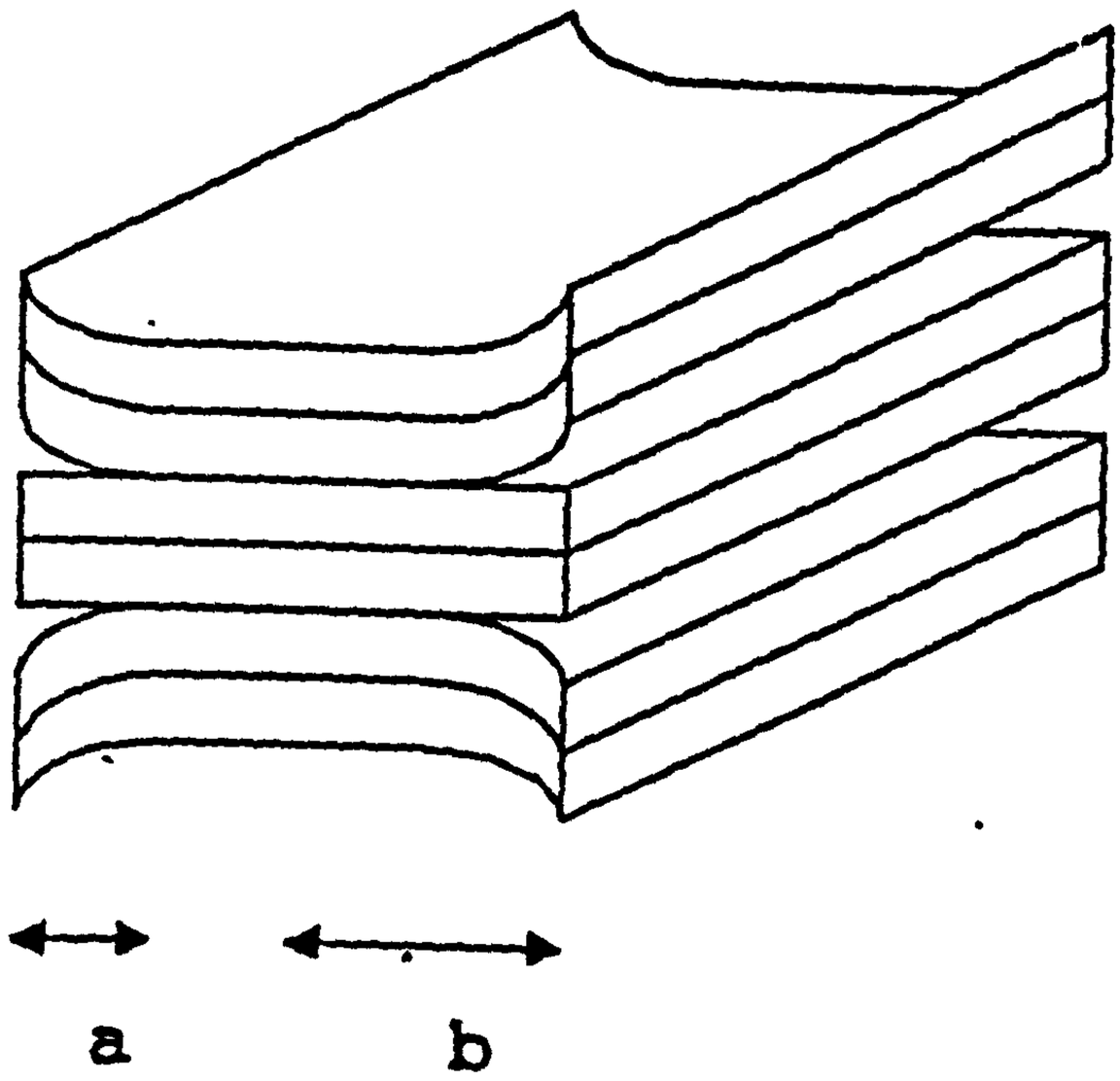

Figure 4F.1 Partially Delaminated Laminate

APPENDIX 4G. DERIVATION OF EQUATION USED TO CALCULATE THE CRITICAL BUCKLING STRESS.

The sign convention for positive moments and forces is shown in Figure 4G.1, where N and Q are the longitudinal and transverse components of force on the cross section, respectively. M is the bending moment.

From the diagram shown in Figure 4G.2, which represents the forces and moments acting on a column element in a deformed configuration, the following analysis can be carried out.

Summation of forces in the x-direction gives:

$$-N\cos\beta-Q\cos(90-\beta)+(N+dN)\cos(\beta+d\beta)+(Q+dQ)\cos(90-(\beta+d\beta)) = 0 \qquad (4G.1)$$

In order that the effect of rotations on the structure can be accounted for, the equilibrium Equations are applied to the structure in a slightly deformed state. For a rotation, β, the square of the rotation is assumed to be small compared with unity. Therefore $\sin\beta$ is replaced by β and $\cos\beta$ replaced by 1.

Now, $\cos\beta=1$

$\cos(90-\beta)=\sin\beta=\beta$

$\cos(\beta+d\beta)=1$

$\cos(90-(\beta+d\beta))=\sin(\beta+d\beta)=\beta+d\beta$ (4G.2)

Substituting Equations (4G.2) into (4G.1) gives:

$$-N+(N+dN)-Q\beta+(Q+dQ)(\beta+d\beta)=0 \qquad (4G.3)$$

which reduces to:

$$\frac{dN}{dx} + Q\frac{d\beta}{dx} + \beta\frac{dQ}{dx} = 0 \qquad (4G.4)$$

Summation of forces in the z-direction gives:

$$N\sin\beta-Q\sin(90-\beta)-(N+dN)\sin(\beta+d\beta)+(Q+dQ)\sin(90-(\beta+d\beta)) = 0 \qquad (4G.5)$$

Substituting Equations (4G.2) into (4G.5) gives:

$$N\beta - Q - (N+dN)(\beta+d\beta) + (Q+dQ) = 0 \qquad (4G.6)$$

which reduces to:

$$-N\frac{d\beta}{dx} - \beta\frac{dN}{dx} + \frac{dQ}{dx} = 0 \qquad (4G.7)$$

Summation of Moments gives:

$$M - (M+dM) + Qdx = 0$$

or,

$$Q = \frac{dM}{dx} \qquad (4G.8)$$

If we are considering slender beams, then transverse shearing stresses and forces are quite small. Therefore, we can assume that all quadratic terms representing nonlinear interaction between small transverse and shearing forces and rotations may be neglected. The equilibrium Equations (4G.4), (4G.7) & (4G.8) become:

$$\frac{dN}{dx} = 0 \qquad (4G.9)$$

$$\frac{dQ}{dx} - N\frac{d\beta}{dx} = 0 \qquad (4G10)$$

$$Q = \frac{dM}{dx} \qquad (4G.8)$$

Substituting Equation (4G.8) in (4G.10):

$$N' = 0 \qquad (4G11)$$

$$M'' - N\beta' = 0 \qquad (4G12)$$

Also, $\beta = -w'$ (4G13)

and $M = -EIw''$ (4G14)

where: ' is the first differential w.r.t. x.

" is the second differential w.r.t. x.

w is the deflection in the z-direction.

E is the Young's Modulus.

I is the cross-section second moment of area.

Substituting Equations (4G.13) and (4G.14) into (4G. 12) we have:

$$(EIw'')'' - Nw'' = 0$$

and for constant EI,

$$EIw^{iv} - Nw'' = 0 \qquad (4G.15)$$

From Equation (4G.11) it appears that N=constant in x, but from boundary conditions we see that for x=0,L, N=-P.

Hence, Equation (4G.15) can be written as:

$$w^{iv} + \lambda^2 w'' = 0 \qquad (4G16)$$

where:

$$\lambda^2 = \frac{P}{EI} \qquad (4G.17)$$

or in the case of a plate,

$$\lambda^2 = \frac{P}{D^*} \qquad (4G.18)$$

where:

$$D^* = \frac{Et^3}{12(1-\nu^2)} \qquad (4G.19)$$

and υ is the Poisson ratio.

Equation (4G.16) applies to each of the three parts shown in Figure 4G.3.

So for the three parts, i=1,2,3 and the following Equation holds:

$$w_i^{iv} + \lambda_i^2 w_i'' = 0 \qquad (4G20)$$

where:

$$\lambda_i^2 = \frac{P_i}{D_i^*} \qquad ; \qquad D_i^* = \frac{Et_i^3}{12\,(1-\nu^2)} \qquad (4G.21)$$

and

P_i is the axial force per unit length in the i^{th} part.

D_i^* is the stiffness of the i^{th} part.

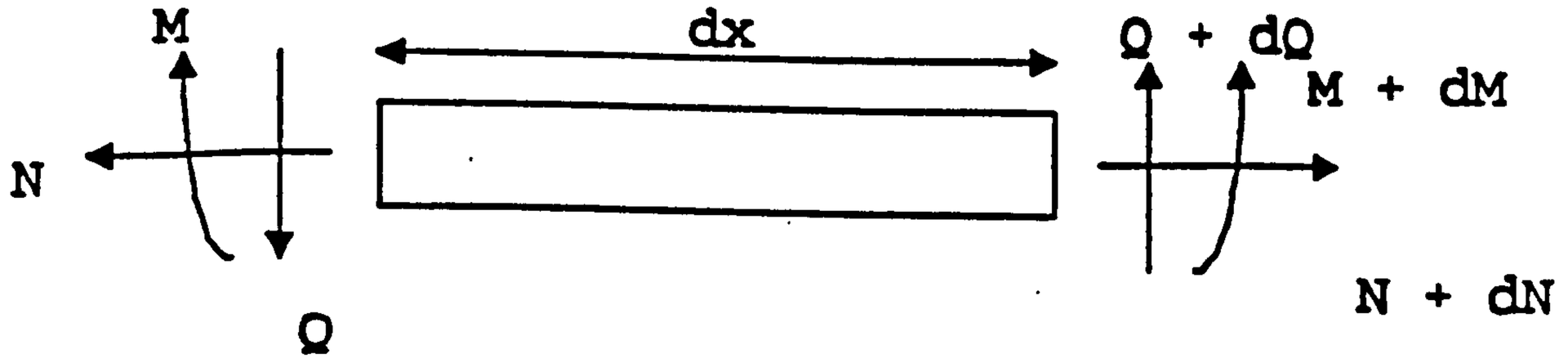

Figure 4G.1 Sign conventions for Positive Moments and Forces

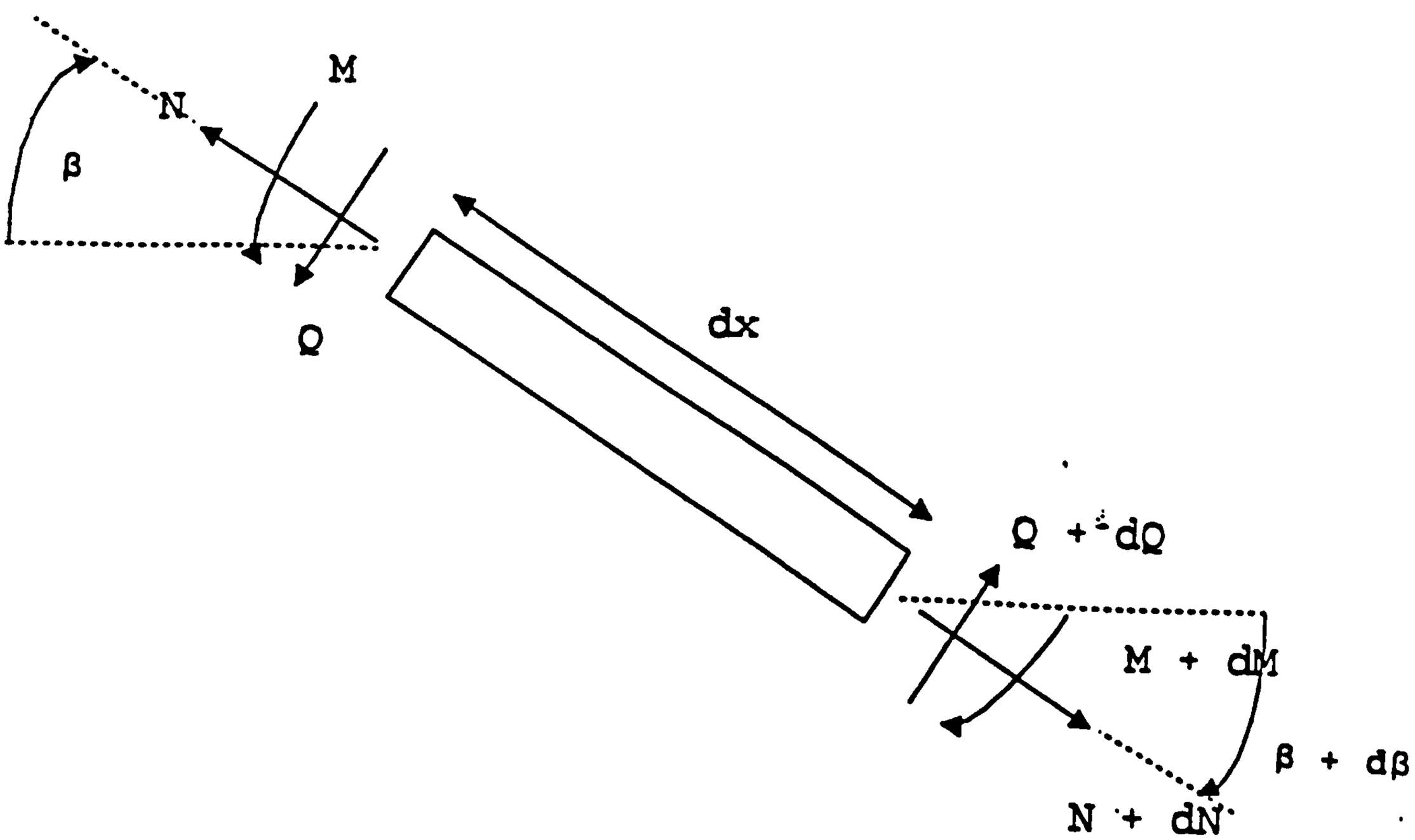

Figure 4G.2 Forces and Moments acting on a Column Element in a Deformed Configuration

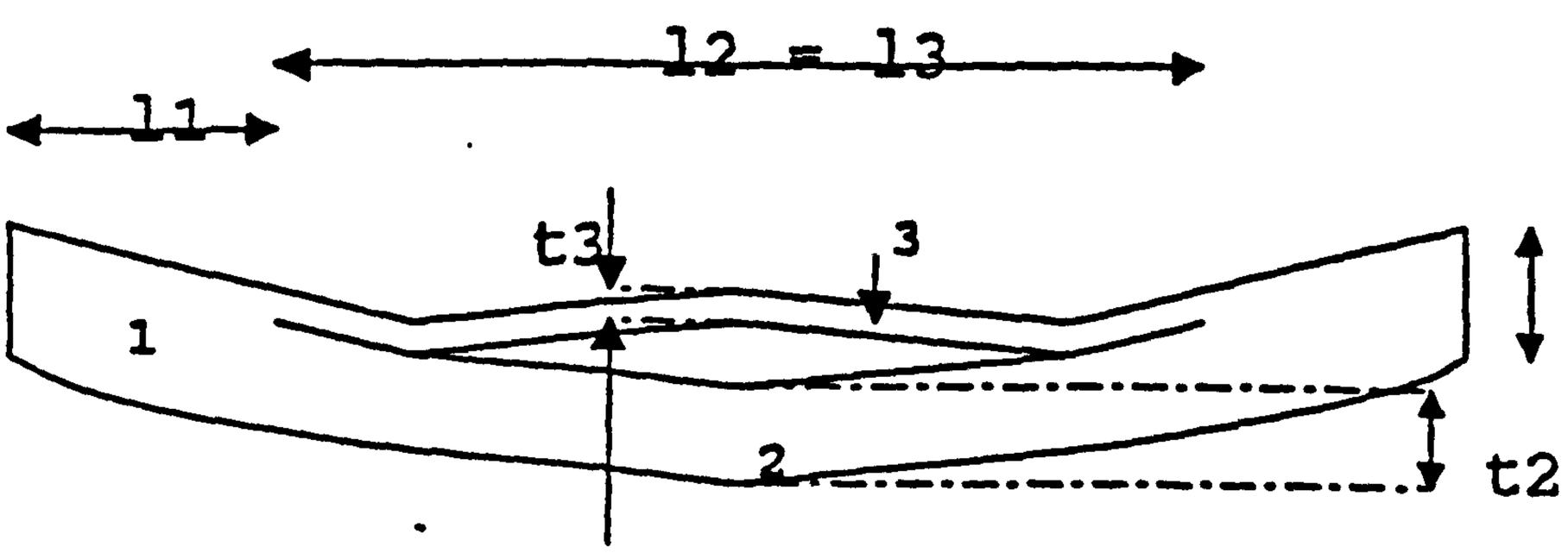

Figure 4G.3 Three Regions of a Delaminated Beam

APPENDIX 4H. THREE DIMENSIONAL SOLID ELEMENTS USED IN FE ANALYSIS

The elements used to generate the three dimensional (3D) finite element model are 3D structural solid elements. The element is defined by eight nodes each having three degrees of freedom: translations in the nodal x, y, and z directions. Figure 4H.1 shows the geometry, node locations and the coordinate system for the element.

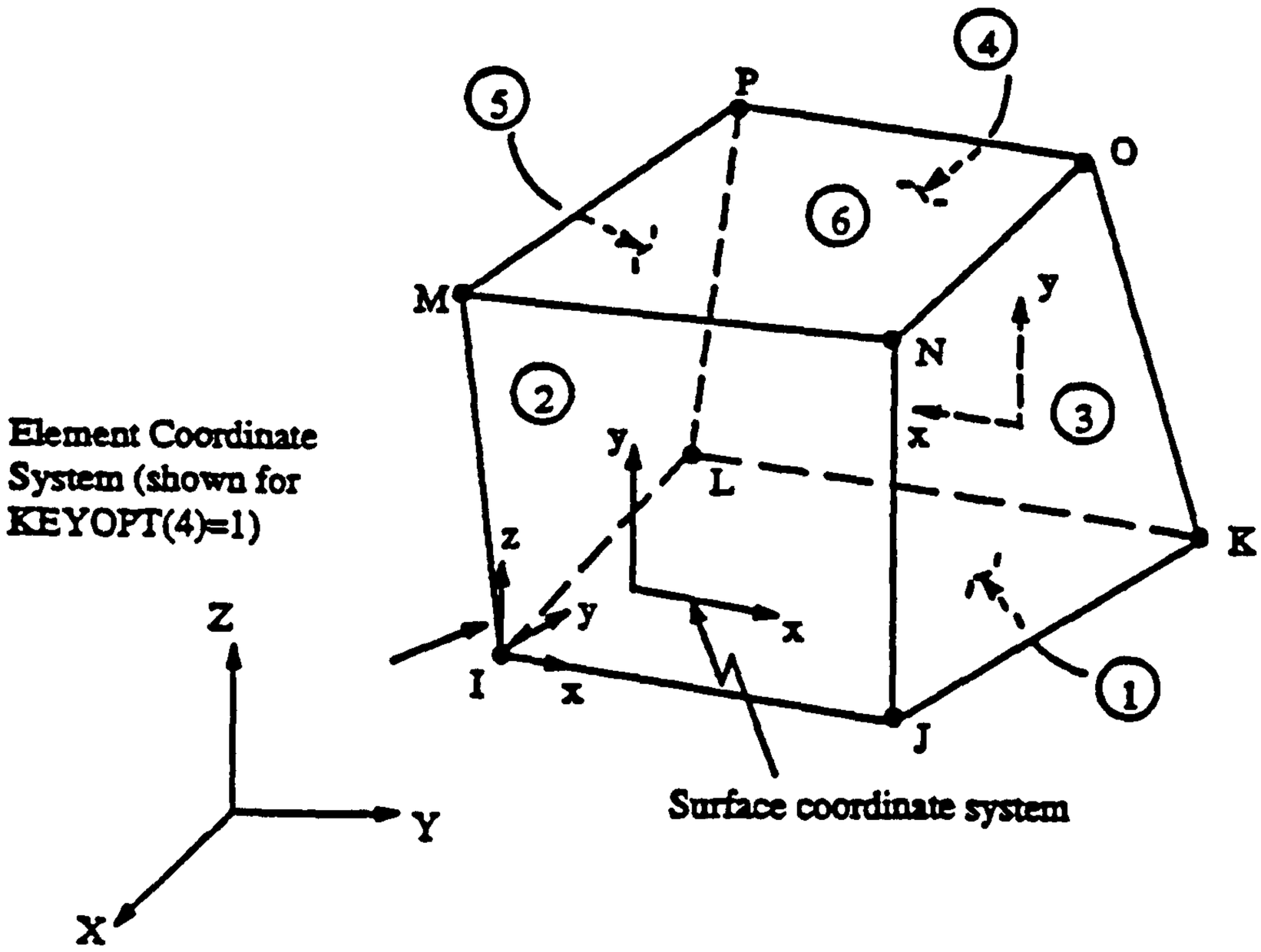

Figure 4H.1 3D Solid Element

APPENDIX 4I. DETAILS OF FE BUCKLING ANALYSIS

Two techniques are available in the ANSYS finite element package for predicting the buckling load and buckling mode shape of a structure. These are a nonlinear buckling analysis and eigenvalue (or linear) buckling analysis. Only the eigenvalue buckling analysis is discussed here as this is the type which has been used in the analysis.

The eigenvalue buckling analysis predicts the theoretical buckling strength of an ideal linear elastic structure. i.e. one which does not contain imperfections, plastic behaviour and does not possess large deflections. This method corresponds to the textbook approach to elastic buckling analysis. For example, an eigenvalue buckling analysis of a column will exactly match the classical Euler solution (Timoshenko & Young). Generally, however real structures do not achieve their theoretical elastic buckling strength, their actual buckling stress is below this level. Figure 4I.1 shows the Load-Deflection Curve for both the nonlinear and eigenvalue buckling curve. The eigenvalue buckling analysis has been carried out in order to calculate the highest possible value of the critical buckling stress. It must be noted, however, that this method often yield unconservative results and should not, therefore, be used for the design or evaluation of actual structures.

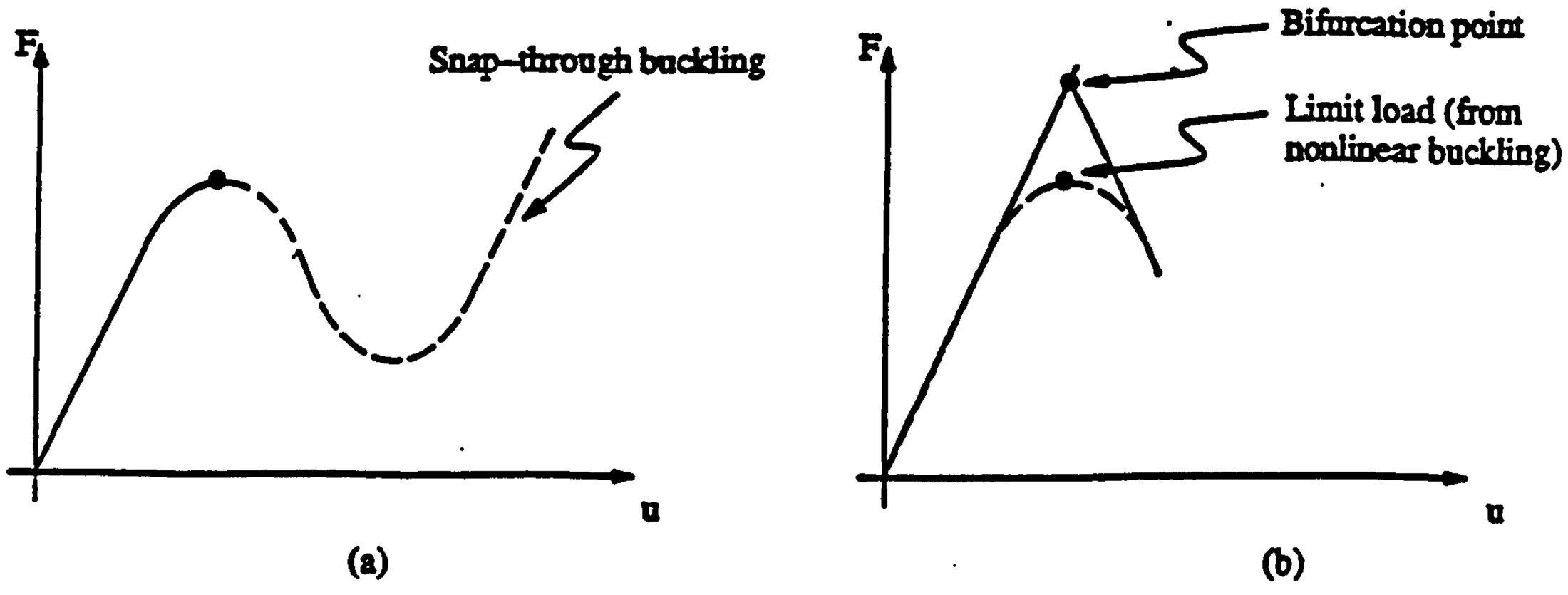

Figure 4I.1 Buckling Curves:

(a) Non-Linear Load-Deflection Curve

(b) Linear (Eigenvalue) Buckling Curve

APPENDIX 4J. TWO DIMENSIONAL STRUCTURAL SOLID ELEMENTS USED IN THE FE ANALYSIS

The element can be used either as a plane stress or plane stress element. It is defined by four nodes each having two degrees of freedom: translations in the nodal x and y directions. The geometry, node locations and the coordinate system for the element is shown in Figure 4J.1.

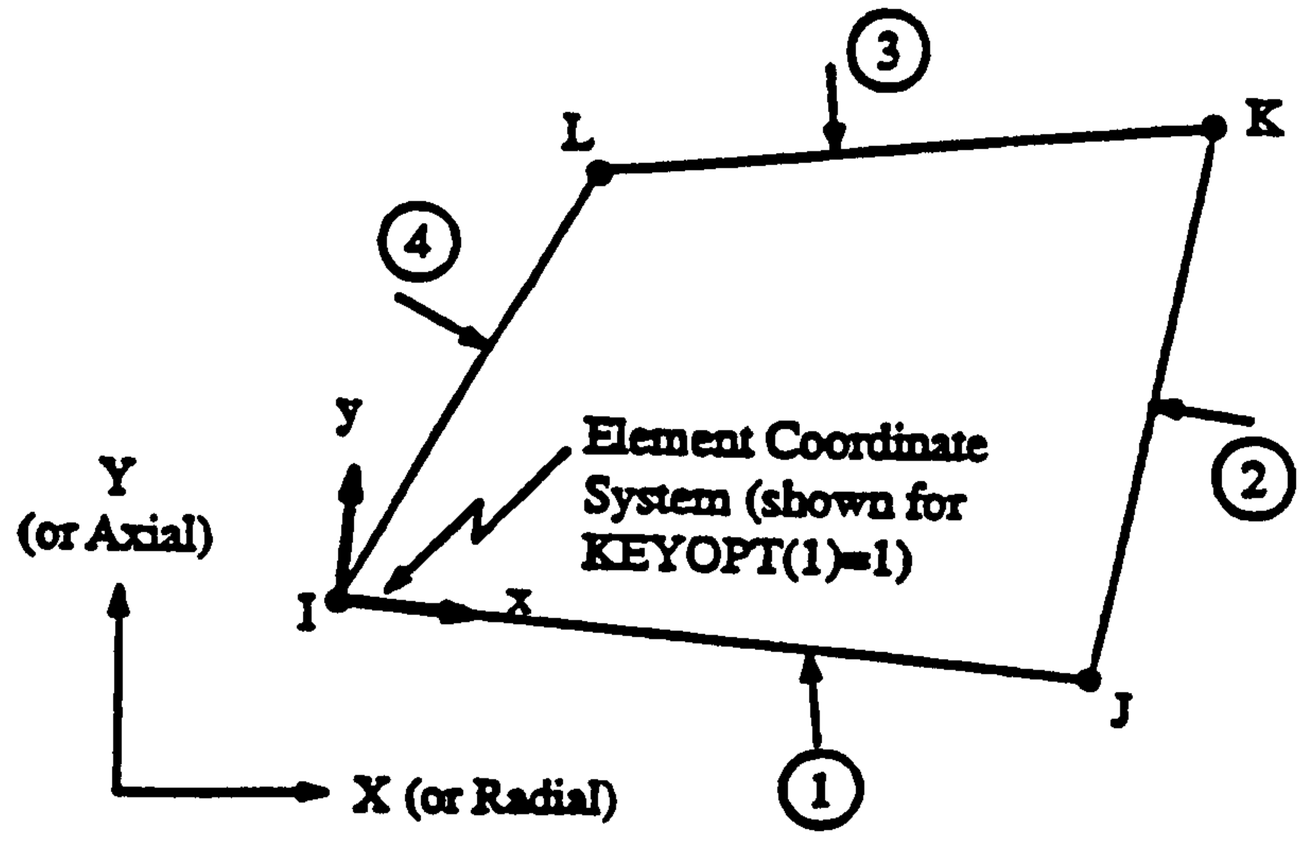

Figure 4J.1 2D Structural Solid Element

APPENDIX 4K. TWO DIMENSIONAL CRACK ELEMENTS USED IN THE FE ANALYSIS

The elements used to represent cracks in finite element models are six-noded triangular structural solid elements. The geometry and node locations are shown in Figure 4K.1. Each node has two degrees of freedom being translations in the nodal x and y directions. The midside nodes (labelled L and N) may be moved to the quarter point towards node I if a singularity is required at node I.

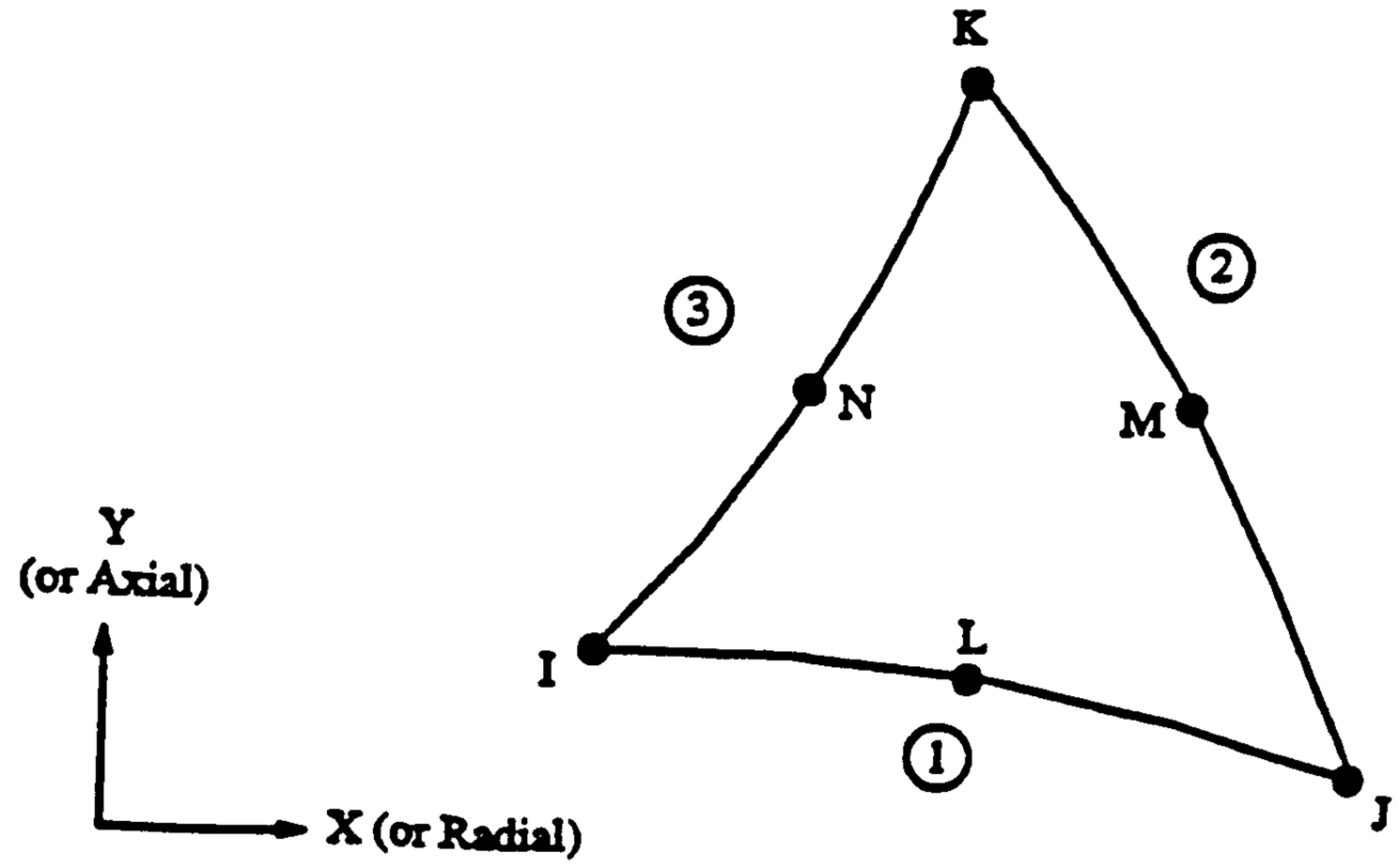

Figure 4K.1 2D Triangular Structural Solid Elements

APPENDIX 6A. COMPARISON BETWEEN 3D AND 2D FINITE ELEMENT TEE JOINT MODELS

6A.1 Three Dimensional (3D) Model

This model was generated using two element types, namely the 3D structural solid element, details of which can be found in Appendix 4H and the 3D layered structural solid element, details of which are given in Appendix 6B. A 3D layered structural solid element was selected in order to represent any number of layers. This type is used in the overlaminate, web and flange. In addition, 3D structural solid elements are used in the fillet. In an experimental three-point bend simulated load, the flange plate is supported by rollers on both sides and a load is applied across the centre of the flange plate

6A.2 Two Dimensional (2D) Model

The elements used to generate the models are 2D structural solid elements which have been used in FE models in Chapter 4 and whose characteristics are given in Appendix 4J. Plane strain conditions are assumed to prevail in the 2D models since the joints on board ships can be considered wide in relation to the length and thickness. One element is modelled per layer of the overlaminate material. For the 2D models, the finite element load is equal to the applied load per unit width of the joint which in this case is 100 mm. Constraints for the 2D case mirrored those adopted for the 3D model.

6A.3 Comparison of 3D and 2D Models

For the purposes of the comparison between the 3D and 2D models only, since the loading and geometric configuration of the joints is symmetrical, only half the joint has been modelled in each case.

It is necessary to compare the relative stiffness and strength of the 2D and 3D tee joint models in order to verify that no accuracy is lost if 2D models are to be used for further analyses. The stiffness and strength representations of both the 3D and the 2D models are discussed in Sections 6A.3.2 and 6A.3.3 respectively.

6A.3.1 Assumed Loads

The load applied to each of the 3D and the 2D models was equivalent to an actual three point bending load of 5500 N. This corresponds to the load at which the experimental load-deflection curve for a tee joint under a three point bending load becomes non-linear (Elliott, 1994).

6A.3.2 Initial Stiffness Comparison

Table 6A.1 gives the deflection values for both the 3D and the 2D models which have been calculated at a load of 5500 N. The deflection value for the 2D model is approximately 5 % lower than that for the 3D model, i.e the 2D model is very slightly stiffer than the 3D model.

6A.3.3 Load Transfer Mechanisms

Table 6A.2 gives the maximum in-plane stress ($\sigma_{i\text{-}p}$) and maximum through-thickness stress ($\sigma_{t\text{-}t}$) in the overlaminate and also the maximum principal stresses (σ_p) and strains (ϵ_p) in the fillet. It can be noted that all the results for the 2D model are very similar to those for the 3D model. For example, the maximum through-thickness stress in the overlaminate for the 2D model is only 3 % higher than that for the 3D model. This indicates that the load is transferred within the 2D and 3D models in a similar manner.

As a result of both the stiffness and strength investigations it has been shown that very little accuracy will be lost if 2D models are used as opposed to 3D models. Thus, all further analyses have been generated in two dimensions.

FE MODEL	MAXIMUM DEFLECTION (mm)
3D	3.2128
2D	3.0447

Table 6A.1 Comparison of Maximum Deflections for 2D and 3D Models.

	FILLET		OVERLAMINATE	
MODEL	σ_p (MPa)	ϵ_p (MPa)	$\sigma_{i\text{-}p}$ (MPa)	$\sigma_{t\text{-}t}$ (MPa)
3D	9.532	0.0057	51.704	6.214
2D	8.541	0.0054	53.065	6.314

Table 6A.2 Comparison of Maximum Stresses for 2D and 3D Models.

APPENDIX 6B. THREE DIMENSIONAL LAYERED SOLID ELEMENTS USED IN THE FE ANALYSIS

Figure 6B.1 shows the geometry and coordinate system of the 3D layered structural solid element used in the finite element generation of a tee joint. Each element is defined by eight nodes each with three translational degrees of freedom. The element allows up to 100 material layers through the thickness.

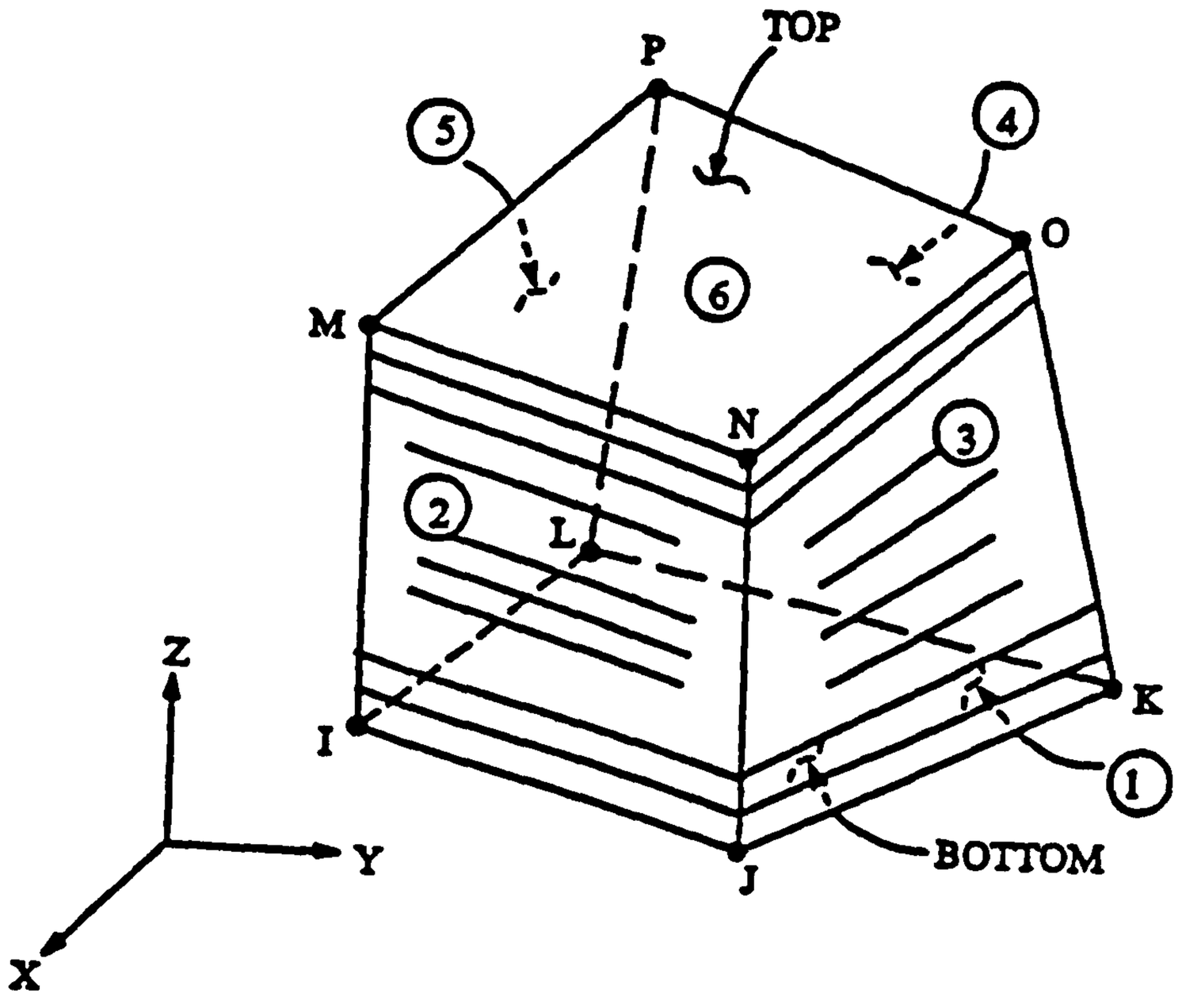

Figure 6B.1 3D Layered Structural Solid Element

APPENDIX 7A. GAP ELEMENTS USED IN THE FINITE ELEMENT CRACK MODELS

The element used in the finite element crack models to prevent the two crack faces from overlapping is a 2D 'point to point' contact element defined by two nodes each having two degrees of freedom. These are translations in the x and y directions. The two nodes may be coincident if required. The element is capable of supporting only compression in the direction normal to its surfaces and also shear in the tangential direction. Figure 7A.1 shows the geometry, node locations and the coordinate system for this element.

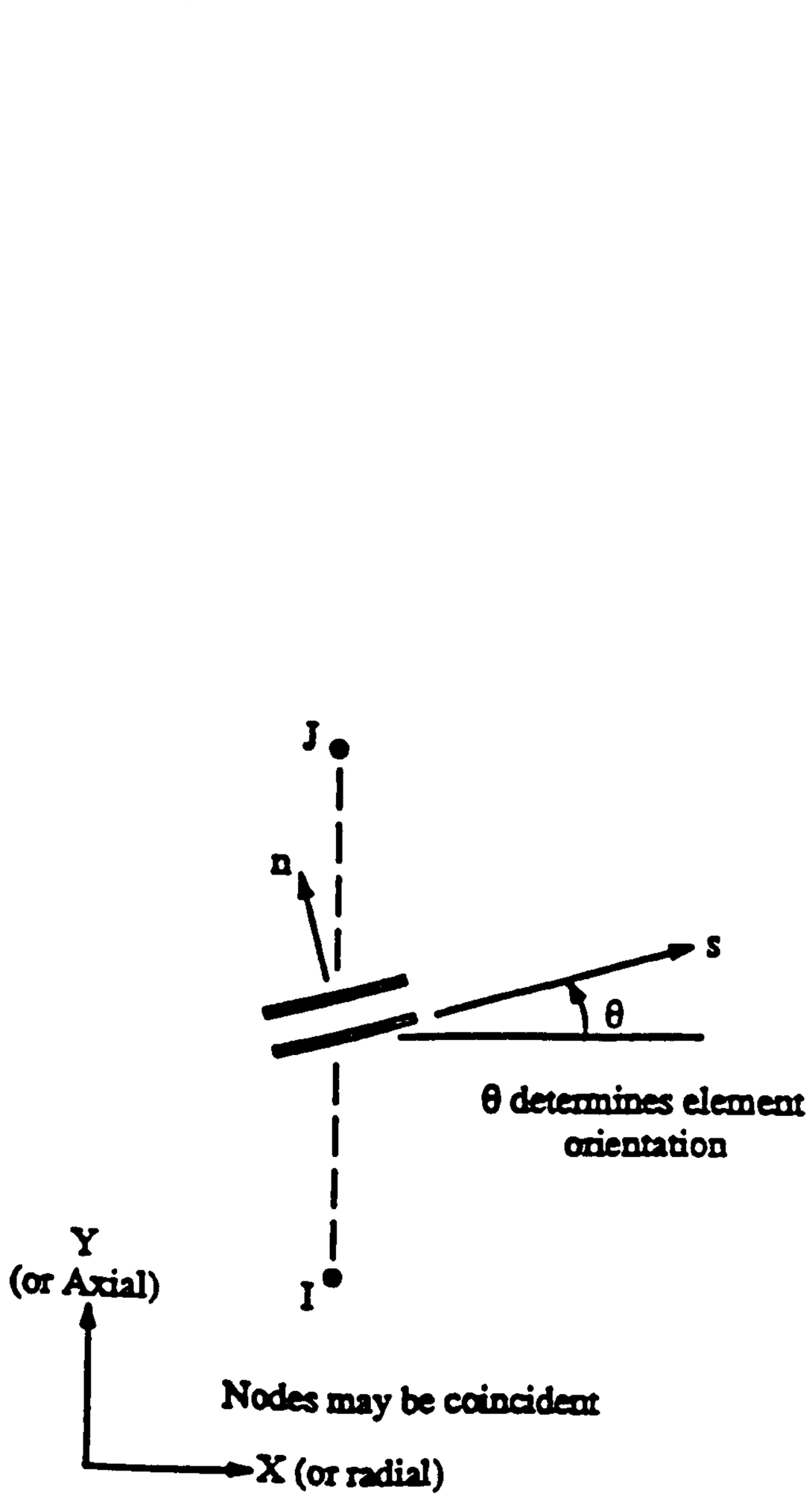

Figure 7A.1 Two Dimensional Point-to-Point Contact Element

APPENDIX 8A. METHOD OF INSERTING CRACK ELEMENTS INTO AN EXISTING FE MODEL

In order to insert crack elements into an existing 2D tee joint model it has been necessary to ensure node compatibility. i.e that nodes belonging to the six-noded crack elements also defined the elements on the outer edge of the existing FE model. However, since the crack elements are six-noded, it had to be ensured that the third (central) node on the outer edge was not generated since the existing FE model is generated from four-noded elements. Figure 8A.1 shows the problem diagrammatically. To prevent this occurring, it was necessary to force the crack elements around the edge of the cracked region to only use two nodes in the definition of their outside edges and thus be compatible with the rest of the tee joint model.

The steps involved in inserting the cracked region in the existing tee joint model are as follows:

(1) Delete the elements of the existing tee joint model which are to be replaced by crack elements.

(2) Generate two-noded 'beam' elements along the boundary between the existing tee joint model and the cracked region. Ensure that the nodes of the beam elements are coincident with the existing nodes of the tee joint model.

(3) Select the two nodes which are to be the crack tips and ensure that a singularity will be present at these nodes by moving the midside nodes of the surrounding crack elements (see Appendix 4K).

(4) Define appropriate areas of the cracked region used to define the crack.

(5) Mesh the areas of the cracked region with crack elements. The elements around the edge of the cracked region will automatically have only two nodes defining their outside edges due to the existence of the two-noded beam elements.

(6) Delete the beam elements as they are only required in the model generation.

(7) Select the nodes along each interface of the cracked region and the rest of the model and merge the node numbers. This ensures that the nodes along the interfaces are truly coincident and that each node along the interface is defining the crack element and the existing tee joint element. This is shown in Figure 8A.2.

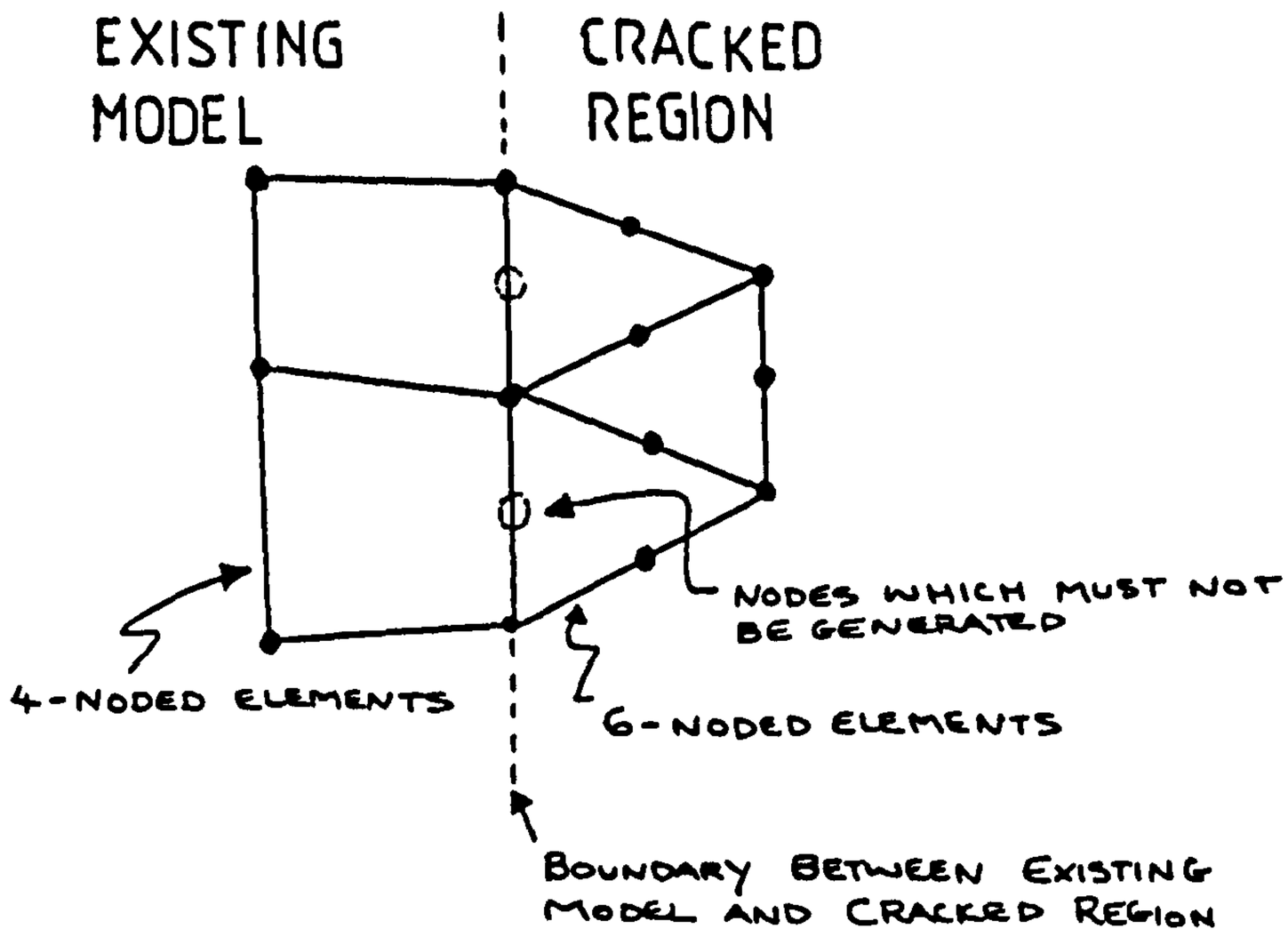

Figure 8A.1 Problem of Inserting Crack Elements into an Existing Model

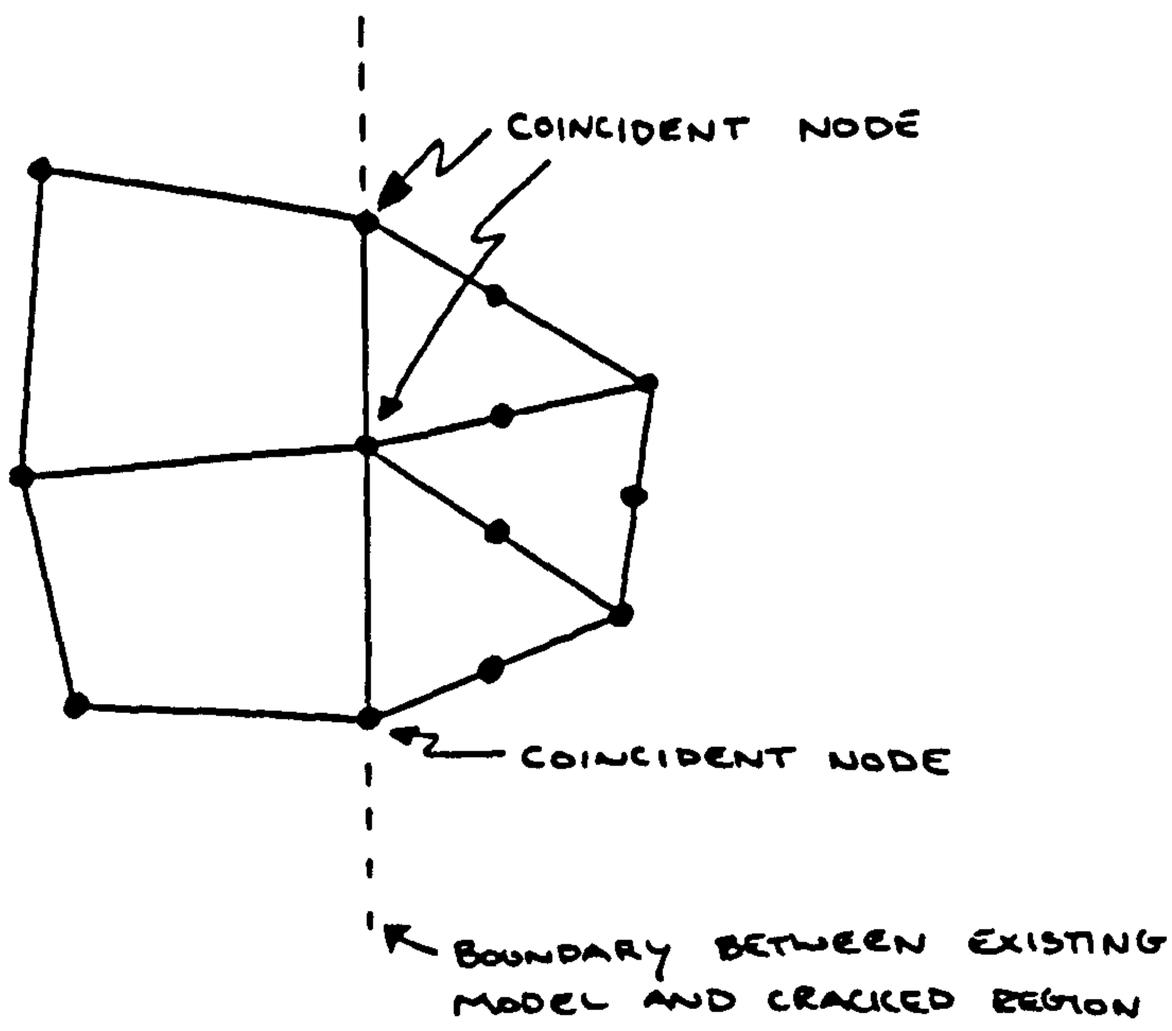

Figure 8A.2 Crack Elements Successfully Inserted into Existing Model with Coincident Nodes along Interface

APPENDIX 8B. ADAPTED MACRO USED IN THE CALCULATION OF THE J - INTEGRAL.

The existing macro available in the FE software package assumes that the crack face is parallel to the global x-direction of the entire model and that the global y-direction is perpendicular to the crack face as shown in Figure 8B.1. This is very restricting since this is not always the case. In the current work, varying curved crack lengths need to be analysed which therefore changes the angle of the crack face to the global x coordinate. Initially, it was thought that the entire model could be rotated so as to make the crack face parallel to the global x coordinate but this proved to be very complicated. Instead, the existing macro has been adapted so that the J-integral could be calculated for a crack tip whose face was at any orientation. The adapted macro is shown at the end of this Appendix.

In the case where curved cracks are being analysed, the tip of the crack must be linear in order that the J-integral can be calculated. A computer program has been written which calculates the angle, θ, through which the local coordinate system at the crack tip must be rotated so that the local x coordinate is parallel to (or anti-parallel to) the global x-direction of the model. The local and global coordinate systems and theta are shown in Figure 8B.2.

The required input to the adapted macro includes:

E	Young's modulus of crack elements (MPa)
NU	Poisson's ratio of the crack elements
CRX	Crack tip x-coordinate in global coordinates (mm)
CRY	Crack tip y-coordinate in global coordinates (mm)
THETA	Value of theta calculated from computer program (radians) (see Figure 8B.2)
POS	Position of crack tip relative to the global coordinate system (see Figure 8B.3)
ROTA	Position of Crack Face Coordinate Axes (see Figure 8B.4)

<u>Calculation of the rotation angle, theta, for use in the adapted macro.</u>

Figure 8B.2 represents a typical left hand crack tip along with its local crack tip

coordinate system. The global crack tip coordinate system is also shown. In order to calculate either the strain energy release rate or the J-integral, it is necessary to locate the local crack tip x-coordinate parallel to the crack face and the local y-coordinate perpendicular to the crack face. The required input to the program used to calculate theta is described below:

(1) CR Crack tip coordinates in cylindrical coordinates (r in mm)
The crack face nodes have been generated using a cylindrical coordinate system in order to generate the crack around the radius of the overlaminate and is shown in Figure 8B.5. The coordinates of the crack tip is required in cylindrical coordinates i.e (r,θ).

(2) GCEX The centre of the cylindrical coordinate system defined in global coordinates (x in mm).
The centre of the cylindrical coordinate system used to generate the crack face nodes is required in global coordinates.

(3) GCTX The coordinates of the crack tip in global coordinates (x in mm)

(4) GCTY The coordinates of the crack tip in global coordinates (y in mm)

(5) GAX The coordinates of the end of the straight part of the crack face in global coordinates (x in mm)

(6) GAY The coordinates of the end of the straight part of the crack face in global coordinates (y in mm)

As mentioned, whilst generating a curved crack, it is necessary to generate a straight region close to the crack tip as shown in Figure 8B.6. The global coordinates required in (5) and (6) are those of the opposite end of the straight region from the crack tip.

Once the value of theta, θ, has been calculated then the local crack tip coordinate system can be located and the values of the strain energy release rate and the J-integral can be calculated using the adapted macro.

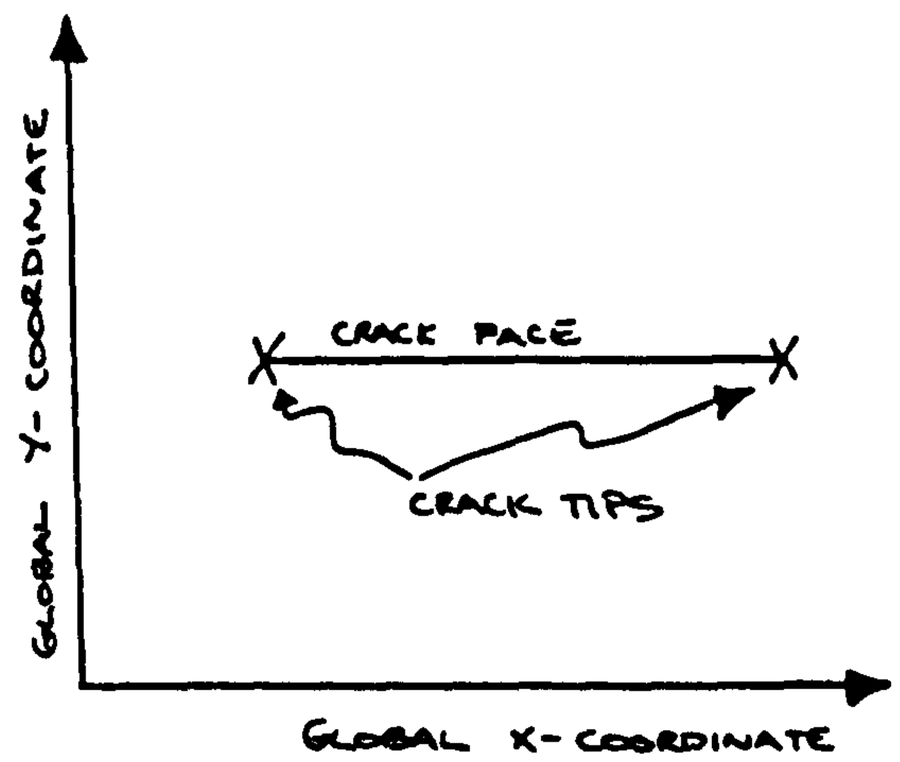

Figure 8B.1 Assumed Crack Coordinate System for use with the Existing Macro

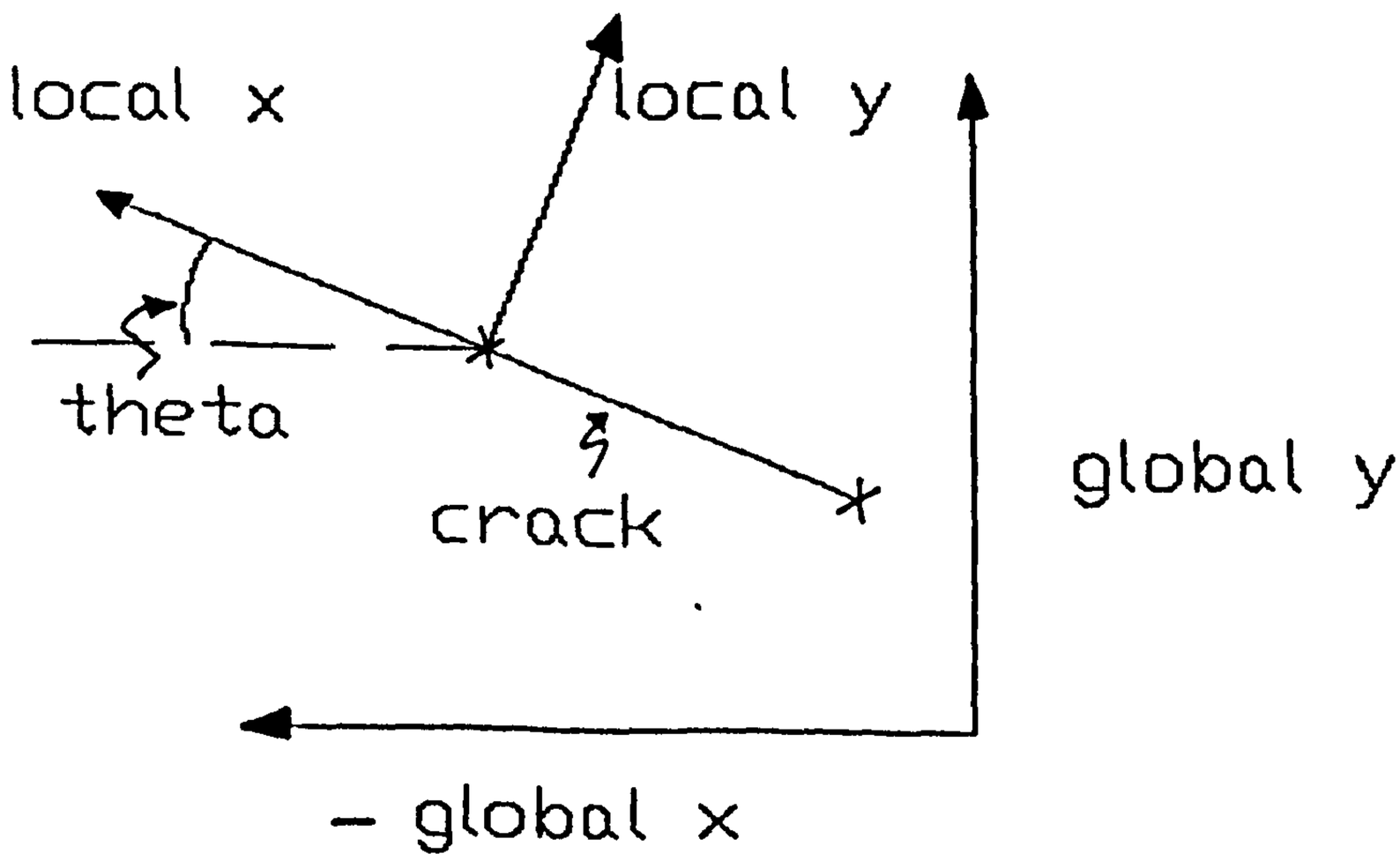

Figure 8B.2 Assumed Location of the Crack for use with the Adapted Macro

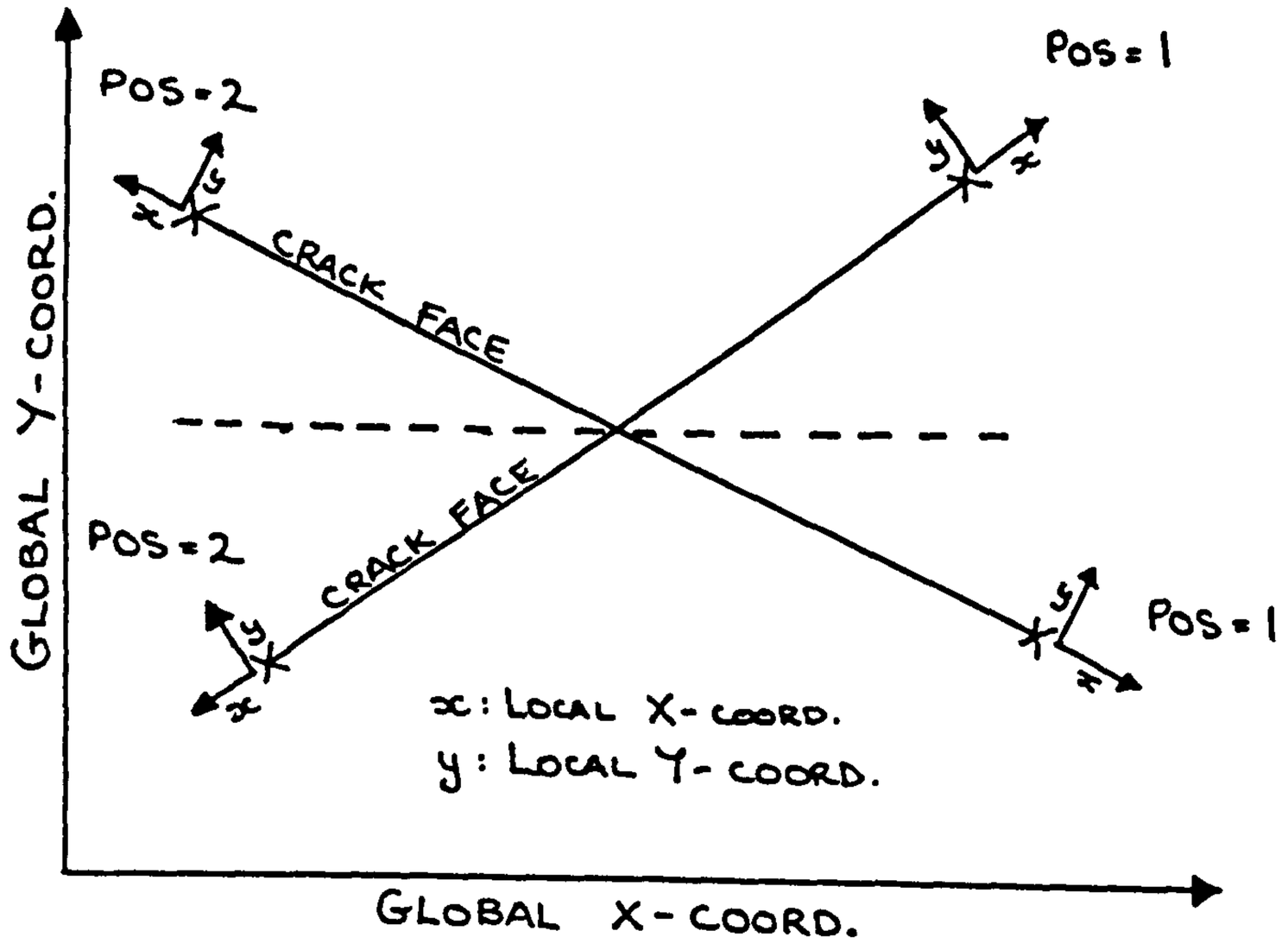

Figure 8B.3 Definition of the Parameter 'POS' in the Adapted Macro

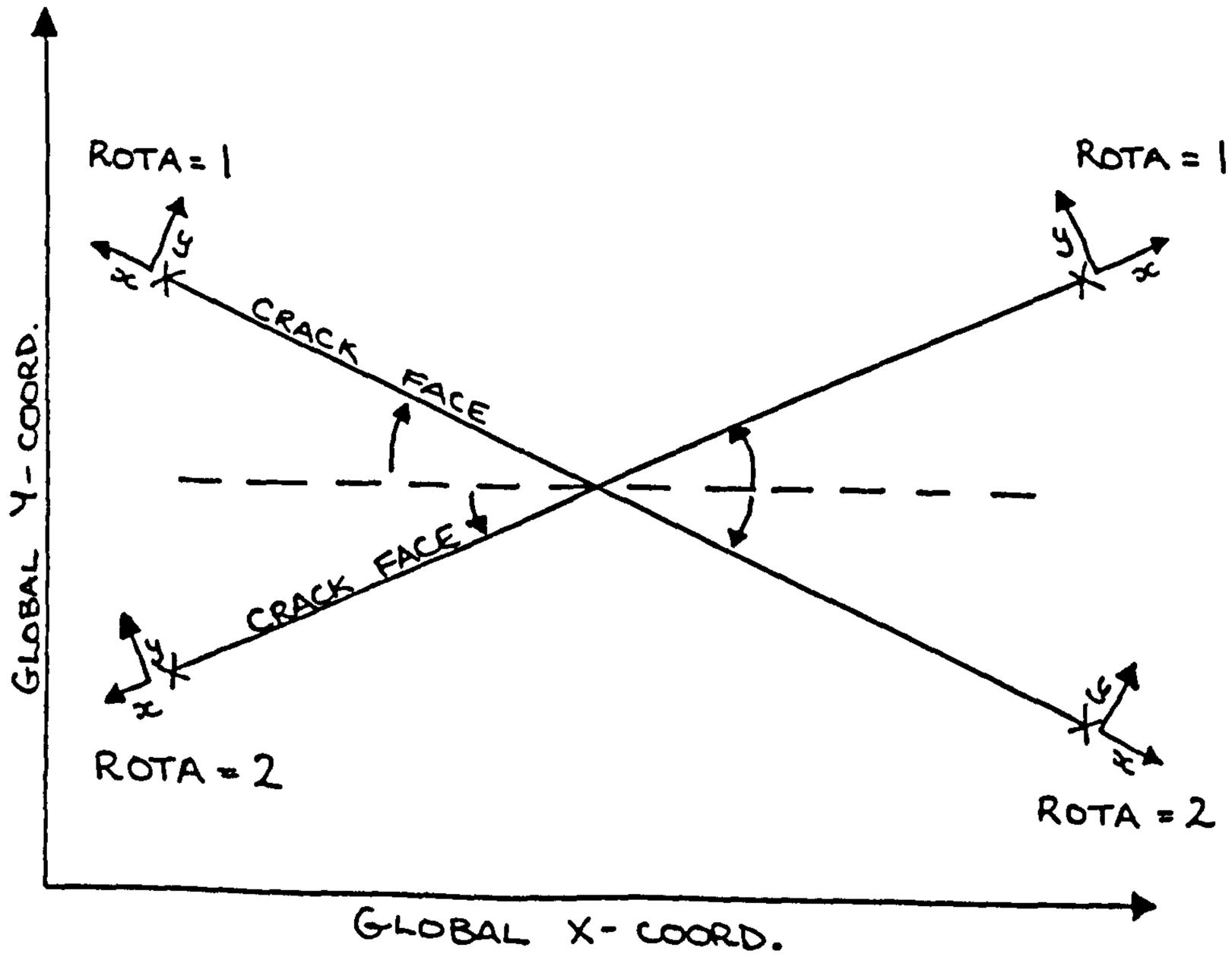

Figure 8B.4 Definition of the Parameter 'ROTA' in the Adapted Macro

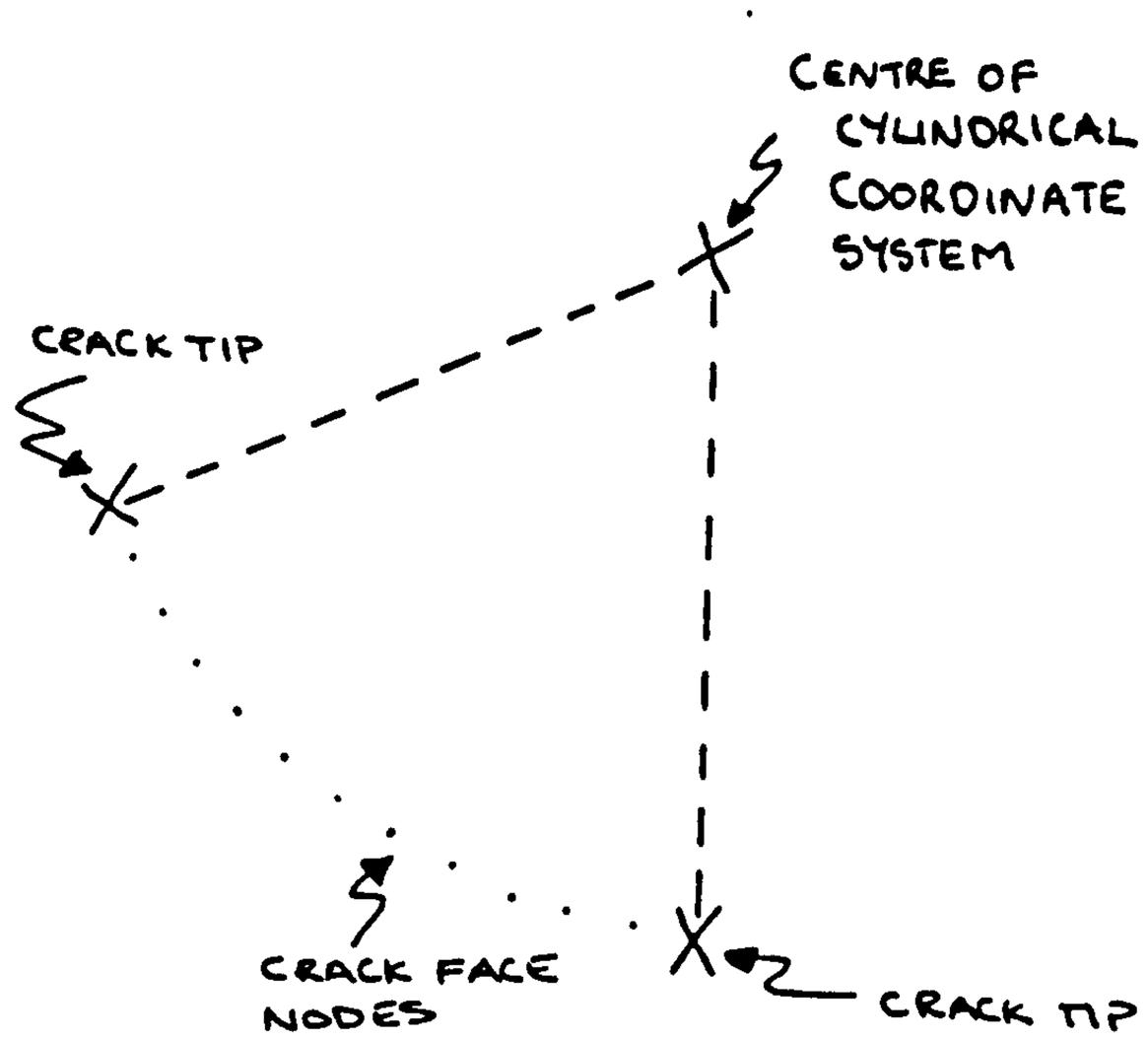

Figure 8B.5 Position of the Cylindrical Coordinate System used to Generate the Crack Face Nodes

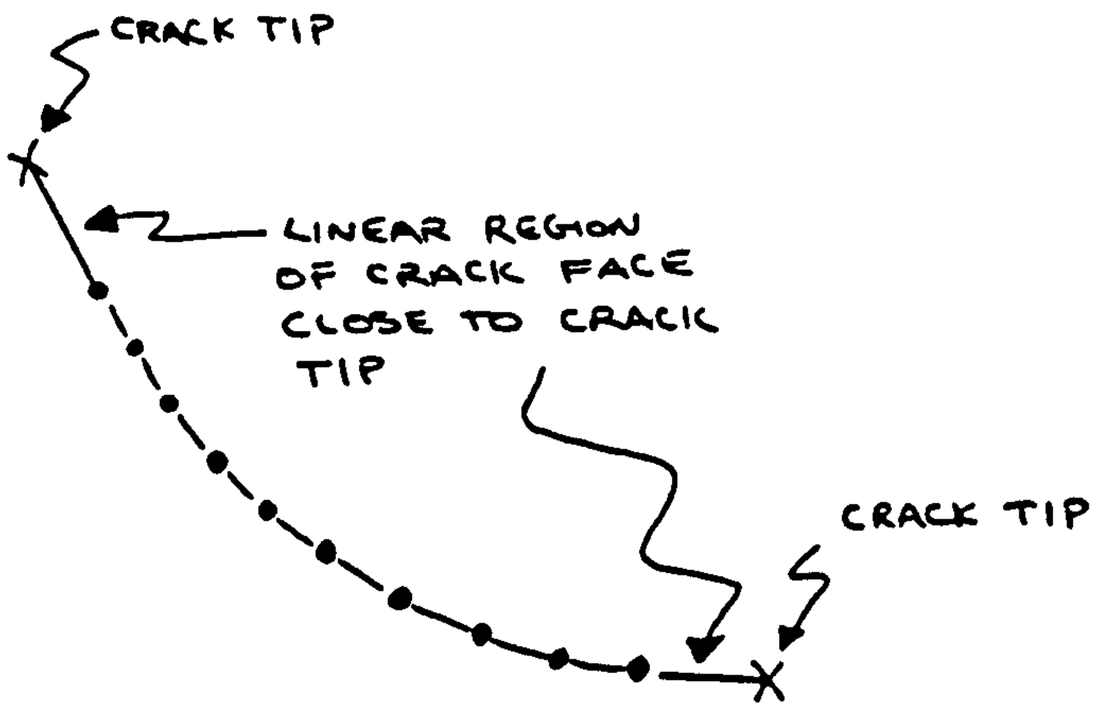

Figure 8B.6 Linear Crack Face close to the Crack Tip

Computer Listings.

(A) Adapted macro used to calculate the J-integral for cracks at any orientation to the global coordinate system.

(B) Computer program used to calculate the rotation angle of the crack local coordinate system. (for input into the adapted macro in (A)).

(A)

```
/nopr
C***
C***
C***    MACRO ADAPTED FROM EXISTING ANSYS MACRO *JIN2.MAC* BY;
C***
C***    HOLLY PHILLIPS
C***    DEPARTMENT OF SHIP SCIENCE
C***    UNIVERSITY OF SOUTHAMPTON
C***    HIGHFIELD
C***    SOUTHAMPTON
C***    SO17 1BJ
C***    UK
C***
C***       AUGUST 1995
C***
C**************** CALCULATE J-INTEGRAL FOR CRACKS WHICH ARE NOT ***********
C**************** NECESSARILY PARALLEL TO THE GLOBAL X-DIRECTION ***********
C***
C******************CHANGE GLOBAL COORDINATES TO LOCAL COORDINATES********
C*************************************************************************
C***
C***    GLOBAL COORDINATES CHANGED FIRST TO A DUMMY COORDINATE SYSTEM
C***    FOR WHICH THE DUMMY POSITIVE X-COORDINATE IS PARALLEL OR ANTI-PARALLEL
C***    TO THE GLOBAL POSITIVE X-COORDINATE.
C***
C***    THE DUMMY POSITIVE Y-COORDINATE MUST BE PARALLEL TO THE GLOBAL
C***    POSITIVE Y-DIRECTION
C***
C***    THIS MACRO IS FOR HALF MODELS. IF IT IS USED FOR FULL MODEL ANALYSES
C***    THEN THE RESULTING VALUE OF THE J-INTEGRAL, JINT, MUST BE HALVED
C***
C***
PDEF,S1,S,1                 * PUT STRESS SIG1 ON THE PATH
PDEF,S2,S,2                 * PUT STRESS SIG2 ON THE PATH
PDEF,S3,S,3                 * PUT STRESS SIG3 ON THE PATH
PCALC,MULT,C11,S1,S1        * CALCULATE STRAIN ENERGY DENSITY FROM PRINCIPAL
PCALC,MULT,C22,S2,S2        *    STRESS COMPONENTS:
PCALC,MULT,C33,S3,S3        *    W = (1/2E)*(S1*S1 + S2*S2 + S3*S3)
PCALC,MULT,C12,S1,S2        *      - (NU/E)*(S1*S2 + S2*S3 + S3*S1)
PCALC,MULT,C23,S2,S3
PCALC,MULT,C31,S3,S1
C=(1/(2*E))
PCALC,ADD,SUM1,C11,C22
PCALC,ADD,SUM1,SUM1,C33,C,C
C=NU/E
PCALC,ADD,SUM2,C12,C23
PCALC,ADD,SUM2,SUM2,C31,C,C
PCALC,ADD,W,SUM1,SUM2,1,-1
PVECT,NORM,NX,NY,NZ         * DEFINE PATH UNIT NORMAL VECTOR
PDEF,SX,S,X                 * PUT STRESS SX ON THE PATH
PDEF,SY,S,Y                 * PUT STRESS SY ON THE PATH
PDEF,SXY,S,XY               * PUT STRESS SXY ON THE PATH
PCALC,MULT,TX,SX,NX         * CALCULATE TRACTION TX
PCALC,MULT,C1,SXY,NY        *   TX = SX*NX + SXY*NY
PCALC,ADD,TX,TX,C1
PCALC,MULT,TY,SXY,NX        * CALCULATE TRACTION TY
PCALC,MULT,C1,SY,NY         *   TY = SXY*NX + SY*NY
PCALC,ADD,TY,TY,C1
*GET,DX,PATH,,LAST,S        * PATH SHIFT DX IS 1% OF PATH LENGTH S
DX=DX/100
```

```
T=TAN(THETA)                * THETA IS THE ROTATION ANGLE IN RADIANS
C=COS(THETA)                * OF THE DUMMY COORDINATE SYSTEM TO THE LOCAL
SI=SIN(THETA)               * COORDINATE SYSTEM
*IF,POS,EQ,1,THEN           * IF POS = 1 THEN DUMMY X PARALLEL TO GLOBAL X
PCALC,ADD,YD,YG,,,,-CRY     * YD IS DUMMY Y COORDINATE
PCALC,ADD,XD,XG,,,,-CRX     * XD IS DUMMY X COORDINATE
*ELSE                       * IF POS = 2 THEN DUMMY X ANTI-PARALLEL TO
PCALC,ADD,YD,YG,,,,-CRY     * GLOBAL X
PCALC,ADD,XD,XG,,-1.0,,CRX
*ENDIF
*IF,THETA,EQ,0.0,THEN       * IF DUMMY COORDINATE SYSTEM AND LOCAL COORDINATE
PCALC,ADD,XL,XD             * SYSTEM ARE THE SAME THEN THETA = 0
PCALC,ADD,YL,YD             * XL IS LOCAL X COORDINATE
*ELSE                       * YL IS LOCAL Y COORDINATE
*IF,ROTA,EQ,1,THEN
PCALC,ADD,AD,XD,,T
PCALC,ADD,A,YD,AD,,-1.0     * IF THETA DOES NOT EQUAL 0 NEED TO TRANSFORM
PCALC,ADD,B,A,,SI           * DUMMY COORDINATES TO LOCAL COORDINATES
PCALC,ADD,CD,XD,,1/C        * ALSO ASSUMES DUMMY TO LOCAL ROTATION IS POSITIVE
PCALC,ADD,XL,CD,B
PCALC,ADD,D,XD,,T
PCALC,ADD,E,YD,D,,-1.0
PCALC,ADD,YL,E,,C
*ELSE
PCALC,ADD,AD,XD,,T
PCALC,ADD,A,YD,AD,,1.0      * IF THETA DOES NOT EQUAL 0 NEED TO TRANSFORM
PCALC,ADD,B,A,,SI           * DUMMY COORDINATES TO LOCAL COORDINATES
PCALC,ADD,CD,XD,,1/C        * ALSO ASSUMES DUMMY TO LOCAL ROTATION IS NEGATIVE
PCALC,ADD,XL,CD,B,,-1.0
PCALC,ADD,D,XD,,T
PCALC,ADD,E,YD,D,,1.0
PCALC,ADD,YL,E,,C
*ENDIF
*ENDIF
PCALC,INTG,J,W,YL           * INTEGRATE ENERGY W.R.T. LOCAL Y
*GET,JA,PATH,,LAST,J        * GET FINAL TERM OF INTEGRAL FOR 1ST TERM OF J
PCALC,ADD,XL,XL,,,,-DX/2    * SHIFT PATH FROM XL TO XL-DX/2 (LOCAL X DIR.)
PCALC,ADD,XL1,XL            * XL1 AND YL1 GIVE COORDINATES OF NEW PATH IN LOCAL
PCALC,ADD,YL1,YL            * COORDINATES
*IF,THETA,EQ,0.0,THEN       * NOW SHIFT NEW LOCAL PATH COORDINATES BACK TO DUMMY
PCALC,ADD,XR,XL
PCALC,ADD,YR,YL
*ELSE
*IF,ROTA,EQ,1,THEN
PCALC,ADD,Z1,XL,,C
PCALC,ADD,Z2,YL,,SI
PCALC,ADD,XR,Z1,Z2,,-1.0
PCALC,ADD,Z1,YL,,1/C
PCALC,ADD,Z2,XR,,T
PCALC,ADD,YR,Z1,Z2
*ELSE
PCALC,ADD,Z1,XL,,C
PCALC,ADD,Z2,YL,,SI
PCALC,ADD,XR,Z1,Z2,,1.0
PCALC,ADD,Z1,YL,,1/C
PCALC,ADD,Z2,XR,,T
PCALC,ADD,YR,Z1,Z2,,-1.0
*ENDIF
*ENDIF
*IF,POS,EQ,1,THEN           * SHIFT NEW DUMMY PATH COORDINATES BACK TO GLOBAL
```

```
PCALC,ADD,XG,XR,,,,CRX
PCALC,ADD,YG,YR,,,,CRY
*ELSE
PCALC,ADD,XG,XR,,-1.0,,CRX
PCALC,ADD,YG,YR,,,,CRY
*ENDIF
PCALC,ADD,XG1,XG              * XG1 AND YG1 GIVE NEW PATH COORDINATES IN GLOBAL
PCALC,ADD,YG1,YG
PDEF,UX1,U,X                  * DEFINE UX AT XG1
PDEF,UY1,U,Y                  * DEFINE UY AT XG1
PCALC,ADD,XL,XL,,,,DX         * REPEAT FOR PATH SHIFT FROM XL-DX/2 TO XL+DX/2
PCALC,ADD,XL2,XL
*IF,THETA,EQ,0.0,THEN
PCALC,ADD,XR,XL
PCALC,ADD,YR,YL
*ELSE
*IF,ROTA,EQ,1,THEN
PCALC,ADD,Z1,XL,,C
PCALC,ADD,Z2,YL,,SI
PCALC,ADD,XR,Z1,Z2,,-1.0
PCALC,ADD,Z1,YL,,1/C
PCALC,ADD,Z2,XR,,T
PCALC,ADD,YR,Z1,Z2
*ELSE
PCALC,ADD,Z1,XL,,C
PCALC,ADD,Z2,YL,,SI
PCALC,ADD,XR,Z1,Z2,,1.0
PCALC,ADD,Z1,YL,,1/C
PCALC,ADD,Z2,XR,,T
PCALC,ADD,YR,Z1,Z2,,-1.0
*ENDIF
*ENDIF
*IF,POS,EQ,1,THEN
PCALC,ADD,XG,XR,,,,CRX
PCALC,ADD,YG,YR,,,,CRY
*ELSE
PCALC,ADD,XG,XR,,-1.0,,CRX
PCALC,ADD,YG,YR,,,,CRY
*ENDIF
PDEF,UX2,U,X
PDEF,UY2,U,Y
PCALC,ADD,XL,XL,,,,-DX/2      * SHIFT PATH BACK TO ORIGINAL POSITION IN LOCAL
*IF,THETA,EQ,0.0,THEN
PCALC,ADD,XR,XL
PCALC,ADD,YR,YL
*ELSE
*IF,ROTA,EQ,1,THEN
PCALC,ADD,Z1,XL,,C
PCALC,ADD,Z2,YL,,SI
PCALC,ADD,XR,Z1,Z2,,-1.0
PCALC,ADD,Z1,YL,,1/C
PCALC,ADD,Z2,XR,,T
PCALC,ADD,YR,Z1,Z2
*ELSE
PCALC,ADD,Z1,XL,,C
PCALC,ADD,Z2,YL,,SI
PCALC,ADD,XR,Z1,Z2,,1.0
PCALC,ADD,Z1,YL,,1/C
PCALC,ADD,Z2,XR,,T
PCALC,ADD,YR,Z1,Z2,,-1.0
*ENDIF
*ENDIF
*IF,POS,EQ,1,THEN             * PATH BACK TO ORIGINAL POSITION IN GLOBAL
PCALC,ADD,XG,XR,,,,CRX
PCALC,ADD,YG,YR,,,,CRY
*ELSE
PCALC,ADD,XG,XR,,-1.0,,CRX
PCALC,ADD,YG,YR,,,,CRY
*ENDIF
C=(1/DX)
PCALC,ADD,C1,UX2,UX1,C,-C     * CALCULATE DERIVATIVE DUX/DX
PCALC,ADD,Z1,UY2,UY1,C,-C     * CALCULATE DERIVATIVE DUY/DX
PCALC,MULT,C1,TX,C1           * DEFINE INTEGRAND
PCALC,MULT,Z1,TY,Z1           *    = TX*DUX/DX + TY*DUY/DX
PCALC,ADD,C1,C1,Z1
PCALC,INTG,J,C1,S             * FORM SECOND INTEGRAL (W.R.T. PATH LENGTH S)
*GET,JB,PATH,,LAST,J          * GET FINAL VALUE OF INTEGRAL FOR 2ND TERM OF J
JINT=(2*(JA-JB))              * GET J-INTEGRAL VALUE AND DOUBLE FOR HALF MODELS
/gopr
```

(A) CONT'D

(B)

```
c       program to calculate theta, the rotation angle of the crack tip
c       coordinate system in relation to the negative global x-axis.
c       This is the value of theta which is required in program coord1.f
c       which calculates the path points in local crack tip coordinates.
c
        PROGRAM THETA
        DOUBLE PRECISION THETA,CR,L,GCEX,GCTX,GCTY
        DOUBLE PRECISION ALPHA,BETA,GAMMA,PI,RAD,X,Y,X1
C
        PI=3.141592654
        RAD = (2.0*PI)/360.0
C
        WRITE(*,210)
        READ(*,*)CR
        WRITE(*,250)
        READ(*,*)GCEX
        WRITE(*,270)
        READ(*,*)GCTX
        WRITE(*,280)
        READ(*,*)GCTY
        WRITE(*,290)
        READ(*,*)GAX
        WRITE(*,300)
        READ(*,*)GAY
C
        X = GAX-GCTX
        Y = GCTY-GAY
        L = SQRT((X*X)+(Y*Y))
C
        ALPHA = ACOS((L/2)/CR)
        BETA = (90.0*RAD)-ALPHA
C
        X1 = GCEX-GCTX
C
        GAMMA = ASIN(X1/CR)
        THETA = GAMMA - BETA
C
        WRITE(*,310)ALPHA,BETA,GAMMA,THETA


210     FORMAT(' CRACK TIP COORD. IN CYLIND. COORDS. (r in mm) ')
250     FORMAT(' ENTER GLOBAL CENTRE OF CYLIND. COORDS. SYS. (x- coord.)')
270     FORMAT(' ENTER CRACK TIP COORD. IN GLOBAL COORDS. (x- coord.) ')
280     FORMAT(' ENTER CRACK TIP COORD. IN GLOBAL COORDS. (y- coord.) ')
290     FORMAT(' ENTER LINE END COORD. IN GLOBAL COORDS. (x- coord.) ')
300     FORMAT(' ENTER LINE END COORD. IN GLOBAL COORDS. (y- coord.) ')
310     FORMAT(' A = ',F10.6,' B = ',F10.6,' G = ',F10.6,' T = ',F10.6)

        STOP
        END
```